THE UNIVERSITY
of EDINBURGH

Complexes of Schiff-base macrocycles and donor-expanded dipyrrins for catalysis and uranyl reduction

James Richard Pankhurst
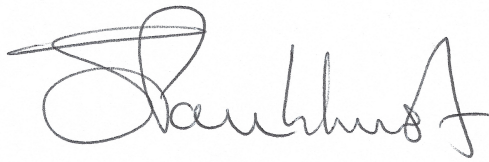
A thesis submitted for the degree of
Doctor of Philosophy

EaStCHEM School of Chemistry
The University of Edinburgh
November 2017

Declaration

The work described in this thesis is entirely my own, except where I have either acknowledged help from a named person or given reference to a published source. This thesis was composed by me and has not been submitted, in whole or in part, for any other degree.

Signature:

Date: 13/11/2017

Lay summary

The work described in this thesis concerns the synthesis and characterisation of metal complexes to explore chemistry related to energy and the environment. Complexes that contain four zinc(II) ions have been prepared and used to turn carbon dioxide and epoxide substrates into polycarbonate materials. Complexes containing one or two ions of copper(II), iron(II), nickel(II) and palladium(II) have been made and tested for their ability to turn carbon dioxide into useful products such as methanol or oxalic acid using electrical current. Turning carbon dioxide into value-added products is desirable as it is a cheap and abundant source of carbon. Furthermore, it is an important area of research as diverting carbon dioxide from entering the atmosphere makes advances towards closing the carbon cycle and reducing our negative impact on the Earth's environment. Other work in this thesis shows that complexes of copper(II) interact with a simple iron(III) salt, $FeCl_3$, and carry out the oxygenation of hydrocarbon compounds; turning C-H bonds into C-O bonds is a fundamental chemical transformation, and doing so under mild conditions using cheap metals such as copper and iron is desirable from an industrial perspective. Finally, complexes of uranium (in the form of uranyl, UO_2^{2+}) have been synthesised. The reduction chemistry of uranium is explored, and the supporting ligand is shown to carry out a new uranium reduction mechanism. This latter study holds relevance to the treatment of nuclear waste and the environmental remediation of uranium.

Abstract

The modern world faces a number of challenges related to energy and the environment. Atmospheric levels of carbon dioxide have now surpassed the 400 ppm mark due to the burning of fossil fuels, yet despite its abundance and potential use as a C_1 feedstock for value-added products, there are both thermodynamic and kinetic barriers associated with the strong carbon-oxygen bonds that preclude its widespread deployment in industry. Nuclear energy is an alternative power source that reduces carbon emissions by billions of tonnes each year, but there are widespread concerns regarding the treatment of the radioactive waste that it accrues (of which the main component is uranyl, $[UO_2]^{2+}$). Most of the work presented in this thesis concerns the synthesis of transition-metal complexes, with the aim of directing catalytic reactivity to convert CO_2 to useful products. Part of this thesis also concerns the synthesis of uranyl complexes and the study of uranyl reduction chemistry, which is relevant to uranyl remediation and nuclear waste treatment at a fundamental level. Making use of Earth-abundant metals to carry out hydrocarbon oxidation catalysis is a further focus of this work, as the efficient production of oxygenated compounds under mild conditions is of importance to the fine-chemical industry.

Chapter 1 reviews important complexes reported in the literature that successfully convert CO_2 to useful products through molecular, homogenous electrocatalysis and ring-opening copolymerisation catalysis. Reactions that exemplify a two-electron reduction of uranyl (*i.e.* uranium(VI) to uranium(IV)) are reviewed, along with uranyl complexes that undergo ligand-centred redox to give ligand-based radicals. The state of the literature on hydrocarbon oxidation catalysis is reviewed in the introduction. The development of multinuclear, macrocyclic complexes and the reactivity of dinuclear Pacman complexes are also presented.

Chapter 2 reports the synthesis and characterisation of a new set of Schiff-base macrocycles and acyclic dipyrrin ligands. A number of attempted synthetic routes towards incorporating a dipyrrin coordination compartment in a macrocyclic setting are discussed. Differences in electronic structures between dipyrromethanes and dipyrromethenes are also examined by theoretical and experimental methods.

Chapter 3 introduces the coordination chemistry of these new macrocycles with zinc(II), where the isolation of dinuclear and tetranuclear complexes is demonstrated using different zinc(II) precursors. Tetranuclear zinc-alkyl complexes presented here are shown to be resistant to insertion chemistry with small molecules, but readily form zinc-oxo, -hydroxyl and -alkoxide clusters upon protonolysis with water and alcohols. These molecular clusters display reactivity towards CO_2: a zinc-hydroxyl complex precipitates $ZnCO_3$ at high temperature; and zinc-alkoxide complexes have been used to catalyse the copolymerisation reaction between CO_2 and cyclohexene oxide to form polycarbonates.

Chapter 4 describes the synthesis of late-transition-metal complexes of macrocyclic ligands and dipyrrins, and explores the relationship between macrocycle geometry and electronic structure. Their reactivities towards CO_2 are assessed here, using cyclic voltammetry to assess the electro-catalytic activity of a number of the complexes.

Chapter 5 reports the oxidation chemistry of hydrocarbon substrates catalysed by copper(II) complexes. High-temperature catalysis occurs with bimetallic copper(II) complexes, and this chapter describes how added $FeCl_3$ acts as a co-catalyst, leading to greater catalyst stability and allowing the catalytic reaction to occur at room temperature. A range of analytical methods have been used to deduce the catalytically active species, and chemical kinetic measurements have been used to deduce a possible reaction mechanism.

Chapter 6 reports the synthesis of a uranyl(VI) dipyrrin complex and details characterisation of its electronic structure by theoretical and experimental methods. Theoretical modelling has indicated that the observed two-electron reduction of uranium(VI) to uranium(IV) is facilitated by the dipyrrin ligand, representing a novel uranyl reduction mechanism.

Acknowledgements

Publications

A list of publications associated with this thesis:

[1] J. R. Pankhurst, T. Cadenbach, D. Betz, C. Finn and J. B. Love, "Towards dipyrrins: oxidation and metalation of acyclic and macrocyclic Schiff-base dipyrromethanes", *Dalton Trans.*, 2015, **44**, 2066-2070;

[2] T. Cadenbach, J. R. Pankhurst, T. A. Hofmann, M. Curcio, P. L. Arnold and J. B. Love, "Macrocyclic platforms for the construction of tetranuclear oxo and hydroxo zinc clusters", *Organometallics*, 2015, **34**, 2608-2613;

[3] J. R. Pankhurst, M. Zegke, L. N. Platts, N. L. Bell, C. A. Lamfsus, L. Maron, L. S. Natrajan, S. Sproules, P. L. Arnold and J. B. Love, "Inner-sphere vs. outer-sphere reduction of uranyl supported by a redox-active, donor-expanded dipyrrin", *Chem. Sci.*, 2017, **8**, 108-116.

Other work published through collaborations:

[4] J. A. Hlina, J. R. Pankhurst, N. Kaltsoyannis and P. L. Arnold, "Metal-metal bonding in uranium-group 10 complexes", *J. Am. Chem. Soc.*, 2016, **138**, 3333-3345;

[5] J. A. Hlina, J. A. L. Wells, J. R. Pankhurst, J. B. Love and P. L. Arnold, "Uranium rhodium bonding in heterometallic complexes", *Dalton Trans.*, 2017, **46**, 5540-5545;

[6] M. Curcio, J. R. Pankhurst, S. Sproules, D. Mignard and J. B. Love, "Triggering redox activity in a thiophene compound: radical stabilization and coordination chemistry", *Angew. Chem. Int. Ed.*, 2017, **56**, 7939-7943;

[7] C. Jandl, J. R. Pankhurst, J. B. Love and A. Pöthig, "Rational synthesis and electronic structure of functionalized trinuclear Pd metal sheet sandwich complexes", *Organometallics*, 2017, **36**, 2772-2783;

[8] S. Hohloch,[†] J. R. Pankhurst,[†] E. E. Jaekel, B. F. Parker, D. J. Lussier, M. E. Garner, C. H. Booth, J. B. Love and J. Arnold, "Benzoquinonoid-bridged dinuclear actinide complexes", *Dalton Trans.*, 2017, **46**, 11615-11625.

Abbreviations

ROCOP	Ring-opening copolymerisation	(TD)DFT	(Time dependent) Density functional theory
ROP	Ring-opening polymerisation	HOMO	Highest occupied molecular orbital
CHO	Cyclohexene oxide	LUMO	Lowest unoccupied molecular orbital
PO	Propylene oxide	SOMO	Singly-occupied molecular orbital
TOF	Turnover frequency	PCM	Polarisable continuum model
TON	Turnover number	NBO	Natural bond order
PCHC	Poly(cyclohexyl carbonate)	(R)ECP	(Relativistic) Effective core potential
PCHO	Poly(cyclohexene oxide)	BDI	β-Diketiminate
SEC	Size-exclusion chromatography	Fc	Ferrocene
PDI	Poly-dispersity index	Fc$^+$	Ferrocenium
NMR	Nuclear magnetic resonance	DIBAL	Diisobutylaluminium hydride
DEPT	Distortionless enhancement by polarisation transfer	BODIPY	Boron dipyrromethene
COSY	Correlation spectroscopy	TFA	Trifluoroacetic acid
HOESY	Heteronuclear nuclear Overhauser effect spectroscopy	PTSA	*para*-Toluenesulfonic acid
(N)IR	(Near) Infra-red	TMEDA	N,N,N',N'-Tetramethylethylene-diamine
UV-vis	Ultra-violet / visible	DMAP	N,N-Dimethylaminopyridine
GC-MS	Gas chromatography mass spectrometry	Cyclam	1,4,8,11-Tetraazacyclotetradecane
TLC	Thin-layer chromatography	DHA	9,10-Dihydroanthracene
FT-ICR	Fourier transfer ion cyclotron resonance	MPPH	2-Methyl-1-phenylpropan-2-yl hydroperoxide
EI	Electron ionisation	MPPOL	2-Methyl-1-phenylpropan-2-ol
ESI	Electro-spray ionisation	HAA	Hydrogen-atom abstraction
MALDI-ToF	Matrix-assisted LASER desorption/ ionisation time-of-flight	MMO	Methane mono-oxygenase
CV	Cyclic voltammetry	TBHP	*tert*-Butyl hydroperoxide
LSV	Linear-sweep voltammetry	BDE	Bond dissociation energy
SWV	Square-wave voltammetry	ILW	Intermediate-level [nuclear] waste
CPE	Controlled-potential electrolysis	HLW	High-level [nuclear] waste
RVC	Reticulated vitreous carbon	PUREX	Plutonium uranium redox extraction
NHE	Normal hydrogen electrode	TBP	*tert*-Butyl phosphate
EXAFS	Extended X-ray absorption fine structure	ESTOC	European station for time series in the ocean of the Canary Islands
CSD	Cambridge structural database		

Contents

Contents

List of Schemes

List of Figures

List of Tables

Chapter 1

Introduction

1.1 Towards closing the carbon cycle

For millions of years, the concentration of carbon dioxide in the environment has been moderated by a closed carbon cycle. This is evident from analysis of ice cores drilled in Lake Vostok, Antartica, which contain air that has been trapped for hundreds of thousands of years. They indicate that the historic peak CO_2 concentration in the atmosphere was below 300 ppm (Figure 1.1 (a)).[1,2] However, since the Industrial Revolution, anthropogenic activity has disrupted the carbon cycle, and has caused a growing rise in atmospheric CO_2 levels through the burning of fossil fuels; once a long-term carbon sink. In 2013 alone, CO_2 emissions amounted to 32.2 Gt (4.52 t per capita).[3] Ongoing atmospheric measurements are taken at Mauna Loa, Hawaii, and show that CO_2 levels have now surpassed the 400 ppm mark (Figure 1.1 (a)).[4] These growing levels of atmospheric CO_2 are exacerbated by deforestation, which is taking place on a massive scale, further reducing the Earth's natural capability to remove CO_2 from the atmosphere. Whilst there are widespread concerns over the effects of increased levels of atmospheric CO_2 and other greenhouse gases on modern global warming and climate change, these effects remain a widely disputed topic.[5] However, further data from Vostok show that there is a distinct and direct correlation between CO_2 concentration and temperature, spanning a 200 ky period, and covering multiple and abrupt glaciation cycles on Earth; historic temperatures are inferred from the the ^{2}H and ^{18}O content in ice.[6]

The oceans are a natural carbon sink, dissolving between a quarter and a third of all atmospheric CO_2 emissions, although it is projected that in the long-term, around 90 % of emissions will be taken up by the ocean.[7] In the ocean, CO_2 forms carbonic acid (H_2CO_3) and bicarbonate (HCO_3^-).[8] There is a distinct correlation between rising levels of atmospheric CO_2 and increasing levels of dissolved CO_2 in

the ocean,[9] and this is accompanied by a decrease in the pH (Figure 1.1 (b); data recorded at ESTOC[i] station, NW Africa).[10,11] Many oceanic lifeforms, such as shellfish and coral, are highly dependent on alkaline pH levels, as they make use of carbonate ions (CO_3^{2-}) to form their calcareous skeletons. The combustion of fossil fuels therefore ultimately results in shell dissolution, decreased metabolism and increased mortality rates in these lifeforms.[12,13]
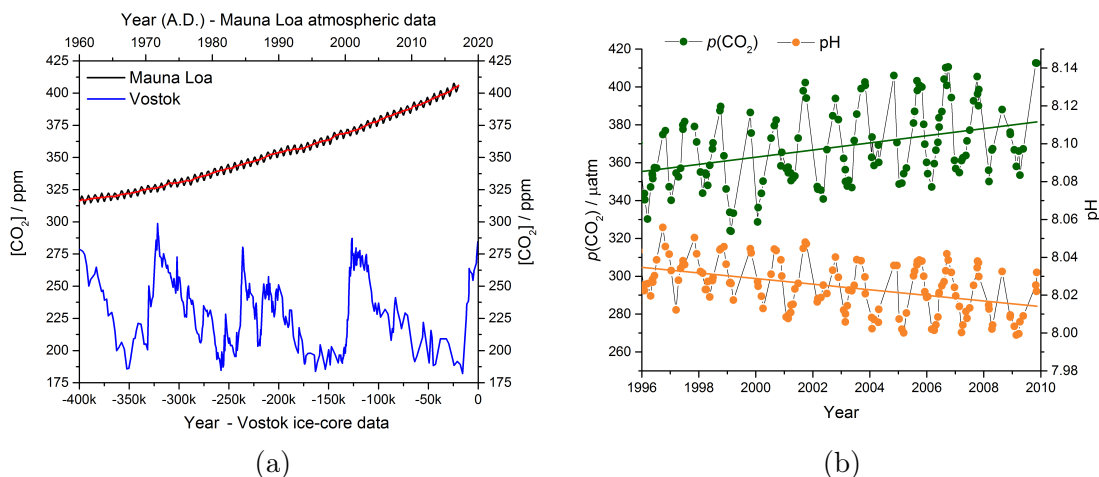
Figure 1.1: Trends in atmospheric and oceanic CO_2. (a) Modern atmospheric CO_2 concentration determined by direct measurements from Mauna Loa, Hawaii, and comparison with historical record determined indirectly from ice-core analysis in Lake Vostok, Antartica.[1] (b) Trends in partial pressure of CO_2 in the Atlantic Ocean and its correlation with local pH, measured from the NW coast of Africa.[11]

Carbon dioxide is a thermodynamic sink from the burning of fossil fuels ($\Delta G_f^\theta = -394 \, \text{kJ mol}^{-1}$)[14] and therefore there is an appreciable energetic barrier to making use of CO_2 as a synthon. Nevertheless, CO_2 is used as a C_1 feedstock for some large-scale synthetic processes, mainly in the production of urea (an important fertiliser), salicylic acid and cyclic carbonates.[15] Whilst there is not enough economic demand for CO_2-derived products to reverse the vast quantities of CO_2 that have been released into the atmosphere, the development of processes that make use of CO_2 as a C_1 feedstock to form value-added products is appealing, as it is cheap and non-toxic. In this regard, the catalytic synthesis of poly-carbonate materials from CO_2 is an attractive approach,[16–18] as these materials are highly useful in a range of applications (including, but not limited to: electronics, construction, data storage and vehicle components)[19] and their widespread synthesis would also divert a portion of CO_2 from the atmosphere.[20] Another promising application is the electrocatalytic reduction of CO_2 to other useful C_1 or C_2 compounds.[21] As this latter approach is capable of producing liquid fuels from CO_2, it is more closely

---

[i]European station for time series in the ocean at the Canary Islands.

related to tackling modern energy problems.[22] The electrochemical conversion of CO_2 to liquid fuels also provides a method of storing energy from intermittent renewable sources (such as tidal, solar and wind) in chemical bonds.[23,24] In the future, CO_2 may play a much more pivotal role in the global economy, as both a carbon and energy source, as conventional, fossil-fuel based carbon and energy sources are depleted.[25]

1.1.1 The ROCOP reaction – turning CO_2 into polymers

A promising method to use carbon dioxide is in the ring-opening copolymerisation (ROCOP) reaction between CO_2 and epoxides. Carrying out this process with a metal complex facilitates an alternating copolymerisation, giving rise to aliphatic poly-carbonate materials. The main steps in the ROCOP propagation mechanism involve: insertion of CO_2 into a metal-alkoxide or -phenoxide bond, yielding the carbonate functionality (Scheme 1.1, k_1); and ring-opening of the epoxide substrate, regenerating the metal-alkoxide species (Scheme 1.1, k_2). Competing side-reactions include further ring-opening of the epoxide from the metal-alkoxide complex, resulting in poly-ether linkages in the product (Scheme 1.1, k_3). Depolymerisation can also occur by "back-biting" reactions, where the metal-alkoxide reacts with the nearby carbonate group to form cyclic carbonate (Scheme 1.1, k_4).[16–18,26–28]
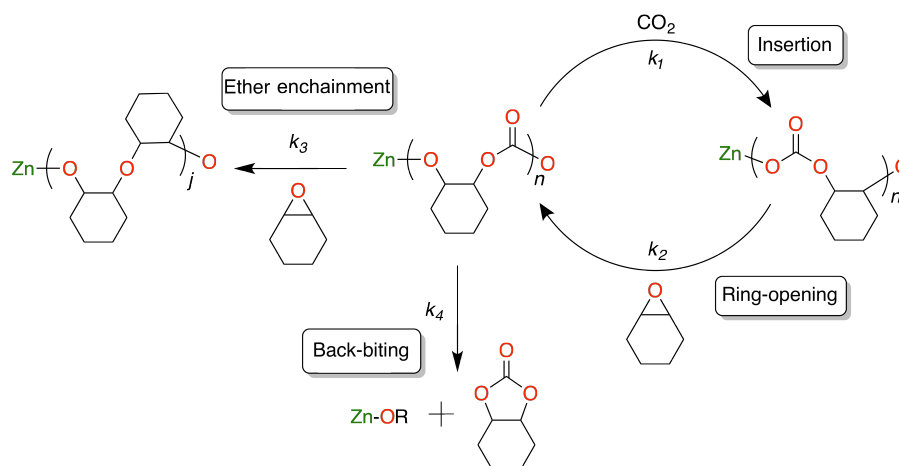
Scheme 1.1: General catalytic cycle of the zinc-catalysed ROCOP reaction between cyclohexene oxide and CO_2, showing propagation of the poly-carbonate, formation of ether-linkages in the polymer, and cyclic carbonate side-products.

A range of complexes of Earth-abundant metals have shown activity in this catalytic reaction, including those of magnesium(II),[29] chromium(III),[27,30,31] iron(III),[32] cobalt(II)/(III),[33–36] nickel(II),[37,38] copper(II),[39] zinc(II),[40–42] and aluminium(III).[43,44] The ROCOP reaction primarily makes use of cyclohexene ox-

ide (CHO)[45] and propylene oxide (PO),[46] as the epoxide substrate.[17,20,47] Whilst a range of different metal complexes have shown promising performances in CO_2/epoxide copolymerisations, there is particular interest in the development of catalysts which are based on zinc. This is due to its relatively low cost, high abundance and redox-stability. Furthermore, the development of zinc catalysts is quite attractive in terms of catalyst characterisation, as the complexes tend to be diamagnetic and therefore can be characterised using NMR spectroscopy. The use of zinc as the active site in these catalytic reactions has a strong precedent; indeed the very first reports of this process were made in 1969, using mixtures of diethyl zinc and water to generate zinc catalysts *in situ*.[26]

Since these early studies, significant advances have been made, greatly improving the poly-carbonate selectivity and catalyst activity. Studies involving a series of zinc β-diketiminate (BDI) complexes have demonstrated that fine-tuning of the supporting ligand system can give rise to superior catalyst performance. For example, changing the proton substituent on the BDI backbone to a cyano group improves the turnover frequency (TOF) and molecular weight of the polymer by an order of magnitude each. Further improvement is observed after making small steric alterations to the phenyl substituents in the ligand sphere.[48] Subsequent mechanistic investigations have also revealed that the best BDI catalysts likely form dimeric structures (Figure 1.2, **I**), and as such, dinuclear mechanisms have been proposed for the catalysis.[28] Other groups have also provided strong kinetic and mechanistic evidence to support that more than one metal centre is involved in the ROCOP reaction,[49–52] and catalyst design is now driven towards preparing well-defined dinuclear complexes (Figure 1.2).[16]

A number of other reports have focussed on preparing high-nuclearity zinc complexes,[53] although the catalytic performances of these in the copolymerisation process are generally inferior to other bimetallic examples, and have generally been explored to a much lesser extent. In one specific example, tetra- and hexa-nuclear zinc(II) phenoxide complexes were found to be poor catalysts in terms of both activity and control.[54] Poor solubility in cyclohexene oxide, poor thermal stability and sterically-hindered metal sites were contributing factors in this case, highlighting the importance of careful ligand-design in the development of ROCOP catalysts.

In general, macrocyclic complexes are attractive candidates for catalysis due to their well-defined, pre-organised geometries and coordination environments. Bimetallic zinc complexes of macrocyclic diphenolate ligands show promising activity in low pressure copolymerisation of CHO and CO_2 (Figure 1.2, **II**).[55,56] A
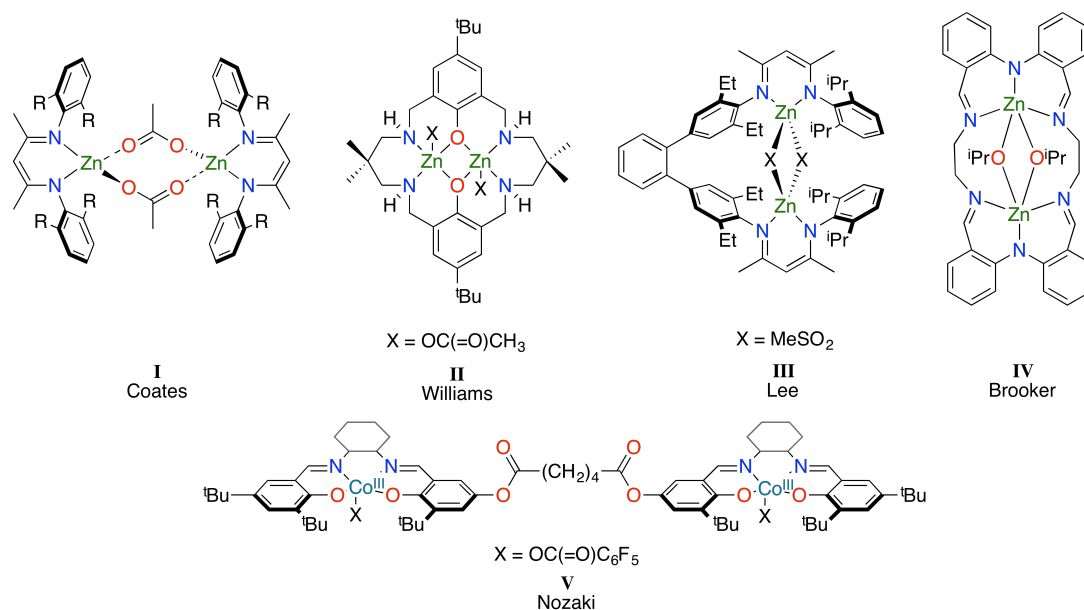
Figure 1.2: Literature examples of bimetallic complexes for the catalytic ROCOP reaction.

similar macrocyclic ligand has also been used to support a hetero-bimetallic complex of magnesium and zinc, which displays improved activity over either related homo-bimetallic complex.[50] Rigid macrocyclic complexes have often displayed poor catalytic activity. For example, the bimetallic BDI complex **III** in Figure 1.2 is a good ROCOP catalyst, attaining TOF of 312 h^{-1}, forming poly-carbonate in 94 % selectivity. In contrast, the related complex that features a second bridging aryl group between BDI units is inactive.[57] It has been highlighted that bimetallic complexes that offer some degree of flexibility in the linker groups are important in attaining high activity, such as with the bimetallic Schiff-base cobalt(III) complex (Figure 1.2, **V**).[58–61] On the other hand, other macrocyclic complexes that also feature flexible linkers are completely inactive towards catalysing the ROCOP reaction (Figure 1.2, **IV**).[62] These studies highlight how subtle and poorly understood the relationship between catalyst structure and activity remains in the field.

In Chapter 3 of this work, the synthesis of bimetallic and tetrametallic zinc(II) complexes will be discussed, as will the use of these high-nuclearity complexes in the ROCOP reaction between CO_2 and epoxides.

1.1.2 Electro-catalytic reduction of CO_2

The ROCOP reaction makes use of the tendency for CO_2 to undergo nucleophilic attack at carbon, and participate in insertion chemistry without any changes in formal oxidation state (which is +4 in CO_2). A second viable way of making use

of CO_2 as a C_1 feedstock is in electrochemical, or electro-catalytic, reduction of CO_2 to useful carbon products, which are in lower oxidation states.

Carbon dioxide can be reduced at an electrode to form the radical anion, at -1.90 V *versus* the normal hydrogen electrode (NHE), or -2.54 V *versus* ferrocene. The first reduction of CO_2 occurs at such strong negative potential because it is accompanied by a conformation change, from a linear conformation in the neutral molecule, to a bent conformation in the radical anion. Thermodynamically, the electrochemical reduction of CO_2 can be made more preferable if it is accompanied by the addition of protons. Because of this, proton-coupled electron-transfer processes involving many electrons occur at much more positive potential, with the formation of methane from CO_2 occurring at only -0.24 V *versus* NHE (Scheme 1.2). However, as more electrons and protons are required for the reduction to occur, the reaction becomes more disfavoured kinetically. [23]

$$
\begin{array}{rcl l}
CO_2 + e^- & \longrightarrow & CO_2^{\cdot -} & (-1.90 \text{ V } \textit{vs.} \text{ NHE or } -2.54 \text{ V } \textit{vs.} \text{ Fc}) \\
CO_2 + 2\,H^+ + 2\,e^- & \longrightarrow & CO + H_2O & (-0.53 \text{ V } \textit{vs.} \text{ NHE or } -1.17 \text{ V } \textit{vs.} \text{ Fc}) \\
CO_2 + 2\,H^+ + 2\,e^- & \longrightarrow & HCO_2H & (-0.61 \text{ V } \textit{vs.} \text{ NHE or } -1.25 \text{ V } \textit{vs.} \text{ Fc}) \\
CO_2 + 4\,H^+ + 4\,e^- & \longrightarrow & HCHO + H_2O & (-0.48 \text{ V } \textit{vs.} \text{ NHE or } -1.12 \text{ V } \textit{vs.} \text{ Fc}) \\
CO_2 + 6\,H^+ + 6\,e^- & \longrightarrow & CH_3OH + H_2O & (-0.38 \text{ V } \textit{vs.} \text{ NHE or } -1.02 \text{ V } \textit{vs.} \text{ Fc}) \\
CO_2 + 8\,H^+ + 8\,e^- & \longrightarrow & CH_4 + 2\,H_2O & (-0.24 \text{ V } \textit{vs.} \text{ NHE or } -0.88 \text{ V } \textit{vs.} \text{ Fc})
\end{array}
$$
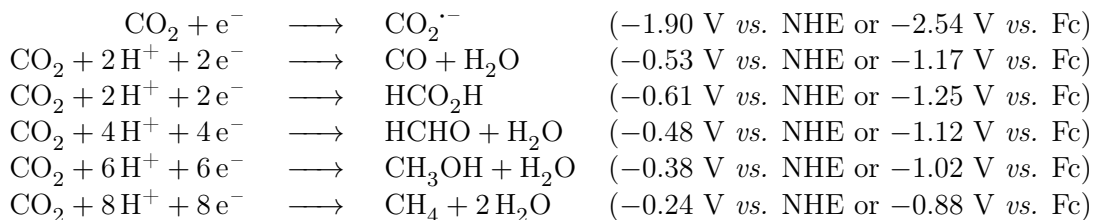
Scheme 1.2: Stoichiometries, potentials and products of the electrochemical reduction of CO_2. The potentials are reported at pH 7, 1 M for all solutes, 1 atm CO_2, 25 °C. [23]

With these thermodynamic and kinetic challenges in mind, there are two potential strategies to prepare liquid fuels from CO_2 that involve at least one electro-catalytic step. The first is to reduce CO_2 to CO, which is kinetically the most straightforward electrochemical reaction. Carbon monoxide obtained from this reaction could then be fed into a Fischer-Tropsch reactor to produce liquid fuel. The second strategy would be to directly form a liquid fuel, such as methanol, using the electro-catalyst, which is kinetically much more difficult and requires intricate catalyst design.

A molecular complex that can mediate electron-transfer from the electrode to the CO_2 substrate, bind intermediate products and collect further electron and proton equivalents, and then release the final product, is considered an electro-catalyst. Such a catalyst should therefore be designed with reversible, metal-based redox activity in mind, such that turnover can be achieved without degradation of the complex. The redox potential of the complex should also be fine-tuned so that it operates at a similar potential for the reaction that it is designed to catalyse. Work by Savéant involves the use of porphyrin complexes of iron(III) that can be electrochemically reduced to iron(0) and carry out highly

efficient electro-catalysis.[63–67] High activities with this class of complexes (as in Scheme 1.3, **VI**) have been realised using nearby phenol groups that act as proton relays between the bulk solution and the bound CO_2 substrate, and also stabilise the intermediate Fe-$CO_2^{\cdot-}$ species through hydrogen-bonding.[68,69] Use of such proton relays has also been shown to improve selectivity for formate over proton-reduction in $[Fe_4N(CO)_{12}]^-$ systems.[70] Additionally, it was reported that the C_6F_5 *meso*-substituents on the porphyrin ligand improve the activity dramatically.[66]
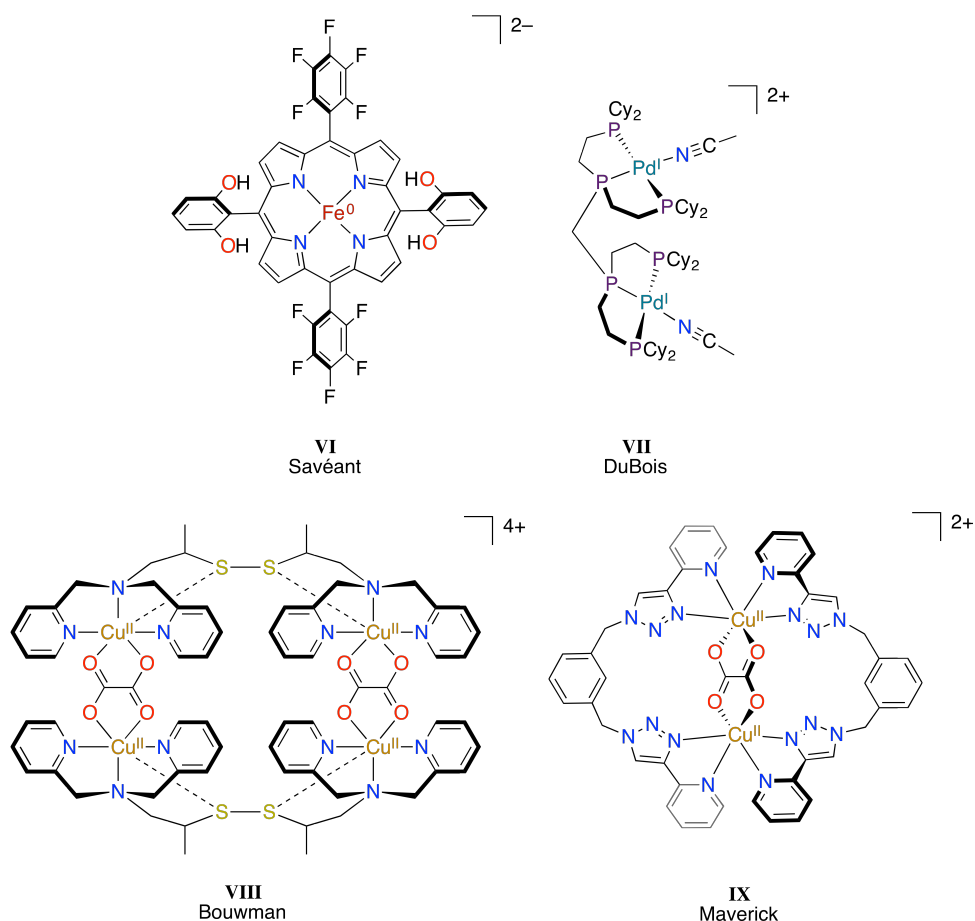
Figure 1.3: Literature examples of CO_2 electroreduction catalysts, highlighting examples that make use of ligand design to improve catalytic performance, through the introduction of internal proton relays or by control of the inter-metallic spacing.

Carbon monoxide dehydrogenase enzymes carry out catalytic reduction of CO_2 to CO. The active site of *Carboxydothermus hydrogenoformans* consists of a $NiFe_4S_4$ cluster, and CO_2 is bound and reduced by the cooperative action of nickel(0) and iron(II), forming a nickel(II)/iron(II) species after the two-electron transfer to CO_2.[71,72] Similar cooperative action between molybdenum(IV) and copper(I) is observed in the *Oligotropha carboxidovorans* enzyme, which also makes

use of a non-innocent sulphido ligand to bind CO_2 at the carbon atom.[73]

Many examples of synthetic, molecular electro-catalysts are designed with careful consideration of the distance between multiple metal centres. For example, the bimetallic palladium(II) complex in Scheme 1.3 (**VII**) features tri-phosphine coordination compartments that are bridged by a methylene group. This complex reacts rapidly with CO_2 to form CO through a bimetallic, cooperative mechanism involving palladium(I), but the formation of inert dimers limits the turnover number (TON) to only 10.[74] Following a subtle change in the ligand scaffold – changing the methylene bridge to a *meta*-aryl bridge – improves the total TON, but reduces the rate of reaction, as the increased separation between palladium centres prevents cooperativity from taking place.[75]

Molecular electro-catalysts of Earth-abundant metals such as copper and iron are attractive targets, as they are far less expensive than those of palladium. In one such example, a bimetallic amino-pyridine copper complex reduces CO_2 to oxalate $(C_2O_4{}^{2-})$ in an intermolecular cooperative mechanism; the initial copper(II) complex is first reduced to copper(I), which reduces CO_2 and binds the resulting radical anion. On approach of a second equivalent of the $(Cu^{II}\text{-}CO_2{}^{\cdot -})_2$ complex, a tetranuclear copper-oxalate complex is formed (Scheme 1.3, **VIII**). Oxalate (or oxalic acid in its protonated form) is a useful C_2 product from CO_2 and forms through radical coupling of two CO_2 radical anions. In this example, $Li_2C_2O_4$ could be liberated from the tetranuclear complex on addition of lithium perchlorate. Unfortunately, only six turnovers were achieved by the complex in a seven hour period, albeit at low over-potential.[76]

Intramolecular, cooperative reactivity was observed with a bimetallic copper(II) metallocyclic complex. Whilst the internuclear separation between metal centres is quite large in the oxidised form of the complex (6.843(2) Å for the nitro complex; 7.615(2) Å for the chlorido complex), the inherent flexibility in the helicate allows the metal centres to move closer together after reduction to copper(I) (using ascorbate) and subsequent reaction with CO_2, such that in the resulting oxalate complex (**XI**), the internuclear separation is 5.4213(7) Å. This copper(II) complex did not act as an electro-catalyst, but oxalic acid could be liberated from the oxalate complex on addition of HCl, thereby closing a potential catalytic cycle.[77]

Chapter 4 of this work investigates the design and synthesis of bimetallic complexes of iron(II), nickel(II), palladium(II) and copper(II), and their attempted use as CO_2 electro-reduction catalysts.

1.2   Oxygenation of hydrocarbon substrates

The oxygenation of hydrocarbon compounds accounts for less than 5 % of all industrial chemical processes.[78–80] Whilst oxidants such as O_2 and H_2O_2 offer "green" alternatives to traditional, toxic chromium and manganese reagents, safety concerns over the formation of explosive mixtures limit their widespread deployment in industry. Nonetheless, these oxidants are used in some large-scale preparations.[81] Global production of propylene oxide from propylene amounted to 7.5 Mt y^{-1} in 2010,[82] and this process traditionally uses HOCl as a reagent; BASF and Dow Chemical now produce propylene oxide using H_2O_2,[83] but this improved method only accounts for 300 kt y^{-1}.[82] As a further example, the anthraquinone oxidation process produces H_2O_2 on a scale of 2.2 Mt y^{-1} (as of 2010)[84,85] and makes use of O_2 as the oxidant. Hydrogen peroxide has also been suggested as a more environmentally benign oxidant in the production of adipic acid, which is produced on a scale of 2.2 Mt y^{-1} as a nylon-6,6 precursor.[86] The traditional method for adipic acid production uses HNO_3 to carry out oxidative cleavage of "KA oil", a mixture of cyclohexanol and cyclohexanone, and the oxidant is thought to contribute to 8 % of global N_2O pollution (400 kt y^{-1});[87] in contrast, H_2O_2 produces only water as a side-product.

In comparison with other industrial sectors, pharmaceutical processes produce up to two orders of magnitude more waste per mass of product.[88] Therefore, catalytic systems that can functionalise complex hydrocarbon substrates selectively, under mild reaction conditions, using environmentally benign oxidants are highly sought after.[89–102] Due to their low toxicity and high natural abundance, the use of salts or molecular complexes of copper and iron are advantageous over those of highly toxic chromium oxidants, or expensive precious-metal catalysts of platinum or palladium.

Nature exploits both copper and iron enzymes to carry out oxygenation reactions of hydrocarbon substrates.[103–108] The iron centre in cytochrome P450 compound I (Figure 1.4, **X**) and peroxidase enzymes forms a reactive, high-oxidation-state iron oxo species ($Fe^{IV}=O$, "ferryl heme") from its reaction with O_2 or water, which subsequently facilitates both hydrogen-atom abstraction (HAA) and hydroxylation of hydrocarbon substrates.[109–111] In the "oxygen rebound" mechanism, the organic radical of the substrate that is formed following HAA is associated with the Fe^{III}-OH intermediate as a "cage-radical".[112] Furthermore, the iron(II) non-heme enzyme *Taurine dioxygenase* makes use of dioxygen to hydroxylate hydrocarbon substrates, also proceeding through a $Fe^{IV}=O$ intermediate that

carries out HAA.[113]

Alternatively, the bimetallic copper(I) active site in the tyrosinase enzyme reacts with O_2 to form a side-on bound Cu^{II}-$(\mu_2{:}\eta^2$-$O_2)$-Cu^{II} motif[114] that oxidises catechol to *ortho*-quinone (Figure 1.4, **XI**).[115] Methane mono-oxygenase (MMO) is thought to contain a similar bimetallic active-site, containing iron in the soluble form (sMMO)[116] and copper in the particulate form (pMMO).[117] The metal-oxygen species in MMO is reactive enough to oxygenate the strong C-H bonds of methane ($H_{\mathrm{Diss}} = 439$ kJ mol^{-1}).[118,119] Following this motivation, much research has been driven towards preparing oxygenation catalysts based on copper and iron.[120] Synthetic analogues have been targeted that incorporate: reactive iron-oxo and -peroxo porphyrins (**XII**);[121–126] non-heme $Fe^{IV}{=}O$ (ferryl)[127–131] or $Fe^V{=}O$ (perferryl, **XIII**)[132] functionalities; and the MOM[133,134] or MO_2M butterfly motifs (**XIV**).[135–138]
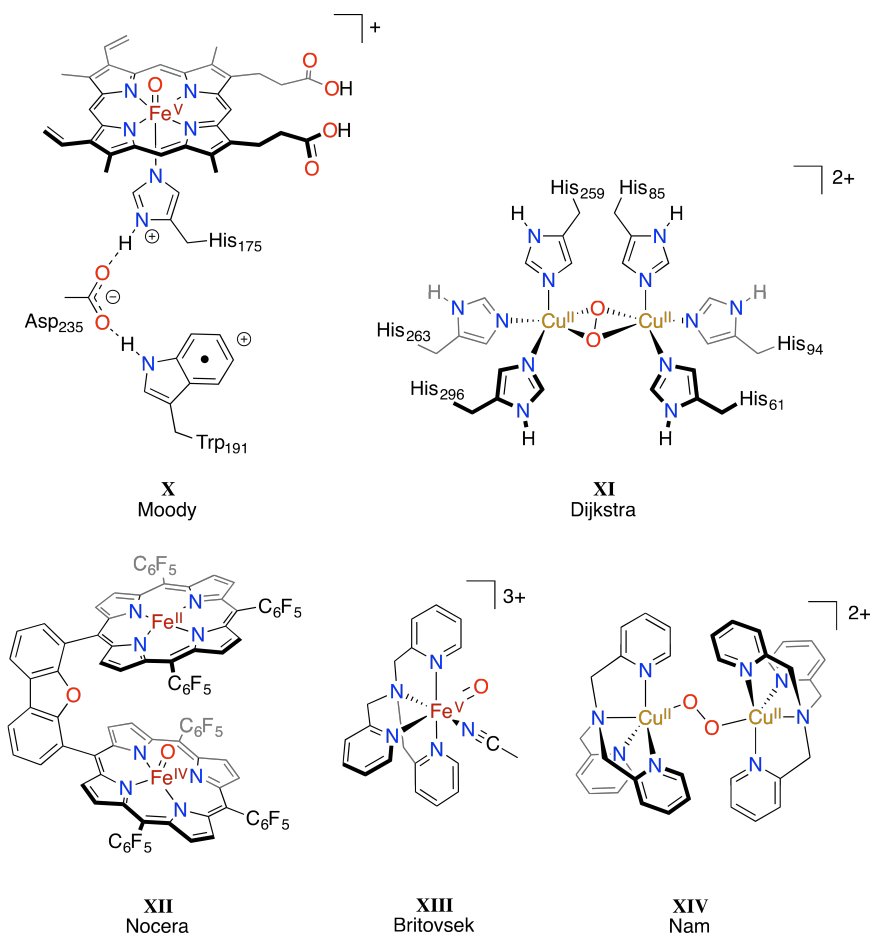
Figure 1.4: Literature examples of copper and iron complexes for catalytic hydrocarbon oxygenation.

Simple transition metal salts of copper have been used in non-biomimetic approaches to oxygenation catalysis, mainly using hydrogen peroxide (H_2O_2) or

tert-butyl hydroperoxide (*t*BuOOH, TBHP) to carry out at least the HAA step in free-radical reactions. The reaction between CuBr and TBHP forms mixtures of *t*BuO· (alkoxyl) and *t*BuOO· (peroxyl) radicals that carry out HAA.[139] $CuCl_2$, CuCl and copper metal have all been shown to catalyse both HAA and oxygenation of π-activated benzylic substrates using TBHP.[140,141] Furthermore, copper acetate has catalysed oxidation of aromatic C-H bonds using O_2 as an oxidant.[142] The related Kharasch-Sosnovsky reaction of *tert*-butyl peroxybenzoate leads to etherification of hydrocarbon substrates and is typically catalysed by copper(I) salts.[143–146] Coordination complexes of copper(I) have also been implemented in Kharasch-Sosnovsky reactions with other dialkyl-peroxides (for example, dicumyl peroxide), where both alkoxyl radicals (from the oxidant) and organic radicals (from the substrate) have been suggested as reactive intermediates.[147] Simple iron salts (most commonly $FeCl_3$) and complexes of iron have also been used for the catalytic oxygenation reactions of hydrocarbon substrates with high bond-dissociation energies (BDEs), including cyclohexane.[148–160] The bulk of iron-catalysed oxygenation reactions with H_2O_2 or TBHP are described by Fenton mechanisms,[161,162] where the role of iron is to generate reactive hydroxyl,[163] *tert*-butoxyl[164] and *tert*-butyl peroxyl[165] free radicals from the hydroperoxide.

Mixtures of metal compounds can also act as *tandem* catalysts[166–168] for oxygenation reactions. Combinations of iron(II) and chromium(III) diketonates carry out the tandem oxygenation and epoxidation catalysis of cyclohexene.[169,170] Additionally, copper acetate and $FeCl_3$ mixtures act as catalysts for a complex series of C-C and C-O bond forming reactions, although these reactions require high loadings.[171] A mixture of Fe_2SO_4 and $CuCl_2$ catalyses oxidation and isomerisation of alkene-containing organo-peroxides, yielding ketone products, with the postulated mechanisms showing the two metal centres participating in tandem.[172] In terms of *cooperative* catalysis, mixtures of copper and iron (in the forms of salts, complexes and nanoparticles) have been used to successfully promote cross-coupling reactions,[173] including those that form new C-C bonds,[174–177] C-O bonds,[178,179] C-S bonds,[180] and also *N*-arylation.[181–183] In contrast, there is surprisingly little use of mixed-metal systems in cooperative catalysis for the direct functionalisation of a hydrocarbon bond. In one example, amination of an allylic C-H bond was achieved by a palladium acetate catalyst, but only when a chromium(III) catalyst was also present to aminate the palladium-allyl intermediate.[184]

In Chapter 4, the use of copper(II)/iron(III) mixtures for hydrocarbon oxidation catalysis will be discussed.

1.3 Nuclear waste and uranyl chemistry

Whilst CO_2 might play an important role in future clean-energy production, for many countries, nuclear power is the present-day, high-power alternative to the combustion of fossil fuels. Nuclear power accounts for around 20 % of UK electricity, displacing approximately 14 Mt of CO_2 from entering the atmosphere (equivalent to around 9 % of UK carbon emissions in 2004).[185] However, the build-up of nuclear waste, and accidental contamination of the environment following reactor accidents, means that public opinion is often against nuclear power, and as such, research into the better treatment of nuclear waste is important.

Nuclear fuel rods consist of pellets made from UO_2, where uranium is in the +4 oxidation state. After irradiation in a nuclear power plant, spent nuclear fuel still contains 95 % UO_2, with short-lived fission products (*e.g.* ^{90}Sr, ^{131}I, ^{137}Cs), and long-lived trans-uranic elements (*e.g.* ^{237}Np, ^{239}Pu, ^{241}Am) making up the remaining 5 %.[186] Whilst spent fuel can be processed to separate out many of the isotopes, much of it must eventually be vitrified in borosilicate glass and buried. The 2010 UK nuclear waste inventory accounts for 189 kt of total nuclear waste, which includes 110 kt of intermediate-level waste (ILW) and 3.3 kt of high-level waste (HLW); all ILW and HLW will be stored in long-term depositories, taking up a volume of 95,920 m^3.[187] Long-term radioactivity coming from nuclear waste in geological depositories will be due to the actinides, which have incredibly long lifetimes; the half-life of ^{239}Pu is 24,100 years and that of ^{237}Np is 2 million years.[188] Environmental contamination due to leaching of nuclear waste from the permanent storage sites, such as Sellafield in the UK, is a major public concern, especially as liquid effluent has deliberately been discharged to the Irish Sea, and accidental atmospheric contamination has also been discharged over the surrounding area due to fires.[189] More widespread contamination has taken place due to nuclear reactor accidents, such as that at Chernobyl in 1986, or at Fukushima in 2011.

Under aerobic, aqueous conditions, uranium adopts its highest oxidation state of +6 in the form of the uranyl dication, UO_2^{2+}, and is highly soluble and mobile in water.[186] Unlike its transition metal bis-oxo congeners, such as MoO_2^{n+}, which adopt bent geometries,[190] the O-U-O bonds in uranyl are linear. This is primarily due to the participation of the oxygen $2p$ atomic orbitals forming σ and π bonding interactions with the uranium $5f$ and $6d$ atomic orbitals,[191] and is also due in part to the inverse trans-influence, where the strong binding of one oxo ligand to uranium encourages strong binding of the second oxo ligand "*trans*" to it.[192]

Combined with the U-O triple-bond character, these characteristics mean that uranyl possesses extremely strong bonds (604 kJ mol^{-1})[191] and is traditionally considered chemically inert, with most chemical changes taking place in the equatorial plane.

The plutonium uranium redox extraction (PUREX) process is capable of separating uranium(VI) and plutonium(IV) ions from the other fission products present in nuclear waste. PUREX is a solvent extraction method where uranium(VI) and plutonium(IV) ions are drawn from the aqueous nitric acid phase into the organic phase by tributyl phosphate (TBP), and its success is dependent on subtle differences in affinities between the extractant and the actinyl ions, as well as the oxidation states of the actinides.[193] Oxidation state control is also a key concept in bio-remediation of uranium-contaminated soils. Bacteria such as *Geobacter sulferreducens* carry out the two-electron, biotic reduction of uranyl, from the +6 oxidation state to the +4 oxidation state. In the +4 oxidation state, uranium salts are far less water-soluble, and are therefore immobilised from the aqueous environment.[194,195]

In order to better develop uranium extraction and remediation technologies, deeper understanding of actinyl redox chemistry and uranyl reduction mechanisms are required. To this end, much research has focussed on synthesising molecular uranyl complexes to study reduction chemistry. The U(VI)/U(V) reduction potential varies significantly based on the coordination environment, but usually occurs around -1.5 V *versus* ferrocene,[196] and due to the accessibility of the +5 oxidation state, the one-electron reduction of uranyl has been studied extensively.[196–206] On the other hand, multiple-electron reduction processes at uranium are rare, and so the two-electron reduction, which is most relevant to uranium remediation by immobilisation, has not been achieved or studied to as great an extent.

The two-electron reduction of uranyl(VI) by $CoCp_2$ has been promoted by the addition of a silyl-triflate reagent, where the formation of strong Si-O bonds and strong binding of triflate to uranium drives both the oxo-abstraction and the two-electron reduction (**XV**, Figure 1.5).[207] A uranyl(VI) β-ketoiminate complex undergoes reductive silylation on addition of excess Me_3SiI, yielding the oxo-silylated iodo uranium(V) complex **XVI**; addition of bipyridine to the uranium(V) complex results in further reduction of uranium on elimination of I_2.[196] A similar uranyl(VI) β-ketoiminate complex is reduced by $CoCp_2^*$, and further reduction to the uranium(IV) complex is encouraged following coordination of a boron Lewis acid to the uranyl oxo groups (**XVII**).[208] Making use of the more reducing +3 oxidation state on uranium, comproportionation of uranium(III) and uranyl(VI)

triflates has led to the formation of multinuclear uranium(IV) polyoxo clusters (**XVIII**).[209] Finally, two-electron reduction of uranyl is thought to occur on photolysis of a phosphine oxide complex in the presence of alcohols, forming uranium(IV) alkoxide complexes; although this claim is disputed.[210,211]
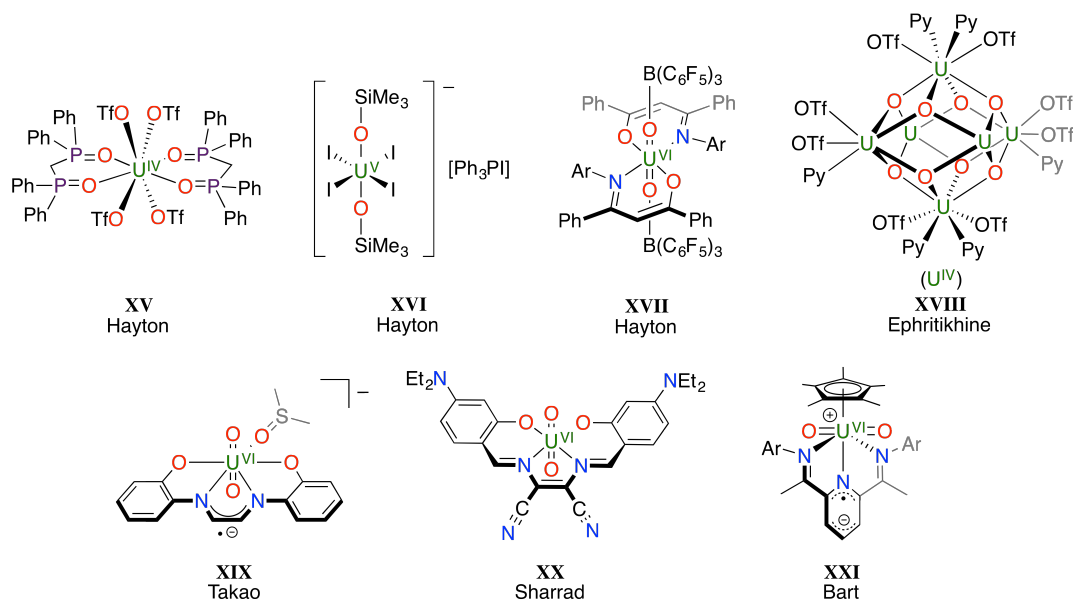
Figure 1.5: Top: complexes that have been used to carry out two-electron reduction of uranyl, and some resulting uranium(IV) products from other two-electron reduction reactions. Bottom: uranyl complexes of radical-containing ligands.

In Chapter 6, the use of a new redox-active dipyrrin ligand in uranyl reduction chemistry will be discussed, ultimately resulting in a two-electron reduction of uranyl through a novel, ligand-mediated electron-transfer mechanism. Redox-active ligands in metal complexes can provide alternative pathways in redox chemistry that are not available to metal complexes of more traditional, "innocent" ancillary ligands.[212–216] While these features have been studied extensively in complexes of the transition metals, the use of redox-active ligands in actinide chemistry is less developed. Low oxidation-state uranium complexes, *i.e.* uranium(III) and uranium(IV), of classical redox-active ligands such as pyridine di-imines (PDI), bipyridines, amidophenolates, and α-di-imines dominate and display reactivity in which ligand-centred redox processes are implicit.[217–226] In contrast, compounds of higher oxidation state uranium *e.g.* uranyl(VI)/(V) with redox-active ligands are rare. Considering the significant advances that have been made in the field of uranyl reduction, outlined above and discussed in further detail in the next section, this is surprising. Uranyl(VI) complexes of expanded porphyrins and analogous π-conjugated macrocycles are known but their impact in reduction chemistry has not been studied.[227,228] The uranyl(VI) complex of an α-di-imine

diphenolate undergoes single-electron reduction leading to the uranyl(VI) ligand-centred radical anion and not the expected uranyl(V) complex (**XIX**, Figure 1.5).[229] Uranyl complexes of maleonitrile-containing Schiff-base complexes exhibit ligand-centred oxidation (**XX**).[230] Oxidation of a $U^{IV}Cp^*(PDI)$ complex forms a uranyl(VI) complex of a PDI-ligand-centred radical anion which subsequently can undergo stoichiometric, stepwise reductive-silylation by Me_3SiI in which electrons arising from Cp^* (through elimination of $[Cp^*]_2$) and the PDI ligand radical-anion are involved (**XXI**).[220]

1.4 Ligand design inspired by nature

1.4.1 Binucleating pyrrolic macrocycles

As discussed in the previous sections, nature makes use of the porphyrin ligand in the active sites of metalloenzymes to carry out transformations of covalent bonds. In all three catalytic processes introduced above – the ROCOP reaction, electrochemical CO_2 reduction, and oxidation catalysis – there are many examples of bimetallic complexes, or dimers, successfully facilitating these reactions. Cooperative, bimetallic action is also observed in other chemical transformations, such as N_2 fixation,[231] reductive coupling of CO,[232] and O_2 reduction for fuel-cell catalysis.[233,234] Drawing inspiration from natural ligands, and with the aim of promoting cooperative, bimetallic reactivity, cofacial diporphyrin complexes were developed (**XXII** Figure 1.6).[235] Complexes of this type are formed of two porphyrin coordination compartments, binding reactive metal ions, and are connected by "spacer" groups. These spacer groups are important as they influence both the relative separation and orientation between coordination pockets, and therefore the separation between the two metal centres, which in turn influences reactivity. Complexes that feature a single, often more rigid, spacer group connecting the two porphyrin units are referred to as Pacman diporphyrin complexes, such as compound **XII** in Figure 1.4.[121,236]

Despite the successes of cofacial and Pacman diporphyrin complexes, carrying out O_2 reduction with cobalt(II),[233,237] N_2 binding with ruthenium(II),[238] and photo-catalytic oxidation of hydrocarbons,[121] their syntheses involve multiple steps and purification by column chromatography, and are therefore low-yielding. In contrast, polypyrrolic Schiff-base macrocycles (**XXV** and **XXVI**) are more straightforwardly prepared in 3 to 5 steps (70 % overall yield), and require no column chromatography in their purification.[239] Upon metallation, macrocycles of this type fold into well-defined Pacman geometries and resemble their porphyrin

analogues, providing similar N_4-coordination compartments. The relative orientation between compartments (the "bite angle") and internuclear separation can similarly be influenced by alteration of the spacer group.[240]
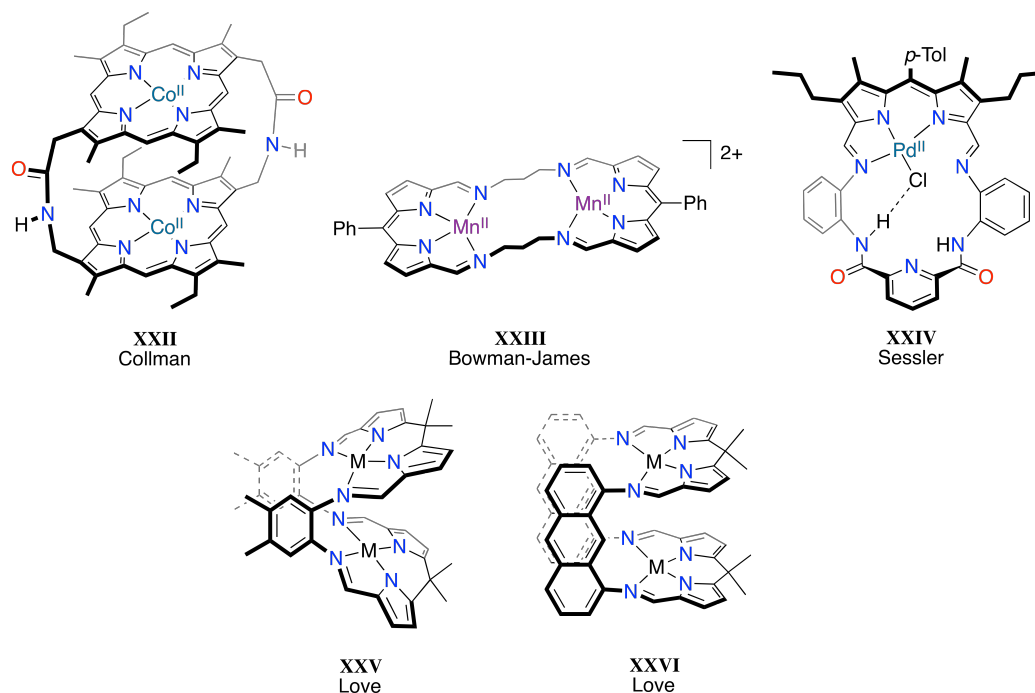
Figure 1.6: Literature examples of dinuclear macrocyclic complexes. Top: a cofacial diporphyrin complex and some macrocyclic dipyrrin complexes. Bottom: dipyrromethane Pacman complexes.

Pacman complexes have been used to explore a range of chemistry, which includes anion-recognition, inorganic cluster synthesis, O_2 reduction catalysis, CS_2 reduction and uranyl reduction, as summarised in Figure 1.7. Bimetallic zinc complexes of the anthracenyl-bridged Pacman macrocycle have displayed selective binding of chloride anions between the two metal centres preferentially over other halides.[241] Similar anion-recognition chemistry has been displayed by the metal-free version of the asymmetric dipyrrin macrocycle **XXIV** (Figure 1.6).[242]

The macrocyclic clefts offered by these complexes are reminiscent of supramolecular flasks, in which unfavourable catalytic and stoichiometric reactions have been shown to take place due to the increased effective concentration and lowered entropy inside the host structure.[243–246] Furthermore, these macrocyclic clefts have been shown to support the building up of inorganic zinc-hydroxide and -oxo clusters (discussed in Chapter 3),[247] as well as magnesium hydroxide cubane clusters;[248] the latter of these is relevant to modelling the active site of photosystem II[249] and artificial photosynthesis.

Bimetallic cobalt(II) Pacman complexes have catalysed the reduction of O_2
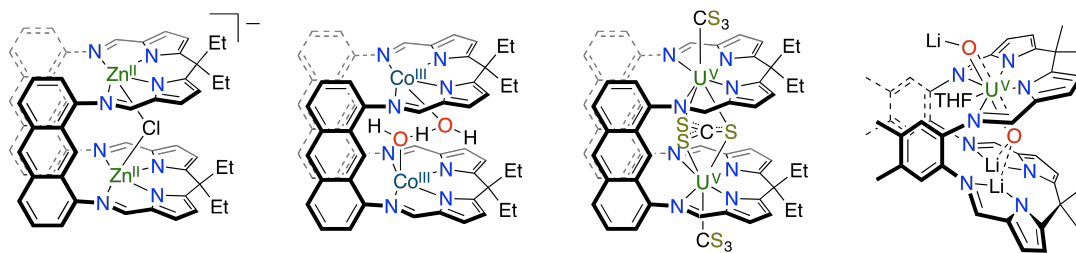
Figure 1.7: Previously discovered forms of reactivity of Pacman complexes: anion-recognition, fuel-cell catalysis, small molecule activation and uranyl reduction.

to water, electro-catalytically and also using ferrocene as an electron source in chemical catalysis.[250–253] In this case, the influence of subtle changes in the ligand framework on reactivity is apparent. In the case of the anthracenyl-bridged macrocycle, the O_2 reduction intermediate is an aqua-hydroxy ion, which binds to both cobalt(III) centres (see Figure 1.7).[253] In contrast, the macrocycle containing the *ortho*-phenylene spacer group reduces O_2 through a peroxo intermediate.[250]

Recently, the coordination of two strongly reducing uranium(III) ions by the anthracenyl-bridged Pacman ligand[254] has resulted in the multi-electron reduction of CS_2 and S_8, resulting in trithiocarbonate (CS_3^{2-}), carbon disulfido (CS_2^{2-}), sulfido (S^{2-}) and persulfido (S_2^{2-}) complexes. The multi-electron oxidation of the $U^{III}U^{III}$ parent complex to form the $U^{V}U^{V}$-CS_3^{2-} complex on reaction with CS_2 is unusual for uranium chemistry; the product from this reaction is shown in Figure 1.7.[255]

In the field of uranyl reduction chemistry, Pacman ligands have been used extensively to study the single-electron reduction of uranium(VI), yielding uranium(V) complexes.[198,256] Such complexes have been isolated through: radical reactions involving cleavage of the N-Si bond, leading to oxo-silylated products;[197,200] lithiation, using LiH, $LiNR_2$ and $LiCR_3$ reagents;[199] and catalytic reduction by DIBAL or Tebbe's reagent.[257] Unlike transition metal Pacman compounds, which selectively form bimetallic complexes, the uranyl analogues contain a vacant coordination pocket that allows further functionalisation. This second coordination pocket has been used to introduce transition metals[258] and lanthanides,[259] to study cation-cation interactions with uranyl, and has also been used to introduce a second reduced uranyl moiety (under forcing conditions) in order to study strong electronic coupling between two uranium(V) centres.[201]

Pacman complexes such as **XXV** and **XXVI** feature two alkyl substituents at the *meso*-position, which is the carbon position that bridges the pyrrole groups in the dipyrromethane moiety. In these macrocycles, the π-conjugation between the two imino-pyrrolide coordination units is disrupted, and in this sense these macro-

cycles differ quite drastically from their porphyrin analogues; in the porphyrin system, the *meso*-positions are unsaturated, such that π-conjugation extends throughout the N_4 coordination pocket. The pyrrolic dipyrrometh*ene* (or dipyrrin) moieties have been incorporated into pyrrolic Schiff-base macrocycles to some extent. Complexes (such as **XXIII**) are formed from a dipyrromethane pro-ligand that is oxidised to the macrocyclic dipyrrin upon metallation; these are called "accordion" complexes due to the flexible alkyl spacer groups that do not enforce a Pacman geometry.[260,261] An asymmetric dipyrromethane Pacman complex of palladium(II), which features a di-amido-pyridine group as the second coordination pocket, has been successfully oxidised to a Pacman dipyrrin complex,[262] but otherwise dipyrrin analogues of **XXV** and **XXVI** have not been reported previously. Attempts to synthesise macrocyclic dipyrrin pro-ligands are discussed in Chapter 2, and addressed further in Chapter 3 in the context of metalation.

1.4.2 Acyclic dipyrrin complexes

In contrast to macrocyclic dipyrrins, acyclic dipyrrin compounds have been studied extensively due to their rich photophysical properties. Boron-dipyrrin compounds (BODIPY dyes, **XXVII**, Figure 1.8) contain a BF_2 unit bonded to the two pyrrole nitrogen atoms, and have been used for molecular sensing (as pH and chemical probes)[263–265] and in luminescent devices.[266] In transition metal chemistry, dipyrrin ligands have been implicated in interesting catalytic transformations. For example, an iron(II) dipyrrin complex carries out C-H bond amination,[267] resulting in the synthesis of *N*-heterocycles (**XXVIII**).[268] Similar dipyrrin cobalt(III)-imido complexes carry out stoichiometric C-H bond activation reactions, and possess unusual electronic structures, exhibiting spin-crossover with changing temperature.[269] In these examples, the dipyrrin ligand acts as a bidentate $(N)_2$-donor. Donor-expanded dipyrrin ligands have been explored in the literature to some extent, although the reported diimino-dipyrrin complexes of nickel(II) have exhibited ligand-centred reactivity with O_2 (**XXIX**, Figure 1.8).[270] These reactions are metal-dependent and lead to asymmetric imino/carboxylate-dipyrrin ligands, or *meso*-hydroxylated dipyrrins.[271] Related bis-amido dipyrrin ligands have since been prepared rationally, and have shown flexible coordination modes, acting as an N_2O_2 donor to copper(II) (**XXX**, Figure 1.8) and an N_3O_1 donor to nickel(II).[272]

Due to the difficulties in preparing macrocyclic dipyrrin ligands, acyclic, donor-expanded dipyrrin ligands were also synthesised as part of this work. The synthesis of transition metal dipyrrin complexes for electro-catalytic CO_2 reduction is

discussed in Chapter 4, and the use of one of these new dipyrrin ligands in the field of uranyl reduction chemistry is presented in Chapter 6.
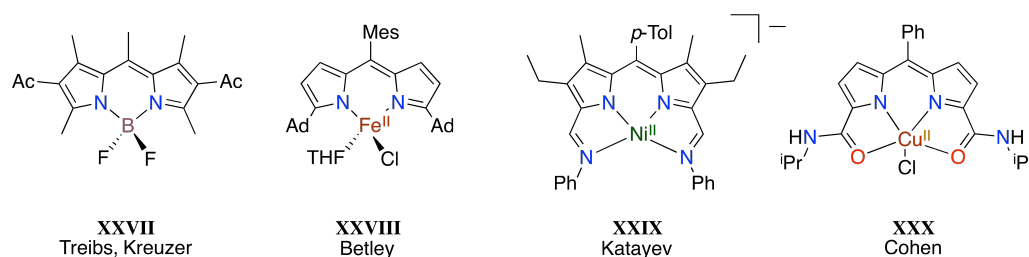
Figure 1.8: Literature examples of acyclic dipyrrin complexes. Mes = 2,4,6-trimethylphenyl; Ad = 1-adamantyl.

1.5   Aims of this thesis

This introduction covers many different topics, but the central theme that runs throughout this work is ligand design, with the aim of using this to influence and discover new and interesting reactivity. The core aims of the work presented in this thesis are:

- Synthesise a novel, macrocyclic Pacman dipyrrin ligand to explore new coordination chemistry;

- Prepare redox-active transition metal complexes for the electro-catalytic reduction of CO_2;

- Explore the use of macrocyclic complexes in catalytic ROCOP and oxidation reactions;

- Investigate uranyl reduction chemistry using a redox-active donor-expanded dipyrrin ligand.

References

[1] J. R. Petit, J. Jouzel, D. Raynaud, N. I. Barkov, J. M. Barnola, I. Basile, M. Bender, J. Chappellaz, M. Davis, G. Delaygue, M. Delmotte, V. M. Kotlyakov, M. Legrand, V. Y. Lipenkov, C. Lorius, L. Pepin, C. Ritz, E. Saltzman and M. Stievenard, *Nature*, 1999, **399**, 429.

[2] D. Luthi, M. Le Floch, B. Bereiter, T. Blunier, J.-M. Barnola, U. Siegenthaler, D. Raynaud, J. Jouzel, H. Fischer, K. Kawamura and T. F. Stocker, *Nature*, 2008, **453**, 379.

[3] "CO_2 Emissions From Fuel Combustion: Highlights", 2015 Edition, International Energy Agency (IEA).

[4] E. Dlugokencky and P. Tans, NOAA/ESRL, esrl.noaa.gov/gmd/ccgg/trends (30/04/2017).

[5] G. A. Florides and P. Christodoulides, *Environ. Int.*, 2009, **35**, 390 .

[6] P. Yiou, C. Genthon, M. Ghil, J. Jouzel, H. Le Treut, J. M. Barnola, C. Lorius and Y. N. Korotkevitch, *J. Geophys. Res.-Sol. Ea.*, 1991, **96**, 20365.

[7] C. L. Sabine, R. A. Feely, N. Gruber, R. M. Key, K. Lee, J. L. Bullister, R. Wanninkhof, C. S. Wong, D. W. R. Wallace, B. Tilbrook, F. J. Millero, T.-H. Peng, A. Kozyr, T. Ono and A. F. Rios, *Science*, 2004, **305**, 367.

[8] U. Siegenthaler and J. L. Sarmiento, *Nature*, 1993, **365**, 119 .

[9] N. R. Bates, M. H. P. Best, K. Neely, R. Garley, A. G. Dickson and R. J. Johnson, *Biogeosciences*, 2012, **9**, 2509.

[10] K. Caldeira and M. E. Wickett, *Nature*, 2003, **425**, 365.

[11] N. R. Bates, Y. M. Astor, M. J. Church, K. Currie, J. E. Dore, M. González-Dávila, L. Lorenzoni, F. Muller-Karger, J. Olafsson and J. M. Santana-Casiano, *Oceanography*, 2014, **27**, 126.

[12] R. A. Feely, C. L. Sabine, K. Lee, W. Berelson, J. Kleypas, V. J. Fabry and F. J. Millero, *Science*, 2004, **305**, 362.

[13] V. J. Fabry, B. A. Seibel, R. A. Feely and J. C. Orr, *ICES J. Mar. Sci.*, 2008, **65**, 414.

[14] D. R. Lide, *Handbook of Chemistry and Physics*, Taylor and Francis, Boca Raton, FL, USA, 1993-1994.

[15] T. Sakakura, J.-C. Choi and H. Yasuda, *Chem. Rev.*, 2007, **107**, 2365.

[16] S. Klaus, M. W. Lehenmeier, C. E. Anderson and B. Rieger, *Coord. Chem. Rev.*, 2011, **255**, 1460.

[17] S. Paul, Y. Zhu, C. Romain, R. Brooks, P. K. Saini and C. K. Williams, *Chem. Commun.*, 2015, **51**, 6459.

[18] G. Trott, P. K. Saini and C. K. Williams, *Phil. Trans. R. Soc. A*, 2016, **374**.

[19] V. Serini, "Ullmann's Encyclopedia of Industrial Chemistry: Polycarbonates", Wiley-VCH, 2000.

[20] A. M. Chapman, C. Keyworth, M. R. Kember, A. J. J. Lennox and C. K. Williams, *ACS Catal.*, 2015, **5**, 1581.

[21] M. Rakowski Dubois and D. L. Dubois, *Acc. Chem. Res.*, 2009, **42**, 1974.

[22] T. R. Cook, D. K. Dogutan, S. Y. Reece, Y. Surendranath, T. S. Teets and D. G. Nocera, *Chem. Rev.*, 2010, **110**, 6474.

[23] E. E. Benson, C. P. Kubiak, A. J. Sathrum and J. M. Smieja, *Chem. Soc. Rev.*, 2009, **38**, 89.

[24] D. L. DuBois, *Inorg. Chem.*, 2014, **53**, 3935.

[25] P. A. Kharecha and J. E. Hansen, *Global Biogeochem. Cy.*, 2008, **22**, 1.

[26] S. Inoue, H. Koinuma and T. Tsuruta, *J. Polym. Sci. Pol. Lett.*, 1969, **7**, 287.

[27] D. J. Darensbourg and J. C. Yarbrough, *J. Am. Chem. Soc.*, 2002, **124**, 6335.

[28] D. R. Moore, M. Cheng, E. B. Lobkovsky and G. W. Coates, *J. Am. Chem. Soc.*, 2003, **125**, 11911.

[29] M. R. Kember and C. K. Williams, *J. Am. Chem. Soc.*, 2012, **134**, 15676.

[30] D. J. Darensbourg, R. M. Mackiewicz, A. L. Phelps and D. R. Billodeaux, *Acc. Chem. Res.*, 2004, **37**, 836.

[31] D. J. Darensbourg, R. M. Mackiewicz, J. L. Rodgers and A. L. Phelps, *Inorg. Chem.*, 2004, **43**, 1831.

[32] A. Buchard, M. R. Kember, K. G. Sandeman and C. K. Williams, *Chem. Commun.*, 2011, **47**, 212.

[33] E. K. Noh, S. J. Na, S. S, S.-W. Kim and B. Y. Lee, *J. Am. Chem. Soc.*, 2007, **129**, 8082.

[34] X.-B. Lu and Y. Wang, *Angew. Chem. Int. Ed.*, 2004, **43**, 3574.

[35] X.-B. Lu, L. Shi, Y.-M. Wang, R. Zhang, Y.-J. Zhang, X.-J. Peng, Z.-C. Zhang and B. Li, *J. Am. Chem. Soc.*, 2006, **128**, 1664.

[36] H. Sugimoto and K. Kuroda, *Macromolecules*, 2008, **41**, 312.

[37] C.-H. Li, H.-J. Chuang, C.-Y. Li, B.-T. Ko and C.-H. Lin, *Polym. Chem.*, 2014, **5**, 4875.

[38] C.-Y. Tsai, F.-Y. Cheng, K.-Y. Lu, J.-T. Wu, B.-H. Huang, W.-A. Chen, C.-C. Lin and B.-T. Ko, *Inorg. Chem.*, 2016, **55**, 7843.

[39] C.-Y. Tsai, B.-H. Huang, M.-W. Hsiao, C.-C. Lin and B.-T. Ko, *Inorg. Chem.*, 2014, **53**, 5109.

[40] R. Eberhardt, M. Allmendinger, G. A. Luinstra and B. Rieger, *Organometallics*, 2003, **22**, 211.

[41] D. J. Darensbourg and M. W. Holtcamp, *Macromolecules*, 1995, **28**, 7577.

[42] D. J. Darensbourg, M. W. Holtcamp, G. E. Struck, M. S. Zimmer, S. A. Niezgoda, P. Rainey, J. B. Robertson, J. D. Draper and J. H. Reibenspies, *J. Am. Chem. Soc.*, 1999, **121**, 107.

[43] H. Sugimoto, H. Ohtsuka and S. Inoue, *J. Polym. Sci. Pol. Chem.*, 2005, **43**, 4172.

[44] T. Aida, M. Ishikawa and S. Inoue, *Macromolecules*, 1986, **19**, 8.

[45] D. J. Darensbourg, P. Rainey and J. Yarbrough, *Inorg. Chem.*, 2001, **40**, 986.

[46] Z. Qin, C. M. Thomas, S. Lee and G. W. Coates, *Angew. Chem. Int. Ed.*, 2003, **42**, 5484.

[47] C. K. Williams and M. A. Hillmyer, *Polym. Rev.*, 2008, **48**, 1.

[48] D. R. Moore, M. Cheng, E. B. Lobkovsky and G. W. Coates, *Angew. Chem. Int. Ed.*, 2002, **41**, 2599.

[49] M. Cheng, D. R. Moore, J. J. Reczek, B. M. Chamberlain, E. B. Lobkovsky and G. W. Coates, *J. Am. Chem. Soc.*, 2001, **123**, 8738.

[50] J. A. Garden, P. K. Saini and C. K. Williams, *J. Am. Chem. Soc.*, 2015, **137**, 15078.

[51] M. R. Kember, A. J. P. White and C. K. Williams, *Macromolecules*, 2010, **43**, 2291.

[52] F. Jutz, A. Buchard, M. R. Kember, S. B. Fredriksen and C. K. Williams, *J. Am. Chem. Soc.*, 2011, **133**, 17395.

[53] D. J. Darensbourg, J. R. Wildeson and J. C. Yarbrough, *Inorg. Chem.*, 2002, **41**, 973.

[54] M. B. Dinger and M. J. Scott, *Inorg. Chem.*, 2001, **40**, 1029.

[55] M. R. Kember, A. J. P. White and C. K. Williams, *Inorg. Chem.*, 2009, **48**, 9535.

[56] M. R. Kember, P. D. Knight, P. T. R. Reung and C. K. Williams, *Angew. Chem. Int. Ed.*, 2009, **48**, 931.

[57] B. Y. Lee, H. Y. Kwon, S. Y. Lee, S. J. Na, S.-i. Han, H. Yun, H. Lee and Y.-W. Park, *J. Am. Chem. Soc.*, 2005, **127**, 3031.

[58] S. Kissling, P. T. Altenbuchner, M. W. Lehenmeier, E. Herdtweck, P. Deglmann, U. B. Seemann and B. Rieger, *Chem.-Eur. J.*, 2015, **21**, 8148.

[59] M. W. Lehenmeier, S. Kissling, P. T. Altenbuchner, C. Bruckmeier, P. Deglmann, A.-K. Brym and B. Rieger, *Angew. Chem. Int. Ed.*, 2013, **52**, 9821.

[60] S. Klaus, S. I. Vagin, M. W. Lehenmeier, P. Deglmann, A. K. Brym and B. Rieger, *Macromolecules*, 2011, **44**, 9508.

[61] K. Nakano, S. Hashimoto and K. Nozaki, *Chem. Sci.*, 2010, **1**, 369.

[62] C. Romain, M. S. Bennington, A. J. P. White, C. K. Williams and S. Brooker, *Inorg. Chem.*, 2015, **54**, 11842.

[63] C. Costentin, M. Robert and J.-M. Savéant, *Chem. Soc. Rev.*, 2013, **42**, 2423.

[64] C. Costentin, S. Drouet, G. Passard, M. Robert and J.-M. Savéant, *J. Am. Chem. Soc.*, 2013, **135**, 9023.

[65] J. Bonin, M. Chaussemier, M. Robert and M. Routier, *ChemCatChem*, 2014, **6**, 3200.

[66] C. Costentin, G. Passard, M. Robert and J.-M. Savéant, *Proc. Natl. Acad. Sci.*, 2014, **111**, 14990.

[67] C. Costentin, M. Robert and J.-M. Savéant, *Acc. Chem. Res.*, 2015, **48**, 2996.

[68] C. Costentin, S. Drouet, M. Robert and J.-M. Savéant, *Science*, 2012, **338**, 90.

[69] C. Costentin, G. Passard, M. Robert and J.-M. Savéant, *J. Am. Chem. Soc.*, 2014, **136**, 11821.

[70] N. D. Loewen, E. J. Thompson, M. Kagan, C. L. Banales, T. W. Myers, J. C. Fettinger and L. A. Berben, *Chem. Sci.*, 2016, **7**, 2728.

[71] J.-H. Jeoung and H. Dobbek, *Science*, 2007, **318**, 1461.

[72] A. Parkin, J. Seravalli, K. A. Vincent, S. W. Ragsdale and F. A. Armstrong, *J. Am. Chem. Soc.*, 2007, **129**, 10328.

[73] H. Dobbek, L. Gremer, R. Kiefersauer, R. Huber and O. Meyer, *Proc. Natl. Acad. Sci.*, 2002, **99**, 15971.

[74] B. D. Steffey, C. J. Curtis and D. L. DuBois, *Organometallics*, 1995, **14**, 4937.

[75] J. W. Raebiger, J. W. Turner, B. C. Noll, C. J. Curtis, A. Miedaner, B. Cox and D. L. DuBois, *Organometallics*, 2006, **25**, 3345.

[76] R. Angamuthu, P. Byers, M. Lutz, A. L. Spek and E. Bouwman, *Science*, 2010, **327**, 313.

[77] U. R. Pokharel, F. R. Fronczek and A. W. Maverick, *Nat. Commun.*, 2014, **5**, 5883.

[78] J. S. Carey, D. Laffan, C. Thomson and M. T. Williams, *Org. Biomol. Chem.*, 2006, **4**, 2337.

[79] S. Caron, R. W. Dugger, S. G. Ruggeri, J. A. Ragan and D. H. B. Ripin, *Chem. Rev.*, 2006, **106**, 2943.

[80] R. W. Dugger, J. A. Ragan and D. H. B. Ripin, *Org. Process Res. Dev.*, 2005, **9**, 253.

[81] F. Cavani and J. H. Teles, *ChemSusChem*, 2009, **2**, 508.

[82] P. Bassler, M. Weidenbach and H. Goebbel, *Chem. Eng. Trans.*, 2010, **21**, 571.

[83] V. Russo, R. Tesser, E. Santacesaria and M. Di Serio, *Ind. Eng. Chem. Res.*, 2013, **52**, 1168.

[84] R. Hage and A. Lienke, *Angew. Chem. Int. Ed.*, 2006, **45**, 206.

[85] J. M. Campos-Martin, G. Blanco-Brieva and J. L. G. Fierro, *Angew. Chem. Int. Ed.*, 2006, **45**, 6962.

[86] K. Sato, M. Aoki and R. Noyori, *Science*, 1998, **281**, 1646.

[87] M. H. Thiemans and W. C. Trogler, *Science*, 1991, **251**, 932.

[88] R. A. Sheldon, *Green Chem.*, 2007, **9**, 1273.

[89] T. J. Osberger, D. C. Rogness, J. T. Kohrt, A. F. Stepan and M. C. White, *Nature*, 2016, **537**, 214.

[90] S. E. Ammann, W. Liu and M. C. White, *Angew. Chem. Int. Ed.*, 2016, **55**, 9571.

[91] J. M. Howell, K. Feng, J. R. Clark, L. J. Trzepkowski and M. C. White, *J. Am. Chem. Soc.*, 2015, **137**, 14590.

[92] S. E. Ammann, G. T. Rice and M. C. White, *J. Am. Chem. Soc.*, 2014, **136**, 10834.

[93] P. E. Gormisky and M. C. White, *J. Am. Chem. Soc.*, 2013, **135**, 14052.

[94] I. I. Strambeanu and M. C. White, *J. Am. Chem. Soc.*, 2013, **135**, 12032.

[95] M. A. Bigi, S. A. Reed and M. C. White, *J. Am. Chem. Soc.*, 2012, **134**, 9721.

[96] P. E. Gormisky and M. C. White, *J. Am. Chem. Soc.*, 2011, **133**, 12584.

[97] N. A. Vermeulen, J. H. Delcamp and M. C. White, *J. Am. Chem. Soc.*, 2010, **132**, 11323.

[98] N. A. Vermeulen, M. S. Chen and M. Christina White, *Tetrahedron*, 2009, **65**, 3078.

[99] J. H. Delcamp, A. P. Brucks and M. C. White, *J. Am. Chem. Soc.*, 2008, **130**, 11270.

[100] J. H. Delcamp and M. C. White, *J. Am. Chem. Soc.*, 2006, **128**, 15076.

[101] M. S. Chen, N. Prabagaran, N. A. Labenz and M. C. White, *J. Am. Chem. Soc.*, 2005, **127**, 6970.

[102] M. S. Chen and M. C. White, *J. Am. Chem. Soc.*, 2004, **126**, 1346.

[103] B. J. Wallar and J. D. Lipscomb, *Chem. Rev.*, 1996, **96**, 2625.

[104] L. Que and R. Y. N. Ho, *Chem. Rev.*, 1996, **96**, 2607.

[105] M. Sono, M. P. Roach, E. D. Coulter and J. H. Dawson, *Chem. Rev.*, 1996, **96**, 2841.

[106] E. I. Solomon, U. M. Sundaram and T. E. Machonkin, *Chem. Rev.*, 1996, **96**, 2563.

[107] P. Basu, B. Katterle, K. K. Andersson and H. Dalton, *Biochem. J.*, 2003, **369**, 417.

[108] G. R. Hemsworth, G. J. Davies and P. H. Walton, *Curr. Opin. Struc. Biol.*, 2013, **23**, 660.

[109] C. M. Casadei, A. Gumiero, C. L. Metcalfe, E. J. Murphy, J. Basran, M. G. Concilio, S. C. M. Teixeira, T. E. Schrader, A. J. Fielding, A. Ostermann, M. P. Blakeley, E. L. Raven and P. C. E. Moody, *Science*, 2014, **345**, 193.

[110] J. T. Groves, *Nat. Chem.*, 2014, **6**, 89.

[111] J. Rittle and M. T. Green, *Science*, 2010, **330**, 933.

[112] J. T. Groves and G. A. McClusky, *J. Am. Chem. Soc.*, 1976, **98**, 859.

[113] J. M. Bollinger, J. C. Price, L. M. Hoffart, E. W. Barr and C. Krebs, *Eur. J. Inorg. Chem.*, 2005, 4245.

[114] C. Citek, S. Herres-Pawlis and T. D. P. Stack, *Acc. Chem. Res.*, 2015, **48**, 2424.

[115] C. A. Ramsden and P. A. Riley, *Bioorg. Med. Chem.*, 2014, **22**, 2388.

[116] R. Banerjee, Y. Proshlyakov, J. D. Lipscomb and D. A. Proshlyakov, *Nature*, 2015, **518**, 431.

[117] M. A. Culpepper, G. E. Cutsail, B. M. Hoffman and A. C. Rosenzweig, *J. Am. Chem. Soc.*, 2012, **134**, 7640.

[118] K. M. Ervin and V. F. DeTuri, *J. Phys. Chem. A*, 2002, **106**, 9947.

[119] A. C. Rosenzweig, *Nature*, 2015, **518**, 309.

[120] L. Que and W. B. Tolman, *Nature*, 2008, **455**, 333.

[121] J. Rosenthal, T. D. Luckett, J. M. Hodgkiss and D. G. Nocera, *J. Am. Chem. Soc.*, 2006, **128**, 6546.

[122] J. T. Groves and T. E. Nemo, *J. Am. Chem. Soc.*, 1983, **105**, 5786.

[123] M. Costas, *Coord. Chem. Rev.*, 2011, **255**, 2912.

[124] Y. Yuan, H. Ji, Y. Chen, Y. Han, X. Song, Y. She and R. Zhong, *Org. Process. Res. Dev.*, 2004, **8**, 418.

[125] M. J. Nappa and C. A. Tolman, *Inorg. Chem.*, 1985, **24**, 4711.

[126] J. P. Collman, X. Zhang, V. J. Lee, E. S. Uffelman and J. I. Brauman, *Science*, 1993, **261**, 1404.

[127] W. Nam, *Acc. Chem. Res.*, 2007, **40**, 522.

[128] S. O. Kim, C. V. Sastri, M. S. Seo, J. Kim and W. Nam, *J. Am. Chem. Soc.*, 2005, **127**, 4178.

[129] J. Kaizer, E. J. Klinker, N. Y. Oh, J.-U. Rohde, W. J. Song, A. Stubna, J. Kim, E. Münck, W. Nam and L. Que, *J. Am. Chem. Soc.*, 2004, **126**, 472.

[130] M. R. Bukowski, P. Comba, A. Lienke, C. Limberg, C. Lopez de Laorden, R. Mas-Ballesté, M. Merz and L. Que, *Angew. Chem. Int. Ed.*, 2006, **45**, 3446.

[131] O. Martínez-Ferraté, G. J. P. Britovsek, C. Claver and P. W. N. M. van Leeuwen, *Inorg. Chim. Acta.*, 2015, **431**, 156.

[132] O. Y. Lyakin, K. P. Bryliakov, G. J. P. Britovsek and E. P. Talsi, *J. Am. Chem. Soc.*, 2009, **131**, 10798.

[133] I. Siewert, C. Limberg, S. Demeshko and E. Hoppe, *Chem. Eur. J.*, 2008, **14**, 9377.

[134] P. Haack, A. Kärgel, C. Greco, J. Dokic, B. Braun, F. F. Pfaff, S. Mebs, K. Ray and C. Limberg, *J. Am. Chem. Soc.*, 2013, **135**, 16148.

[135] J. L. Que and W. B. Tolman, *Angew. Chem. Int. Ed.*, 2002, **41**, 1114.

[136] P. L. Holland, C. J. Cramer, E. C. Wilkinson, S. Mahapatra, K. R. Rodgers, S. Itoh, M. Taki, S. Fukuzumi, L. Que and W. B. Tolman, *J. Am. Chem. Soc.*, 2000, **122**, 792.

[137] K. Shimizu, R. Maruyama, T. Hatamachi and T. Kodama, *J. Phys. Chem. C*, 2007, **111**, 6440.

[138] I. Garcia-Bosch, R. E. Cowley, D. E. Diaz, M. A. Siegler, W. Nam, E. I. Solomon and K. D. Karlin, *Chem. -Eur. J.*, 2016, **22**, 5133.

[139] E. Boess, L. M. Wolf, S. Malakar, M. Salamone, M. Bietti, W. Thiel and M. Klussmann, *ACS Catal.*, 2016, **6**, 3253.

[140] M. M. Hossain and S.-G. Shyu, *Tetrahedron*, 2016, **72**, 4252.

[141] G. Rothenberg, L. Feldberg, H. Wiener and Y. Sasson, *J. Chem. Soc. Perk. T. 2*, 1998, 2429.

[142] X. Chen, X.-S. Hao, C. E. Goodhue and J.-Q. Yu, *J. Am. Chem. Soc.*, 2006, **128**, 6790.

[143] J. Eames and M. Watkinson, *Angew. Chem. Int. Ed.*, 2001, **40**, 3567.

[144] M. S. Kharasch and G. Sosnovsky, *J. Am. Chem. Soc.*, 1958, **80**, 756.

[145] A. L. J. Beckwith and A. A. Zavitsas, *J. Am. Chem. Soc.*, 1986, **108**, 8230.

[146] M. B. Andrus and J. C. Lashley, *Tetrahedron*, 2002, **58**, 845.

[147] R. T. Gephart, C. L. McMullin, N. G. Sapiezynski, E. S. Jang, M. J. B. Aguila, T. R. Cundari and T. H. Warren, *J. Am. Chem. Soc.*, 2012, **134**, 17350.

[148] M. Nakanishi and C. Bolm, *Adv. Synth. Catal.*, 2007, **349**, 861.

[149] S. Enthaler, K. Junge and M. Beller, *Angew. Chem. Int. Ed.*, 2008, **47**, 3317.

[150] D. Li, K. Schröder, B. Bitterlich, M. K. Tse and M. Beller, *Tetrahedron Lett.*, 2008, **49**, 5976.

[151] F. Shi, M. K. Tse, Z. Li and M. Beller, *Chem. -Eur. J.*, 2008, **14**, 8793.

[152] G. B. Shul'pin, C. C. Golfeto, G. Süss-Fink, L. S. Shul'pina and D. Mandelli, *Tetrahedron Lett.*, 2005, **46**, 4563.

[153] B. Join, K. Möller, C. Ziebart, K. Schröder, D. Gördes, K. Thurow, A. Spannenberg, K. Junge and M. Beller, *Adv. Synth. Catal.*, 2011, **353**, 3023.

[154] K. Möller, G. Wienhöfer, K. Schröder, B. Join, K. Junge and M. Beller, *Chem. -Eur. J.*, 2010, **16**, 10300.

[155] F. Gelalcha, B. Bitterlich, G. Anilkumar, M. Tse and M. Beller, *Angew. Chem. Int. Ed.*, 2007, **46**, 7293.

[156] G. Anilkumar, B. Bitterlich, F. G. Gelalcha, M. K. Tse and M. Beller, *Chem. Commun.*, 2007, 289.

[157] G. J. P. Britovsek, J. England and A. J. P. White, *Inorg. Chem.*, 2005, **44**, 8125.

[158] J. England, C. R. Davies, M. Banaru, A. J. P. White and G. J. P. Britovsek, *Adv. Synth. Catal.*, 2008, **350**, 883.

[159] J. England, R. Gondhia, L. Bigorra-Lopez, A. R. Petersen, A. J. P. White and G. J. P. Britovsek, *Dalton Trans.*, 2009, 5319.

[160] F. Jia and Z. Li, *Org. Chem. Front.*, 2014, **1**, 194.

[161] P. Wardman and L. P. Candeias, *Radiat. Res.*, 1996, **145**, 523.

[162] E. Neyens and J. Baeyens, *J. Haz. Mat.*, 2003, **98**, 33.

[163] W. P. Kwan and B. M. Voelker, *Environ. Sci. Technol.*, 2003, **37**, 1150.

[164] S. I. Dikalov and R. P. Mason, *Free Radical Bio. Med.*, 1999, **27**, 864.

[165] L. Gan, S. Huang, X. Zhang, A. Zhang, B. Cheng, H. Cheng, X. Li and G. Shang, *J. Am. Chem. Soc.*, 2002, **124**, 13384.

[166] R. Jira, *Angew. Chem. Int. Ed.*, 2009, **48**, 9034.

[167] J. Smidt, W. Hafner, R. Jira, J. Sedlmeier, R. Sieber, R. Rüttinger and H. Kojer, *Angew. Chem.*, 1959, **71**, 176.

[168] C. A. Huff and M. S. Sanford, *J. Am. Chem. Soc.*, 2011, **133**, 18122.

[169] A. Fusi, R. Ugo and G. M. Zanderighi, *J. Catal.*, 1974, **34**, 175.

[170] A. F. Noels, A. J. Hubert and P. Teyssie, *J. Organomet. Chem.*, 1979, **166**, 79.

[171] S. Li, W. Jia and N. Jiao, *Adv. Synth. Catal.*, 2009, **351**, 569.

[172] Y. Nonami, J. Baran, J. Sosnicki, H. Mayr, A. Masuyama and M. Nojima, *J. Org. Chem.*, 1999, **64**, 4060.

[173] N. Panda and A. K. Jena, *Organic Chem. Curr. Res.*, 2015, **4**, 130.

[174] H. Huang, H. Jiang, K. Chen and H. Liu, *J. Org. Chem.*, 2008, **73**, 9061.

[175] A. Hamze, J.-D. Brion and M. Alami, *Org. Lett.*, 2012, **14**, 2782.

[176] C. M. Rao Volla and P. Vogel, *Tetrahedron Lett.*, 2008, **49**, 5961.

[177] N. Panda, A. K. Jena and S. Mohapatra, *Chem. Lett.*, 2011, **40**, 956.

[178] S. Yang, C. Wu, H. Zhou, Y. Yang, Y. Zhao, C. Wang, W. Yang and J. Xu, *Adv. Synth. Catal.*, 2013, **355**, 53.

[179] X. Liu and S. Zhang, *Synlett*, 2011, **2011**, 268.

[180] S. Kovacs and Z. Novak, *Org. Biomol. Chem.*, 2011, **9**, 711.

[181] Z. Wang, H. Fu, Y. Jiang and Y. Zhao, *Synlett*, 2008, 2540.

[182] D. Guo, H. Huang, Y. Zhou, J. Xu, H. Jiang, K. Chen and H. Liu, *Green Chem.*, 2010, **12**, 276.

[183] N. Panda, A. K. Jena, S. Mohapatra and S. R. Rout, *Tetrahedron Lett.*, 2011, **52**, 1924.

[184] S. A. Reed and M. C. White, *J. Am. Chem. Soc.*, 2008, **130**, 3316.

[185] "The Role of Nuclear Power in a Low Carbon Economy", Sustainable Development Commission (SDC) position paper, 2006.

[186] P. C. Burns, R. C. Ewing and A. Navrotsky, *Science*, 2012, **335**, 1184.

[187] "The 2010 UK Radioactive Waste Inventory: Main Report", Department of Energy and Climate Change (DECC) and the Nuclear Decommissioning Authority (NDA), 2010.

[188] R. C. Ewing, *Proc. Natl. Acad. Sci.*, 1999, **96**, 3432.

[189] J. Gray, S. R. Jones and A. D. Smith, *J. Radio. Prot.*, 1995, **15**, 99.

[190] A.-K. Duhme, S. C. Davies and D. L. Hughes, *Inorg. Chem.*, 1998, **37**, 5380.

[191] R. G. Denning, *J. Phys. Chem. A*, 2007, **111**, 4125.

[192] E. O'Grady and N. Kaltsoyannis, *J. Chem. Soc., Dalton Trans.*, 2002, 1233.

[193] C. Madic, M. Lecomte, P. Baron and B. Boullis, *C. R. Phys.*, 2002, **3**, 797 .

[194] K. E. Fletcher, M. I. Boyanov, S. H. Thomas, Q. Wu, K. M. Kemner and F. E. Löffler, *Environ. Sci. Technol.*, 2010, **44**, 4705.

[195] W. Gao and A. J. Francis, *Appl. Environ. Microb.*, 2008, **74**, 4580.

[196] J. L. Brown, C. C. Mokhtarzadeh, J. M. Lever, G. Wu and T. W. Hayton, *Inorg. Chem.*, 2011, **50**, 5105.

[197] P. L. Arnold, D. Patel, C. Wilson and J. B. Love, *Nature*, 2008, **451**, 315.

[198] P. L. Arnold, J. B. Love and D. Patel, *Coord. Chem. Rev.*, 2009, **253**, 1973.

[199] P. L. Arnold, A.-F. Pécharman, E. Hollis, A. Yahia, L. Maron, S. Parsons and J. B. Love, *Nat. Chem.*, 2010, **2**, 1056.

[200] P. L. Arnold, A.-F. Pécharman and J. B. Love, *Angew. Chem. Int. Ed.*, 2011, **50**, 9456.

[201] P. L. Arnold, G. M. Jones, S. O. Odoh, G. Schreckenbach, N. Magnani and J. B. Love, *Nat. Chem.*, 2012, **4**, 221.

[202] P. L. Arnold, E. Hollis, G. S. Nichol, J. B. Love, J.-C. Griveau, R. Caciuffo, N. Magnani, L. Maron, L. Castro, A. Yahia, S. O. Odoh and G. Schreckenbach, *J. Am. Chem. Soc.*, 2013, **135**, 3841.

[203] P. L. Arnold, A.-F. Pécharman, R. M. Lord, G. M. Jones, E. Hollis, G. S. Nichol, L. Maron, J. Fang, T. Davin and J. B. Love, *Inorg. Chem.*, 2015, **54**, 3702.

[204] S. Fortier and T. W. Hayton, *Coord. Chem. Rev.*, 2010, **254**, 197.

[205] E. A. Pedrick, G. Wu and T. W. Hayton, *Inorg. Chem.*, 2014, **53**, 12237.

[206] G. Nocton, P. Horeglad, V. Vetere, J. Pécaut, L. Dubois, P. Maldivi, N. M. Edelstein and M. Mazzanti, *J. Am. Chem. Soc.*, 2010, **132**, 495.

[207] E. A. Pedrick, G. Wu and T. W. Hayton, *Inorg. Chem.*, 2015, **54**, 7038.

[208] D. D. Schnaars, G. Wu and T. W. Hayton, *J. Am. Chem. Soc.*, 2009, **131**, 17532.

[209] J.-C. Berthet, P. Thuery and M. Ephritikhine, *Chem. Commun.*, 2005, 3415.

[210] S. Kannan, A. E. Vaughn, E. M. Weis, C. L. Barnes and P. B. Duval, *J. Am. Chem. Soc.*, 2006, **128**, 14024.

[211] S. Kannan, M. A. Moody, C. L. Barnes and P. B. Duval, *Inorg. Chem.*, 2006, **45**, 9206.

[212] D. L. J. Broere, R. Plessius and J. I. van der Vlugt, *Chem. Soc. Rev.*, 2015, **44**, 6886.

[213] P. J. Chirik and K. Wieghardt, *Science*, 2010, **327**, 794.

[214] W. Kaim, *Eur. J. Inorg. Chem.*, 2012, **2012**, 343.

[215] O. R. Luca and R. H. Crabtree, *Chem. Soc. Rev.*, 2013, **42**, 1440.

[216] V. Lyaskovskyy and B. de Bruin, *ACS Catal.*, 2012, **2**, 270.

[217] N. H. Anderson, S. O. Odoh, U. J. Williams, A. J. Lewis, G. L. Wagner, J. Lezama Pacheco, S. A. Kozimor, L. Gagliardi, E. J. Schelter and S. C. Bart, *J. Am. Chem. Soc.*, 2015, **137**, 4690.

[218] C. Camp, V. Mougel, P. Horeglad, J. Pécaut and M. Mazzanti, *J. Am. Chem. Soc.*, 2010, **132**, 17374.

[219] P. L. Diaconescu and C. C. Cummins, *Dalton Trans.*, 2015, **44**, 2676.

[220] J. J. Kiernicki, D. P. Cladis, P. E. Fanwick, M. Zeller and S. C. Bart, *J. Am. Chem. Soc.*, 2015, **137**, 11115.

[221] J. J. Kiernicki, B. S. Newell, E. M. Matson, N. H. Anderson, P. E. Fanwick, M. P. Shores and S. C. Bart, *Inorg. Chem.*, 2014, **53**, 3730.

[222] S. J. Kraft, P. E. Fanwick and S. C. Bart, *Inorg. Chem.*, 2010, **49**, 1103.

[223] S. J. Kraft, P. E. Fanwick and S. C. Bart, *J. Am. Chem. Soc.*, 2012, **134**, 6160.

[224] S. J. Kraft, U. J. Williams, S. R. Daly, E. J. Schelter, S. A. Kozimor, K. S. Boland, J. M. Kikkawa, W. P. Forrest, C. N. Christensen, D. E. Schwarz, P. E. Fanwick, D. L. Clark, S. D. Conradson and S. C. Bart, *Inorg. Chem.*, 2011, **50**, 9838.

[225] E. M. Matson, S. R. Opperwall, P. E. Fanwick and S. C. Bart, *Inorg. Chem.*, 2013, **52**, 7295.

[226] S. A. Pattenaude, C. S. Kuehner, W. L. Dorfner, E. J. Schelter, P. E. Fanwick and S. C. Bart, *Inorg. Chem.*, 2015, **54**, 6520.

[227] J. L. Sessler, P. J. Melfi and G. D. Pantos, *Coord. Chem. Rev.*, 2006, **250**, 816.

[228] I. T. Ho, Z. Zhang, M. Ishida, V. M. Lynch, W.-Y. Cha, Y. M. Sung, D. Kim and J. L. Sessler, *J. Am. Chem. Soc.*, 2014, **136**, 4281.

[229] K. Takao, S. Tsushima, T. Ogura, T. Tsubomura and Y. Ikeda, *Inorg. Chem.*, 2014, **53**, 5772.

[230] H. C. Hardwick, D. S. Royal, M. Helliwell, S. J. A. Pope, L. Ashton, R. Goodacre and C. A. Sharrad, *Dalton Trans.*, 2011, **40**, 5939.

[231] J. A. Pool, E. Lobkovsky and P. J. Chirik, *Nature*, 2004, **427**, 527.

[232] B. Wayland and X. Fu, *Science*, 2006, **311**, 790.

[233] J. P. Collman, P. Denisevich, Y. Konai, M. Marrocco, C. Koval and F. C. Anson, *J. Am. Chem. Soc.*, 1980, **102**, 6027.

[234] G. Givaja, M. Volpe, M. Edwards, A. Blake, C. Wilson, M. Schröder and J. Love, *Angew. Chem. Int. Ed.*, 2007, **46**, 584.

[235] J. P. Collman, P. S. Wagenknecht and J. E. Hutchison, *Angew. Chem. Int. Ed.*, 1994, **33**, 1537.

[236] B. J. Pistorio, C. J. Chang and D. G. Nocera, *J. Am. Chem. Soc.*, 2002, **124**, 7884.

[237] J. P. Collman, M. S. Ennis, D. A. Offord, L. L. Chng and J. H. Griffin, *Inorg. Chem.*, 1996, **35**, 1751.

[238] J. P. Collman, J. E. Hutchison, M. A. Lopez and R. Guilard, *J. Am. Chem. Soc.*, 1992, **114**, 8066.

[239] J. B. Love, *Chem. Commun.*, 2009, 3154.

[240] E. Askarizadeh, A. M. J. Devoille, D. M. Boghaei, A. M. Z. Slawin and J. B. Love, *Inorg. Chem.*, 2009, **48**, 7491.

[241] A. M. J. Devoille, P. Richardson, N. L. Bill, J. L. Sessler and J. B. Love, *Inorg. Chem.*, 2011, **50**, 3116.

[242] J. L. Sessler, E. Katayev, G. D. Pantos, P. Scherbakov, M. D. Reshetova, V. N. Khrustalev, V. M. Lynch and Y. A. Ustynyuk, *J. Am. Chem. Soc.*, 2005, **127**, 11442.

[243] C. J. Hastings, M. D. Pluth, R. G. Bergman and K. N. Raymond, *J. Am. Chem. Soc.*, 2010, **132**, 6938.

[244] T. Murase, S. Horiuchi and M. Fujita, *J. Am. Chem. Soc.*, 2010, **132**, 2866.

[245] V. F. Slagt, J. N. H. Reek, P. C. J. Kamer and P. W. N. M. van Leeuwen, *Angew. Chem. Int. Ed.*, 2001, **40**, 4271.

[246] Z. J. Wang, K. N. Clary, R. G. Bergman, K. N. Raymond and F. D. Toste, *Nat. Chem.*, 2013, **5**, 100.

[247] T. Cadenbach, J. R. Pankhurst, T. A. Hofmann, M. Curcio, P. L. Arnold and J. B. Love, *Organometallics*, 2015, **34**, 2608.

[248] J. W. Leeland, F. J. White and J. B. Love, *J. Am. Chem. Soc.*, 2011, **133**, 7320.

[249] J. Barber, *Philos. Trans. R. Soc., B*, 2008, 2665.

[250] G. Givaja, M. Volpe, M. Edwards, A. Blake, C. Wilson, M. Schröder and J. Love, *Angew. Chem. Int. Ed.*, 2007, **46**, 584.

[251] M. Volpe, H. Hartnett, J. W. Leeland, K. Wills, M. Ogunshun, B. J. Duncombe, C. Wilson, A. J. Blake, J. McMaster and J. B. Love, *Inorg. Chem.*, 2009, **48**, 5195.

[252] E. Askarizadeh, S. B. Yaghoob, D. M. Boghaei, A. M. Z. Slawin and J. B. Love, *Chem. Commun.*, 2010, **46**, 710.

[253] A. M. J. Devoille and J. B. Love, *Dalton Trans.*, 2012, **41**, 65.

[254] P. L. Arnold, C. J. Stevens, J. H. Farnaby, M. G. Gardiner, G. S. Nichol and J. B. Love, *J. Am. Chem. Soc.*, 2014, **136**, 10218.

[255] P. L. Arnold, C. J. Stevens, N. L. Bell, R. M. Lord, J. M. Goldberg, G. S. Nichol and J. B. Love, *Chem. Sci.*, 2017, **8**, 3609.

[256] P. L. Arnold, A. J. Blake, C. Wilson and J. B. Love, *Inorg. Chem.*, 2004, **43**, 8206.

[257] M. Zegke, G. S. Nichol, P. L. Arnold and J. B. Love, *Chem. Commun.*, 2015, **51**, 5876.

[258] P. L. Arnold, D. Patel, A. J. Blake, C. Wilson and J. B. Love, *J. Am. Chem. Soc.*, 2006, **128**, 9610.

[259] P. L. Arnold, E. Hollis, F. J. White, N. Magnani, R. Caciuffo and J. B. Love, *Angew. Chem. Int. Ed.*, 2011, **50**, 887.

[260] W. Reiter, A. Gerges, S. Lee, T. Deffo, T. Clifford, A. Danby and K. Bowman-James, *Coord. Chem. Rev.*, 1998, **174**, 343 .

[261] N. N. Gerasimchuk, A. Gerges, T. Clifford, A. Danby and K. Bowman-James, *Inorg. Chem.*, 1999, **38**, 5633.

[262] E. A. Katayev, Y. A. Ustynyuk, V. M. Lynch and J. L. Sessler, *Chem. Commun.*, 2006, 4682.

[263] S. Madhu, M. R. Rao, M. S. Shaikh and M. Ravikanth, *Inorg. Chem.*, 2011, **50**, 4392.

[264] S. Madhu and M. Ravikanth, *Inorg. Chem.*, 2014, **53**, 1646.

[265] V. Lakshmi and M. Ravikanth, *J. Mater. Chem. C*, 2014, **2**, 5576.

[266] A. Loudet and K. Burgess, *Chem. Rev.*, 2007, **107**, 4891.

[267] E. R. King and T. A. Betley, *Inorg. Chem.*, 2009, **48**, 2361.

[268] E. T. Hennessy and T. A. Betley, *Science*, 2013, **340**, 591.

[269] E. R. King, G. T. Sazama and T. A. Betley, *J. Am. Chem. Soc.*, 2012, **134**, 17858.

[270] E. A. Katayev, K. Severin, R. Scopelliti and Y. A. Ustynyuk, *Inorg. Chem.*, 2007, **46**, 5465.

[271] E. A. Katayev, H. V. Lavrov and V. N. Khrustalev, *J. Porphyr. Phthalocya.*, 2008, **12**, 1137.

[272] V. S. Thoi, J. R. Stork, E. T. Niles, E. C. Depperman, D. L. Tierney and S. M. Cohen, *Inorg. Chem.*, 2008, **47**, 10533.

Chapter 2

Synthesis and electronic structure of ligands

This chapter outlines the straightforward synthesis of the acyclic and macrocyclic poly-pyrrolic Schiff-base compounds that are used as ligands for a number of metal complexes in later chapters. A number of synthetic strategies towards preparing macrocyclic dipyrrins will be discussed and a comparison of electronic structures between dipyrromethanes and dipyrrins will be made.

2.1 Ligand synthesis

2.1.1 Synthesis of *meso*-substituted dipyrromethanes

Dipyrromethanes are prepared from the condensation reaction between pyrrole and a carbonyl compound. The use of ketones in this reaction leads to dipyrromethanes that are disubstituted at the *meso*-position, for example, the reaction of pyrrole and 3-pentanone affords 5,5-diethyl dipyrromethane.[1] These disubstituted dipyrromethanes are not able to undergo oxidation to dipyrrins.

A single *meso*-substituent may be incorporated if an aldehyde is used in the condensation reaction, and the proton-substituent that remains at the *meso*-position provides a possibility for oxidation to dipyrrins to occur.[2–4] The pentafluoroaryl-*meso*-substituent (C_6F_5) was chosen for this work for several reasons: to improve the solubility of the larger macrocycles; to enhance the acidity of the *meso*-proton and promote oxidation to dipyrrins; and to better stabilise low oxidation-state metal complexes. Savéant's work on C_6F_5-substituted iron-porphyrin complexes for electro-catalytic CO_2 reduction is testament to the ability of this group to stabilise low oxidation states and enhance electro-catalytic activity.[5,6]

The solvent-free method, reported by Lindsey, was used to prepare 5-pentafluorophenyl-dipyrromethane, **1**, in 45 % yield, using 10 mol% $InCl_3$ as the catalyst (Scheme 2.1).[7] In the ^{1}H NMR spectrum there are resonances for two equivalent pyrrolic N-H protons at 8.14 ppm, three inequivalent pyrrole proton

environments at 6.73, 6.16 and 6.03 ppm and one *meso*-proton at 5.90 ppm. The $^{19}F\{^1H\}$ NMR spectrum also features three resonances at -141.5, -155.8 and -161.2 ppm, consistent with a mono-substituted C_6F_5-group undergoing free rotation. A single product was detected by GC-MS, eluting with a retention time of 38 minutes with the expected molecular ion peak at 312 m/z; neither *N*-confused-dipyrromethane or tripyrrane were detected, which are previously reported side-products of this reaction.
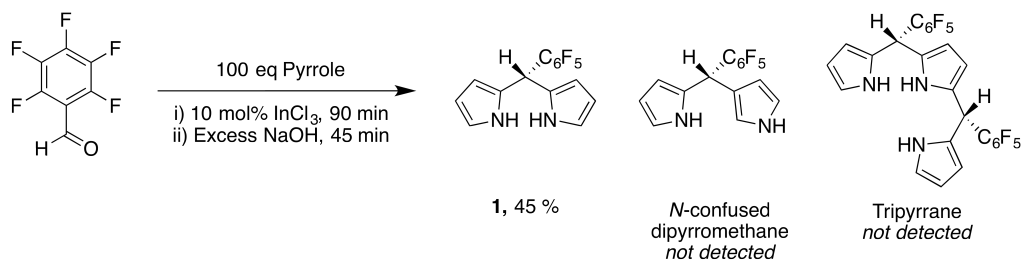
Scheme 2.1: Synthesis of 5-pentafluorophenyl-dipyrromethane, **1**.[7]

2.1.2 Formylation of dipyrromethanes

The Vilsmeier-Haack reaction is an established procedure for the formylation of pyrrolic compounds, and it may be used with dipyrromethanes to formylate both of the unsubstituted α-positions.[8,9] 1,9-diformyl-5-pentafluorophenyl-dipyrromethane was synthesised according to a reported procedure, affording **2** as a brown solid in 75 % yield (Scheme 2.2).[4] The synthesis of **2** is supported by ^1H NMR spectroscopy, as there is a large change in the chemical shift for the pyrrole N-H resonance to 10.39 ppm and the appearance of a resonance at 9.29 ppm that is attributed to the aldehyde protons. Furthermore, the doublet multiplicity of the two pyrrole β-proton resonances and the evident C_2-symmetry of the compound indicate that both pyrrole α-positions have been formylated successfully. The $^{13}C\{^1H\}$ NMR spectrum includes a single aldehyde resonance at 179.2 ppm. In the $^{19}F\{^1H\}$ NMR spectrum, the C_6F_5-substituent appears as a set of three resonances at -140.4, -153.5 and -160.3 ppm. An additional set of low-intensity ^{19}F NMR resonances at -141.3, -154.5 and -160.6 ppm are assigned to a trace impurity that may be the source of the brown colour of the compound.

The procedure reported by Lindsey claims that the brown colour of **2** cannot be removed. Attempts to purify **2** by column chromatography (silica, 80:20:1 ethyl acetate : hexanes : NEt$_3$) or by vacuum sublimation led to decomposition of the compound. However, **2** can be recrystallised from hot aqueous ethanol (80 % ethanol, v/v) on slow cooling to room temperature. Large, colourless, block
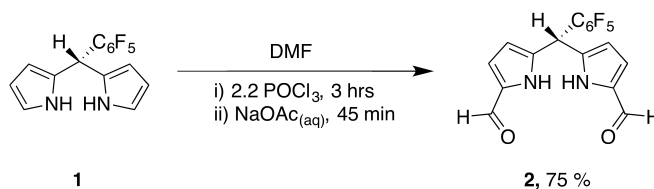
Scheme 2.2: Synthesis of 1,9-diformyl-5-pentafluorophenyl-dipyrromethane, **2**.[4]

crystals of **2** were obtained using this method and the previously unreported solid-state structure was determined by X-ray diffraction (Figure 2.1).

The solid-state structure of **2** was refined in the P$\bar{1}$ space group and the asymmetric unit consists of two molecules. In each molecule, the O1-C1-N1-H1 dihedral angle is 4.8° – 5.8°, and the two molecules are aligned such that a pair of hydrogen-bonds form between their formyl-pyrrole units (r, H1-O1 ≈ 2.0 Å). The tetrahedral geometry of the *meso*-carbon is evident from its bond angles with neighbouring carbon atoms, which lie in the range 110.0(2)° – 114.7(2)°.
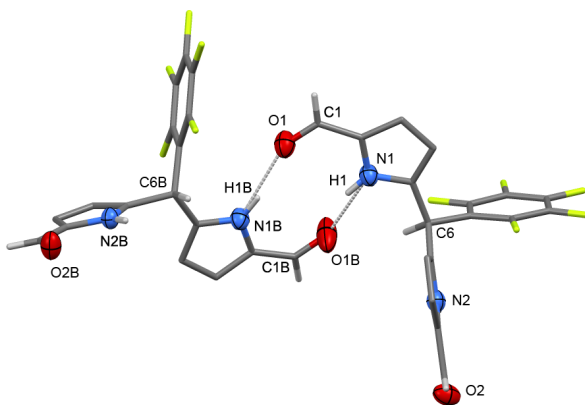
Figure 2.1: Solid-state structure of **2**, showing the asymmetric unit. Displacement ellipsoids are drawn at 50 % probability and for clarity, the protons at the pyrrole β-positions have been omitted.

2.1.3 Donor-expanded dipyrromethanes and dipyrrins

The Schiff-base condensation reaction between 1,9-diformyl-dipyrromethanes and a variety of primary amines enables the synthesis of many 1,9-diimino-dipyrromethane compounds. The use of mono-amine reagents in this reaction leads to acyclic, donor-expanded dipyrromethanes and dipyrrins.[10–14] One such dipyrromethane, containing *para-tert*-butyl-phenyl imine substituents, has been synthesised and successfully oxidised to its dipyrrin congener. A second dipyrrin compound, featuring *tert*-butyl imine substituents was synthesised directly, without isolation of the dipyrromethane intermediate.

If diamino compounds are used in the Schiff-base condensation reaction, a [2+2] cyclisation ensues, affording macrocyclic compounds.[15–18] Two different macrocycles were prepared using this method; one features *ortho*-phenylene "spacer" groups between the two donor-expanded dipyrromethane compartments, whereas the other features 1,8-anthracenyl spacer groups.

Acyclic dipyrrins

The aryl-substituted diimino-dipyrromethane, **3**, was prepared from the acid-promoted condensation reaction between **2** and *p*-^{t}Bu-aniline in methanol.[i] Although many acids could be used for this reaction, trifluoroacetic acid (TFA) was found to give high yields. The iminium-acetate salt of **3** was not isolated, but instead neutralised with NEt$_3$ to afford the free-base form in 74 % yield (Scheme 2.3). ^{1}H NMR spectroscopy indicates a symmetric product in solution, with single resonances for the imino-protons at 8.18 ppm and the ^{t}Bu groups at 1.32 ppm. Two additional resonances, of doublet mulitiplicity, observed at 7.12 and 7.36 ppm are consistent with the introduction of two *para*-substituted aryl groups. Finally, there is a resonance for the *meso*-proton at 5.69 ppm that indicates the compound is saturated at that position. Further evidence for the introduction of an imine functional group is provided by the strong infra-red absorption band at 1623 cm^{-1}.

Oxidation of **3** to its dipyrrin congener HL^1 was achieved straightforwardly, by use of the two-electron oxidant 2,6-dichloro-4,5-dicyano-benzoquinone (DDQ). This reaction proceeded cleanly in 1 hour, to afford the dipyrrin in quantitative yields. Loss of the *meso*-proton ^{1}H NMR resonance observed for **3** concludes that the oxidation reaction was successful.
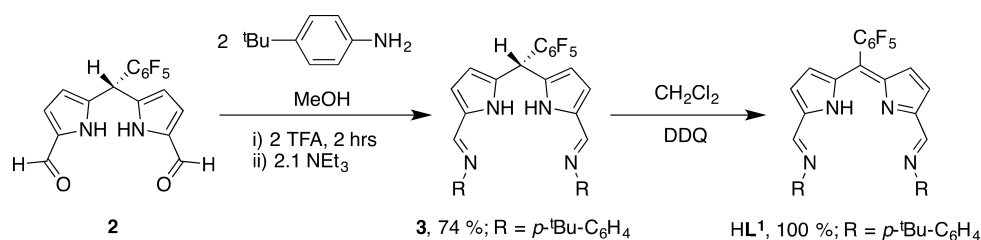
Scheme 2.3: Synthesis of dipyrromethane **3** and oxidation to dipyrrin HL^1.

A major problem in the synthesis of **3** is that the unreacted *p*-^{t}Bu-aniline and the by-product salt, [Et$_3$NH][CF$_3$CO$_2$], are extremely difficult to remove from

---

[i]**3** and HL^1 were first synthesised by Dr Daniel Betz. The improved synthesis, electronic absorption spectra and DFT calculations were carried out by myself.

the product. Even when the condensation reaction was carried out with sub-stoichiometric amounts of the amine, it was still present in the product. Attempts to purify the product by recrystallisation from a number of solvent systems and methods were not met with success. Column chromatography and vacuum sublimation methods both led to decomposition of the product. Furthermore, heating the product to 100 °C (the apparent limit of its thermal stability) under dynamic vacuum did not remove the amine, despite it having a boiling temperature of 90 – 93 °C at atmospheric pressure. Due to the high solubilities of **3** and HL^1, the impurities could not be washed away with organic solvents. It was found that washing a hexanes solution of HL^1 with water removed the aniline and salt, but that process led to hydrolysis of the imine. Hence, all further characterisation and reactions were carried out in the presence of these impurities.

In order to overcome the difficulties inherent in the synthesis of HL^1, a different synthetic approach was devised to prepare the alkyl-substituted diimino-dipyrrin, HL^2. It was thought that replacement of the large aryl imine-substituents in HL^1 with ^{t}Bu-substituents might increase rigidity and aid crystallisation of the dipyrrin; useful both for purification and characterisation. Furthermore, due to the volatility of ^{t}BuNH$_2$ (boiling temperature of 47 °C), any unreacted amine could be removed more readily. In order to avoid salt formation from an acid-promoted reaction and basic work-up procedure, the equilibrium of the Schiff-base reaction was exploited to drive the reaction towards the targeted product; a large excess of the reactant, ^{t}BuNH$_2$, was used (7 equivalents), and Na$_2$SO$_4$ was also added as a drying agent to remove water, one of the products. Heating at 50 °C for 48 hours in toluene was sufficient to obtain the product as a red solid in moderate yield of 48 % (Scheme 2.4).
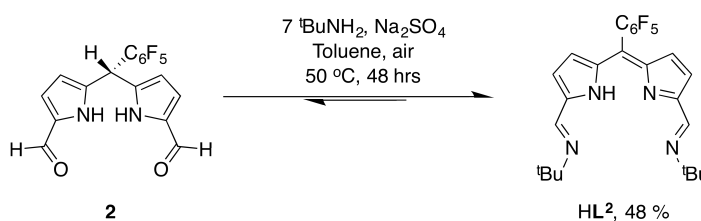
Scheme 2.4: Synthesis of dipyrrin HL^2.

Unlike HL^1, which required a separate oxidation step to afford the dipyrrin, HL^2 oxidises in air during its synthesis. The ^{1}H NMR spectrum for HL^2 indicates a symmetric product with single resonances for the imine-protons at 7.71 ppm and the ^{t}Bu groups at 0.76 ppm. A single set of resonances was observed in the ^{19}F{^{1}H} NMR spectrum, at −160.9, −152.2 and −138.2 ppm, that are assigned

to the C_6F_5-substituent. Furthermore, there is a resonance in the $^{13}C\{^1H\}$ NMR spectrum at 123.0 ppm that is assigned to the *meso*-carbon; this ^{13}C resonance is not observed during a DEPT-90 experiment, meaning that the *meso*-carbon is quaternary.

The solid-state structure of HL^2 was determined by X-ray crystallography and displays the expected planar geometry around the *meso*-carbon, with the bond angles around C10 summing to 360° (Figure 2.2). Interestingly, whilst HL^2 was found to adopt a C_2-symmetric solution-state structure by NMR spectrscopy, in the solid state, one of the imine groups is twisted away from the donor-compartment, lowering the symmetry to C_1. This twisting may have implications for the coordination chemistry with metal complexes, which is described in later chapters. HL^2 was refined in the P$\bar{1}$ space group and was found to contain two molecules of HL^2 in the asymmetric unit; each molecule is arranged head-to-tail in a co-planar arrangement with a different, symmetry equivalent molecule of HL^2 (in different asymmetric units). There is a short-contact of 3.529(6) Å between these co-planar pairs that implies π-stacking.

(a) (b)
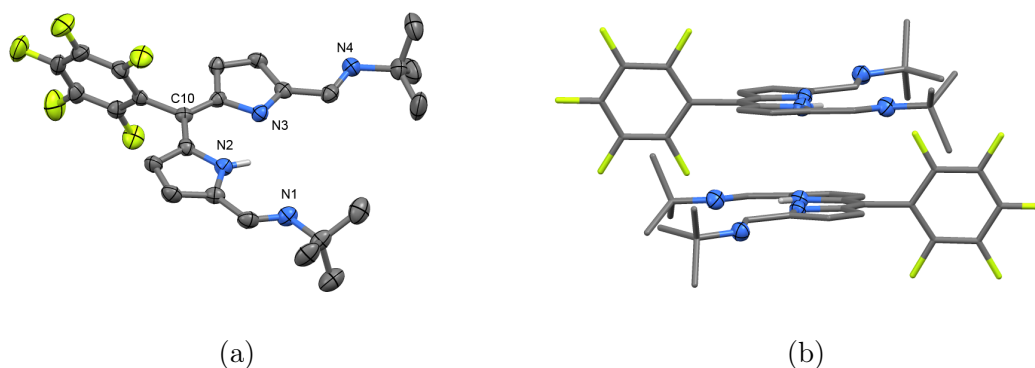
Figure 2.2: Solid-state structure of HL^2, showing (a) one of two HL^2 molecules in the asymmetric unit and (b) π-stacking in a pair of symmetry-equivalent molecules. Displacement ellipsoids are drawn at 50 % probability and for clarity, only the pyrrolic protons are shown.

Application of this second synthetic procedure to the synthesis of HL^1 also resulted in direct formation of the dipyrrin, negating the requirement for work-up of the intermediate dipyrromethane and subsequent oxidation reaction. Whilst the use of this procedure avoided the formation of $[Et_3NH][CF_3CO_2]$, unreacted p-^tBu-aniline was still present. However, the aerobic oxidation of dipyrromethane **3** using this second procedure indicates that the ease of oxidation of the dipyrromethane is not governed by the imine-substituent. Rather, it seems that changing the polarity of the solvent, from methanol to toluene, is enough to promote the aerobic oxidation reaction.

Macrocyclic compounds

The *ortho*-phenylene-bridged macrocycle H_4L^3 and the 1,8-anthracenyl-bridged macrocycle H_4L^4 were prepared from the acid-promoted Schiff-base condensation between equimolar amounts of **2** and the appropriate diamine. Upon neutralisation of the reaction mixtures with NEt_3, the free-base forms of the macrocycles precipitate from their methanol solutions as dull-yellow solids. Unlike the acyclic dipyrrins discussed above, the macrocyclic compounds are insoluble in methanol and can be isolated by filtration, washing with methanol to remove excess reactants, salts and side-products. The macrocycles were prepared in yields of 38 % for H_4L^3 and 42 % for H_4L^4 (Scheme 2.5). Due to the light-sensitivity of 1,8-diaminoanthracene, crude H_4L^4 is often prepared as a brown solid, but can be purified by precipitation from a chloroform solution on addition of excess methanol, affording a yellow solid.

Interestingly, the successful synthesis of H_4L^3 and H_4L^4 relies heavily on the acid used. For H_4L^3, TFA is used to promote the condensation reaction, whereas for H_4L^4, *para*-toluene sulfonic acid (PTSA) must be used. If other acids are used, both syntheses result in the formation of dark intractable solids, with NMR spectra that are not consistent with either compound.
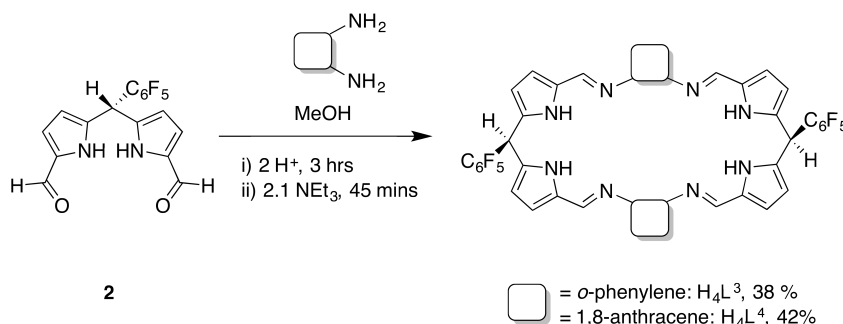
Scheme 2.5: Synthesis of macrocyclic compounds H_4L^3 and H_4L^4. For H_4L^3, H^+ = TFA; for H_4L^4, H^+ = PTSA.

For both macrocycles, characteristic ^1H NMR resonances for the imine protons were observed at 8.09 ppm for H_4L^3 and 8.38 ppm for H_4L^4. Imine IR absorption bands were also recorded at 1620 cm^{-1} for H_4L^3 and at 1614 cm^{-1} for H_4L^4. No higher-order cyclisation products were observed by ESI-MS, with only the expected molecular ion peaks observed at 937 m/z for H_4L^3 and at 1080 m/z for H_4L^4. Single crystals of both macrocycles were grown and their solid-state structures were determined by X-ray crystallography (Figure 2.3).

The crystal structure for H_4L^3 was refined in the Pnn2 space group. Unlike previous examples of macrocyclic ligands, H_4L^3 crystallises without any protic

solvent molecules hydrogen-bonded within the cleft.[19] Instead, in the asymmetric unit, there is one macrocycle molecule and four THF solvent molecules that are hydrogen-bonded to the pyrrolic N-H protons ($r \approx 2$ Å). All of the hydrogen-bonded solvent molecules are situated on one face of the macrocycle. Each imino-pyrrole unit is twisted with respect to its neighbouring units; this non-folded configuration minimises ring-strain in the molecule. Interestingly, the two *ortho*-phenylene groups are co-planar and situated in the same plane, with a small torsion angle of 3.22°. All eight nitrogen atoms in the macrocycle are situated no more than 0.35 Å away from the mean plane that includes all twelve *ortho*-phenylene carbon atoms. This arrangement minimises the occupied volume in the unit cell and presumably forms in order to maximise packing in the crystal lattice.

<div align="center">(a)   (b)</div>
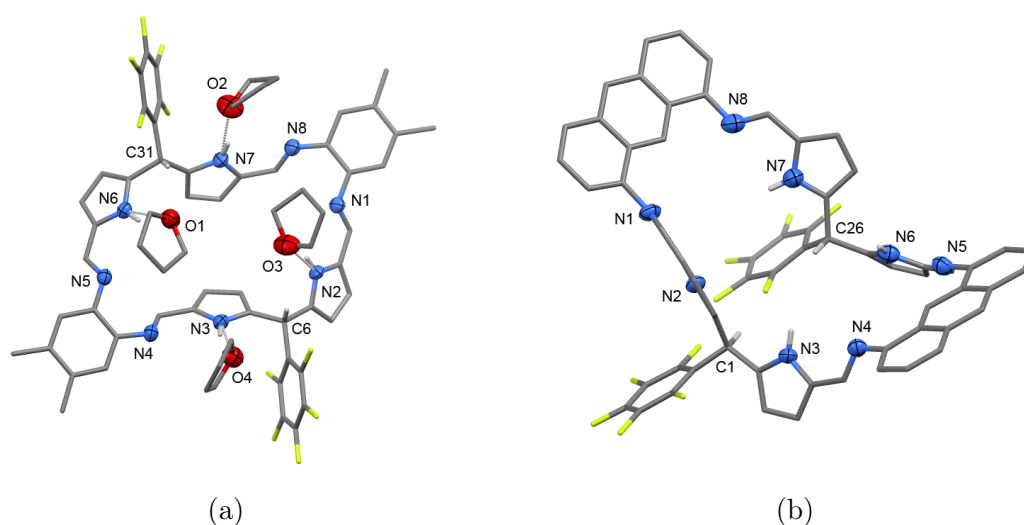
Figure 2.3: Solid-state structures of (a) H_4L^3 and (b) H_4L^4, showing their asymmetric units. Displacement ellipsoids are drawn at 50 % probability and for clarity, only the pyrrole- and *meso*-protons are shown. For H_4L^4, three molecules of methanol and one of water hydrogen-bonded in the cleft are omitted.

The crystal structure for H_4L^4 was refined in the $P\bar{1}$ space group. In this case there are protic solvent molecules in the cleft; three of methanol and one of water that are hydrogen-bonded to both the pyrrolic N-H protons and imine nitrogen atoms. In contrast with the rigid, Pacman-shaped structures that anthracene-bridged macrocycles form with metal ions, the metal-free macrocycle adopts a relaxed bowl-like geometry, folding about the *meso*-carbon positions. The "bite" angle, which describes the internal angle between the two anthracenyl spacer-groups, is quite large at 127.3(1)°. The nitrogen atoms on each half of the macrocycle (on one side of the *meso*-positions) are positioned no more than 0.4 Å away from the mean plane that includes and extends from their nearest

anthracene-group carbon atoms, as was similar in the structure of H_4L^3.

With two different substituents at the *meso*-position, the [2+2] cyclisation reaction could result in either *syn-* or *anti*-isomers, where the relative positions of the *meso*-substituents dictate the identity of the isomer. Importantly, both H_4L^3 and H_4L^4 crystallise as the *syn*-isomer only and there is no evidence to support a mixture of isomers by NMR spectroscopy, which clearly shows a single set of resonances for ^1H, ^{13}C and ^{19}F nuclei. Considering the relatively low isolated yields of both macrocycles (*ca.* 40 %) it is conceivable that the *syn*-isomer precipitates from the reaction mixture preferentially, with the *anti*-isomer remaining in solution. Similar macrocycles have previously been isolated in much higher yields of 80 % using the same Schiff-base condensation reaction; but these macrocycles are symmetrically di-substituted at the *meso*-position and have only one possible conformation.[10] Furthermore, every metal complex of H_4L^4, which will be discussed in later chapters, has been characterised as the *syn*-isomer only.

2.2 Dipyrromethane oxidation strategies

Whilst the oxidation of acyclic dipyrromethanes occurs readily, macrocycles H_4L^3 and H_4L^4 could not be cleanly oxidised with DDQ, instead resulting in a myriad of unidentifiable products by NMR spectroscopy. Similar decomposition was observed on reaction of H_4L^3 or H_4L^4 with 2,3,5,6-tetrachloro-benzoquinone (chloranil), Ag_2O, I_2 or $Ce(NH_4)_2(NO_3)_6$. Despite previous reports of similar macrocyclic dipyrromethanes being oxidised with $KMnO_4$ or MnO_2, no discernable products could be isolated from those reactions with H_4L^3 or H_4L^4.[20,21]

As the dipyrromethane macrocycles could not be directly oxidised, a key synthetic target was the oxidised form of the macrocycle precursor, a 1,9-diformyl-dipyrrin. If this compound could be synthesised, a macrocyclic dipyrrin might be prepared from the Schiff-base condensation reaction with either diamine as described in section 2.1. Scheme 2.6 outlines the numerous routes attempted to isolate a 1,9-diformyl-dipyrrin, none of which were met with success.

Direct oxidation of **2** by DDQ or chloranil simply led to decomposition. In contrast, dipyrromethane **1** was readily oxidised by DDQ or chloranil to afford the dipyrrin **4**, which is a well documented reaction in the literature.[22] Unfortunately, dipyrrin **4** could not be formylated at the 1- and 9-positions using the Vilsmeier-Haack reaction; at room temperature, no reaction occurs after 3 hours, and heating to 70 °C causes decomposition. This is perhaps unsurprising, as formylation of a dipyrrin in the absence of coordinated boron has not been reported previously,
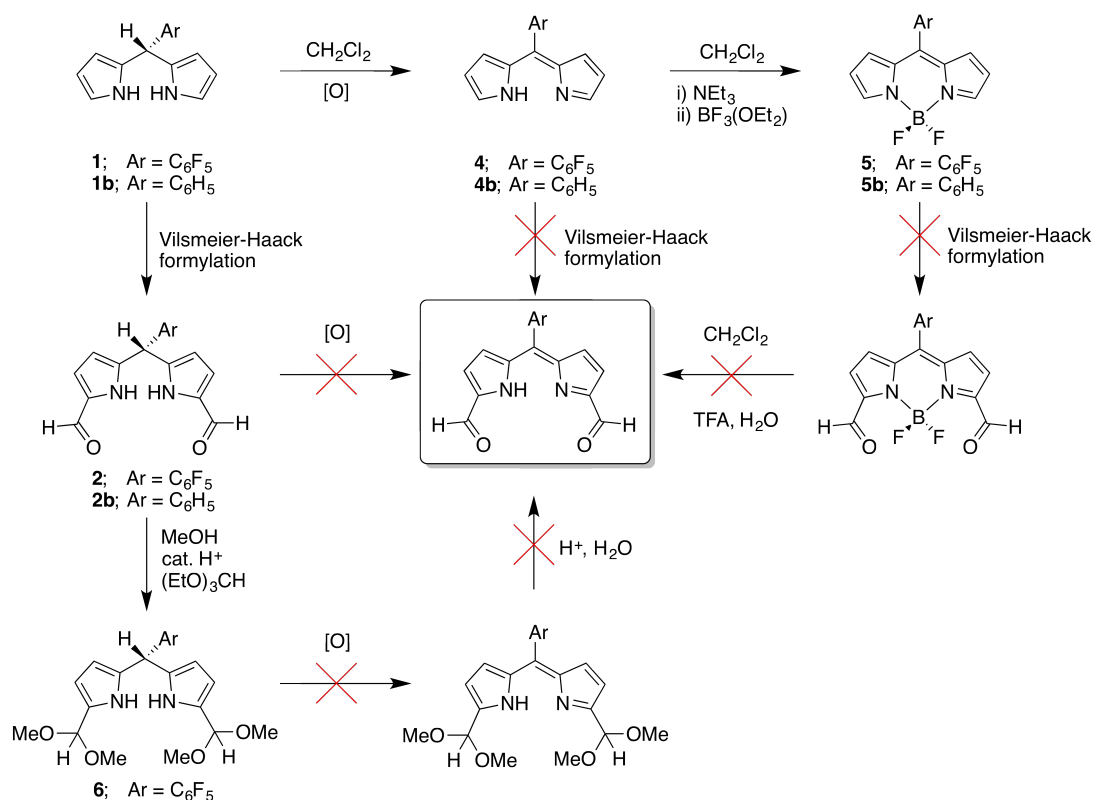
Scheme 2.6: Attempted synthetic pathways towards a 1,9-diformyl-dipyrrin.

whereas there are a few reports of 1,9-diformyl-BODIPY compounds in the literature. The reported syntheses involve *in situ* oxidation of a 1,9-diformyl-dipyrromethane by DDQ at high temperature in toluene, followed by rapid and sequential addition of NEt_3 and $BF_3(OEt_2)$; the yields of this reaction are typically 15 % after purification by column chromatography.[9,23–25] Unfortunately, isolation of the pure diformyl-BODIPY compounds could not be reproduced, and neither could it be formed from the direct reaction of **2** with NEt_3 and $BF_3(OEt_2)$, or by formylation of the BODIPY compound **5**.

There is one report in the literature of a Schiff-base condensation reaction between 4,5-*ortho*-phenylene diamine and a 1,9-diformyl-BODIPY compound.[26] In that case, the [2+2] cyclisation reaction does not occur. Instead, both amine groups condense with one aldehyde group, yielding an asymmetric, acyclic BODIPY compound with an imidazole group at one of the α-positions of the dipyrrin. It would be interesting to use 1,8-diaminoanthracene in this reaction, as an imidazole would not be able to form due to the increased distance between the two amine groups. The diformyl-BODIPY compound would therefore be a promising precursor for the synthesis of an anthracenyl-bridged, macrocyclic dipyrrin, especially as there is precedent for the removal of the BF_2 unit using

simple Brønsted acids.[27]

It seems that the introduction of the aldehyde groups in the 1- and 9-positions in the dipyrromethane **2** is the cause of decomposition during the oxidation reaction, and as such a protection strategy was attempted. The 1,9-diacetal compound, **6**, was successfully synthesised in 95 % yield by the acid-catalysed acetal reaction of **2** in methanol; PTSA was used as the acid catalyst. The introduction of acetal groups to both 1- and 9-positions is supported by ^{1}H NMR spectroscopy, which features a single resonance at 9.34 ppm that is assigned to the two equivalent acetal C-H protons, and a singlet resonance at 3.49 ppm for the four methoxy acetyl-substituents. Unfortunately, the acetal compound also decomposed on oxidation with DDQ or chloranil.

It was suspected that the electron-withdrawing nature of the C_6F_5 *meso*-substituent was destabilising the various dipyrromethane compounds during the oxidation reactions. The reactions summarised in Scheme 2.6 were repeated, starting from a dipyrromethane with a phenyl *meso*-substituent, but the 1,9-diformyl-dipyrrin could not be isolated this way either.

Macrocyclic dipyrrins have been reported in the literature. Those macrocycles typically feature an alkyl bridge between the two donor compartments, such that there is no π-conjugation between the two compartments and the macrocycle has much greater flexibility overall.[15,28] It was thought that the difficulty in oxidising macrocycles H_4L^3 and H_4L^4 might stem from the aromatic spacer-groups between the two donor compartments, as oxidation to a dipyrrin would lead to extended π-conjugation across the whole molecule, introducing ring-strain unless the macrocycle could rapidly fold to a Pacman structure to break the conjugation and avoid decomposition. In an attempt to alleviate this problem, the imine groups in H_4L^3 were reduced using excess $NaBH_4$ in THF, to afford the macrocyclic amino-dipyrromethane H_8L^3 (Scheme 2.7). The ^{1}H NMR spectrum of H_8L^3 indicates that the macrocycle is symmetric, with a single resonance observed for the four amine protons at 6.98 ppm, and another single resonance observed for the eight methylene protons at 4.14 ppm. In this environment, all of these methylene protons experience scalar relaxation from the nearby quadrupolar moment on nitrogen, meaning that multiplicity in these resonances due to mutual coupling is not resolved. However, correlation spectroscopy reveals that magnetisation-transfer between these two proton environments occurs, supporting their assignment. Despite the reduction in π-conjugation in the spacer group linking the two dipyrromethane units, and despite the more flexible alkyl connection between them, attempted oxidation of H_8L^3 still led to decomposition.
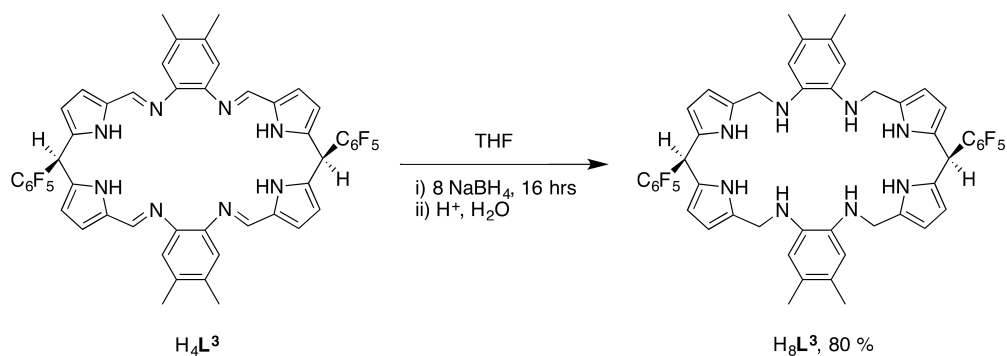
Scheme 2.7: Reduction of the imine functional groups in H_4L^3 to afford macrocyclic amino-dipyrromethane H_8L^3.

2.3   Electronic structures of donor-expanded dipyrromethanes and dipyrrins

The electronic structures of the acyclic dipyrromethanes and dipyrrins, and the macrocyclic dipyrromethanes were studied, to investigate whether there is an underlying reason why the macrocyclic dipyrromethanes could not be oxidised. The compounds were studied by electrochemical methods, electronic absorption spectroscopy and by computational methods.

2.3.1   Electrochemistry

Due to the low purity of the dipyrromethane **3** and dipyrrin HL^1, the electrochemical behaviour of those compounds could not be reliably studied by cyclic voltammetry (CV). Measured against a glassy-carbon working electrode in CH_2Cl_2, dipyrrin HL^2 undergoes two reduction processes at E_p^c -1.51 V and E_p^c -2.02 V *versus* the ferrocenium/ferrocene redox couple ($Fc^+/Fc = 0$ V; Figure 2.4 (a)). These two processes are assigned as irreversible due to the lack of associated oxidation waves on the return scan, and indicates poor stability of the reduced species. The areas of the cathodic CV waves are similar, meaning that both processes involve the same number of electrons; these reductions are likely to involve one-electron each.

Macrocycles H_4L^3 and H_4L^4 undergo irreversible reduction behaviour only, with no oxidation processes measured for either compound in the electrochemical window provided by $[^nBu_4N][PF_6]$ in THF or CH_2Cl_2. At a scan rate of 100 mV s^{-1}, H_4L^3 undergoes an irreversible reduction at E_p^c -1.41 V (Figure 2.4 (b)). An anodic wave is not observed on the return scan unless the scan-rate is increased to 400 mV s^{-1}; at this scan-rate, an associated anodic wave is observed at E_p^a -0.71

(a)

(b)

(c)
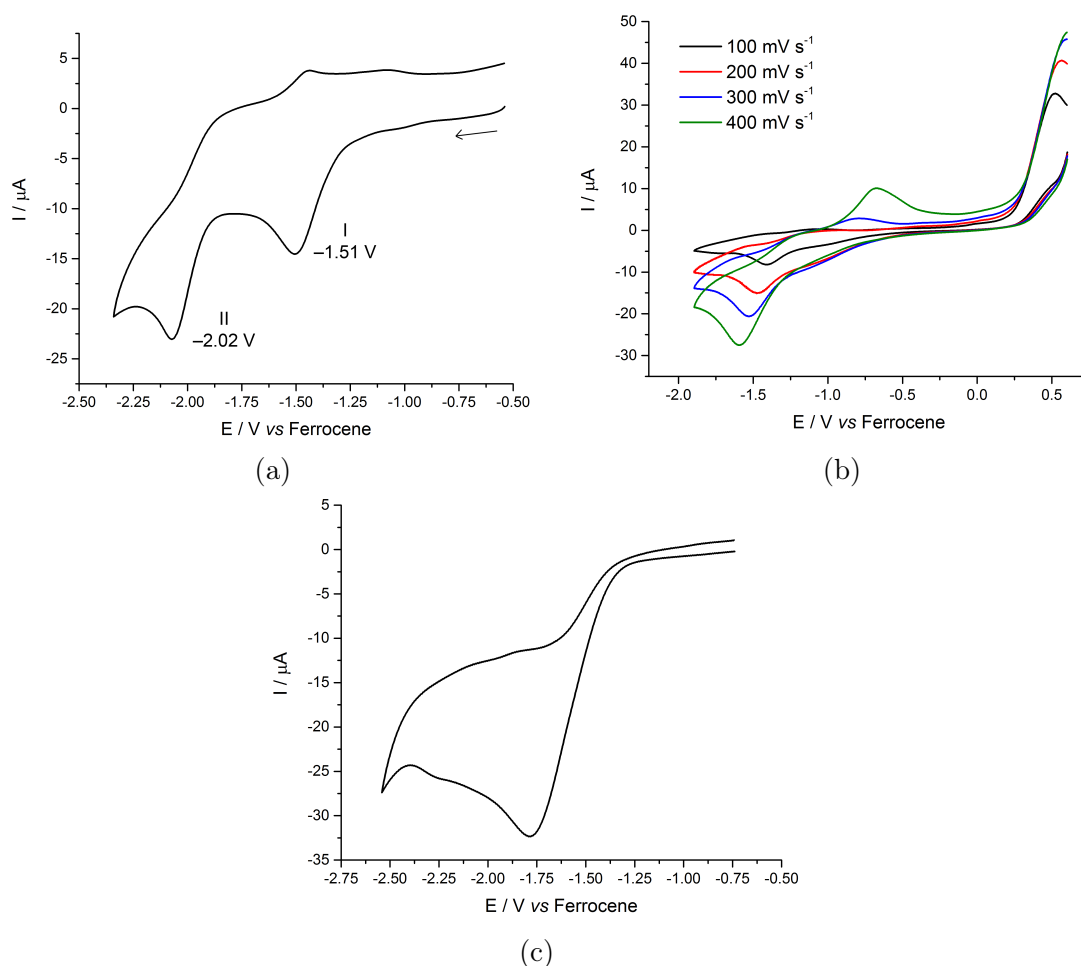
Figure 2.4: Cyclic voltammograms of (a) HL^2 at 100 mV s^{-1} (b) H_4L^3 at variable scan-rates, and (c) H_4L^4 at 100 mV s^{-1}. HL^2 was measured using a glassy-carbon working electrode in CH_2Cl_2. A Pt working electrode was used to study H_4L^3 (THF) and H_4L^4 (CH_2Cl_2). All potentials are referenced *versus* Fc$^+$/Fc. A 0.1 M solution of [$^nBu_4N$][PF_6] was used as the supporting electrolyte.

V, 700 mV from the cathodic peak potential. This indicates that reduction of H_4L^3 at -1.41 V generates an unstable species that undergoes rapid chemical change, that then undergoes irreversible oxidation at -0.71 V. This process is summarised as an $E_iC_iE_i$ mechanism, where E denotes electron-transfer, C denotes chemical change and the subscript i denotes irreversibility (the subscript r would denote reversibility).

In CH_2Cl_2, macrocycle H_4L^4 undergoes irreversible reduction at E_p^c -1.78 V, but in this case, no associated anodic waves were observed even at 500 mV s^{-1}. (Figure 2.4 (c)).

2.3.2 Electronic absorption spectroscopy

Due to the intense colours of the donor-expanded dipyrromethanes and dipyrrins discussed in this chapter, both in the solid- and solution-state, it was thought that electronic absorption spectroscopy would provide insight into the electronic structures of those compounds. The measured absorption spectra were complemented by spectra simulated by time-dependent density functional theory (TD-DFT) and molecular orbital calculations, in order to provide a detailed description of the electronic transitions in these compounds. Good approximations for the absorption spectra were obtained from simulations using the B3LYP functional and 6-311G(d,p) basis set, and the polarisable continuum model (PCM) solvent model was employed to simulate solvation by CH_2Cl_2.

The dominant absorption band for **3** is centered at 373 nm and is comprised of a mixture of H→(L+1)[ii] (59 %) and (H−1)→L (32 %) transitions; the H→L transition appears as a shoulder at 413 nm (Figure 2.5 (a)). Upon oxidation to HL^1, both the (H−1)→L and H→L transitions are bathochromically shifted to 520 and 540 nm, respectively, while the H→(L+1) transition remains in the UV-region at 290 nm (Figure 2.5 (b)). Only the transitions departing to the LUMO are bathochromically shifted upon oxidation, due to a 1.6 eV stabilisation of that molecular orbital; this is typical for dipyrromethane compounds.[29]

As H_2L^2 could not be isolated, its electronic absorption spectrum was simulated only. The simulated spectrum consists of a number of transitions in the UV-region, dominated by a band centred at 260 nm; many transitions contribute to this absorption band, with the (H−1)→(L+2) transition being the highest contributor (47 %). The lowest energy transitions are the H→L and the (H−1)→L transitions at 321 nm and 299 nm, respectively, that make up a shoulder of the dominant absorption band. In the case of the *t*Bu-substituted donor-expanded dipyrrin, oxidation to HL^2 results in a broad absorption band in the visible-light region, at 480 nm; the measured spectrum was simulated particularly well by TD-DFT methods and indicates that this absorption band arises due to the H→L transition only.

In the case of H_4L^3, the lowest energy absorption band, measured experimentally at 356 nm, consists of a mixture of the (H−1)→L (34 %) and H→(L+1) transitions. The H→L transition makes a negligible contribution and is predicted to occur at 415 nm. As detailed above, the oxidised macrocycle H_2L^3 has not been synthesised, but its structure and absorption spectrum was predicted by DFT

[ii]Where H denotes HOMO and L denotes LUMO.
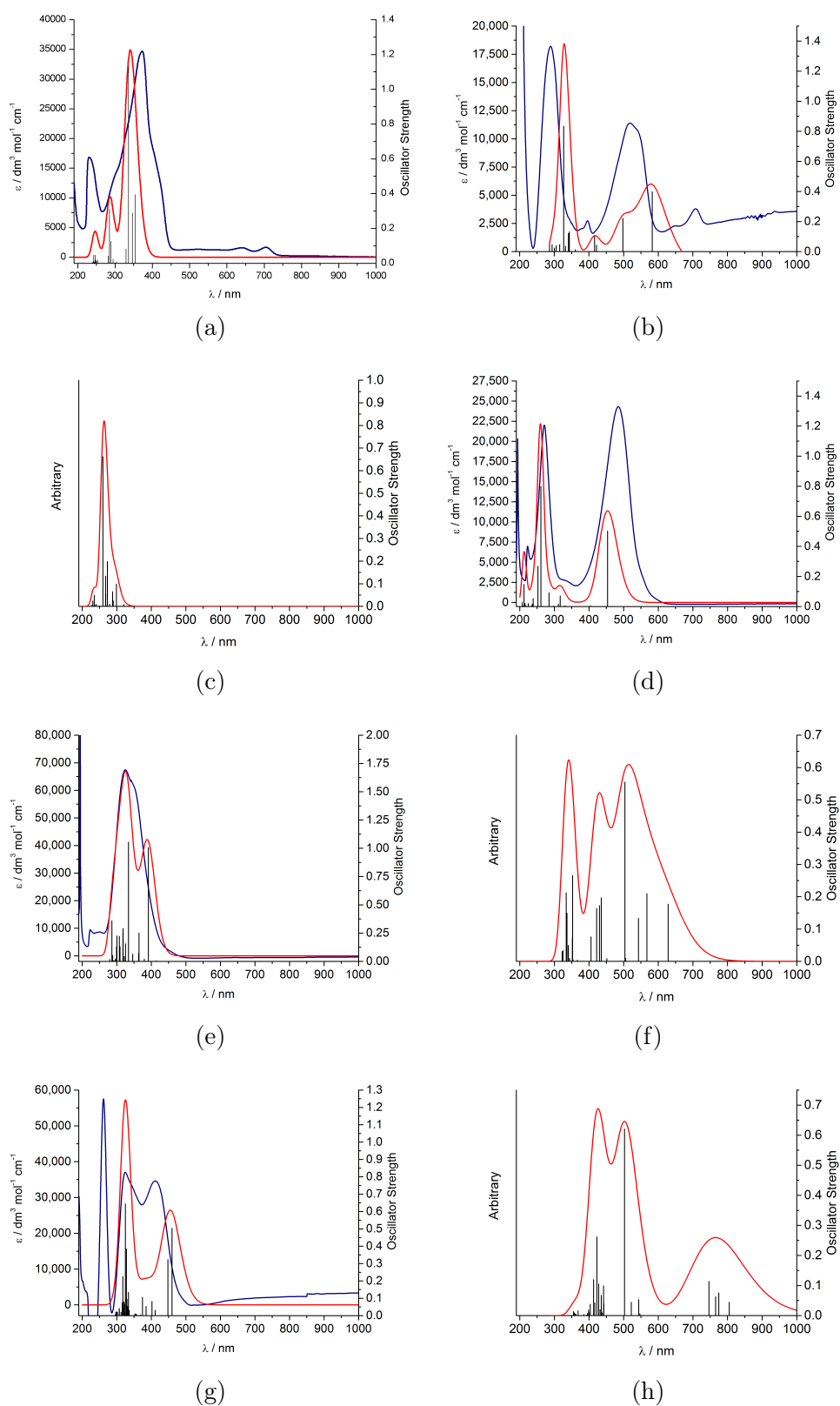
Figure 2.5: Experimental (blue) and simulated (red) electronic absorption spectra of (a) dipyrromethane **3** (b) dipyrrin HL^1 (c) dipyrromethane H$_2$L^2 (simulated only) (d) dipyrrin HL^2 (e) dipyrromethane H$_4$L^3 (f) dipyrrin H$_2$L^3 (simulated only) (g) dipyrromethane H$_4$L^4 and (h) dipyrrin H$_2$L^4 (simulated only). Spectra simulated by TD-DFT, using the B3LYP functional, 6-311G(d,p) basis set and PCM CH$_2$Cl$_2$ solvent model.

calculations. Interestingly, using a completely flat macrocycle as the initial-guess geometry, the optimisation calculation resulted in a Pacman geometry. The simulated absorption spectrum consists of a broad absorption band that arises due to a number of transitions with large oscillator strengths that make significant contributions: H→L at 712 nm; H→(L+1) at 629 nm; (H−1)→L at 567 nm; (H−1)→(L+1) at 543 nm; and (H−2)→L at 504 nm. In the case of macrocycle H_4L^3, the DFT calculations indicate that oxidation leads to a stabilisation of both the LUMO (by 1.37 eV) and LUMO+1 (by 1.35 eV), making the compound absorbant across the spectral width of the visible-light region. The LUMO in the oxidised macrocycle is identical to those of the acyclic dipyrrins, consisting of a conjugated π-system over the imino-dipyrrin manifold. LUMO+1 is identical, but located on the second coordination compartment.

The changes in electronic structure of H_4L^4 upon oxidation are similar to those for H_4L^3. The lowest-energy band in the absorption spectrum for H_4L^4 was measured at 420 nm, and whilst the absolute energies for the bands in the experimental spectrum were not accurately represented by the simulated spectrum, the overall features were adequately modelled. This band at 420 nm was predicted by TD-DFT to occur at 455 nm and consists of a mixture of H→L (78 %) and (H−1)→L (18 %) transitions at 460 nm, as well as the (H−1)→(L+1) (73 %) and H→(L+1) transitions at 448 nm. Oxidation of the anthracenyl-bridged macrocycle to give H_2L^4 is predicted to result in the largest bathochromic shift of the lowest-energy absorption band, as the simulated spectrum features a strong absorption band centred at 765 nm. According to the model, this predicted band consists of four significant transitions: H→L at 805 nm; H→(L+1) at 775 nm; (H−1)→L at 765 nm; and (H−1)→ (L+1) at 746 nm. The bathochromic shift of the transitions to the LUMO and LUMO+1 are reflected by a 1.13 eV stabilisation of the LUMO and a 1.15 eV stabilisation of LUMO+1, whilst the other MOs remain relatively unchanged.

This investigation into the electronic structures of acyclic and macrocyclic dipyrromethanes and dipyrrins by electronic absorption spectroscopy has highlighted that the frontier molecular orbitals are dominated by the donor-expanded dipyrrin manifold. There is little difference in the overall description of the electronic structures of these compounds, and the various imine-substituents seem only to tune the energies of the frontier dipyrrin orbitals. The use of TD-DFT methods to simulate absorption spectra has allowed the electronic structures to be compared with compounds that could not be synthesised and provide further insight. Given that, from a molecular orbital description, there are no significant differences

in electronic structure between acyclic and macrocyclic dipyrromethanes upon oxidation, it seems that the difficulty in isolating macrocyclic dipyrrins stems from the structure of the molecules. The rapid rearrangement and folding to Pacman geometries that is required during the oxidation of H_4L^3 and H_4L^4 may be the cause of decomposition that has been observed. In Chapter 4, coordination of transition metals will be explored as a templating procedure to promote oxidation to dipyrrins.

References

[1] A. Sobral, N. Rebanda, M. da Silva, S. Lampreia, M. Silva, A. Beja, J. Paixão and A. M. R. Gonsalves, *Tetrahedron Lett.*, 2003, **44**, 3971 .

[2] D. Fan, M. Taniguchi, Z. Yao, S. Dhanalekshmi and J. S. Lindsey, *Tetrahedron*, 2005, **61**, 10291.

[3] K. Hanson, A. Tamayo, V. V. Diev, M. T. Whited, P. I. Djurovich and M. E. Thompson, *Inorg. Chem.*, 2010, **49**, 6077.

[4] J. Lindsey, M. Taniguchi and D. Fan, "Methods and Intermediates for the Synthesis of Porphyrins", US Patent 7,951,939, 2011.

[5] J. Bonin, M. Chaussemier, M. Robert and M. Routier, *ChemCatChem*, 2014, **6**, 3200.

[6] C. Costentin, G. Passard, M. Robert and J.-M. Savéant, *Proc. Natl. Acad. Sci.*, 2014, **111**, 14990.

[7] J. K. Laha, S. Dhanalekshmi, M. Taniguchi, A. Ambroise and J. S. Lindsey, *Org. Process Res. Dev.*, 2003, **7**, 799.

[8] M. Ptaszek, B. E. McDowell and J. S. Lindsey, *J. Org. Chem.*, 2006, **71**, 4328.

[9] S. Madhu, M. R. Rao, M. S. Shaikh and M. Ravikanth, *Inorg. Chem.*, 2011, **50**, 4392.

[10] G. Givaja, A. J. Blake, C. Wilson, M. Schröder and J. B. Love, *Chem. Commun.*, 2003, 2508.

[11] P. D. Beer, A. G. Cheetham, M. G. B. Drew, O. D. Fox, E. J. Hayes and T. D. Rolls, *Dalton Trans.*, 2003, 603.

[12] N. E. Borisova, M. D. Reshetova, M. V. Kuznetcov and Y. A. Ustynyuk, *Synthesis*, 2007, 1169.

[13] S. D. Reid, C. Wilson, C. I. De Matteis and J. B. Love, *Eur. J. Inorg. Chem.*, 2007, 5286.

[14] K. A. Ames, S. R. Collinson, A. J. Blake, C. Wilson, J. B. Love, D. W. Bruce, B. Donnio, D. Guillon and M. Schröder, *Eur. J. Inorg. Chem.*, 2008, 5056.

[15] R. Li, T. A. Mulder, U. Beckmann, P. D. Boyd and S. Brooker, *Inorg. Chim. Acta*, 2004, **357**, 3360 .

[16] J. L. Sessler, E. Katayev, G. D. Pantos and Y. A. Ustynyuk, *Chem. Commun.*, 2004, 1276.

[17] J. L. Sessler, V. Roznyatovskiy, G. D. Pantos, N. E. Borisova, M. D. Reshetova, V. M. Lynch, V. N. Khrustalev and Y. A. Ustynyuk, *Org. Lett.*, 2005, **7**, 5277.

[18] J. W. Leeland, F. J. White and J. B. Love, *Chem. Commun.*, 2011, **47**, 4132.

[19] J. B. Love, *Chem. Commun.*, 2009, 3154.

[20] J. L. Sessler, E. Katayev, G. D. Pantos, P. Scherbakov, M. D. Reshetova, V. N. Khrustalev, V. M. Lynch and Y. A. Ustynyuk, *J. Am. Chem. Soc.*, 2005, **127**, 11442.

[21] E. A. Katayev, Y. A. Ustynyuk, V. M. Lynch and J. L. Sessler, *Chem. Commun.*, 2006, 4682.

[22] A. Loudet and K. Burgess, *Chem. Rev.*, 2007, **107**, 4891.

[23] C. Yu, L. Jiao, H. Yin, J. Zhou, W. Pang, Y. Wu, Z. Wang, G. Yang and E. Hao, *Eur. J. Org. Chem.*, 2011, 5460.

[24] N. L. Bill, J. M. Lim, C. M. Davis, S. Bahring, J. O. Jeppesen, D. Kim and J. L. Sessler, *Chem. Commun.*, 2014, **50**, 6758.

[25] V. Lakshmi and M. Ravikanth, *J. Mater. Chem. C*, 2014, **2**, 5576.

[26] S. Madhu and M. Ravikanth, *Inorg. Chem.*, 2014, **53**, 1646.

[27] M. Yu, J. K.-H. Wong, C. Tang, P. Turner, M. H. Todd and P. J. Rutledge, *Beilstein J. Org. Chem.*, 2015, **11**, 37.

[28] W. Reiter, A. Gerges, S. Lee, T. Deffo, T. Clifford, A. Danby and K. Bowman-James, *Coord. Chem. Rev.*, 1998, **174**, 343 .

[29] C. Bonnier, D. D. Machin, O. Abdi and B. D. Koivisto, *Biomol. Chem.*, 2013, **11**, 3756.

Chapter 3

Multinuclear zinc complexes for CO_2 sequestration

This chapter describes the synthesis and structural characterisation of multinuclear zinc(II) complexes of the macrocycles discussed in the previous chapter. Their stoichiometric reactions with CO_2 are also discussed, as is their application as catalysts for the copolymerisation reaction between cyclohexene oxide and CO_2, affording polycarbonate materials. The synthesis and characterisation of complexes **7** to **10** was carried out by myself in collaboration with Dr Thomas Cadenbach and Tommy A. Hofmann.

3.1 Synthesis of dinuclear zinc complexes

The dinuclear zinc(II) complexes $Zn_2(L^3)$ (**7a**) and $Zn_2(THF)_2(L^4)$ (**7b**) were prepared in high yields of 90 % and 70 % respectively from the trans-amination reaction of $H_4L^{3,4}$ with two equivalents of $Zn\{N(SiMe_3)_2\}_2$ (Scheme 3.1).
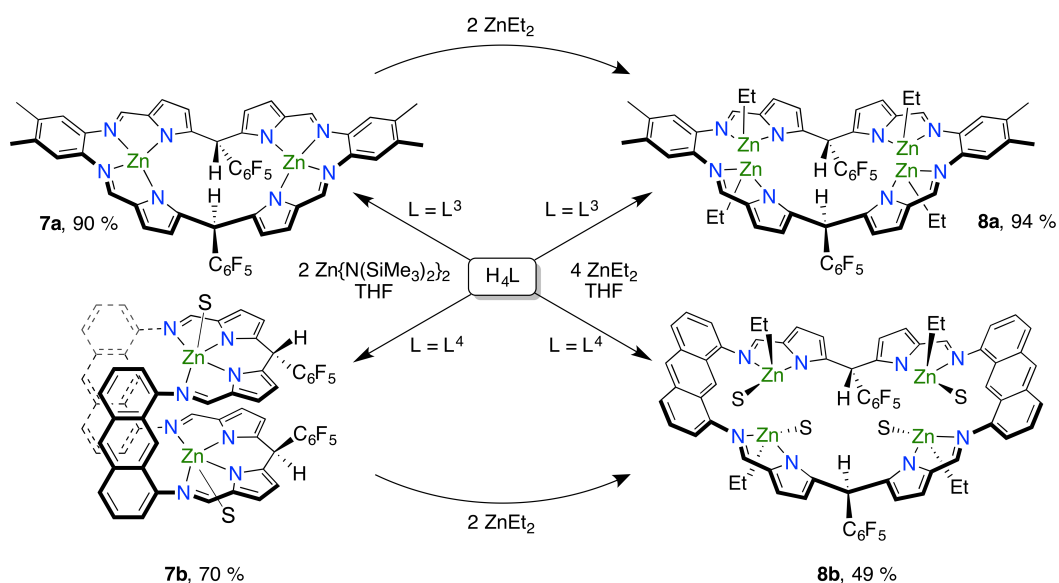
Scheme 3.1: Synthesis of the dinuclear zinc(II) complexes, **7a** and **7b**, and the tetra-nuclear complexes **8a** and **8b**. S = THF.

The ^{1}H NMR spectrum for **7a** in C_6D_6 indicates that a symmetric product is formed, with a single set of resonances observed for the macrocycle. Deprotonation of the pyrrole nitrogens is indicated by the presence of free $HN(SiMe_3)_2$ at 0.10 ppm and the disappearance of the N-H resonance for H_4L^3, and the *meso*-proton resonance has shifted to 6.99 ppm from 5.88 ppm in H_4L^3. Upon metalation, macrocyclic, pyrrolic Schiff-base ligands fold either at the aromatic spacer groups to form Pacman geometries, or at the *meso*-carbon position to form bowl-shaped geometries, and both have been observed for macrocycles that are similar to L^3 (this is discussed in more detail in Chapter 4). It is not possible to deduce whether **7a** adopts a bowl or Pacman configuration from its NMR spectra, and its X-ray crystal structure has not been determined, as diffraction-quality single crystals of **7a** could not be grown using a variety of methods from several different solvent mixtures. However, based on the bowl configuration that is adopted by the macrocycle in its tetrametallic congener (discussed below), as well as its copper(II), iron(II) and palladium(II) analogues (discussed in Chapter 4), it is assumed that **7a** also adopts the bowl configuration. The MALDI-ToF[i] mass spectrum of **7a** features the expected molecular ion peak at 1063 m/z with an isotope distribution that is consistent with a dinuclear zinc complex.

In the case where a Pacman geometry is formed, following metalation of the proton *meso*-substituted macrocycles $H_4L^{3,4}$, three isomers could be observed depending on the relative orientations of the *meso*-substituents. In the *anti*-isomer, one C_6F_5 group would be exogenous to the macrocyclic cleft and the other endogenous. In the *syn-exo* and *syn-endo* isomers, both C_6F_5 groups would be either exogenous or endogenous to the cleft, respectively. The ^{1}H NMR spectrum for **7b** in d_8-THF indicates that two symmetric isomers are formed from the reaction, in a 3:1 ratio, and the chemical shifts of these isomers are well-resolved. For the major isomer, the imine and *meso*-protons appear at 8.21 and 5.69 ppm respectively, whereas for the minor isomer those resonances appear at 8.00 and 5.99 ppm. These Pacman isomers are presumably the *syn-endo* and *syn-exo* isomers, which would both form from folding of the *syn*-isomer of the metal-free macrocycles (as discussed in Chapter 2, the *anti*-isomer of H_4L was never observed). Single crystals of **7b** were grown from a THF solution and the solid-state structure for the *syn-endo* isomer was determined by X-ray crystallography (Figure 3.1).

In the solid state, two structurally similar molecules of **7b** occupy the asymmetric unit. The macrocycle adopts a Pacman configuration and coordinates one zinc(II) centre in each N_4-donor pocket. One THF solvent molecule is coordinated

---

[i]Matrix-assisted LASER desorption/ionisation time-of-flight mass spectrometry.
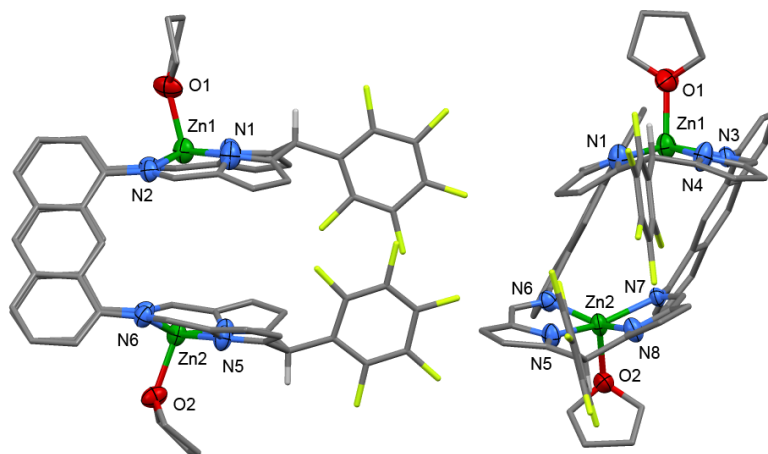
Figure 3.1: Orthogonal views of the solid-state structure of **7b** (*syn-endo* isomer), showing one of two molecules in the asymmetric unit. Displacement ellipsoids are drawn at 50 % probability and for clarity, only the *meso*-protons are shown.

to each zinc ion on the *exo*-face, resulting in a distorted square-pyramidal coordination geometry for each zinc; the sum of N_4-equatorial bond angles is 352.2°, the zinc centres are situated 0.372 – 0.414 Å from their local N_4-plane, and the internuclear separation is 6.236(1) Å. Importantly, **7b** crystallises as the *syn-endo* isomer only, with the C_6F_5-substituents pointing into the macrocycle cleft. There is a twist-angle of 57.72° between the N_4-donor plane and the anthracene spacer-groups; anthracenyl-Pacman complexes are commonly twisted in this way and so this may not be solely attributed to the C_6F_5-substituents pointing into the cleft.[1]

Two isomers are observed after folding of the anthracenyl-macrocycle, L^4, into the Pacman geometry in **7b**. In contrast, only a single isomer was observed for **7a** and further supports that a bowl configuration is adopted in that case; in the bowl geometry, the bulky C_6F_5-substituents must point away from the hinge, and therefore a single *syn*-isomer is enforced.

A number of macrocyclic zinc(II) complexes that are similar to those of $L^{3,4}$ have been reported previously. In those examples, the macrocyclic ligands feature two alkyl-substituents at the *meso*-carbon. The zinc chemistry of one such macrocycle, that also features an *ortho*-phenylene spacer group, is not straightforward, resulting in the isolation of expanded, tri-nuclear [3+3] macrocyclic complexes when $Zn(OAc)_2$ is used as a zinc(II) transfer reagent; the bimetallic [2+2] macrocylic product was only obtained after boiling the pro-ligand with $Zn(BF_4)_2$ in chloroform.[2] In contrast, the room-temperature reactions of similar macrocycles with $Zn(BF_4)_2$ in THF produced fluoride-bridged complexes resulting from F-abstraction from the $[BF_4]^-$ anion, *e.g.* $[Zn_2(\mu-F)_2(H_4L)][BF_4]_2$.[3] In

both the tri-nuclear and fluoride-bridged complexes, the pyrrole nitrogens remain protonated. In contrast, the reproducible and straightforward synthesis of the bimetallic complex **7a** is high yielding, and is likely to be due to the choice of the silyl-amide starting material rather than a consequence of the changes in the macrocycle.

Where disubstituted macrocycles feature the anthracenyl spacer-group, Pacman geometries are adopted, similar to that observed for **7b**, although previous bimetallic zinc(II) complexes were found to be complex aggregates in solution and only formed crystalline materials in the presence of anions such as Cl^- and OH^-, which were accommodated within the dinuclear macrocyclic cleft.[4] In these latter compounds, the internuclear separations determined by X-ray crystallography ranged from 3.871(1) Å for a bound μ-OH to 4.532(1) Å for a bound μ-Cl; the internuclear distance for the anion-free complex was predicted by DFT calculations to be 4.98 Å. These distances are considerably shorter than those in **7b** and reflect the flexibility of the N_4-donor set, which facilitates distortion of the zinc cation out of the N_4-plane into the cleft; in **7b** this movement is exogenous to the cleft due to binding of THF. More straightforward solution-state structures are displayed by **7b** in comparison with previous examples and its solid-state structure has been determined crystallographically; both of these points are attributed to the change in *meso*-substituent, from ethyl to C_6F_5.

3.2   Synthesis of tetranuclear zinc complexes

In contrast to reactions involving zinc-silylamide, the reactions between $H_4L^{3,4}$ and $ZnEt_2$ do not form the dinuclear complexes **7a,b**, but instead form the tetranuclear complexes $Zn_4Et_4(L^3)$ (**8a**) and $Zn_4Et_4(THF)_4(L^4)$ (**8b**). This is in stark contrast to previously reported Pacman chemistry, in which dialkyl *meso*-substituted, anthracenyl-bridged macrocycles afforded bimetallic zinc(II) complexes on reaction with $ZnEt_2$.[4] The X-ray crystal structure of **8b** was determined (Figure 3.2) and shows that each zinc(II) centre is coordinated to an N_2 imino-pyrrolide chelate in the macrocycle. Each zinc(II) ion has retained an ethyl group and is coordinated by a molecule of THF, giving a distorted tetrahedral coordination geometry around each zinc atom with bond angles in the range 82.1(2) – 141.2(4)°. In order to accommodate four ZnEt(THF) units, the macrocycle adopts a bowl-shaped structure, hinging at the *meso*-carbon with a wide bite-angle of 162.1(1)° between anthracenyl groups. This is very unusual for this class of macrocyclic complex, as previous complexes of anthracene-bridged macrocycles have only been observed

to adopt Pacman configurations. The internuclear separations in **8b** are large due to this bowl configuration, in the range 6.981(3) – 7.192(1) Å between nearest neighbours. Whilst high nuclearity complexes of zinc(II) are common in the literature, their molecular structures are often quite complex and difficult to predict, usually owing to the incorporation of many bridging ligands forming a molecular cluster, with supporting ligands coordinated on the periphary.[5–10] In this respect, the structure of **8b** is unusual in that the four zinc(II) ions are well separated, which is because its four, bidentate chelating groups are well separated in the macrocyclic framework.
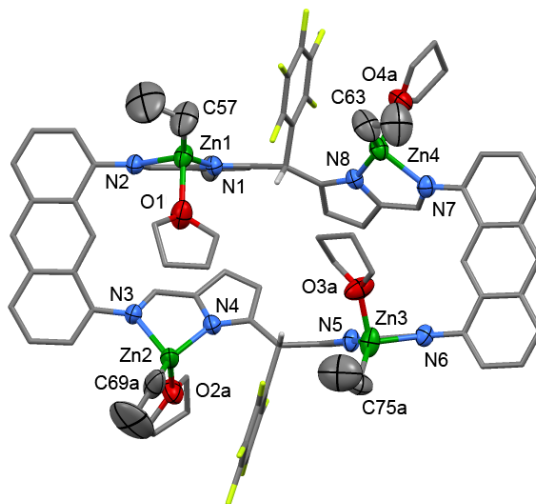
Figure 3.2: Solid-state structure of **8b**. Displacement ellipsoids are drawn at 50 % probability; for clarity, only the *meso*-protons are shown and disordered atoms on the ethyl ligands, THF ligands and C_6F_5-substituents are omitted.

The ^{1}H NMR spectrum for **8b** in d_8-THF features a single set of sharp resonances for the macrocycle, and resonances at 0.99 and 0.12 ppm are consistent with four ethyl ligands per macrocycle. In the ^{19}F{^{1}H} NMR spectrum, the resonance for the *ortho*-F nucleus of the C_6F_5-substituent is broadened severely at 300 K, but heating the sample to 330 K causes this resonance to sharpen slightly, at −140.27 ppm. This indicates that there is some restricted rotation of the *meso*-substituent, and that 300 K is close to the coalescence temperature.

Whilst the X-ray crystal structure of **8a** could not be determined, due to the high moisture-sensitivity of the complex (discussed below), variable temperature NMR spectroscopy proved highly informative and was used to deduce its structure. At 300 K in C_6D_6, the ^{1}H NMR spectrum of **8a** consists of a single set of sharp resonances for the macrocycle protons, and resonances for the four ethyl ligands are observed at 1.32 and 0.42 ppm. In the ^{19}F{^{1}H} NMR spectrum in C_6D_6, the resonance for the *ortho*-F nucleus was broad at 300 K and sharpened at 333

K, appearing at -140.24 ppm. Such temperature-dependence in the $^{19}F\{^1H\}$ NMR spectra for **8a** and **8b** was not observed for **7a,b** and implies that there is restricted rotation of the C_6F_5-group due to coordination of four ZnEt(THF) units. However, no nuclear Overhauser interactions were observed between the *ortho*-F nucleus and ethyl-protons at 300 or 243 K using ^{19}F-^1H HOESY NMR experiments, despite a separation of 2.8 – 3.0 Å between the ethyl-groups and *ortho*-F atoms in the solid-state structure of **8b**.

Changing the solvent for **8a**, from C_6D_6 to d_8-THF, caused dramatic changes in the NMR spectra. In the $^{19}F\{^1H\}$ NMR spectrum at 300 K, both the *ortho*- and *meta*-F resonances were broadened, and on cooling the solution to 243 K, both of these resonances were split into two resonances each, indicating completely frozen rotation of the C_6F_5-substituent at that temperature. Unlike the ^1H NMR spectrum measured at 300 K in C_6D_6, which consisted of sharp resonances, all of the resonances in the spectrum measured in d_8-THF were severely broadened, and only sharpened after heating to 330 K. At 243 K, the ^1H NMR spectrum for **8a** resolves to give two sets of resonances of 1:1 intensity for all proton-environments with the exception of the *meso*-proton. The temperature- and solvent-dependence of the ^1H NMR spectra for **8a** is best interpreted for **8a** adopting a bowl structure. In such a structure, the *meso*-positions form the hinge of the macrocycle. Unhindered, torsional flexing of the macrocycle about this hinge produces a C_2-symmetric structure that renders each proton-environment equivalent at higher temperatures. Due to the thermal barrier for the flexing vibrational mode, this symmetry is broken at low temperature, giving rise to an asymmetric structure, but because the *meso*-protons are located on the hinge of the macrocycle, they are equivalent even at low temperature. The spectrum measured at 300 K in d_8-THF appears broad due to the inclusion of coordinated solvent within the cleft; this will increase steric interactions within the cleft and raise the thermal barrier for the torsional flexing mode.

Conversion of **7a** to **8a**, and also of **7b** to **8b**, was achieved on addition of two equivalents of $ZnEt_2$ to the dinuclear complexes. The *ortho*-F resonances in both $^{19}F\{^1H\}$ NMR spectra, which appeared sharp in the bimetallic complexes, broadened on addition of $ZnEt_2$ and the ^1H NMR spectra for both products are identical to those of **8a,b**. Importantly, the resonances for the four ethyl groups in each complex are equivalent, indicating a conversion to **8a,b** by alkyl-transfer from one zinc centre to another in each pocket. This conversion also reveals an interesting change in the anthracene-bridged macrocycle configuration, from a Pacman structure in **7b** to a bowl structure in **8b**.

3.2.1 Attempted small-molecule insertion chemistry with zinc-alkyl complexes

Due to the literature precedent for zinc-carbon and -hydroxide bonds participating in insertion chemistry with CO_2,[11–13] similar reactions with the tetranuclear zinc-alkyl complexes were attempted. Unfortunately, no insertion of carbon dioxide was observed with either **8a** or **8b**, even at 80 °C under 2 atm CO_2. In d_8-THF, resonances for an anticipated carboxylate product were not observed, only the ^{13}C NMR resonance of dissolved CO_2 was observed at 125.7 ppm for both cases, and the resonances for the starting compounds were unchanged.

Similarly, a reaction with either **8a** or **8b** with dihydrogen was not observed at 80 °C under 2 atm H_2. A successful reaction with H_2 would result in heterolysis of the H-H bond, liberation of ethane gas and formation of a zinc-hydride complex, but ^1H NMR resonances for either of these products were not observed. Similarly, no ^2H NMR resonances corresponding to zinc-deuteride complexes were observed from the reactions of **8a** or **8b** with D_2 gas under the same conditions. Zinc-hydride complexes could conceivably facilitate insertion of other small molecule substrates, such as CO_2 to yield zinc-formate complexes.[14]

Protonolysis of the ethyl ligands was achieved with pyridinium chloride, in an attempt to isolate tetranuclear chloro-zinc complexes. These targeted complexes could in turn be reduced with a strong reductant, such as KC_8, to form a tetranuclear zinc(I) complex on elimination of KCl. Such a complex could conceivably act as a four-electron reductant for small molecules, perhaps even dinitrogen given the proximity and strong reducing nature of the four Zn(I) centres. Whilst gas evolution was observed on addition of pyridinium chloride to a THF solution of **8a** or **8b**, single crystals that were grown from both reaction mixtures were found to be tetrahedral $ZnCl_2(Py)_2$ by X-ray crystallography. It seems that the presence of pyridine, a strong σ-donor ligand, is capable of demetalating the complex after protonolysis of the ethyl ligands. To avoid the addition of pyridine, similar reactions with $[Et_3NH][Cl]$ and HCl in diethyl ether were performed; both seemed to result in decomposition of the macrocycles, as the ^1H NMR spectra consisted of a multitude of resonances, and no crystalline products could be isolated from the reaction mixtures.

3.3 Synthesis of hydroxo- and oxo-zinc complexes

Several attempts were made to determine the solid-state structure of **8a** by X-ray crystallography. However, due to its high sensitivity to adventitious moisture, only

the hydrolysis product, $Zn_4(\mu_4-O)(Et)_2(THF)_2(L^3)$ (**9**) was found to crystallise. In the solid-state structure of **9** (Figure 3.3), the macrocycle adopts a Pacman geometry of C_{2v} symmetry. Two of the zinc(II) centres are bound by the pyrrole-nitrogen atoms in each pocket, whilst the other two zinc(II) centres are coordinated by bridging imine-nitrogen atoms on each *ortho*-phenylene group; these imino-zinc centres have retained their ethyl groups. A central oxo dianion is bound to all four zinc centres and is formally described as acting as an L-type donor to the two pyrrolide-zinc centres and an X-type donor to the two imino-zinc centres, resulting in a charge-neutral complex. The bridging μ_4-oxo dianion in the Zn_4O core results in short $Zn\cdots Zn$ distances of 2.8604(6) – 2.8371(6) Å, and the core itself is near-planar, with adjacent Zn-O-Zn bond angles of 90° and nonequivalent opposite Zn-O-Zn bond angles of 160.45(12)° and 174.81(14)°.
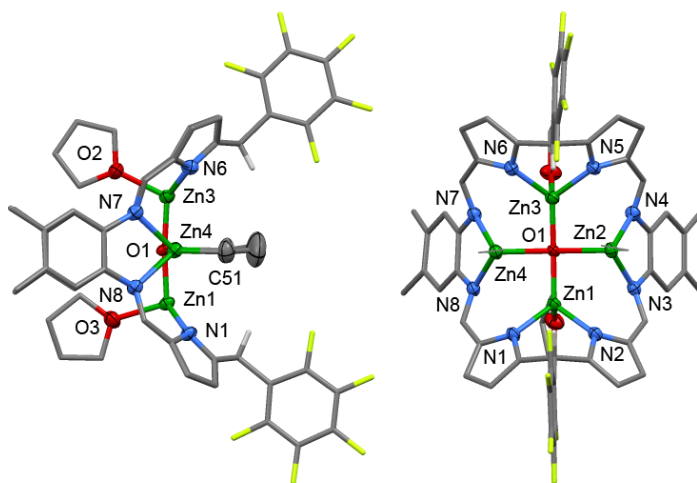
Figure 3.3: Orthogonal views of the solid-state structure of **9**. Displacement ellipsoids are drawn at 50 % probability; for clarity, only the *meso*-protons are shown and disordered atoms on the ethyl ligands are omitted.

While the $Zn_4(\mu-O)$ structural motif has been characterised numerous times[15] (187 CSD hits, Zn-O-Zn angle 108.8 $\pm$ 6.7°), including with associated alkyl groups, *e.g.* $Zn_4Et_n(\mu-O)$,[16,17] with the exception of zinc-hydroxo cubanes, the near-planar Zn_4O core in **9** is highly unusual. The planar environment for oxygen O1 in **9** is unique and is presumably enforced by the rigid macrocyclic architecture. DFT calculations on **9** were carried out to explore the nature of the bonding in the unusual $Zn_4(\mu-O)$ unit (section 3.3.1, below).

Complex **9** was prepared numerous times during crystallisation attempts with **8a**, but it was also prepared through rational synthesis. Addition of one equivalent of H_2O to **8a** produces a ^1H NMR spectrum consistent with the solid-state

structure of **9**, with two equivalent ethyl groups per macrocycle with resonances at 1.51 and 0.30 ppm. The sharpness of the *ortho*-F resonance in the room-temperature $^{19}F\{^1H\}$ NMR spectrum further indicates a loss of ethyl ligands from the face of the N_4-donor pockets and supports a change in geometry from a bowl configuration to a Pacman configuration upon partial hydrolysis. Further hydrolysis results in complete loss of the Zn-Et groups, presumably to form the mixed zinc-oxo/hydroxide complex $Zn_4(\mu-O)(OH)_2(L^3)$, but this compound has not been isolated or characterised.
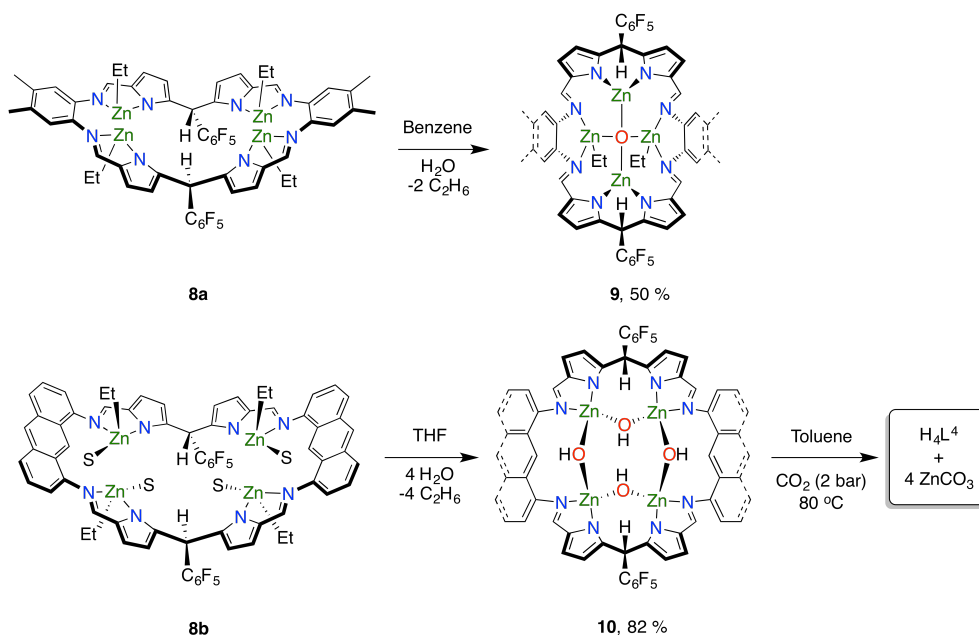
Scheme 3.2: Synthesis of the tetrametallic oxo- and hydroxo-zinc(II) complexes **9** and **10** and subsequent reaction of **10** with CO_2 to yield $ZnCO_3$.

Due to the increased separation between the N_4-coordination compartments in the anthracene-bridged macrocycle, the formation of a Zn_4O cluster is not possible. However, complete hydrolysis of **8b** with four equivalents of H_2O leads to the clean formation of $\{Zn(\mu_2-OH)\}_4(L^4)$ (**10**) in high yield of 82 %. The ^1H NMR spectrum of **10** shows a complete loss of the ethyl ligands and the appearance of two resonances at 4.14 and 3.36 ppm that are of equal intensity. These resonances are assigned to two non-equivalent, bridging hydroxide ligands, which each integrate as two protons per macrocycle. The hydroxyl protons undergo H/D exchange in a D_2O-shake experiment and disappear from the ^1H NMR spectrum. The solid-state structure of **10** was determined by X-ray crystallography and shows that the zinc(II) centres are coordinated in a similar manner to **8b**, bound to each imino-pyrrole chelate (Figure 3.4).

Each zinc(II) centre is connected to its two neighbours by a bridging hydroxide
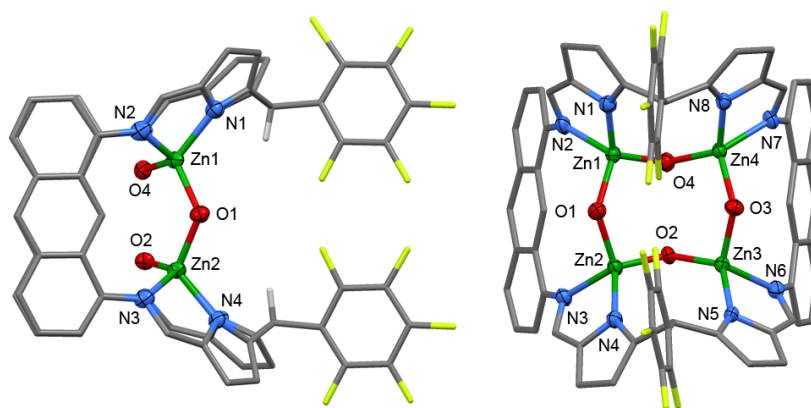
Figure 3.4: Orthogonal views of the solid-state structure of **10**. Displacement ellipsoids are drawn at 50 % probability and for clarity, all protons and one THF solvent molecule in the asymmetric unit have been omitted.

ligand, which has the effect of closing the relaxed bowl-geometry observed for **8b** to a rigid Pacman geometry of C_{2v} symmetry. In comparison with the bimetallic Pacman complex **7b**, which had a twist angle of 57.72°, the anthracenyl spacer-groups are practically orthogonal with the N_4-donor planes in **10** (twist angle = 2.44°). The formation of bridging hydroxides also has the effect of shortening the $Zn \cdots Zn$ distances greatly, which lie in the range 3.229(1) – 3.4465(9) Å. In order to accommodate this $\{Zn(\mu_2-OH)\}_4$ cluster, the two N_4-donor pockets are distorted from their planar arrangement and point into the cleft. The *syn-exo*-isomer of **10** is observed in the solid state and, unlike the case for **7b**, only one isomer is observed in solution, indicating that the stereochemistry of **10** is dictated by that of **8b**. This simple, molecular $\{Zn(\mu_2-OH)\}_4$ ring structural motif seen in **10** has little precedent. The hexameric complex $\{Zn(\mu-OH)(^tBu)\}_6$ is formed on hydrolysis of Zn^tBu_2 and is an aggregate of two trimeric $\{Zn(\mu-OH)(^tBu)\}_3$ rings;[18] otherwise, only simple cubanes and extended polymeric structures display a similar formulation and aggregation to **10**.[19]

3.3.1 DFT calculations for 9

The X-ray crystal structure for **9** was accurately represented by the B3LYP functional and 6-31G(d,p) basis set, with less than 1.0 % relative error in important bond parameters around the metal centres in the optimised structure. A combination of natural bond orbital (NBO) population analysis, molecular orbital theory and group theory was applied to describe the bonding in the Zn_4O cluster. Population analysis indicates that the most significant bonding interactions in the

C_{2v} Zn_4O cluster arise from σ-donation from the central oxo dianion into unoccupied 4s and 4p orbitals on the four zinc centres (Figure 3.5). Specifically, there is a b_1 set of atomic orbitals that combine to describe the $\sigma\{2p_x(O1)\text{-}4s(Zn2,4)\}$ interaction and a $b2$ set that describes the $\sigma\{2p_y(O1)\text{-}4s(Zn1,3)\}$ interaction, with interaction energies of 20 kcal mol^{-1} for each reported by second-order perturbation theory. An a_1 $p_z(\pi)$ interaction extending over the Zn_4O cluster also makes a minor contribution to the bonding (5 kcal mol^{-1}). While Zn-O d-p(π) orbital interactions are observed, due to the $3d^{10}$ electron configuration for zinc(II), both the bonding and anti-bonding molecular orbitals (HOMO-126 and HOMO-51, respectively) are fully occupied and these interactions do not therefore contribute to the bonding. Importantly, no Zn-Zn covalent bonds were observed by molecular orbital calculations or NBO population analysis; therefore, the proximity of the zinc centres is due to the presence of the oxo-group and the constraints of the macrocyclic bonding environment only.
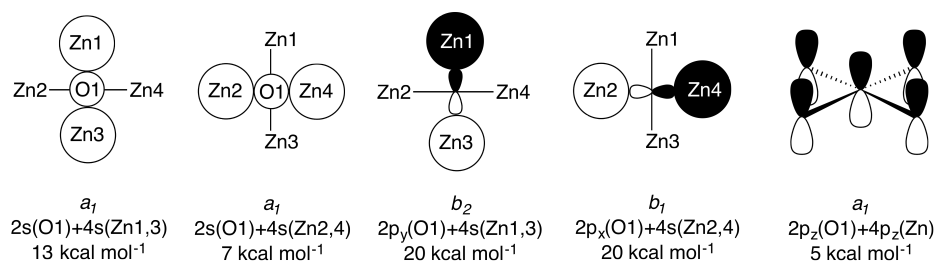
Figure 3.5: Symmetry-allowed atomic orbital contributions to the bonding in the planar Zn_4O core in **9**. The interaction energies given are approximated from second-order perturbation analysis.

3.3.2   Reactivity of hydroxo-Zn complexes with CO_2

The insertion chemistry of the alkyl ligands in **9** towards H_2 and CO_2 was explored. However, just as for complexes **8a,b**, no zinc-hydride or zinc-carboxylate complexes were formed.

At 80 °C and under 2 atm CO_2, the hydroxo-complex **10** reacted to yield the free, protonated macrocycle H_4L^4, observed by ^1H NMR spectroscopy. A white solid was also deposited from the reaction mixture that is assumed to be $ZnCO_3$, giving the insolubility of this solid and the literature precedent for its formation from metal-hydroxide bonds.[20] Interestingly, the clean formation of the protonated macrocycle closes a potential cycle for the conversion of CO_2 into $ZnCO_3$, although in order to achieve turn-over, a series of stoichiometric reactions involving $ZnEt_2$ and water would be required at high temperature, with high pressure gas-loading. This process is therefore clearly not viable for catalysis or

CO_2 sequestration on a large scale. Alternatively, H_4L^4 could potentially act as a catalyst for the sequestration of CO_2 as $ZnCO_3$ from $Zn(OH)_2$, through the formation of **10** *in situ*:

$$Zn(OH)_2 \xrightarrow[H_4L^4]{CO_2} ZnCO_3$$
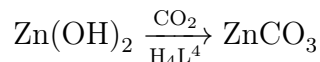
3.4 ROCOP catalysis of epoxides and CO_2

An introduction to the zinc-catalysed, ring-opening copolymerisation (ROCOP) reaction is given in Chapter 1. The tetranuclear zinc(II) complexes **8a,b** are unusual in comparison with other Pacman complexes in that the metal ions are coordinated by individual imino-pyrrolide units. These complexes are therefore viable for ROCOP catalysis due to the ancillary alkyl ligands (which can be exchanged for alkoxide initiating groups) and the proximity of multiple zinc(II) ions. The general ROCOP reaction and expected products are given in Scheme 3.3. These polymerisation studies were carried out by Shyeni Paul, in a collaboration with Prof. Charlotte K. Williams (then at Imperial College London).
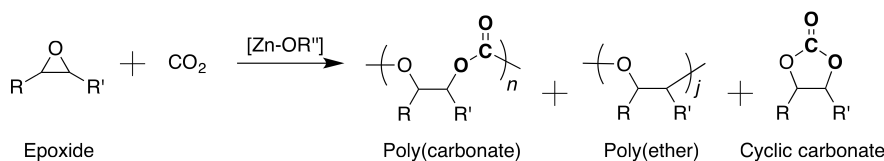
Scheme 3.3: General ROCOP reaction between epoxides and CO_2, catalysed by a zinc(II)-alkoxide complex. The desired product of the reaction is poly(carbonate), with poly(ether) and cyclic-carbonate compounds forming as side-products.

3.4.1 Scope of the catalytic reaction

The tetranuclear zinc(II) complexes **8a** and **8b** were tested as pre-catalysts for the ROCOP reaction between cyclohexene oxide (CHO) and CO_2. As discussed in the previous section, insertion of CO_2 into the metal-alkyl bond was not successful at 2 atm, and so instead, **8a** and **8b** were reacted with four equivalents of *n*-hexanol *in situ*, to form more reactive zinc-hexoxide complexes through protonolysis of the metal-carbon bond. Characterisation of the resulting zinc-hexoxide complex is discussed in Section 3.4.5, below.

Integration of the cyclohexyl methine ^{1}H NMR resonances for CHO (3.14 ppm), poly(cyclohexylcarbonate) (PCHC, 4.65 ppm), poly(cyclohexeneoxide) (PCHO, 3.43 ppm) and cyclohexene carbonate (4.05 ppm) was used to determine the yields, %conversion and %selectivity from the reaction. Size-exclusion chromatography

(SEC) was used to determine both the molecular weight and poly-dispersity index (Đ) of the resulting polymers.[ii]

Initial reactions used neat CHO and 1 atm CO_2, at 80 °C, using 0.1 mol% of the pre-catalyst and 0.4 mol% n-hexanol (Table 3.1, entries 1 and 5). Under low-pressure conditions, both **8a** and **8b** were active but slow, with turnover frequencies (TOFs) of 9 h^{-1} and 3 h^{-1}, respectively. Of the two, **8a** performed best, converting 22 % of the epoxide, forming low molecular-weight polymer (5920 g mol^{-1}) with quite a broad distribution (Đ = 1.39). However, the polymer consists primarily of ether linkages, and is mainly PCHO, with only 7 % carbonate linkages. In comparison, **8b** converted only 7 % of the epoxide, and an assessment of the resulting polymer could not be made due to the low yield.

Pre-catalyst **8a** was also tested with methanol as an initiator (Table 3.1, entry 2). The presumed zinc-methoxide complex formed *in situ* was slightly more active than the zinc-hexoxide complex, with a TOF of 13 h^{-1}, forming higher molecular-weight polymer (20,000 g mol^{-1}). However, the molecular weight distribution was severely worsened (Đ = 2.19) and the incorporation of carbonate linkages was not improved. Methanol was therefore not considered a suitable initiator, and only n-hexanol was used in all future reactions.

Table 3.1: Preliminary testing of **8a** and **8b** as pre-catalysts for the ring-opening copolymerisation reaction of neat cyclohexene oxide, or propylene oxide, with various pressures of CO_2.

Entry	Catalyst	$[CO_2]$ / atm	T / °C	Conv.[a] / %	TOF[b] / h^{-1}	Selectivity[c] / %	M_n / Da (Đ)[d]
1	**8a**	1	80	22	9	7	5920 (1.39)
2*	**8a**	1	80	31	13	6	20,000 (2.19)
3	**8a**	30	80	51	21	56	34,700 (1.89)
4	**8a**	50	80	14	6	29	32,100 (1.57)
5	**8b**	1	80	7	3	0	− (−)
6	**8b**	50	80	3	1	68	824 (1.09)
7**	**8a**	50	80	3	1	0	− (−)
8**	**8b**	50	80	1	0	0	− (−)

Reactions carried out in neat CHO, using 0.1 mol% catalyst loading and 0.4 mol% n-hexanol. * 0.4 mol% methanol used instead of n-hexanol. ** Carried out in neat PO instead of CHO. [a] Conversion calculated from relative amounts of CHO, PCHC and PCHO by ^{1}H NMR integration. [b] TON = moles epoxide consumed / moles catalyst; TOF = TON / time. [c] Calculated from relative amounts of PCHC and PCHO by ^{1}H NMR integration. [d] Both M_n and Đ determined by SEC in THF, calibrated using narrow molar-mass polystyrene standards.

Complex **8a** is clearly an active pre-catalyst for the ring-opening polymerisation (ROP) reaction of cyclohexene oxide. In order to promote CO_2 insertion and incorporation of a greater number of carbonate linkages, the pressure was increased

---

[ii]Some of the SEC data are somewhat peculiar, and are currently being reassessed by the Williams group, but are reported here in their current state for completeness.

(Table 3.1, entries 3 and 4). Increasing the pressure to 30 atm improved both the activity (21 h^{-1}) and the conversion of epoxide (51 %), but most importantly, the amount of carbonate linkages was improved drastically, at 56 %. The molecular weight of the resulting polymer was also much higher (34,700 g mol^{-1}), although the distribution was still broad at 1.89. Increasing the pressure further, to 50 atm, had a detrimental effect on the catalyst activity, selectivity for carbonate linkages, and conversion of epoxide. This decrease in catalyst activity may be due to gas expansion of the solution at high pressure, which effectively dilutes the concentration of the catalyst. The optimal CO_2 pressure was taken as 30 atm.

High-pressure conditions were applied to the reaction catalysed by **8b** (50 atm, Table 3.1, entry 6). The activity of the catalyst was lowered further, to 1 h^{-1}, although the selectivity for carbonate linkages was high at 68 %. The resulting polymer was of very low molecular weight (824 g mol^{-1}) but had a narrow weight distribution (Đ = 1.09).

Finally, the ROCOP reaction between propylene oxide (PO) and 50 atm CO_2 was tested using **8a** and **8b** as pre-catalysts, but neither complex was active for its copolymerisation (Table 3.1, entries 7 and 8). Therefore, only CHO was used as a monomer in further reactions.

3.4.2   Optimisation of the catalytic reaction

Whilst a reasonable selectivity for carbonate linkages in the polymer was attained using **8a** in 10 M (neat) CHO at 30 atm (56 %), attempts were made to optimise the reaction conditions to improve the selectivity further. Attempts to promote CO_2 insertion over sequential ether enchainment have already been made by varying the pressure. In order to kinetically disfavour the competing ROP reaction, the CHO concentration was lowered by the addition of toluene as a solvent. During dilution, the absolute concentration of the catalyst was kept constant, but the concentration relative to the epoxide (*i.e.* the catalyst loading / mol%) increased slightly, up to 0.67 mol%.

Dilution of CHO from 10 M to 5 M and 1.5 M (Table 3.2, entries 1, 2 and 3) also lowered the TOF, from 21 h^{-1} to 15 h^{-1}, to 6 h^{-1}. At 1.5 M the conversion was highest at 90 %, with good selectivity for carbonate linkages at 83 %. The selectivity was even higher at a concentration of 5 M (90 %), although the conversion of epoxide was lower at this concentration, at 70 %. A concentration of 5 M (entry 2) was deemed optimal, due to the higher TOF and better molecular-weight distribution in the polymer (1.61 − 1.77 at 5 M, compared to 3.09 at 1.5 M).

Table 3.2: Optimisation of the poly(carbonate) selectivity, through dilution of cyclohexene oxide.

Entry	Catalyst	[CHO] / M ([Cat.] / mol%)	Conv.[a] / %	TOF[b] / h^{-1}	Selectivity[c] / %	M$_n$ / Da (Đ)[d]
1	**8a**	10 (0.1)	51	21	56	34,700 (1.89)
2	**8a**	5 (0.2)	70	15	90	394,000 (1.61)
						6800 (1.77)
3	**8a**	1.5 (0.67)	90	6	83	166,000 (3.09)
4*	**8a**	5 (0.2)	0	0	–	– (–)
5	**8b**	5 (0.2)	2	0.5	88	– (–)

Reactions carried out in neat CHO, at 80 °C, under 30 atm CO_2. Concentration of CHO varied by dilution with toluene, maintaining a constant absolute catalyst/n-hexanol concentration (1:4). * Carried out at 1 atm CO_2. [a] Conversion calculated from relative amounts of CHO, PCHC and PCHO by ^{1}H NMR integration. [b] TON = moles epoxide consumed / moles catalyst; TOF = TON / time. [c] Calculated from relative amounts of PCHC and PCHO by ^{1}H NMR integration. [d] Both M$_n$ and Đ determined by SEC in THF, calibrated using narrow molar-mass polystyrene standards.

Using the optimal epoxide concentration of 5 M with a low CO_2 pressure of 1 atm caused the reaction to fail (Table 3.2, entry 4). Likewise, applying the optimised conditions to the reaction catalysed by **8b** did not improve the activity of the catalyst (Table 3.2, entry 5). Due to the poor activity of **8b** under all conditions, that complex was not investigated further.

In summary, the optimised ROCOP reaction uses 0.2 mol% of **8a**, 0.8 mol% n-hexanol, 30 atm CO_2 and 5 M CHO in toluene, at 80 °C (Table 3.2, entry 2, Scheme 3.4). Under these conditions, the catalyst has a modest activity with a TOF of 15 h^{-1}, converting 70 % of the epoxide substrate. The resulting polymer has a high number of carbonate linkages (90 %) and very high molecular weight (394,000 g mol^{-1}, with a second low molecular-weight polymer of 6800 g mol^{-1}) but has quite a broad molecular weight distribution, with Đ values between 1.61 and 1.77. The SEC trace is bimodal and indicates that the polymer chains stem from more than one initiating group, which is quite common in ROCOP catalysis and is ascribed to adventitious water in the reaction, most likely due to the high pressure CO_2, which is present in a dynamic atmosphere.
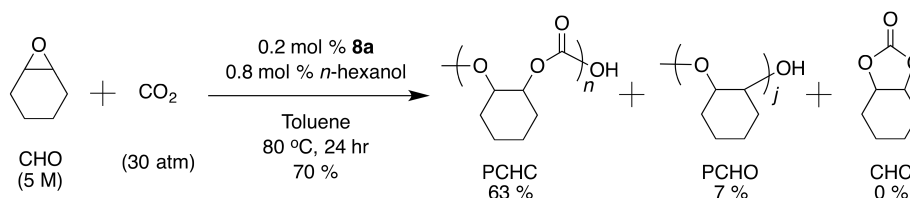
Scheme 3.4: Optimised ROCOP reaction between cyclohexene oxide (CHO) and CO_2, catalysed by **8a** after *in situ* protonolysis with n-hexanol. The desired product of the reaction is poly(cyclohexyl carbonate) (PCHC), with poly(cyclohexene oxide) (PCHO) and cyclohexyl carbonate (CHC) compounds forming as side-products.

In comparison with state-of-the-art examples from the literature, the perfor-

mance of **8a** in the optimised catalytic reaction is quite modest, but does represent a novel mode of reactivity for this class of macrocyclic complexes. Whilst the highest TOF for **8a** (50 h^{-1}, below) is comparable with many complexes in the literature,[21] it is much lower that that of dimeric zinc β-diiminates (*ca.* 2000 h^{-1} at 0.1 mol% loading and 7 atm CO_2)[22] or a cobalt(III) Schiff-base complex (10,882 h^{-1} at 0.01 mol% loading and 25 atm CO_2).[23] In terms of the quality of the resulting polymer, the dispersity is quite high in those obtained from **8a**, whereas a Mg/Zn hetero-bimetallic macrocycle has obtained polymers with dispersities close to 1 (at 50 atm, 90 °C).[24] In this work, high CO_2 pressures were required to obtain high selectivity for carbonate linkages in the polymers, and whilst high CO_2 pressures are also commonly used in the literature, there are examples where 1 atm CO_2 has been used to form poly(carbonate), using manganese(III) porphyrins,[25] and bimetallic cobalt(II) macrocycles.[26]

3.4.3   ROCOP reaction monitoring

To determine whether the ROCOP reaction, catalysed by **8a**, was a controlled polymerisation, a series of reactions were carried out under the optimised conditions, and interrupted at different times in order to monitor the progress of the reaction (Table 3.3). In line with a controlled polymerisation reaction, the %conversion of the epoxide increases linearly with time, up until 8 hours. After this point, the %conversion begins to plateau, which is likely where the reaction rate is limited by the increased viscosity of the solution. This plateau in conversion at 8 hours is accompanied by a decrease in the TOF values, which decrease from 50 h^{-1} at 2 hours down to 23 h^{-1} and 15 h^{-1} after 8 hours. The selectivity for PCHC remains high throughout the reaction, around 80 – 90%. Unfortunately, due to the poor SEC data, it is not possible to comment on the growth of the molecular weight of the polymer with time.

Table 3.3: Monitoring the progress of the ROCOP reaction, catalysed by **8a**, by interrupting a series of repeated reactions at various times.

Entry	Time	Conv.[a] / %	TOF[b] / h^{-1}	Selectivity[c] / %
1	2	20	50	78
2	4	39	49	90
3	8	59	37	88
4	14	64	23	89
5	24	70	15	90

Reactions were carried out in 5 M CHO, at 80 °C, under 30 atm CO_2, using a catalyst loading of 0.2 mol% **8a** and a *n*-hexanol concentration of 0.8 mol%. [a] Conversion calculated from relative amounts of CHO, PCHC and PCHO by ^{1}H NMR integration. [b] TON = moles epoxide consumed / moles catalyst; TOF = TON / time. [c] Calculated from relative amounts of PCHC and PCHO by ^{1}H NMR integration.

3.4.4 Polymer end-group analysis

The bimodal SEC trace mentioned above indicates that two different polymers are growing during the ROCOP reaction, due to different initiating groups at the metal. This gives rise to a polymer chain of very high molecular weight (*ca.* 300,000 g mol^{-1}) and a different chain of low molecular weight (*ca.* 10,000 g mol^{-1}). Analysis of the polymers obtained from the optimised reaction was attempted using MALDI-ToF mass spectrometry, but was unsuccessful due to the very high molecular weight of the polymer.
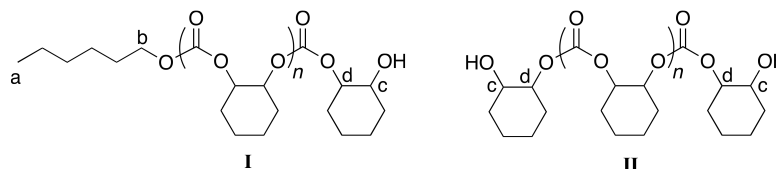
Figure 3.6: End-groups in the synthesised poly(carbonate), determined by ^{1}H NMR spectroscopy.

In the ^{1}H NMR spectrum of the obtained polymer, resonances that are assigned to the expected hexyl initiator-group were observed, at 0.88 ppm for the methyl protons (H_a), and 2.26 ppm for the methylene protons nearest the first carbonate group (H_b). An additional resonance observed at 4.40 ppm is assigned to the methine proton next to a cyclohexyl alcohol end-group, on the other end of the polymer (H_c, Figure 3.6, structure I). This methine resonance integrates in a 1:1 ratio with the methyl resonance from the hexyl group, but its expected ratio is 1:3. The observed 1:1 ratio is likely to arise from two additional cyclohexyl alcohol end-groups, on either end of a second polymer chain (H_c, Figure 3.6, structure II). This second, dihydroxyl-terminated, structure is supported by a ^{1}H NMR resonance at 3.30 ppm that is assigned to the methine proton of a terminal

cyclohexyl alcohol group, nearest the first carbonate group in the polymer chain (H_d).

Whilst the incorporation of a hexyl initiator group was clearly intentional, with the addition of n-hexanol, the cyclohexanol initiator group was not. Such an initiator arises due to the presence of water in the reaction, and could form through two conceivable ways. The first is that water reacts with CHO, forming cyclohexanediol through hydrolysis of the epoxide. This alcohol then reacts with **8a**, forming the catalytically-active Zn-(cyclohexoxide) species. The second possibility is that water reacts with **8a** in the first instance, forming a Zn-OH species that facilitates the first ring-opening reaction with CHO to initiate the copolymerisation.

3.4.5 Protonolysis reactions with the ROCOP pre-catalyst 8a

Whilst the use of the pre-catalyst **8a** is convenient from a synthetic standpoint – it is synthesised from the straightforward reaction of H_4L^3 and $ZnEt_2$ – its *in situ* transformation to the alkoxide complex means that the speciation of the active catalyst is ill-defined. This becomes more apparent from the fact that the SEC trace is bimodal and may in part be due to the reaction between **8a** and n-hexanol being carried out in a large volume of CHO, in which the concentration of water and other impurities will be comparable to that of the pre-catalyst. In an attempt to alleviate this problem, the tetranuclear Zn-hexoxide complex was synthesised on a preparative scale before application in catalysis.

The tetranuclear Zn-hexoxide complex, $\{Zn(\mu_2-OC_6H_{13})\}_4(L^3)$ (**11**) was isolated in 84 % yield from the reaction of **8a** with four equivalents of n-hexanol in THF. The reaction proceeds rapidly, with gas evolution observed at the onset of alcohol addition. In C_6D_6, a symmetric product is implied by ^{1}H NMR spectroscopy, with a single set of resonances for the macrocycle that are clearly shifted in comparison with **8a**: the imine protons appear at 8.07 ppm; the two pyrrole β-H environments appear as doublets at 7.02 and 6.17 ppm; the aryl protons appear at 6.94 ppm; and the *meso*-protons appear at 6.38 ppm. Importantly, the ethyl resonances, that appear at 1.32 and 0.42 ppm for **8a** in C_6D_6, have disappeared. In their stead are a number of resonances, of triplet and quartet multiplicity, in the region 1.89 to 0.57 ppm that are assigned to the new hexoxide ligands. There are two triplet resonances at higher chemical shifts of 3.83 and 3.70 ppm that integrate as four protons each per macrocycle; their chemical shifts indicate that these are hexoxide methylene protons next to oxygen, and their integration implies that there are four hexoxide ligands in total. The fact that the macrocycle

overall is symmetric, but the hexoxide ligands appear in two distinct environments, is reminiscent of the tetranuclear zinc-hydroxide complex **10**, in which the four μ_2-bridging hydroxide ligands appeared in two chemical environments. From these data it seems that there are two sets of μ_2-bridging hexoxide ligands, where two ligands bridge the zinc centres between pyrrole groups, over the *meso*-position, and the other two ligands bridge the zinc centres between imine groups, over the arene spacer group. If these hexoxide ligands were not bridging, and were isolated on single metal centres, then they would appear as a single resonance, with integration of eight protons per macrocycle.

In the ^{19}F NMR spectrum of **11**, the resonance for the C_6F_5 *ortho*-F is severely broadened, which has only been observed for bowl-shaped tetranuclear complexes so far. This provides further evidence that the complex remains tetranuclear. Many attempts were made to grow single crystals of **11** for X-ray structural analysis, but they were not met with success. The solubility of the complex is quite poor, even in THF, meaning that the compound often precipitated from solution before it crystallised.

The synthesis of other zinc-alkoxide and -phenoxide derivatives of **8a**, through protonolysis with other alcohols, was not straightforward. The reaction of **8a** with *iso*-propanol occurred readily, evolving ethane gas from the THF solution. The ^{1}H NMR spectrum of the isolated product contained a number of broad resonances in d_8-THF at 300 K, that resembled a symmetric product, and implied successful loss of the ethyl groups from **8a**. Fluxionality was suspected from the breadth of the NMR resonances and so the solution was cooled. At 213 K, the resonances were much less broad and, with molecular motion minimised, the spectrum revealed that the complex was in fact fully asymmetric, with four inequivalent imine proton resonances appearing at 8.86, 8.68, 8.48 and 8.40 ppm and two inequivalent *meso*-proton resonances appearing at 6.22 and 5.97 ppm. Importantly, a resonance at 11.98 ppm was only observable at this temperature and is assigned to a single pyrrole N-H proton, based on its integration of one proton per macrocycle. In addition, only three *iso*-propoxyl ligands were observed, with the *ipso*-protons appearing as a broad singlet at 4.29 ppm, and the six inequivalent methyl groups clearly resolved in the region 1.45 to 0.66 ppm. These observations indicate that the product of the reaction between **8a** and *iso*-propanol is the trinuclear *iso*-propoxide complex, $Zn_3(O^iPr)_3(HL^3)$ (**12**), that forms as the result of partial demetalation upon protonolysis. This complex was isolated with a crystal yield of 45 %.

At 330 K, the ^{1}H NMR spectrum for **12** was more sharp than at 300 K due

to thermal averaging. The four macrocycle imine protons appear as a single resonance at 8.36 ppm and the three *iso*-propoxide *ipso*-protons appear at 4.11 ppm; their methyl groups integrate as 18 protons at 1.02 ppm.

Large, red, block crystals of **12** were grown by diffusion of hexane vapour into a benzene solution and the solid-state structure was determined by X-ray crystallography, confirming that **12** is indeed a trinuclear complex (Figure 3.7). In the solid state, **12** adopts a highly distorted bowl-structure with a smaller bite-angle between the two halves of the macrocycle in comparison with other bowl-shaped complexes of the same ligand (which will be discussed in more detail in Chapter 4). The bite angle is 102° in **12**, compared with 152° in $Cu_2Py_4(L^3)$ (**13a**, 2 pyridine molecules in cleft), 117° in $Fe_2(THF)_3(L^3)$ (**15a**, 1 THF molecule in cleft), and 111° in $Pd_2(L^3)$ (**20**, no molecules in cleft). This small bite-angle is attributed to coordination of the ligand to an L-shaped, trinuclear zinc-*iso*-propoxide cluster, which resembles a cube with two vertices removed. In this cluster, the zinc centres are bridged by two μ_2-alkoxide ligands and one μ_3-alkoxide ligand. Each zinc centre is four-coordinate in a highly distorted tetrahedral coordination geometry, with bond angles ranging from 81.58(8)° to 143.47(9)°, and in order to accommodate this, an imine-group from one of the imino-pyrrole chelates is non-coordinating (N5). The internuclear distances between nearest neighbours in the cluster are 3.0071(5) Å (Zn1···Zn3) and 2.8213(6) Å (Zn2···Zn3). The Zn-O bond lengths, that describe the edges of the cluster, are fairly regular and are in the range 1.920(2) Å to 2.143(2) Å. However, the cluster is distorted, with inequivalent bond angles across the hinge, of 121.4(1)° (Zn2-O1-Zn1) and 111.21(8)° (O3-Zn3-O2).

Demetalation of the tetranuclear zinc-*iso*-propoxide complex that presumably forms initially would yield one equivalent of $Zn(O^iPr)_2$ per equivalent of **12**. This makes *iso*-propanol an inappropriate initiator for the catalytic reactions involving pre-catalysts **8a** or **8b**, as the simple Lewis acid that is formed will likely contribute to the competing ring-opening polymerisation of the epoxide to form poly-ether,[27] thereby reducing selectivity for the desired poly(carbonate) product. Demetalation was not observed during the reaction of **8a** with *n*-hexanol, which may be a result of the longer-chain alkoxide ligands imparting kinetic stabilisation towards the tetranuclear cluster. The pK_a for *n*-hexanol is predicted at 16.6 in water[28] and is essentially identical to that of *iso*-propanol (pK_a = 16.5 in water).[29] Therefore, whilst demetalation occurs through protonolysis of the zinc-pyrrolide bond, the formation of **12** cannot be attributed to a difference in acidity of *iso*-propanol in comparison with *n*-hexanol.

The reaction between **8a** and four equivalents of phenol occurred readily and
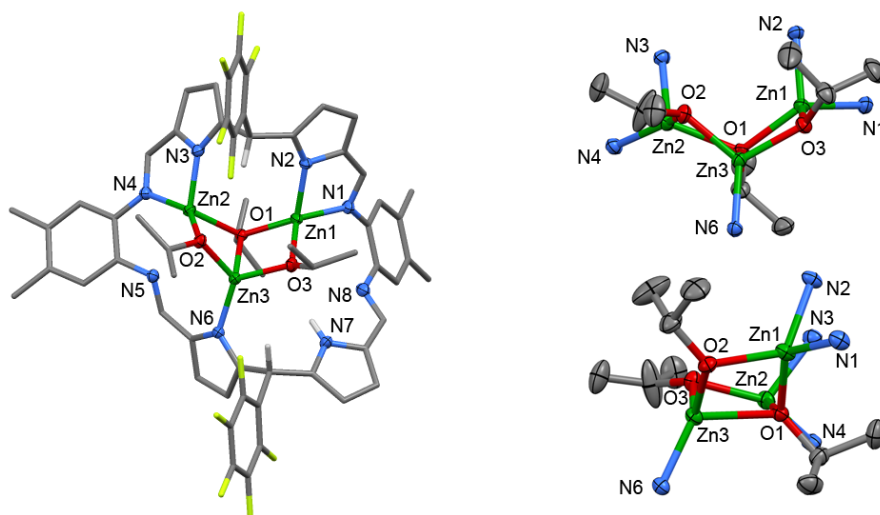
Figure 3.7: Solid-state structure of **12** and orthogonal views of the $Zn_3(O^iPr)_3$ cluster with coordinating atoms from the macrocycle. Displacement ellipsoids are drawn at 50 % probability. For clarity, only the *meso*- and pyrrole-protons are shown, whilst four benzene solvent molecules in the lattice and disordered atoms on one *iso*-propoxide ligand are omitted.

resulted in a compound which has a similar ^{1}H NMR spectrum to that of **12**, with a single N-H proton resonance observed at 11.76 ppm at 300 K (C_6D_6); this indicates that a similar demetalation reaction has occurred. In an attempt to introduce a kinetic barrier against demetalation, a reaction between **8a** and 2,6-di-*tert*-butyl-phenol was attempted. No reaction was observed at room temperature, with the ^{1}H NMR spectrum of **8a** unchanged in the presence of the di-substituted phenol. However, after heating at 90 °C for 24 h, the ^{1}H NMR spectrum had clearly changed and implied that partial protonolysis has occurred. In this case, no N-H proton was observed, indicating that demetalation had indeed been avoided. However, a triplet resonance at 6.91 ppm, that is assigned to the *para*-proton of the new zinc-phenoxide ligands, integrates as only two phenoxides per macrocycle. A quartet resonance at 0.55 ppm also integrates as two ethyl ligands per macrocycle, indicating that the product from this reaction is a tetranuclear, heteroleptic zinc-ethyl/phenoxide complex $Zn_4\{OPh(2,6-tBu)_2\}_2Et_2(L^3)$. Although zinc-phenoxide bonds have been shown to initiate the ROCOP reaction,[30] this heteroleptic complex was not considered suitable for ROCOP catalysis as the ethyl ligands are inactive towards CO_2 insertion and are also likely to be hydrolysed by trace moisture in the dynamic CO_2 atmosphere. This heteroleptic complex is therefore likely to produce a mixture of two polymers propagating from the catalyst.

After these attempted protonolysis reactions, only complex **11** was used as an isolated catalyst for the ROCOP reaction, and only *n*-hexanol was considered as

an acceptable initiator for the *in situ* generation of catalysts using complexes **8a** and **8b**.

3.4.6 Performance of 11 in ROCOP catalysis

The isolated tetranuclear Zn-hexoxide complex **11** was applied to the optimised ROCOP reaction (entry 2, Table 3.4), so as to compare its performance with the analogous Zn-hexoxide complex formed *in situ* (entry 1). Surprisingly, the pre-prepared catalyst did not perform as well as the pre-catalyst **8a**; the conversion of epoxide was lowered by 20 %, the TOF was diminished to 11 h^{-1}, and the selectivity for carbonate linkages was also lowered by 9 %. In terms of the polymer, that prepared by **11** was of much lower molecular weight (7400 g mol^{-1}) with an incredibly broad distribution (Đ = 9.75), although the SEC trace was not bimodal in this case.

Considering that the polymers obtained from the pre-catalyst **8a** contained a mixture of di-hydroxyl and hexyl terminal groups, it may be that the improved performance of **8a** is due to a mixture of active species, or a heteroleptic complex. The tetranuclear alkyl complex **8a** is known to be highly moisture-sensitive, forming the μ-oxo complex **9** readily. The hydroxyl or hexoxyl derivative of **9** might therefore be one of the catalytically active species.

Table 3.4: Comparison of the performance of Zn-hexoxide catalysts formed *in situ*, from **8a**, and *ex situ* (**11**).

Entry	Catalyst	Conv.[a] / %	TOF[b] / h^{-1}	Selectivity[c] / %	M$_n$ [d] / g mol^{-1}	Đ [d]
1	**8a***	70	15	90	394,000	1.61
					6800	1.77
2	**11**	50	11	81	7400	9.75

Reactions were carried out in 5 M CHO, at 80 °C, under 30 atm CO_2, using a catalyst loading of 0.2 mol%. * *n*-hexanol initiator added with a concentration of 0.8 mol%. [a] Conversion calculated from relative amounts of CHO, PCHC and PCHO by ^{1}H NMR integration. [b] TON = moles epoxide consumed / moles catalyst; TOF = TON / h. [c] Calculated from relative amounts of PCHC and PCHO by ^{1}H NMR integration. [d] M$_n$ and Đ both determined by SEC in THF, calibrated using narrow molar-mass polystyrene standards.

Although the exact speciation of the active catalyst is unknown, the performance of the pre-catalyst **8a** is quite good. Importantly, the high selectivity for carbonate linkages shows that, after some optimisation of the reaction conditions, the catalytic system has a high efficiency for CO_2 sequestration, and the successful co-polymerisation is a novel mode of reactivity for this class of macrocyclic complexes.

Furthermore, the high performance of **8a** in comparison with **8b** highlights

the importance of ligand structure in catalyst design. The structures of the Zn-hexoxide derivatives of **8a** and **8b** are assumed to be similar to one another, and analogous to that of the Zn-hydroxide complex **10**. The poor activity of the anthracenyl-pillared pre-catalyst **8b** might be due to subtle differences in the geometry of the Zn-hexoxide cluster; perhaps a small increase in the Zn···Zn distances (in comparison with **8a**) renders the cluster too thermodynamically stable, and therefore resistant to the chemical changes that are required for CO_2 insertion and propagation of the polymer chain.

References

[1] E. Askarizadeh, A. M. J. Devoille, D. M. Boghaei, A. M. Z. Slawin and J. B. Love, *Inorg. Chem.*, 2009, **48**, 7491.

[2] G. Givaja, A. J. Blake, C. Wilson, M. Schroder and J. B. Love, *Chem. Commun.*, 2005, 4423.

[3] E. Tomat, L. Cuesta, V. M. Lynch, and J. L. Sessler, *Inorg. Chem.*, 2007, **46**, 6224.

[4] A. M. J. Devoille, P. Richardson, N. L. Bill, J. L. Sessler and J. B. Love, *Inorg. Chem.*, 2011, **50**, 3116.

[5] B. Yu, Y.-X. Sun, C.-J. Yang, J.-Q. Guo and J. Li, *Z. Anorg. Allg. Chem.*, 2017, **643**, 689.

[6] Y. Mikata, R. Ohnishi, R. Nishijima and H. Konno, *Inorg. Chem.*, 2016, **55**, 11440.

[7] M. Fondo, A. M. Garcia-Deibe, N. Ocampo, J. Sanmartin, M. R. Bermejo, E. Oliveira and C. Lodeiro, *New J. Chem.*, 2008, **32**, 247.

[8] D. A. Brown, N. J. Fitzpatrick, H. Müller-Bunz and Á. T. Ryan, *Inorg. Chem.*, 2006, **45**, 4497.

[9] Y. Sun, Q. Zeng, S. Gou, W. Huang, C. Duan and J. Yao, *J. Incl. Phenom. Macro.*, 2002, **42**, 131.

[10] B.-H. Ye, X.-Y. Li, I. D. Williams and X.-M. Chen, *Inorg. Chem.*, 2002, **41**, 6426.

[11] C. Romain, J. A. Garden, G. Trott, A. Buchard, A. J. P. White and C. K. Williams, *Chem. -Eur. J.*, 2017, **23**, 7367.

[12] M. Cokoja, C. Bruckmeier, B. Rieger, W. A. Herrmann and F. E. Kühn, *Angew. Chem. Int. Ed.*, 2011, **50**, 8510.

[13] N. Kitajima, S. Hikichi, M. Tanaka and Y. Morooka, *J. Am. Chem. Soc.*, 1993, **115**, 5496.

[14] W. Sattler and G. Parkin, *J. Am. Chem. Soc.*, 2011, **133**, 9708.

[15] F. Allen, *Acta Crystallogr., Sect. B*, 2002, **58**, 380.

[16] L. A. Lesikar and A. F. Richards, *Polyhedron*, 2010, **29**, 1411 .

[17] A. Pettersen, A. Lennartson and M. Høakansson, *Organometallics*, 2009, **28**, 3567.

[18] W. Bury, E. Krajewska, M. Dutkiewicz, K. Sokolowski, I. Justyniak, Z. Kaszkur, K. J. Kurzydlowski, T. Plocinski and J. Lewinski, *Chem. Commun.*, 2011, **47**, 5467.

[19] C. Agnew, K. B. Dillon, A. E. Goeta and A. L. Thompson, *Inorg. Chim. Acta*, 2009, **362**, 4260.

[20] K. Sokolowski, W. Bury, I. Justyniak, A. M. Cieslak, M. Wolska, K. Soltys, I. Dziecielewski and J. Lewinski, *Chem. Commun.*, 2013, **49**, 5271.

[21] G. W. Coates and D. R. Moore, *Angew. Chem. Int. Ed.*, 2004, **43**, 6618.

[22] D. R. Moore, M. Cheng, E. B. Lobkovsky and G. W. Coates, *Angew. Chem. Int. Ed.*, 2002, **41**, 2599.

[23] W.-M. Ren, Z.-W. Liu, Y.-Q. Wen, R. Zhang and X.-B. Lu, *J. Am. Chem. Soc.*, 2009, **131**, 11509.

[24] J. A. Garden, P. K. Saini and C. K. Williams, *J. Am. Chem. Soc.*, 2015, **137**, 15078.

[25] H. Sugimoto, H. Ohshima and S. Inoue, *J. Polym. Sci. Pol. Chem.*, 2003, **41**, 3549.

[26] M. R. Kember, F. Jutz, A. Buchard, A. J. P. White and C. K. Williams, *Chem. Sci.*, 2012, **3**, 1245.

[27] M. H. Chisholm, J. C. Huffman and K. Phomphrai, *J. Chem. Soc. Dalton*, 2001, 222.

[28] M. J. Citra, *Chemosphere*, 1999, **38**, 191.

[29] W. Reeve, C. M. Erikson and P. F. Aluotto, *Can. J. Chem.*, 1979, **57**, 2747.

[30] D. J. Darensbourg, J. R. Wildeson, J. C. Yarbrough and J. H. Reibenspies, *J. Am. Chem. Soc.*, 2000, **122**, 12487.

Chapter 4

Transition metal complexes for reduction of carbon dioxide

This chapter discusses the synthesis of several late-transition-metal complexes of both macrocyclic ligands L^3 and L^4, as well as the acyclic, donor-expanded dipyrrin ligand L^2. Structural characterisation of these complexes has been carried out principally using X-ray crystallography. Bimetallic copper(II) complexes have been used to investigate thoroughly the relationship between the macrocycle geometry and the electronic structure, using voltammetric methods and EPR spectroscopy. Most of the complexes presented in this chapter have been tested for electrocatalytic activity towards CO_2 reduction.

4.1 Synthesis and electronic structure of copper(II) complexes

In the literature it has been demonstrated that macrocyclic dipyrromethanes may undergo oxidation to dipyrrins during metallation with transition metals under aerobic conditions.[1,2] Copper(II) has been implicated in this chemistry, and copper(II) complexes of the macrocycles L^3 and L^4 are therefore attractive targets, as the air-stability and redox-activity of copper(II) complexes makes their use in catalysis and electro-catalysis promising. As discussed in the introduction, there is some literature precedent for copper(II) carrying out CO_2 reduction,[3,4] and it was hoped that the well-defined geometries provided by the macrocyclic ligands L^3 and L^4 might promote reactivity in this case.

4.1.1 Synthesis of dinuclear copper(II) complexes

The aerobic reaction of macrocycles H_4L^3 or H_4L^4 with two equivalents of $Cu(OAc)_2$ in CH_2Cl_2, in the presence of NEt_3, yielded dark yellow residues after

removal of the solvent (OAc = $^-O_2CCH_3$, Scheme 4.1). The product was found to be stable on alumina and the crude product was therefore purified by column chromatography, eluting the pure product as an orange fraction with CH_2Cl_2 (R_f = 0.9). A green fraction was fairly mobile in the presence of NEt_3 (R_f = 0.5), but was immobile if the base was not used in the synthesis. It was later found that NEt_3 was not required, and only lowered the yield of the product considerably, down to 35 %. The base-free addition of $Cu(OAc)_2$ to H_4L^3 or H_4L^4 afforded the bimetallic copper(II) complexes **13a** and **13b**, respectively, in variable yield between 20 and 70 % after purification by column chromatography.
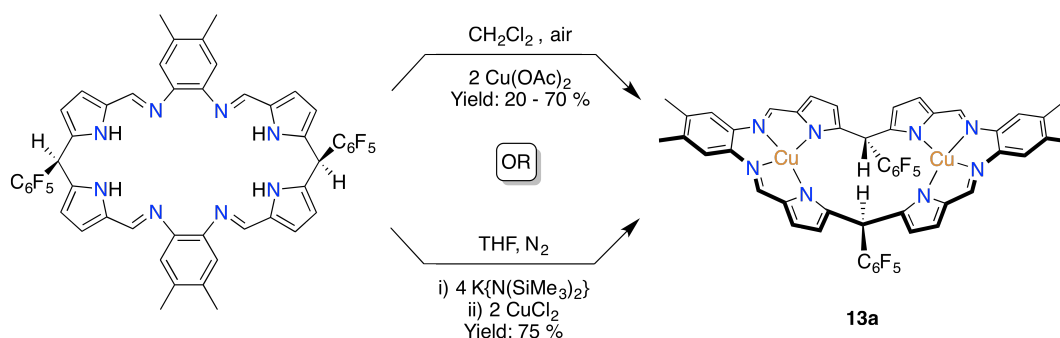
Scheme 4.1: Synthetic routes to **13a** as a representative scheme for the synthesis of both complexes **13a** and **13b**.

Due to the unpaired electron on each d^9 copper(II) centre, complexes **13a** and **13b** are strongly paramagnetic and completely NMR-silent, precluding structural characterisation using that method. Instead, the syntheses of these compounds are supported by their electrospray-ionisation mass spectra (ESI-MS). Molecular ion peaks were observed at 1058 m/z for **13a** and at 1203 m/z for **13b**, which correspond to the expected molecular masses for those complexes minus two protons, *i.e.* conceivably macrocyclic dipyrrin complexes. The isotope patterns for these peaks also support the synthesis of bimetallic copper(II) complexes, and match very well with simulated spectra. Upon metalation of H_4L^3 and H_4L^4, a lowering of the imine vibrational frequencies is observed in the solid-state IR spectra, from 1620 cm^{-1} to 1552 cm^{-1} for **13a**, and from 1614 cm^{-1} to 1574 cm^{-1} for **13b**, indicating coordination of the imine groups to the copper(II) centres in both cases.

Single crystals of **13a** were grown from a pyridine solution on slow evaporation of the solvent, and crystals of **13b** were grown from a THF solution by slow diffusion of hexanes. The solid-state structures were determined by X-ray crystallography and in both cases, the macrocyclic ligands are non-oxidised dipyrromethanes, which is evident from the bond angles around the *meso*-carbon

atoms (mean $a = 110.2°$ for **13a** and 111.0° for **13b**). This is contrary to the mass spectrometry data and implies that the *meso*-protons are lost under ionising conditions. This is perhaps unsurprising, considering that those *meso*-protons are observed with ^{1}H NMR resonances around 5.9 ppm in the NMR spectra of the pro-ligands, indicating that they are acidic and possess low bond-dissociation enthalpies.
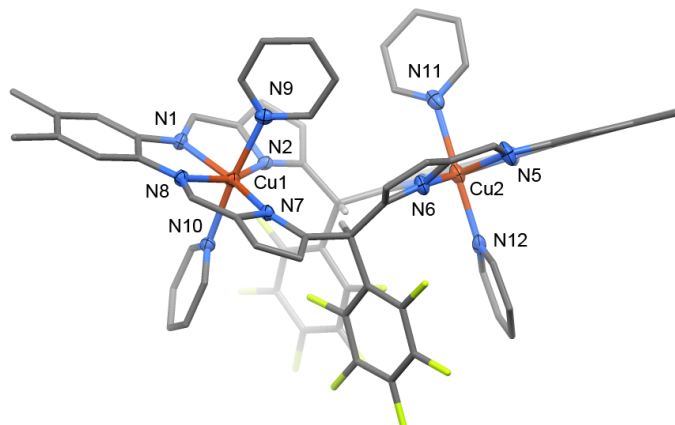
Figure 4.1: Solid-state structure of **13a**. Displacement ellipsoids are drawn at 50 % probability and for clarity, three pyridine solvent molecules in the asymmetric unit have been omitted and only the *meso*-protons are shown.

Whilst *meso*-disubstituted macrocyclic ligands adopt Pacman geometries upon metalation with transition metals,[5–7] **13a** adopts a bowl-conformation in a similar manner to the zinc(II) analogue (**7a**, Chapter 3). The *meso*-carbon atoms in the dipyrromethane units form the hinge of the macrocycle, leaving two planar coordination pockets that comprise two imino-pyrrole chelating units and the aromatic spacer group. This conformation results in a wide bite-angle of 152° between the two N_4-coordination compartments and a large Cu···Cu separation of 6.493(6) Å. The traditional bimetallic copper(II) Pacman complex exhibits much smaller bite angles (52 – 62°) and shorter Cu···Cu separations of 3.47 – 4.05 Å.[8]

Both copper(II) centres in **13a** are in distorted octahedral coordination geometries. With a mean value of 2.05 Å, the copper-imine bonds are shorter than the mean copper-pyrrolide bond distances (2.18 Å) and is likely due to the steric constraints around the *meso*-position, pulling the pyrrole groups away from the idealised coordination positions. The N_4-donor pockets are planar, with the equatorial bond angles around copper summing to 359.0°. Each copper centre has two axially-coordinated pyridine ligands with long average bond lengths of 2.15 Å, indicative of Jahn-Teller distortions, as expected for a d^9 cation. Based on

the solid-state structures of the analogous iron(II) and palladium(II) complexes discussed below, the bowl-conformation and the torsion between N_4-donor compartments for **13a** is not due to the coordination of two pyridine solvent molecules within the cleft.

Structurally similar bowl-shaped complexes of *meso*-disubstituted macrocyclic ligands have been reported for calcium(II)[9] and uranium(III).[10] With those complexes, it seems that the large ionic radii of the metals[i] drive the folding of the ligand to the bowl-conformation; in those examples, the *meso*-positions are located further away from the hinge of the molecule, resulting in larger coordination compartments for those large metal cations. This also has the effect of creating much narrower bite-angles between the two pockets, which are reported as 99° for the calcium(II) complex[9] and 98° for the uranium(III) complex.[10] It seems that the steric interactions around the *meso*-position are important in dictating the conformation of the macrocycle upon metalation, and that by reducing the steric encumbrance at that position (in this case, changing an alkyl group to a proton), results in a bowl-conformation for smaller metal cations. As the *meso*-proton crystallographic positions are geometrically placed for **13a**, they are pointed at each other with a short distance of 2.1 Å; this distance would not be possible if methyl groups were situated at the *meso*-positions. For **13a**, the C_6F_5 *meso*-substituents are co-parallel, but the aryl rings are not overlapping. This arrangement seems to arise in order to reduce steric interactions rather than as a consequence of π-stacking, and may be the cause of the 24.8° torsional twist between the two N_4-donor compartments.

In the case of **13a**, all of the macrocycle nitrogen-atoms are involved in coordination of the metal centre. In contrast, in those examples where *meso*-disubstituted, first-row transition metal macrocycles do form bowl-shaped complexes, they often remain protonated at the pyrrole nitrogens and feature bridging anions within the cleft, such as hydroxide or acetate ligands.[8,12] In these examples, it is this incorporation of additional anionic ligands that seems to be the driving force for forming a bowl-shaped complex, despite the small ionic radii of the metals, as the charge-balance in these cases mean that the pyrrole groups are not required for coordination, releasing strain on the macrocycle.

Due to the large separation between the imine-nitrogen donors in the anthracene-pillared macrocycle L^4, a bowl-conformation is not possible for its bimetallic complexes. Therefore, in the solid-state, **13b** adopts a classic Pacman geometry, with a Cu···Cu separation of 4.818(3) Å and a twisting angle of 30° between the

---

[i]Crystal radii / Å: U^{III}, 1.165; Ca^{II}, 1.140; Cu^{II}, 0.870; Zn^{II}, 0.740.[11]

anthracenyl spacer-groups and N_4-donor compartments, which is common.[7,13,14] Unlike the zinc(II) analogue, **7b**, which exists as a mixture of isomers in solution and adopts the *syn,endo*-isomer in the solid state, **13b** adopts the *syn,exo*-isomer in the solid state. The exclusion of the C_6F_5 *meso*-substituents from the cleft in the case of **13b** means that the macrocycle has a much smaller twist angle of 30°, which was 57.7° for **7b**.

The internuclear separation of 4.818(3) Å for **13b** is also shorter than that for **7b** (6.236(1) Å) and is likely due to the absence of coordinated solvent ligands pulling the metal cations out of their coordination pockets in the former. Interestingly, the Cu···Cu distance for **13b** is also very short compared to related cobalt(II),[14] palladium(II),[7] uranium(III)[10] and uranium(VI)[15] complexes of *meso*-disubstituted, anthracenyl-bridged macrocycles, which have internuclear distances of 5.377 – 5.9243 Å. The separation in **13b** is more similar to the short Zn···Zn distance reported for related dinuclear zinc(II) complexes that are bridged by coordinated anions,[16] and is also more similar to the intermetallic separations offered by diporphyrinanthracene[17,18] and dicorroleanthracene[19] ligands (4.52 – 4.68 Å). The small *meso*-proton substituent appears responsible for this short Cu···Cu distance, as it has the effect of closing the macrocycle cleft, such that **13b** has a negative bite angle of −8.03° between the two N_4-donor planes. This contrasts with *meso*-disubstituted anthracenyl Pacman complexes, which have positive bite-angles (14.83° for the copper(II) analogue), where the larger *meso*-substituents influence a bending of the coordination pockets away from the macrocycle cleft.[20]
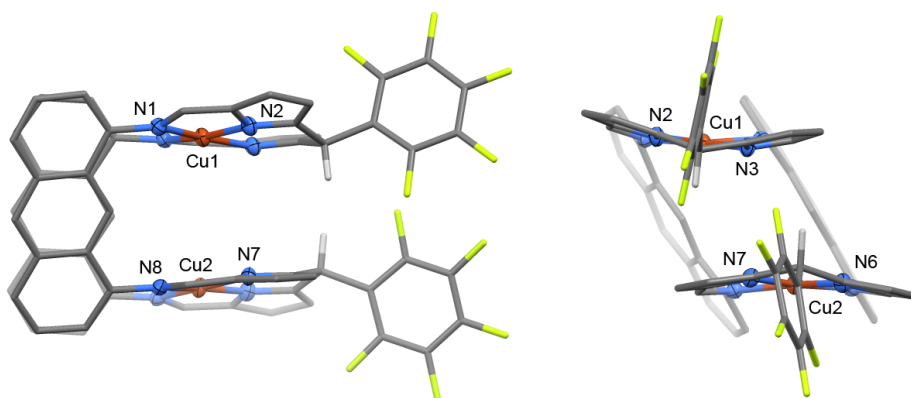
Figure 4.2: Orthogonal views of the solid-state structure of **13b**. Displacement ellipsoids are drawn at 50 % probability and for clarity, only the *meso*-protons are shown.

As the aerobic metallation of H_4L^3 or H_4L^4 with $Cu(OAc)_2$ did not result in macrocyclic dipyrrin complexes, improved syntheses of those complexes were

developed, as the yields from the initial method were variable and were at times as low as 25 %. Higher, reproducible yields of 75 % were obtained using a salt-metathesis procedure, carried out under anhydrous, anaerobic conditions. Deprotonation of the pyrrole nitrogens was carried out *in situ*, using four equivalents of K{N(SiMe$_3$)$_2$} to afford K$_4$L^3, or four equivalents of Li{N(SiMe$_3$)$_2$} to afford Li$_4$L^4 (K$_4$L^4 has poor solubility in THF). Reaction of these alkali-metal salts with two equivalents of anhydrous CuCl$_2$ afforded **13a** and **13b**, which were purified by column chromatography as discussed above.

4.1.2 Geometric/electronic structure relationships

The folding of **13a** to the bowl conformation means that **13a** and **13b** are not only structurally very different, but that the copper(II) centres also reside in different coordination pockets, with different relative orientations between the ions. The electronic structures of **13a** and **13b** were studied using a combination of DFT molecular-orbital calculations, EPR spectroscopy and electrochemistry, to see if the different geometries and coordination arrangements imposed by changes in the ligand structure had any electronic consequences.

DFT calculations

The molecular-orbital (MO) structures of **13a** and **13b** were investigated by DFT methods. The crystal structures were used as initial-guess geometries, and their optimised geometries in the triplet spin-state were adequately determined by the UB3LYP functional and 6-31G(d,p) basis set.

For the geometry optimisation of **13a**, the coordinated pyridine solvent molecules were required to represent the bowl geometry; their omission resulted in nonsensical folding of the complex. Unlike in the crystal structure, one of these pyridine ligands is rotated away from the copper centre, but this has not introduced significant error to the rest of the complex. Overall, there is only 5.3 % relative error in the calculated bond distances between the copper centres and the macrocycle donor atoms and 6.4 % relative error in the bond angles. However, the torsion between the two coordination compartments is greatly overestimated in the calculated structure, at 51° compared with 26° in the crystal structure.

Population analysis initially implies that the singly-occupied molecular orbital (SOMO) of **13a** is largely ligand-based, as shown by the MO plot in Figure 4.3 (a). However, it can be quite difficult to interpret the MO structure of open-shell

systems when the canonical α- and β-orbitals are spatially separated, as is the case here. Using Gaussian's ability to "biorthogonalize" spatially-separated pairs of MOs, these orbitals are transformed into single $\alpha\beta$ MOs, allowing a more intuitive interpretation of the orbital structure. Applying this technique to **13a** indicates that the SOMO has a total of 71 % copper d-character, with a 52 % contribution from one centre and a 19 % contribution from the other; SOMO-1 is equivalent, with the contributions reversed. Calculation of the total unpaired spin-density, $\rho(\alpha) - \rho(\beta)$, also reveals that the unpaired electron density is situated in the copper $d_{x^2-y^2}$ orbitals, with only minor spin-delocalisation onto the ligand nitrogen atoms. The total spin-density plot shown in Figure 4.3 (b) is equivalent to the combined SOMO and SOMO-1 orbitals obtained after "biorthogonalization", which describes a σ^* interaction between the nitrogen p-orbitals and the copper $d_{x^2-y^2}$ orbitals on each metal.
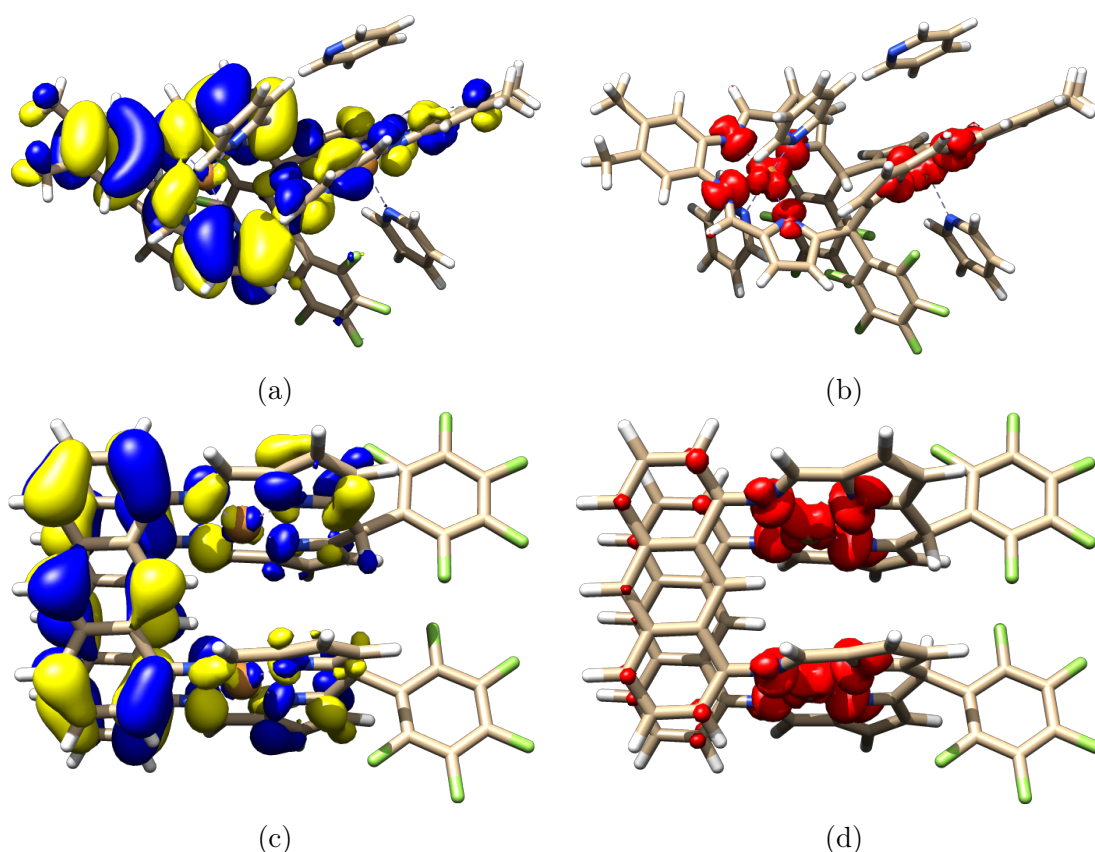
Figure 4.3: (a) SOMO of **13a**, before "biorthogonalization". (b) Total spin-density for the unpaired electrons in **13a**. (c) SOMO of **13b**, before "biorthogonalization". (d) Total spin-density for the unpaired electrons in **13b**. All calculated by DFT using the UB3LYP functional and 6-31G(d,p) basis set.

The crystal structure of **13b** was well represented by the UB3LYP functional and 6-31G(d,p) basis set, with less than 2 % relative error in the metal-ligand bond

lengths, and a good approximation for the Cu$\cdots$Cu distance at 4.78 Å (4.818(3) Å experimentally). The bond angles around the copper(II) centres are also accurately represented, with less than 1.25 % relative error in the calculated structure. As for **13a**, the SOMO and SOMO-1 for **13b** predicted by population analysis feature high ligand-character, with major contributions from the anthracenyl spacer group and minor contributions from the donor-expanded dipyrromethane manifold (Figure 4.3 (c)). Biorthogonalization of the α- and β-orbitals reveals that the SOMO and SOMO-1 feature high metal-character, which is in agreement with the calculated spin-density for **13b**; the unpaired electrons reside in $d_{x^2-y^2}$ orbitals on each copper(II) centre, with only minor delocalisation onto the donor nitrogen-atoms (Figure 4.3 (d)).

Comparing the molecular orbitals and spin-densities of **13a** and **13b**, it seems that despite the differences in molecular geometries and arrangement of donor-groups in those complexes, the local electronic structures around each copper(II) centre are very similar. However, the different relative orientation of the two copper centres in the bowl conformation compared to that in the Pacman conformation might have an impact on the electronic structure that is not represented by DFT calculations. In order to investigate these potential differences, which may result from long-range magnetic interactions between the two copper nuclei, EPR spectroscopy was carried out on both **13a** and **13b**.

EPR spectroscopy

Whilst the paramagnetism exhibited by the bimetallic copper(II) complexes hinders structural characterisation by NMR spectroscopy, the unpaired electron on each d^9 copper(II) centre means that EPR spectroscopy can be used to probe both the electronic and geometric structures of those complexes. For both complexes, the solution-state X-band EPR spectra were broad and uninformative at room temperature, but much higher resolution was obtained from frozen THF/toluene solutions, measured at 80 K.[ii]

For **13b**, the EPR spectrum is characteristic of an $S = 1$ spin-system, resulting from exchange coupling of the two copper(II) nuclei (Figure 4.4 (a)). Due to Zeeman splitting in a magnetic field, the m_s states of an $S = 1$ system ($m_s = +1, 0, -1$) will become non-degenerate, and whilst the formal selection rule for an EPR transition is that $\Delta m_s = 1$, the $\Delta m_s = 2$ transition may be observed in some cases. Because the microwave frequency of the EPR spectrometer is fixed

---

[ii]EPR measurements were carried out by Daniel Sells and EPR simulations by Prof. Eric McInnes, at the University of Manchester.

(at 9.4 GHz for X-band), this formally forbidden transition is observed at half the magnetic field that the dominant, allowed transition is observed at. This half-field $\Delta m_s = 2$ transition[21,22] was observed and measured for **13b**, supporting the $S = 1$ spin-state and exchange coupling between the two copper(II) nuclei (Figure 4.4 (b)).
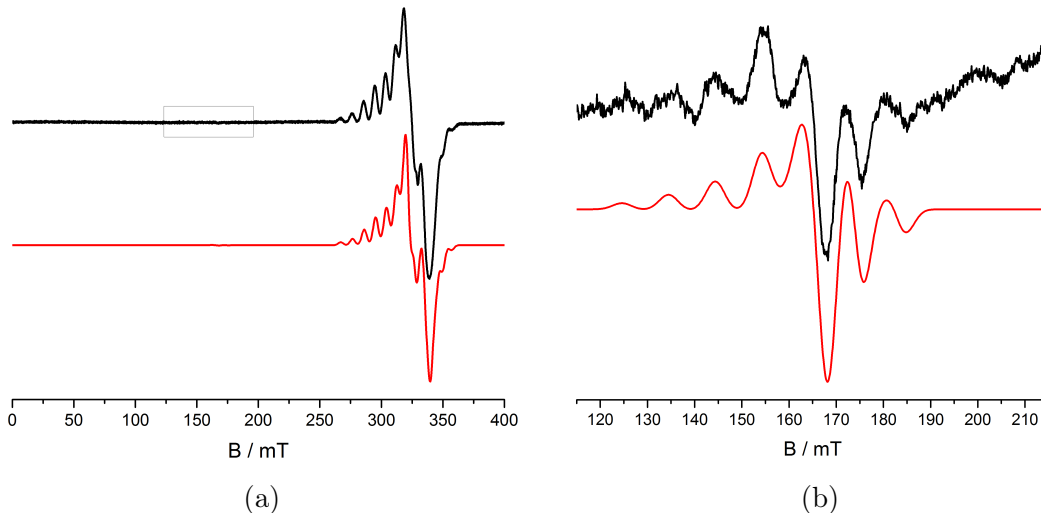
Figure 4.4: Experimental EPR spectra (black) and simulations (red) for **13b**, measured at 80 K on an X-band spectrometer (9.4 GHz), as a THF/toluene glass. (a) The full spectrum, with the black box representing the region for the half-field transition, (b), which was measured separately.

The hyperfine structure is well resolved at 80 K, for both the $\Delta m_s = 1$ and half-field transitions. For an unpaired electron interacting with n nuclei with nuclear spins, I, there will be $2nI + 1$ EPR lines. The half-field $m_s = -1 \rightarrow m_s = +1$ transition gives seven lines, as is expected for an unpaired electron interacting with two equivalent $^3/_2$ nuclei (copper has two major isotopes – ^{63}Cu and ^{65}Cu, summing to 100 % natural abundance – and both isotopes have the same nuclear spin, $I = {}^3/_2$). However, the $\Delta m_s = 1$ signal has more than seven lines and implies zero-field splitting. This is where the m_s states are non-degenerate in the absence of an applied magnetic field, perhaps due to the interaction of the unpaired electrons with each other. This has the effect that, when the magnetic field is applied, the energies of the two $\Delta m_s = 1$ transitions ($-1 \rightarrow 0$ and $0 \rightarrow +1$) are not equal and will be measured at slightly different field strengths. On the other hand, the $\Delta m_s = 2$ transition is unaffected by this because that transition bypasses the $m_s = 0$ state, and so the expected seven lines are observed in that case.

Simulations used the simple spin-Hamiltonian (equation 4.1).[iii] The exchange

---

[iii]β, electronic Bohr magneton; **B**, applied magnetic field; $\mathbf{g}_i$ and $\mathbf{A}_i$, local **g** and Cu-hyperfine

matrix, $\mathbf{J}$, comprises an isotropic component, $\mathbf{J}^{\text{iso}}$, which is a scalar, and an anisotropic moment, $\mathbf{J}^{\text{dip}}$. The EPR spectra were simulated with the assumption that this anisotropic moment is dipolar in nature, such that the matrix has principle components $(+1 \ +1 \ -2)^*\mathbf{J}^{\text{dip}}$, where $\mathbf{J}^{\text{dip}}$ is a scalar.

$$H = \sum_{i=1,2} \beta.\mathbf{B}.\mathbf{g}_i.\hat{s}_i + \hat{s}_i.\mathbf{A}_i.\hat{I}_i + \hat{s}_1.\mathbf{J}.\hat{s}_2 \qquad (4.1)$$

It was assumed that the two copper sites are axially symmetric, such that $g_x = g_y$ and $A_x = A_y$, given that there is no evident super-hyperfine coupling between the unpaired electrons and the nitrogen atoms in the N_4-donor set. The two CuN_4 donor planes were assumed to be co-parallel in solution, as they are found in the solid-state structure, given the rigidity of the two anthracenyl spacer groups. A large value of J^{iso} was arbitrarily set at $+50 \text{ cm}^{-1}$, which describes an antiferromagnetic interaction with the Hamiltonian written as in equation 4.1; when this value is much greater than $\beta.\mathbf{B}.\mathbf{g}$ and $\mathbf{A}$, it has no effect on the simulated spectrum.

Initially, the principal axis of the $\mathbf{g}$ and $\mathbf{A}$ tensors, $g_z A_z$, was assumed to lie normal to the CuN_4 coordination plane and was also assumed to be co-parallel with J_z^{dip}, the principal axis of the $\mathbf{J}^{\text{dip}}$ tensor that describes the dipolar interaction between the two copper nuclei. As J_z^{dip} describes the $\text{Cu}\cdots\text{Cu}$ dipolar interaction, it should be co-parallel with the $\text{Cu}\cdots\text{Cu}$ vector and is not truly co-parallel with $g_z A_z$. However, the half-field transition is particularly sensitive to the Euler angle, θ, which describes the angle between two coordinate systems (in this case, that of $\mathbf{g}$ and $\mathbf{A}$, and that of $\mathbf{J}$). By varying θ to obtain the best match between the simulated and experimental spectra, the angle between $g_z A_z$ and J_z^{dip} can be obtained.[8,23,24] In practice, this describes the angle between the $\text{Cu}\cdots\text{Cu}$ vector and the local z-axes of the copper nuclei, allowing a comparison between the solid- and solution-state structures to be made. Based on this method, the Euler angle was predicted to be 30°, which is an exact match for the twisting angle between the CuN_4-plane and the anthracenyl spacer-group in the crystal structure. This shows that the twisting in the Pacman geometry is not unique to the solid-state structure, but is a permanent structural feature.

The internuclear distance may also be extracted from the magnitude of $\mathbf{J}^{\text{dip}}$, and this was predicted to be 5.52 Å by the EPR simulation.[8,23,24] This is an over-estimation of the internuclear distance measured in the crystal structure, which is 4.818(3) Å, and suggests a relocation of the $\text{Cu}\cdots\text{Cu}$ separation in

---

matrices; $\mathbf{J}$, exchange matrix.

solution.
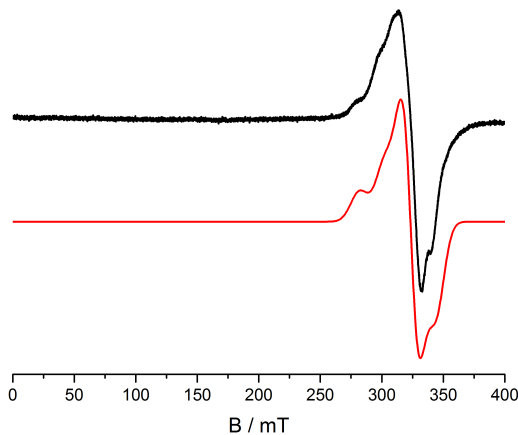
Figure 4.5: Experimental EPR spectrum (black) and simulation (red) for **13a**, measured at 80 K on an X-band spectrometer (9.4 GHz), as a THF/toluene glass.

For **13a**, the EPR spectrum features much broader linewidths, even at 80 K. The hyperfine structure is nevertheless resolved, and the four-line spectrum observed would be expected for an unpaired electron interacting with one $I = {}^3/_2$ nucleus. This indicates that any exchange interaction between the two copper(II) nuclei is weaker than the hyperfine interaction, and could be due to the increased separation between the two sites, which is 6.493(6) Å in the solid-state structure. Given that the unpaired electrons are predicted (by the DFT calculations discussed above) to occupy the $d_{x^2-y^2}$ orbitals on each copper(II) centre, the weak exchange interaction implied by EPR spectroscopy seems to be a consequence of the increased internuclear separation, rather than the change in relative orientation of the copper centres, *i.e.* the bowl conformation compared to the Pacman conformation. If the unpaired electron resided in the d_{z^2} orbital, then the relative orientations of the Jahn-Teller axes might have a greater influence on the exchange interactions.

As a $\Delta m_s = 2$ transition was not measured for **13a**, an accurate prediction of the internuclear separation could not be made as for **13b**. However, test simulations gave a rough upper limit of $|J^{\text{dip}}| \leqslant 0.005$ cm^{-1}, which would give an internuclear distance of approximately 7 Å. This compares well with the distance of 6.493(6) Å measured in the solid-state structure.

The g-values determined for **13a** ($g_{xy} = 2.07$, $g_z = 2.15$) and **13b** ($g_{xy} = 2.03$, $g_z = 2.17$) are anisotropic and significantly shifted from that of the free electron ($g_e = 2.0023$). These values are similar to those determined for the *ortho*-phenylene bridged, *meso*-disubstituted Pacman complex Cu$_2$(L$^{\text{Me}}$),[8] as well as those for copper(II) cofacial diporphyrins,[24] reflecting similarities in the

coordination environments, despite the gross structural differences.

Table 4.1: Summary of EPR parameters for **13b** and **13a** and a comparison with those measured for the Pacman complex $Cu_2(L^{Me})$ [8] and the diporphyrinanthracene complex Cu_2-DPA. [24] n.g.: values not given in the literature.

Complex	g_z	$g_{x,y}$	A_z / $\times 10^{-4}$ cm^{-1}	A_{xy} / $\times 10^{-4}$ cm^{-1}	J_z^{dip} / cm^{-1}	J_{xy}^{dip} / cm^{-1}
13b	2.17	2.03	200	10	−0.22	+0.011
13a	2.15	2.07	200	10	–	–
$Cu_2(L^{Me})$	2.16	2.02	210	20	n.g.	n.g.
Cu_2-DPA	2.193	2.05	205	30	n.g.	n.g.

Electrochemistry

The electrochemical behaviours of **13a** and **13b** were investigated by cyclic voltammetry (CV). Against a Pt-disc working electrode in THF, **13a** undergoes quasi-reversible oxidation at E_p^a −0.10 V *versus* ferrocene and two, quasi-reversible reduction processes at E_p^c −1.47 V and −1.76 V. A comparison of the peak areas reveals that the oxidation wave accounts for twice the amount of charge passed for either reduction processes, and the oxidation is therefore ascribed to the concerted two-electron oxidation of the $Cu^{II}Cu^{II}$ complex to the $Cu^{III}Cu^{III}$ complex. This is supported by the molecular orbital calculations and EPR spectroscopy discussed above, that show both SOMO and SOMO−1 are metal-based orbitals; as such, metal-based redox is expected to occur before any ligand-based redox.

The two, one-electron reductions are assigned to step-wise reduction of copper, with the reduction to the mixed-valent $Cu^{II}Cu^{I}$ complex occurring at −1.47 V, and the reduction to the $Cu^{I}Cu^{I}$ complex at −1.76 V. Copper commonly adopts square-planar coordination geometries in both the +2 and +3 oxidation states, but the tetrahedral geometry is more commonly adopted in the +1 oxidation state. Reduction of one copper(II) centre to the +1 oxidation state is likely to induce geometric distortion in the associated coordination pocket, which would alter the potential at which the second copper(II) centre is reduced. Oxidation to copper(III) is likely to be concerted due to the lack of geometric distortion on the assumption of that oxidation state.

Due to the high intrinsic resistance of THF during electrochemical measurements, the voltammogram for **13a** was remeasured in DMF, using a glassy-carbon disc working electrode (Figure 4.6 (a)). The electrochemical behaviour is identical to that discussed above, but the redox potentials are different. At 100 mV s^{-1}, **13a** undergoes quasi-reversible oxidation at E_p^a −0.26 V and two quasi-reversible reduction processes at E_p^c −1.18 V and −1.43 V. Based on the measured redox

potential for **13a**, Ag[BPh$_4$] would be a suitable oxidant to chemically affect the Cu(III)/Cu(II) oxidation, and CoCp$_2^*$ would be a suitable reductant to isolate the Cu^{I}Cu^I complex. [25]

(a)   (b)
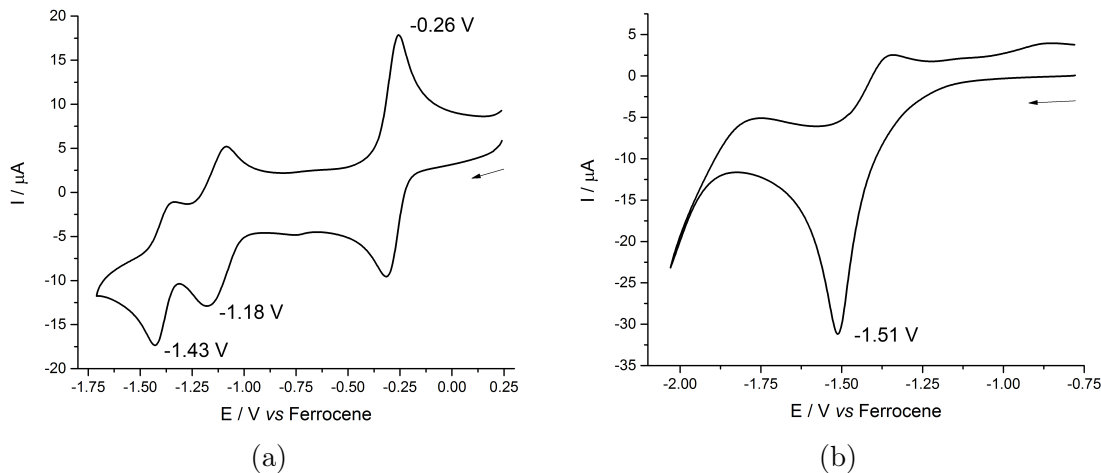
Figure 4.6: Cyclic voltammograms of (a) **13a** and (b) **13b**. Both measured at 100 mV s^{-1} on a glassy-carbon working electrode. **13a** was measured in 0.1 M [^{n}Bu$_4$N][PF$_6$] in DMF, whereas **13b** was measured in 0.1 M [^{n}Bu$_4$N][BF$_4$] in CH$_2$Cl$_2$.

Unlike **13a**, **13b** does not undergo any oxidation processes in the electrochemical window provided by CH$_2$Cl$_2$ and [^{n}Bu$_4$N][BF$_4$]. Only an irreversible reduction wave is observed at E_p^c -1.51 V *versus* ferrocene (Figure 4.6 (b)), and no associated oxidation features were observed on the return scan, even at faster scan-rates up to 500 mV s^{-1}. In the case of **13b**, the Cu(II)/Cu(I) reduction appears at a single potential, which may be a result of the more rigid anthracenyl spacer-groups preventing any significant geometric distortion in the coordination pockets following reduction of copper(II). In comparison, the anthracenyl-bridged, *meso*-disubstituted copper(II) Pacman complex also undergoes irreversible, metal-centred reduction,[20] but the metal-centred reduction in the diamagnetic cobalt(II) analogue is quasi-reversible.[14] It might be that the electronic communication between the two paramagnetic copper(II) centres, as evidenced by EPR spectroscopy, is responsible for the irreversibility of the Cu(II)/Cu(I) reduction. In contrast, electronic isolation of the metal centres, as in the case of **13a**, renders the electrochemical redox behaviour more reversible, and makes complexes of the bowl-conformation better suited to electro-catalysis.

4.1.3   Chemical redox reactions of 13a

Chemical oxidation of **13a** was carried out with two equivalents of Ag[BPh$_4$], in an attempt to isolate the Cu^{III}Cu^{III} complex, [Cu$_2$(L^3)][BPh$_4$]$_2$. Whilst Ag metal

did precipitate from the reaction mixture, indicating successful oxidation, the reaction did not proceed cleanly, and the NMR spectra of the crude material contained many resonances. However, the diamagnetism of the product does offer some proof that the d^9 copper(II) centres had been oxidised, rather than the dipyrromethane unit of the ligand. Unfortunately, single crystals for X-ray crystallography could not be obtained.

Chemical reduction of **13a** was achieved with two equivalents of $CoCp_2^*$, affording the diamagnetic Cu^ICu^I complex, $[Cu_2(L^3)][CoCp_2^*]_2$. Unlike the oxidation reaction, the chemical reduction proceeded cleanly, and a single product was observed by ^1H NMR spectroscopy in C_6D_6, with the imine protons appearing as a single resonance at 9.06 ppm, and the *meso*-protons also appearing as a single resonance at 6.72 ppm. The diamagnetism of the product again supports metal-centred reduction, with the formation of a d^{10} copper(I) complex. This copper(I) complex has been characterised by NMR spectroscopy only, and its chemical reactivity has not been explored.

A number of attempts were made to oxidise the dipyrromethane in **13a**, using oxidants such as DDQ and H_2O_2. However, the formation of a large number of products was implied by thin-layer chromatography (TLC), and no peaks consistent with the desired bimetallic copper(II) dipyrrin macrocycle were observed by ESI-MS. Despite a report by Sessler of a macrocyclic palladium(II) dipyrromethane complex being oxidised to the corresponding palladium(II) dipyrrin using $VOCl_3$ (which included chloride transfer to maintain the +2 oxidation state on palladium),[26] the reaction between $VOCl_3$ and **13a** did not proceed cleanly, and no single products could be isolated from the mixture.

It was observed that orange-brown solutions of **13a** slowly turned to very dark indigo after standing in air over the course of a few weeks, in a wide range of solvents including benzene, THF, acetonitrile and CH_2Cl_2. Some single crystals were isolated from a concentrated benzene solution, and the solid-state structure of this indigo-coloured compound was determined by X-ray crystallography.[iv] The X-ray crystal structure reveals that the product of the slow, aerobic oxidation of **13a** is the desired bimetallic copper, macrocyclic-dipyrrin complex, **14** (Figure 4.7). Interestingly, the macrocycle adopts the Pacman-configuration in **14**, and represents a switching of geometry from the bowl-conformation in **13a**; the extended π-conjugation of the dipyrrin means that the *meso*-position cannot be located at the hinge, due to the increased rigidity. The bond angles around the

---

[iv]The crystals were grown, and the structure determined by Nico Giordano, during the course of a collaboration with Prof. Simon Parsons, investigating the interactions between **13a** and O_2 or peroxides through high-pressure crystallography.

meso-carbons are planar, summing to 360°.

In the asymmetric unit of the crystal structure, there are two distinct molecules of **14**. Each molecule of **14** has a hexane solvent molecule located within the macrocyclic cleft, at slightly different orientations, and at distances of approximately 4 Å. At 4.052(1) and 4.1706(8) Å, the internuclear Cu···Cu separation in **14** is much shorter than that found in **13a** (6.493(6) Å), but longer than other copper(II) Pacman complexes, where separations of 3.5 to 4.0 Å are more common.[8] In comparison with other, *ortho*-phenylene bridged macrocycles, the bite angles of 62.4° and 66.5° in **14** are slightly wider than previously reported Pacman complexes of the transition metals, which typically span the range 45° – 62°.[8] The twist angles of 18.1° and 21.9° exhibited by **14** are typical for Pacman complexes.
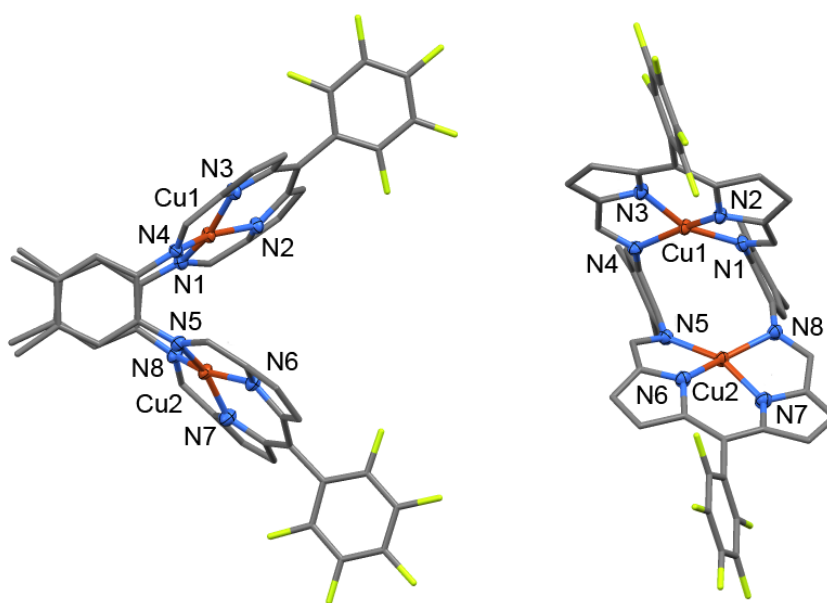
Figure 4.7: Orthogonal views of the solid-state structure of **14**. Displacement ellipsoids are drawn at 50 % probability and for clarity, one benzene and two hexane solvent molecules have been omitted, and only one macrocycle out of two in the asymmetric unit is shown.

There is some ambiguity in terms of the copper oxidation state in **14**. The complex is clearly charge-neutral due to the absence of non-coordinating anions or cations in the asymmetric unit. Such a charge-neutral complex could be described as either: two copper(I) centres coordinated by a closed-shell, mono-anionic dipyrrin ligand; or alternatively by two copper(II) centres coordinated by a radical, dianionic ligand. There is some distortion in the copper coordination geometries, with neither centre residing in strict square-planar coordination geometries, which supports the former assignment to some extent. The sum of the equatorial bond angles in **14** lie in the range 364° – 366°, whilst the *trans* N-Cu-N angles lie

between 155.5° and 159.9°.
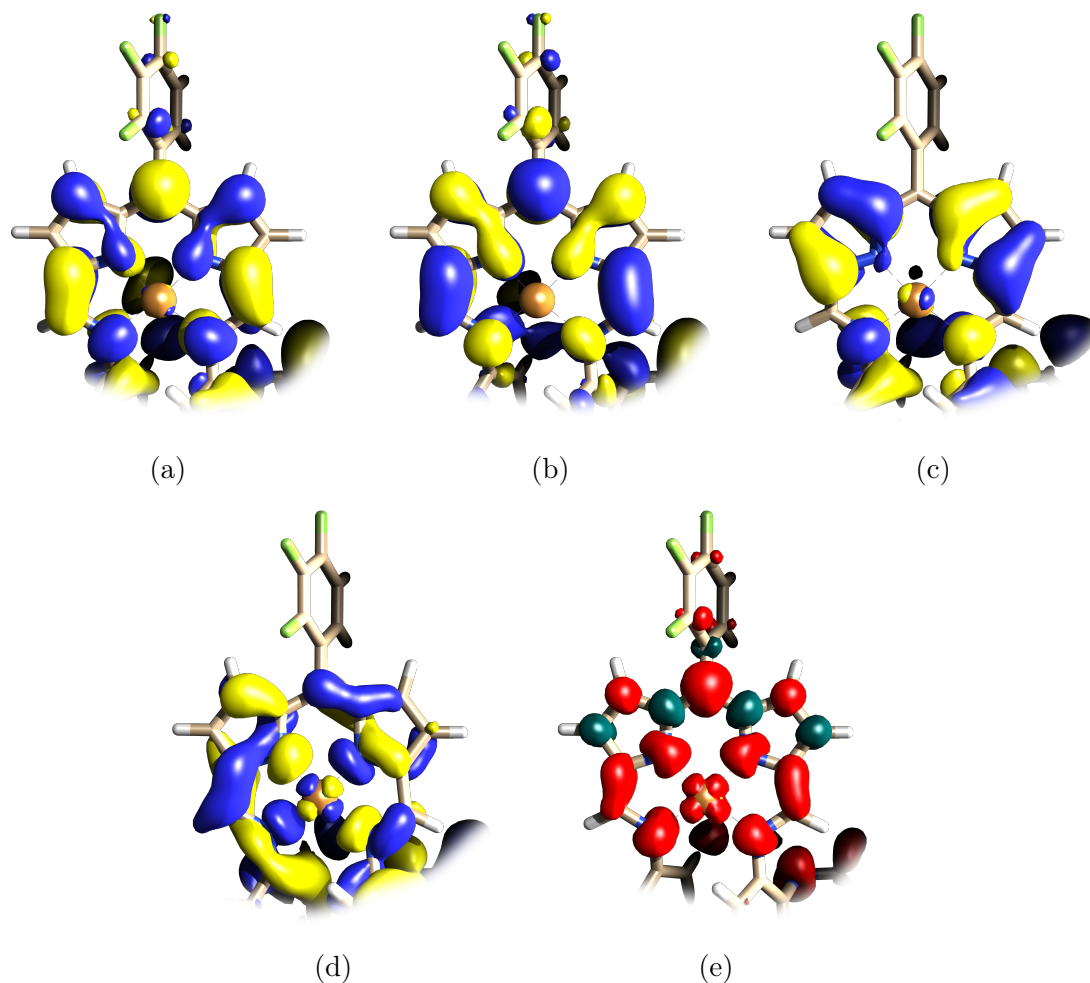
Figure 4.8: (a) SOMO (highest energy); (b) SOMO−1; (c) SOMO−2; (d) SOMO−3; and (e) overall spin-density for **14** in the quintet spin-configuration. Calculated using CAM-B3LYP/ 6-31G(d,p) with GD3BJ empirical dispersion correction. Viewed downwards from the top of the coordination pocket, with the second pocket clipped for clarity.

On the other hand, **14** is paramagnetic and NMR silent, meaning that the former, closed-shell electron configuration is not possible. Using the X-ray crystal structure as a starting point, the geometries of **14** in the singlet and quintet spin-states were optimised, using the CAM-B3LYP functional and 6-31G(d,p) basis set; the GD3BJ empirical dispersion correction was also applied. Comparing the free energies of the two structures, the quintet spin-state is indeed more stable by 19.08 kcal mol^{-1}. The spin-density of the quintet structure is spread over the donor-expanded dipyrrin manifold as well as the $d_{x^2-y^2}$ orbitals on the two copper centres, further supporting the $+2$ oxidation state on copper and the radical nature of the macrocyclic ligand. The four SOMOs of **14** are non-degenerate, and the d-orbital on copper makes only a minor (7 %) contribution

to the lowest-energy SOMO-3; the higher energy SOMOs are all predominantly ligand-based. Unfortunately, such small amounts of the complex were isolated in crystalline form that this predicted electronic structure cannot be confirmed through magnetometry, electrochemistry or EPR spectroscopy.

Many attempts were made to rationally synthesise **14** on a preparative scale for further characterisation, without success. These attempts included: stirring a benzene solution of **13a** in air, at room temperature and under reflux, for 20 days; sparging a benzene solution of **13a** with air for 7 days at room temperature; and stirring a benzene solution of **13a** in air under a UV lamp for 3 days. TLC implied that all of these reactions formed some indigo-coloured product, and those products were isolated from the crude reaction mixtures using column chromatography. However, the yields of the isolated material was minuscule in each case and the products from each reaction produced no macrocyclic signals in the ESI mass spectrum.

4.2 Synthesis of iron(II) complexes

4.2.1 Macrocyclic, dinuclear iron(II) complexes

In Chapter 3, it was shown that high-nuclearity zinc(II) complexes of L^3 and L^4 could be obtained using a zinc-alkyl starting material instead of zinc-silylamide. Similar, tetranuclear complexes of iron(II) were targeted using the iron(II) *neo*-silyl starting material, $Fe\{CH_2(SiMe_3)\}_2(Py)_2$, which was prepared *in situ* according to Scheme 4.2.[27] A tetranuclear complex of iron(II) should exhibit interesting reactivity due to the range of accessible oxidation states of iron, which includes the 0 oxidation state. The small internuclear separation of these metal centres in the macrocyclic setting might facilitate multi-electron reduction of bound substrates, conceivably even N_2 given the literature precedent of nitrogen fixation by molecular iron complexes.[28–32]

Addition of an excess of $Fe\{CH_2(SiMe_3)\}_2Py_2$, six molar equivalents, to either H_4L^3 or H_4L^4 afforded red solids that were paramagnetic and NMR-silent (Scheme 4.2). The products were incredibly sensitive to both air and moisture, turning black instantly in air, or slowly in a N_2-atmosphere glove box. The sensitivity of the complexes has precluded their characterisation by mass spectrometry and elemental analysis, and determination of their solid-state structures was also difficult, as large red crystals of either complex rapidly turned black under Fomblin oil in air. However, the solid-state structures for both complexes were ultimately determined by X-ray crystallography, and this revealed that for both macrocycles,
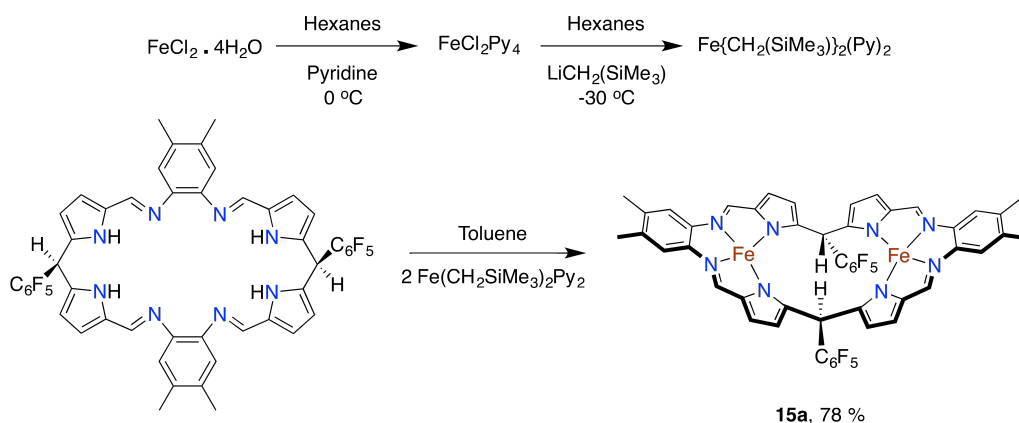
Scheme 4.2: Top: synthesis of Fe{CH$_2$(SiMe$_3$)}$_2$Py$_2$, an Fe(II) transfer-reagent.[27] Bottom: synthesis of **15a** as a representative scheme for the synthesis of both **15a** and **15b**.

addition of excess Fe{CH$_2$(SiMe$_3$)}$_2$Py$_2$ to H$_4$L^3 or H$_4$L^4 affords the bimetallic complexes, Fe$_2$(THF)$_3$(L^3) (**15a**) and Fe$_2$(Py)$_2$(L^4) (**15b**), respectively.

In the crystal structure of **15a**, the macrocycle adopts the bowl-conformation (Figure 4.9). There are two inequivalent iron(II) centres, with Fe1 coordinated to two axial THF solvent molecules in a pseudo-octahedral coordination geometry, and Fe2 coordinated to one exogenous, axial THF molecule in a pseudo-square pyramidal coordination geometry. The equatorial macrocycle donor-atoms form a planar arrangement around Fe1, with the equatorial bond angles summing to 360.26°. In comparison, the equatorial bond angles around Fe2 sum to 355.71° and appears to be the result of the single THF ligand pulling that ion away from its idealised position. Whilst the Fe2-O3 bond distance of 2.137(1) Å is similar to the Fe2-N bond distances (2.121(1) – 2.175(2) Å), the Fe1-O1 and Fe1-O2 bond distances of 2.226(1) Å and 2.31(2) Å are longer, which is most likely due to a Jahn-Teller distortion in the octahedral coordination geometry.

The internuclear Fe···Fe distance for **15a** is 6.062(1) Å, which is shorter than that found for the copper(II) analogue discussed above (6.493(6) Å) and is presumably due to the incorporation of fewer coordinated solvent molecules within the cleft in the case of the former. This is also reflected by the more narrow bite angle of 126.5° between the two coordination compartments, compared to the 152° bite angle found in the copper(II) analogue. The torsional twist between the two pockets is also less pronounced in **15a**, at 16.0°, which was measured at 24.8° for **13a**.

For the refined structure of **15b**, the R-factor is quite high at 12.5, but the two macrocycles in the asymmetric unit (**15b** and **15b'**) were both modelled fairly well with anisotropy (Figure 4.10). The cause of the high R-factor seems to be

Figure 4.9: Solid-state structure of **15a**. Displacement ellipsoids are drawn at 50 % probability and for clarity, modelled disorder on one THF molecule has been omitted, and only the *meso*-protons are shown.

the five THF solvent molecules that could not be adequately modelled even with imposing many restraints. As the molecules of interest were modelled well, their bond metrics will be reported and discussed despite the R-factor. Both iron(II) centres in the anthracenyl-Pacman complex reside in distorted square-pyramidal coordination geometries (sum of equatorial bond angles are 355°), with coordinated pyridine molecules taking up the axial coordination sites, exogenous to the cleft. All of the Fe-pyridine bond distances lie in the range of the Fe-N bond distances with the macrocycle (2.04(1) Å – 2.19(1) Å), and coordination of pyridine pulls the iron centres out of the N_4-donor planes, by 0.301 – 0.417 Å. Although the twist angles between the anthracenyl spacer-groups and the N_4 coordination pockets are similar to that for **13b** (35° for **15b** compared with 30° for **13b**), coordination of pyridine to the iron(II) centres increases the internuclear separation to 5.702(3) Å (**15b**) and 5.748(3) Å (**15b'**), compared with 4.818(3) Å for **13b**.

The two non-equivalent molecules of **15b** in the asymmetric unit are located with a close-contact of 3.95(2) Å between the anthracenyl spacer-groups of the two non-equivalent molecules. These molecules are facing the same way, which appears to be an effect of packing in the crystal structure. Inside the unit cell there are a total of four molecules of **15b**, generated by the inversion-symmetry operator in the P$\bar{1}$ space group, and these are arranged such that the polar C_6F_5-groups are all located in the centre of the unit cell along with the majority of the THF solvent molecules, with intermolecular $C \cdots F$ and $F \cdots F$ distances around 3.2 Å. Arranged in this way, the anthracenyl-groups for each molecule pack in an alternating manner with those of the neighbouring unit cells, with intermolecular $C \cdots C$ distances typically 3.8 Å (Figure 4.11).

Red, single crystals isolated from one attempted synthesis of **15b** were deter-

Figure 4.10: Orthogonal views of the solid-state structure of **15b**. Displacement ellipsoids are drawn at 50 % probability and for clarity, five disordered molecules of THF solvent have been omitted, only one of two molecules of **15b** in the asymmetric unit are shown, and only the *meso*-protons are shown.
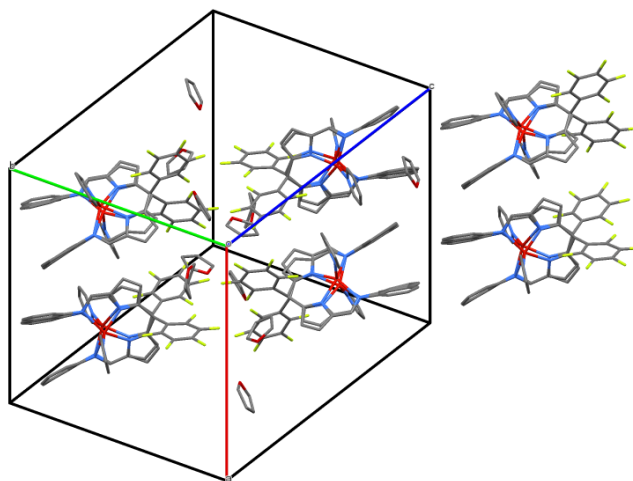
Figure 4.11: Packing arrangement in the solid-state structure of **15b**, showing the full unit cell and two molecules of **15b** from a neighbouring cell.

mined by X-ray crystallography to be the μ-hydroxo-bridged bimetallic complex, $[Fe_2(\mu-OH)(L^4)][Li(THF)_4]$ (**16**, Figure 4.12), which seems to have formed from the reaction of **15b** with a small amount of adventitious water. This complex is mono-anionic, evident from the single tetrahedral $[Li(THF)_4]^+$ counter-ion present within the asymmetric unit; the source of lithium is most likely LiCl from the *in situ* formation of the iron-alkyl transfer reagent. Formally, this implies that either the complex is a mixed-valent iron(II)/iron(III) complex with a bridging μ-oxo ligand, or it is an iron(II)/iron(II) complex with a bridging μ-hydroxo ligand. Due to the poor quality of the crystal and low resolution of the data that was collected, it is not possible to differentiate between a bridging hydroxo- or oxo-ligand crystallographically. Furthermore, **16** was only isolated as a small

amount of single crystals, meaning that further characterisation could not be carried out. However, in terms of describing the formation of **16** using a balanced chemical equation, a hydroxo-complex seems most reasonable:

$$\text{Fe}_2(\text{L}^4) + \text{H}_2\text{O} + \text{LiCl} \longrightarrow [\text{Fe}_2(\mu-\text{OH})(\text{L}^4)][\text{Li}] + \text{HCl} \qquad (4.2)$$
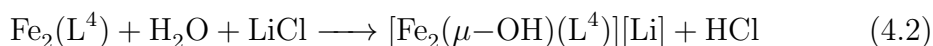
Although the quality of the X-ray crystallographic data for **16** is poor, some geometric attributes will be discussed. The inclusion of the assumed bridging-hydroxide ligand between the two metal centres results in an internuclear separation of approximately 4 Å, which is short compared to the structures of **15b** and **13b**. In comparison, a previously reported bimetallic zinc(II) complex of the anthracenyl-bridged Pacman ligand, which features two ethyl *meso*-substituents, coordinates anionic ligands between the two metal centres within the cleft. In those zinc(II) complexes, incorporation of the hydroxide anion, to give $[\text{Zn}_2(\text{OH})(\text{L}^{\text{A}})]^-$ resulted in an internuclear separation of 3.87 Å, which increased with the incorporation of larger anions, such as chloride (r, $\text{Zn}\cdots\text{Zn} = 4.53$ Å).[16] The Fe-O-Fe bond angle in **16** is fairly linear at *ca.* 160° and the coordination of the hydroxide ligand has the effect of distorting the macrocyclic coordination pockets considerably; the sum of equatorial bond angles around iron(II) in the N_4-donor set is approximately 330°, and with the pyrrole groups pointing into the cleft of the macrocycle, the coordination compartments are more reminiscent of calix[4]pyrrole ligands rather than porphyrins.[33,34] Due to the bridging hydroxo ligand enforcing a more rigid Pacman-geometry, the twist angle is negligible for **16**, with the anthracenyl groups and N_4-donor planes practically orthogonal. Finally, the hydroxo O-atom and the endogenous *ortho*-F atoms of the C_6F_5 groups are separated by only 3 Å, suggesting that there is a hydrogen bond interaction between the hydroxide and *meso*-substituents.

Figure 4.12: Orthogonal views of the solid-state structure of **16**. Displacement ellipsoids are drawn at 50 % probability and for clarity, only the *meso*-protons are shown, and in the side-on view (left), the $[\text{Li}(\text{THF})_4]^+$ moiety has been omitted.

Interestingly, the anhydrous synthesis of **15b** results in both molecules in the asymmetric unit adopting the *syn-exo* isomer, with the C_6F_5 *meso*-substituents pointing away from the cleft of the macrocycle. In comparison, adventitious water present during synthesis means that **16** crystallises as the *syn-endo* isomer only, even though the more constrained geometry in that complex leads to a shorter distance between the two C_6F_5 groups. Because of the rigidity of the macrocycle, imposed by the anthracenyl spacer-groups, an *endo/exo* isomerisation is not likely, and so **15b** must exist as a mixture of the *syn-endo* and *syn-exo* isomers.

4.2.2 Iron(II) complexes of a donor-expanded dipyrrin

Coordination of iron(II) to a mono-anionic dipyrrin ligand means that an ancillary ligand is required on iron to maintain a charge-neutral complex. This opens up the possibility to explore reactivity that is not possible with the coordinatively saturated dipyrromethane congeners. For example, alkyl ligands would provide a reactive Fe-C bond that could be used to explore insertion chemistry of CO_2[35] or CO[36], leading to carboxylate or acyl complexes of iron, respectively. Alkyl or alkoxide ligands would also make the complex viable for catalytic reactions, including ROCOP reactions of CO_2 as discussed in Chapter 3.[37] Complexes with ancillary halide ligands also present interesting synthetic targets, as these may be reduced with alkali metal reductants, such as potassium graphite (KC_8) or sodium amalgam (Na/Hg), possibly facilitating reduction of gaseous substrates; there is literature precedent for low oxidation states of iron carrying out reduction of N_2,[28–32] CO_2,[38] and H_2.[39,40] Additionally, ancillary halide ligands may be exchanged for non-coordinating anions, such as $[PF_6]^-$, to form reactive cationic complexes with increased Lewis-acidity at the iron(II) centre. Iron(II) complexes of L^2 with ancillary alkyl and halide ligands were targeted, as shown in Scheme 4.3.
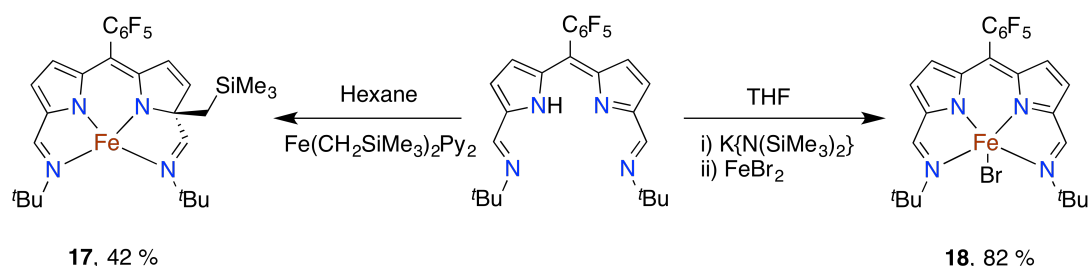
Scheme 4.3: Synthetic routes to Fe(II) dipyrrin complexes.

Attempted synthesis of an iron(II)-alkyl dipyrrin complex

The dipyrrin HL^2 was reacted with one equivalent of $Fe\{CH_2(SiMe_3)\}_2(Py)_2$ in hexanes, rapidly forming a rose-red solution with some suspended red solids. After heating this solution to redissolve these solids and allowing it to cool slowly, single crystals were grown and the solid-state structure of the product was determined by X-ray crystallography (Figure 4.13). The product from this reaction, $Fe(Py)(L^2CH_2SiMe_3)$ (**17**), is an iron(II) dipyrromethene complex, but unexpectedly, the *neo*-silyl group has carried out nucleophilic attack at the pyrrole α-position (C20), adjacent to the imine substituent in the ligand framework. Addition of the *neo*-silyl group at the pyrrole α-position means that the extended π-conjugation is disrupted, and C20 is clearly tetrahedral (bond angles range from $113.7(2)°$ to $104.4(2)°$). However, the *meso*-carbon remains trigonal planar. No other ions were found in the asymmetric unit, meaning that the ligand now acts as an asymmetric, dianionic dipyrromethene (referring to this ligand as a dipyrrin is not appropriate here due to the unusual electronic structure). Whilst the radical dipyrrin ligands found in the macrocyclic copper(II) complex **14** and the reduced uranyl complex $[\mathbf{21}^{\cdot-}][CoCp_2]$ (Chapter 6) are formally dianionic, there are no examples of dianionic, closed-shell dipyrromethene ligands in the literature.
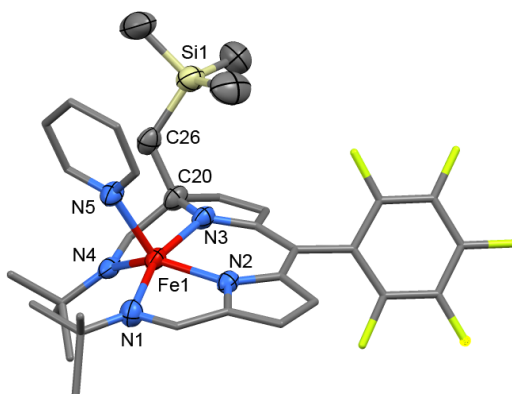
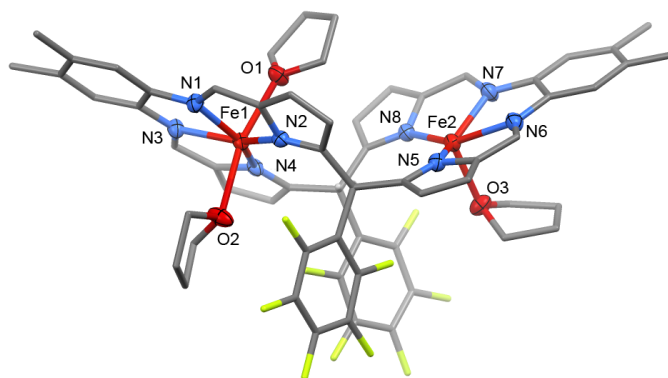
Figure 4.13: Solid-state structure of **17**. Displacement ellipsoids are drawn at 50 % probability and for clarity, all protons and one hexane solvent molecule have been omitted.

Reactions between porphyrins and butyl-lithium have been reported to result in nucleophilic attack of the butyl anion, but this occurs at the *meso*-position rather than at the already-substituted pyrrole α-position.[41] Similarly, the nucleophilic attack at C20 in complex **17** to form an α,α-disubstituted pyrrole group is a novel form of reactivity for dipyrrin complexes, but is not without precedent in pyrrole chemistry in general. An *N*-alkylated, α-formyl pyrrole forms an α,α-disubstituted pyrrole on reaction with $POCl_3$ and NaOAc, by migration of the alkyl (Scheme

4.4, left).[42] Furthermore, pyrrole substituted at the α-position by an aryl group also yields the α,α-disubstituted pyrrole on reaction with trichloroacetyl chloride and K_2CO_3 (Scheme 4.4, right).[43]
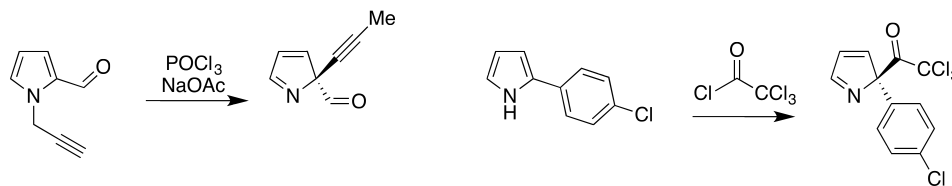
Scheme 4.4: Literature examples of synthesis of α,α-disubstituted pyrroles.[42,43]

With the inclusion of a pyridine ligand, the five-coordinate iron(II) centre in **17** resides in an irregular coordination environment, which is perhaps best described as a heavily distorted square-pyramidal geometry. Due to the distortion in the N_4-donor set in the dipyrrin ligand, one of the imino-N donors (N4) is located 1.411 Å from the plane described by the remaining dipyrrin donors. The base of the square-pyramidal coordination geometry (N1 – N4) is therefore tilted, at 22.81°, in comparison with the planar portion of the dipyrrin ligand. The Fe-pyridine bond is practically perpendicular to the base of the square-pyramid, at 86.95°, and the iron(II) centre is located 0.406 Å from the base.

Attempts were made to isolate the iron-alkyl dipyrrin complex at lower temperatures, in case the nucleophilic attack on the dipyrrin by the *neo*-silyl ligand was brought about through heating during crystallisation. However, no crystalline material could be isolated through room-temperature crystallisation attempts. The *in situ* synthesis of the iron-alkyl dipyrrin complex was also carried out at room temperature, and then heated under separate atmospheres of 2 bar CO and 2 bar CO_2, as it was thought that the insertion reaction might occur before nucleophilic attack on the dipyrrin. Unfortunately, no crystalline materials were isolated from either of these reactions after slow-cooling of the solutions.

Due to the strong paramagnetism at the iron(II) centre, structural information on the alkyl-dipyrrin complex, **17** or its possible insertion products could not be obtained using NMR spectroscopy.

Synthesis of an iron(II)-halide complex

A salt-metathesis procedure was implemented to prepare the bromo-iron(II) dipyrrin complex, $FeBr(L^2)$ (**18**). Deprotonation of HL^2 was carried out using $K\{N(SiMe_3)_2\}$, immediately turning the orange THF solution of HL^2 magenta. The potassium salt KL^2 was not isolated, but was added directly to $FeBr_2$, rapidly

forming a dark blue solution. After filtration and slow evaporation of the solvent, yellow crystals formed and the solid-state structure was determined by X-ray crystallography (Figure 4.14).
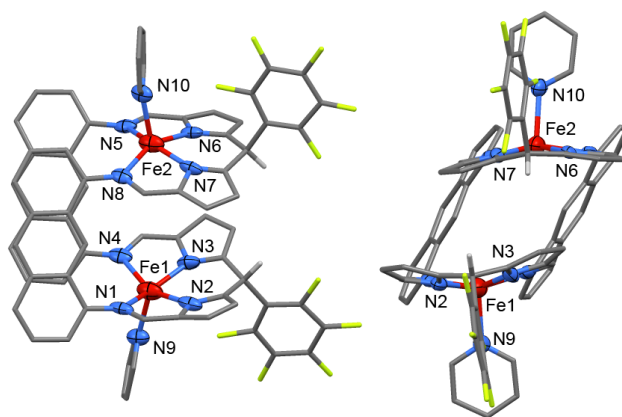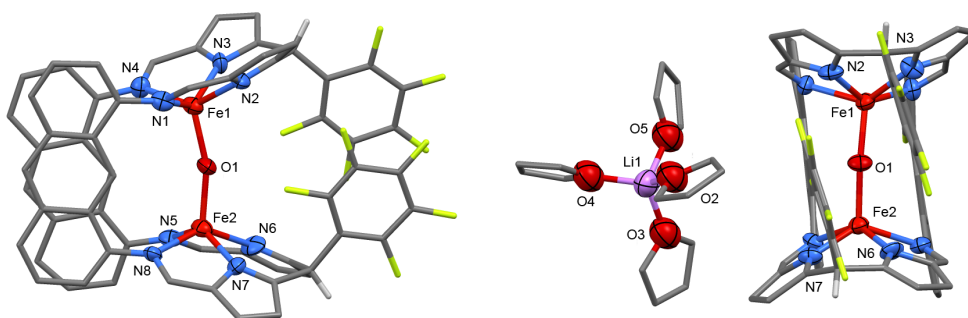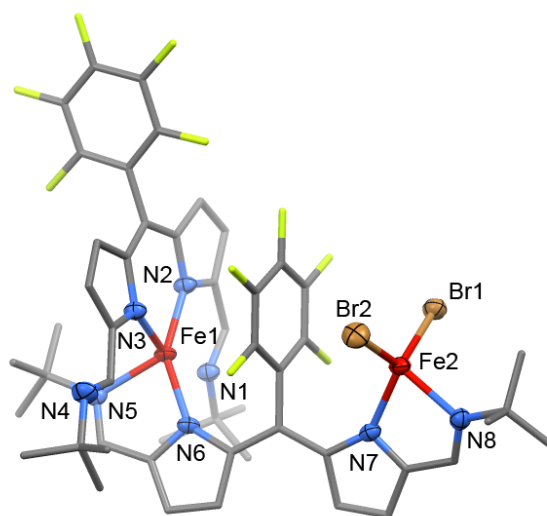

Figure 4.14: Solid-state structure of **18**. Displacement ellipsoids are drawn at 50 % probability and for clarity, all protons, one THF solvent molecule, and modelled disorder on one *tert*-butyl group have been omitted.

It was found that in the crystal structure, **18** exists as a dimeric species that is the result of significant ligand rearrangement and redistribution. One iron(II) centre (Fe1) is coordinated by the two pyrrolide N-donors from one dipyrrin ligand. The imine N-donors from this dipyrrin do not coordinate the iron centre, as one of the imine groups (that includes N4) is rotated away and excluded from the coordination pocket, whilst the second imine group (that includes N1) points towards Fe1 but is located 2.502(5) Å away from the metal centre, which is greater than the sum of ionic radii of iron(II) and nitrogen (2.24 Å) and indicates only a weak interaction. Fe1 is also coordinated by one imino-pyrrolide N_2-donor set from a second dipyrrin ligand. This latter dipyrrin has an unusual geometry at the *meso*-position, in that both pyrrolide groups point towards the C_6F_5 substituent; the second N_2-donor set of this ligand is formally charge neutral and chelates an $FeBr_2$ unit. Whilst this structure does formally have the formula $\{FeBr(L^2)\}_2$, its formation requires considerable rearrangement from the presumed monomeric solution-state structure, including breaking of π-conjugation and rotation of one dipyrrin ligand, and ligand-scrambling between the two iron(II) centres. Whilst the solution-state structure has not been determined by NMR, due to the paramagnetic nature of the complex, the fact that it forms blue-coloured solutions in both polar and non-polar solvents, and is yellow in the solid state suggests very different

structures in the dipyrrin chromophore.

The two iron(II) centres in the dimeric form of **18** are not only coordinated by different ligand sets, but also reside in different coordination geometries. The two bromide ligands and two N-donors from the dipyrrin provide a tetrahedral coordination sphere around the four-coordinate Fe2 centre, where the bond angles are between 122.52(4)° and 80.0(2)°. In contrast, the four-coordinate Fe1 centre is in a distorted trigonal pyramidal coordination geometry, with N2, N5 and N6 occupying the basal positions, and N3 occupying the apical position. In comparison to the long Fe1$\cdots$N1 distance, the bond distances between Fe1 and its other coordinated nitrogen atoms are between 2.006(4) Å and 2.223(5) Å, where the longest bond distance is between Fe1 and N3, a pyrrolide donor.

4.3 Synthesis of nickel(II) and palladium(II) complexes

The bimetallic nickel(II) complex $Ni_2(L^3)$ (**19**) was first prepared from the reaction of H_4L^3 with two equivalents of $Ni(OAc)_2$, in either CH_2Cl_2, THF or MeCN. A red fraction was isolated after passing the crude product mixture through alumina, using CH_2Cl_2 as the eluent, and this fraction was found to contain **19** in low yields of up to 20 %. A molecular ion peak was observed by ESI-MS at 1050 m/z, and its isotope distribution pattern is consistent with that expected for a bimetallic nickel(II) complex. Single crystals of **19** were grown from a variety of solvent systems under various conditions, but in all cases the crystals exhibited a plate morphology, giving rise to very weak X-ray diffraction. The crystal structure for this compound has therefore not been determined.

An alternative, salt-metathesis procedure was implemented to prepare **19** in higher yields of 50 %. As for the synthesis of the copper(II) analogue, the potassium salt K_4L^3 was prepared *in situ* in THF, and then reacted with $NiBr_2(DME)$ (Scheme 4.5). The product from this reaction was also purified by flash column chromatography, as above.

The nickel(II) complex could not be characterised by NMR spectroscopy, as it was strongly paramagnetic. This is unexpected, as the two d^8 nickel(II) ions are located in loosely square-planar coordination environments, and should therefore exhibit a diamagnetic d-electron configuration. It was suspected that coordinating solvent molecules, such as THF, might occupy the axial positions; in this case, the octahedral coordination geometry would always exhibit paramagnetism with a d^8 electron configuration, having two unpaired electrons in the e_{2g} set. However, batches of **19** synthesised in the absence of coordinating solvent were
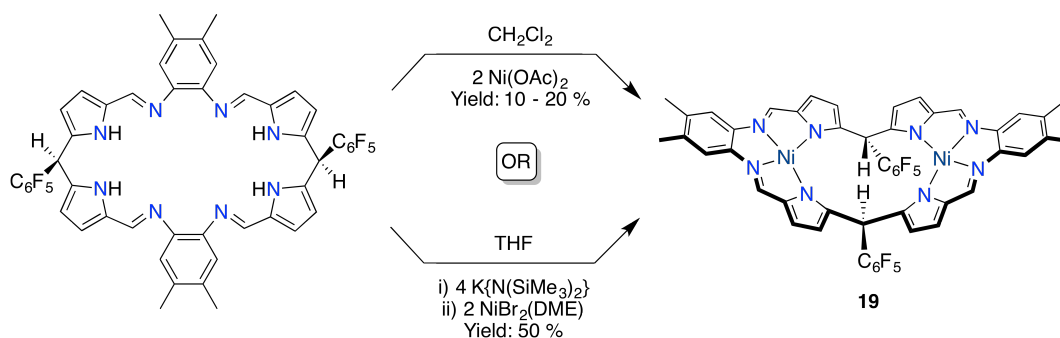
Scheme 4.5: Synthetic routes to the dinuclear nickel(II) complex, **19**.

also paramagnetic. A plausible explanation for this would be if the coordination pockets are equatorially distorted around the nickel(II) centres, in which case the crystal-field splitting of the *d*-orbitals would be somewhere between square-planar and tetrahedral, encouraging a paramagnetic electron configuration.

A bimetallic palladium(II) complex, $Pd_2(L^3)$ (**20**), was also synthesised, from the reaction of H_4L^3 with $Pd(OAc)_2$ in THF (Scheme 4.6). As for the nickel(II) complex, **20** was also isolated by column chromatography, eluting the product as a red fraction with CH_2Cl_2. However, for the palladium complex, the use of the acetate starting material resulted in the product being formed in an acceptable yield of 56 %. In contrast to the nickel(II) complex, **20** is diamagnetic, and was successfully characterised by NMR spectroscopy. In $CDCl_3$, the ^1H NMR spectrum of **20** is consistent with a symmetric macrocyclic product, with a single set of ligand resonances; the imine protons appear at 7.30 ppm, and the *meso*-proton appears at 6.43 ppm.
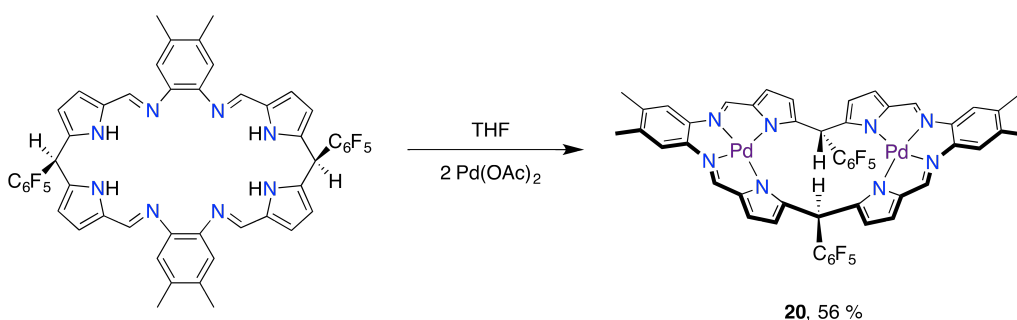
Scheme 4.6: Synthesis of the dinuclear palladium(II) complex, **20**.

Single crystals were grown by slow vapour-diffusion of hexanes into a THF solution of **20**, and although they also appeared as thin plates, the X-ray diffraction was intense enough for the structure to be determined crystallographically. However, the collected data was quite poor, and refinement became unstable when the structure was modelled with anisotropy and calculated proton positions.

Therefore the atom positions in the structure have been modelled isotropically.
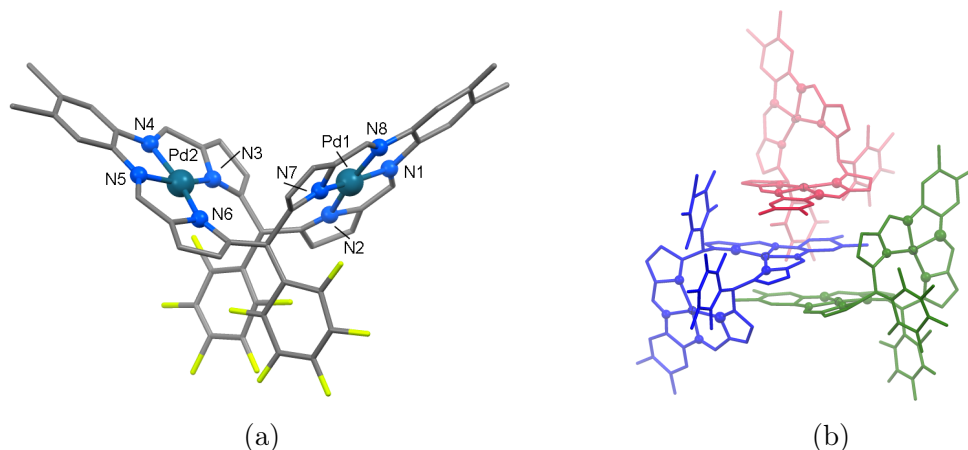
Figure 4.15: Solid-state structure of **20**, showing (a) a single molecule and (b) the helical stacked trimer in the asymmetric unit. The structure has been refined isotropically and without modelled protons.

The crystal structure (Figure 4.15) reveals that the macrocycle in **20** adopts the bowl conformation, much like its copper(II) and iron(II) congeners. However, in this case, there are no coordinating solvent molecules within the macrocycle cleft, and **20** therefore exhibits an interesting crystal packing arrangement. In the asymmetric unit, three molecules of **20** are arranged in a helical, π-stacked trimer, where one planar N_4-coordination pocket from each molecule is situated approximately 3.3 Å from its neighbour in the trimer. The second N_4-coordination pocket in each molecule of **20** also contributes to other trimers in adjacent asymmetric units. Considering the three coplanar coordination pockets in one π-stacked trimer, they describe a short left-handed (M) helix, although there is no helicity extending from this trimer with other symmetry-generated trimers within the expanded crystal structure.

4.4   Electrochemical CO_2 reduction

Many of the complexes that have been discussed in this chapter were tested for their activity as catalysts for the electro-catalytic reduction of CO_2. Cyclic voltammetry is a useful technique for assessing the electrochemical reactivity of redox-active compounds towards CO_2, and can be used both to identify electro-catalytic activity in initial screenings, as well as for more in-depth measurements to determine kinetic information, such as the turnover frequency.[44] Due to the high sensitivity of the technique, only small amounts of the analyte are required. Suitable proton sources for the proton-coupled electron-transfer reaction between

the complex and CO_2 substrate can also be determined using CV, before bulk electrolysis is performed. Ideally, the complex should display Nernstian redox-behaviour during the cyclic voltammetry experiment, which would imply that both the oxidised and reduced forms are stable during turnover, limiting catalyst deactivation. Addition of a proton source in the absence of CO_2 should leave the voltammogram unchanged, and this would indicate that the competing proton-reduction reaction to H_2 is minimised. Finally, sparging the solution with CO_2 should lead to a large increase in the peak current for the reduction wave of the complex, which would indicate electro-catalysis. For this experiment, DMF is the ideal solvent due to its low intrinsic resistance and the high solubility of CO_2 in that solvent (0.20 – 0.23 M at saturation).[45,46] Furthermore, Pt-electrodes should be avoided due to their propensity to carry out heterogeneous proton-reduction.

In the case where a complex appears, qualitatively, to have high electro-catalytic activity, further analysis can be performed to gain more quantitative information. Foot-of-the-wave analysis is a technique that can provide estimates for the catalytic rate constant (k / M^{-1} s^{-1}) and the turnover frequency (TOF / M^{-1} s^{-1}) from a single CV measurement, without performing a lengthy series of bulk-electrolysis experiments.[44] Firstly, the voltammogram for the catalyst without the substrate is measured, and the peak-current for the relevant redox couple (i_P^0 / A) accounts for many parameters that are difficult to determine individually, such as the real surface area of the electrode (S / cm^2) and the concentration of the active form of the catalyst near the electrode surface (C_P^0 / $mol\,cm^3$). The Randels-Sevcik equation describes how these parameters contribute to i_P^0 (Equation 4.3[v]).

$$i_P^0 = 0.446 \times FSC_P^0 \sqrt{D_P} \sqrt{\frac{F\nu}{RT}} \qquad (4.3)$$

The current measured in the catalytic wave (i / A) is then divided by i_P^0 and plotted according to Equation 4.4.[vi] For a perfect electro-catalyst, the catalytic wave would be sigmoidal and Equation 4.4 would be linear. However, due to side-phenomena and catalyst decomposition, most catalytic waves are not sigmoidal, and plots from Equation 4.4 are only linear for the first portion of the catalytic wave. The slope from this linear foot-of-the-wave is equal to $2.24\sqrt{RT/F\nu 2kC_A^0}$,

---

[v]Other parameters not mentioned: F is the Faraday constant, 96,485 C mol^{-1}; D_P is the diffusion coefficient of the active form of the catalyst / cm^2 s^{-1}; R is the gas constant, 8.314 J K^{-1} mol^{-1}; and T is the temperature / K.

[vi]E is the applied potential / V; E_{PQ}^0 is the standard potential for the redox couple between the active form of the catalyst P and the inactive form Q.

from which the rate constant, k, can be determined.[vii]

$$\frac{i}{i_P^0} = \frac{1}{1 + \exp[\frac{F}{RT}(E - E_{PQ}^0)]}$$ (4.4)

Once the rate constant is known, the relationship between the TOF and the applied overpotential (η / V) can be determined according to Equation 4.5.[viii] Taking the log of the TOF and extrapolating the straight line back to zero overpotential gives the most important value; TOF_0. This is the intrinsic activity of the catalyst and allows it to be compared fairly with other electrocatalysts from the literature. The standard reduction potential of CO_2 to CO (in DMF, using water as a proton source) has been determined previously as -0.690 V *versus* the normal hydrogen electrode (NHE), or -1.33 V *versus* ferrocene.[46] Figure 4.16 shows idealised plots that lead to determining TOF_0 through foot-of-the-wave analysis.

$$TOF = \frac{2k}{1 + \exp[\frac{F}{RT}(E_{AC}^0 - E_{PQ}^0 - \eta)]}$$ (4.5)
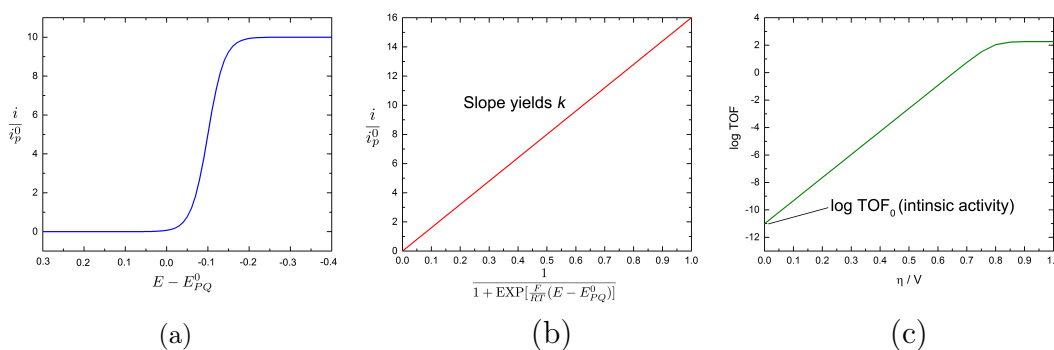
Figure 4.16: Determination of the intrinsic activity of an electro-catalyst by foot-of-the-wave analysis. Idealised plots show: (a) the catalytic wave, plotted after adjusting the current and potential to take into account the peak height and position of the catalyst in absence of the substrate; (b) the foot-of-the-wave equation (equation 4.4 in the text), which gives the rate constant from the slope; and (c) the relationship between logTOF and the overpotential, where the intrinsic catalyst activity is given by the y-axis intercept.

4.4.1   Screening of copper(II) complexes

The voltammetry for **13a** has already been discussed above. Addition of 4.6 M water to the solution of **13a** left the voltammogram mostly unchanged. There

---

[vii]ν is the scan-rate / V s^{-1}; C_A^0 is the concentration of CO_2, which is 0.23 M at saturation in DMF.

[viii]E_{AC}^0 is taken here as the standard potential for the reduction of CO_2 to CO in DMF (-1.33 V *versus* ferrocene)[46]; η is the overpotential / V ($\eta = E_{AC}^0 - E$).

was a slight cathodic shift of the peak potentials for all processes (*ca.* 50 to 100 mV), and some loss of the current for the return Cu(III)/Cu(II) reduction wave (3 μA, 25 %). In the presence of CO_2, the quasi-reversibility of the two Cu(II)/Cu(I) reduction processes is lost and there is a slight increase in the peak current at the second reduction wave (7 μA, 30 %). This is indicative of a reaction between the $Cu^I Cu^I$ complex and CO_2, but the very small current increase implies that this reaction is stoichiometric rather than catalytic (Figure 4.17 (b)). Using phenol as a stronger proton source (pK_a, phenol = 9.98; pK_a, water = 15.7)[47] did not increase the peak-current at the second reduction potential.
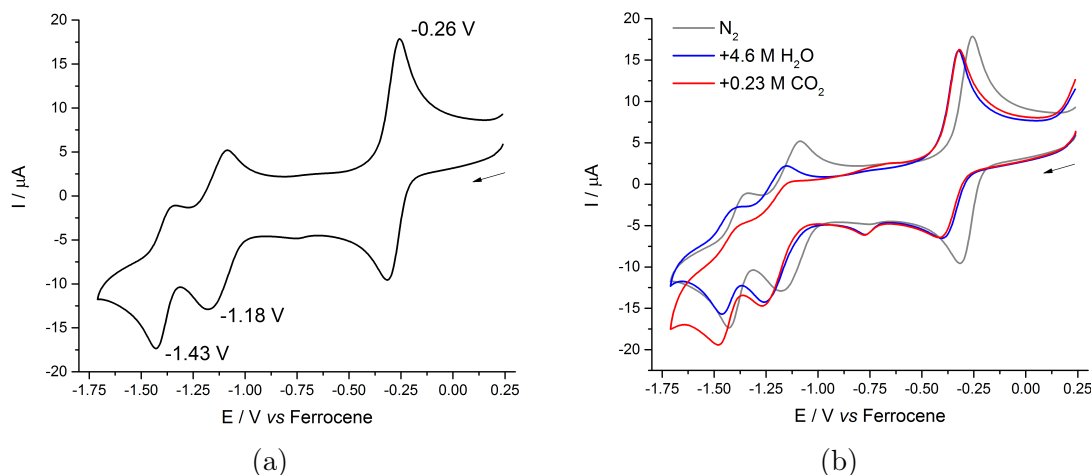
Figure 4.17: Cyclic voltammograms of **13a**, measured at 100 mV s^{-1} on a glassy-carbon working electrode in a 0.1 M [^{n}Bu$_4$N][PF$_6$] solution in DMF. (a) CV measured under N_2. (b) Overlaid CVs measured under N_2, then in the presence of 4.6 M H_2O and again after sparging with CO_2.

Despite the lack of electro-catalytic activity, a stoichiometric electrochemical reduction of CO_2 in the presence of **13a** was attempted. It was thought that this might yield a copper complex featuring a reduced CO_2 moiety, which would give useful information about the intermediates involved along the CO_2 reduction pathway. Controlled-potential electrolysis (CPE) was conducted for two hours at -1.60 V *versus* ferrocene using a reticulated vitreous-carbon (RVC) electrode, a 1 mM solution of **13a**, 5 M water as the proton source, and 0.23 M CO_2. Throughout this experiment, a gas evolved from the electrode surface, which could conceivably be either CO, from the two-electron reduction of CO_2, or H_2 from the reduction of H$^+$. Due to the lack of a suitable GC instrument, the composition of this gas has not been determined. However, the proton-coupled, two-electron reduction of CO_2 (in the absence of an electro-catalyst) occurs at -1.17 V *versus* ferrocene, and proton reduction occurs at -0.69 V. Given that the CV analysis did not indicate any catalysis was taking place, the gas evolution observed is most likely to be from heterogeneous electron-transfer from the electrode. Unfortunately, the

product of this electrochemical reaction derived from **13a** could not be cleanly isolated from the electrolyte solution, and the product could not be characterised.

4.4.2 Screening of iron(II) complexes

Screening of the bimetallic iron(II) macrocycle, 15a

An optimised DFT structure for **15a** could not be obtained, as convergence did not occur. Instead, the molecular orbital structure of **15b** was explored in order to obtain some insight into what redox processes might be expected for the macrocyclic iron(II) complexes in the CV experiment. The geometry for **15b** was optimised in a DFT calculation, using the UB3LYP functional and 6-31G(d,p) basis set, and represented the X-ray crystal structure of the pyridine adduct well. The five SOMOs for the high-spin quintet state featured a large amount of ligand-character, but the calculated spin-density reveals that the four unpaired electrons reside on the metal centres, with only minor spin-delocalisation onto the ligand (Figure 4.18). This indicates that, as for the copper(II) complexes, metal-centred redox should be expected to take place for the macrocyclic iron(II) complexes.
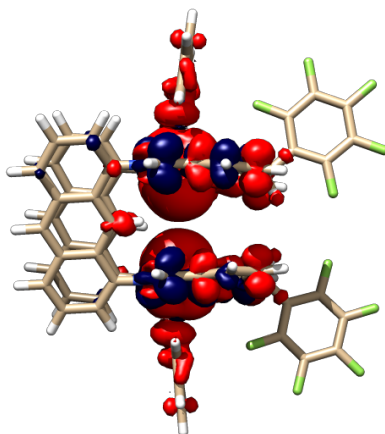
Figure 4.18: Spin-density plot of **15b**, calculated with the UB3LYP functional and 6-31G(d,p) basis set.

The cyclic voltammogram of **15a**, measured at 100 mV s^{-1} in DMF, displays a range of redox processes and reveals that there are many accessible oxidation states for iron in **15a** (Figure 4.19 (a)). Two quasi-reversible oxidation processes were observed at E_p^a -0.03 V and $+0.22$ V *versus* ferrocene and are assigned to step-wise oxidation, first forming the mixed-valent Fe^{III}Fe^{II} complex, and then the Fe^{III}Fe^{III} complex. As for the step-wise reduction of **13a**, it is assumed that

oxidation of **15a** occurs step-wise due to a geometric distortion in one coordination pocket upon oxidation of one metal, which perturbs the thermodynamics governing the second oxidation process.

An irreversible reduction was observed at E_p^c -2.27 V that is assigned to the Fe(II)/Fe(I) couple and describes the concerted, two-electron reduction to the Fe^{I}Fe^I complex. The integrated area of this peak is equal to the combined areas for both Fe(III)/Fe(II) oxidation waves, supporting a two-electron reduction. A second irreversible reduction was observed at E_p^c -2.77 V, which is assigned to the two-electron reduction of the Fe^{I}Fe^I complex to the Fe^{0}Fe^0 complex. In comparison with iron-porphyrin complexes that have displayed efficient electro-catalytic reduction of CO_2, the reduction potentials for both the Fe(II)/Fe(I) and Fe(I)/Fe(0) redox couples for **15a** are approximately 700 mV more negative.[48] Nevertheless, the accessibility of the Fe(0) oxidation state is promising in terms of reduction chemistry, and this oxidation state could be accessed chemically, using sodium naphthalenide, which has a formal oxidation potential of -2.95 V *versus* ferrocene in DMF.[25]

Figure 4.19: Cyclic voltammograms of **15a**, measured at 100 mV s^{-1} on a glassy-carbon working electrode in a 0.1 M [^{n}Bu$_4$N][PF$_6$] solution in DMF. (a) CV measured under N$_2$. (b) Overlaid CVs measured under N$_2$, then in the presence of 1 M benzoic acid, and again after sparging with CO_2. * Denotes a solvent-based impurity that is present in the background scan.

Due to the high moisture-sensitivity of **15a**, water is not a suitable proton source. Addition of anhydrous benzoic acid to the solution of **15a** left the features in the voltammogram largely unchanged, with a small increase in the peak current for the Fe(II)/Fe(I) reduction wave (10 µA). The change in the pH of the solution seems to have extended the electrochemical window in the cathodic direction by a small amount, such that the Fe(I)/Fe(0) reduction wave is more prominent. Sparging the solution with anhydrous CO_2 results in the loss of the Fe(I)/Fe(0)

reduction feature, and a marginal increase in the peak current for the Fe(II)/Fe(I) reduction wave. This indicates that it is the Fe^IFe^I complex that reacts with CO_2, but from the marginal current response, this reaction is not electro-catalytic (Figure 4.19 (b)).

Screening of the iron(II) dipyrrin complex, 18

The voltammetry of the bromo-iron(II) dipyrrin complex **18** was not straightforward. Measured in DMF, the CV of **18** featured 6 anodic waves on the return, anodic scan (between 0 and -1.8 V) that are not clearly attributed with the three most prominent cathodic waves that were observed on the forward, cathodic scan (Figure 4.20 (a)).

(a)

(b)

(c)

(d)
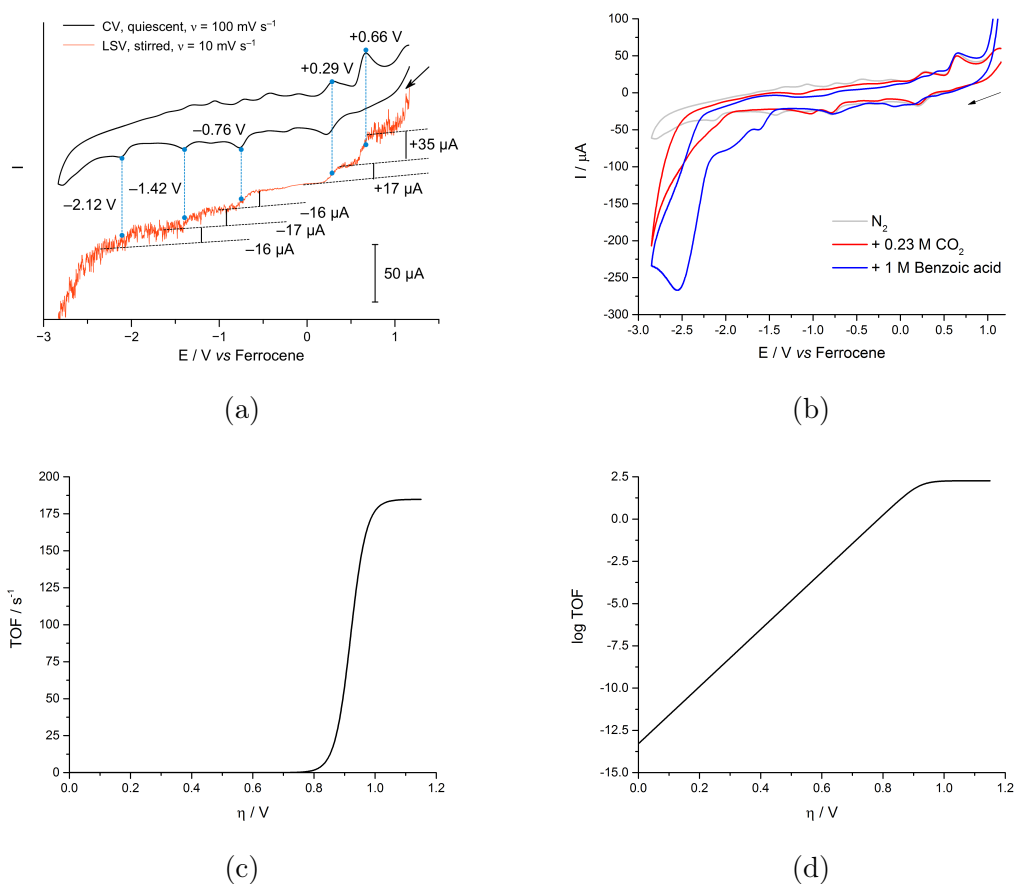
Figure 4.20: Screening of electrocatalytic activity of **18** by voltammetry. (a) Cyclic voltammogram of **18**, measured under N_2 at 100 mV s^{-1}, overlaid with the linear-sweep voltammogram, measured at 10 mV s^{-1} with stirring. (b) Cyclic voltammograms of **18**, measured at 100 mV s^{-1} under N_2, CO_2 and in the presence of benzoic acid. (c) Relationship between TOF and η, determined from foot-of-the-wave analysis. (d) Relationship between log TOF and η, yielding log TOF_0 at the y-axis intercept. All measured with a glassy-carbon working electrode, in a 0.1 M [$^nBu_4$N][PF_6] solution, in DMF.

In the case where the CV is complicated, it is often helpful to measure the linear-sweep voltammogram (LSV) whilst stirring the solution. With stirring, the measured current for a redox process is limited by mass-transport rather than diffusion, and the LSV therefore appears as a series of steps rather than waves. The sign of these steps indicates whether a process is an oxidation (positive current) or a reduction (negative current), and the height of the step is proportional to the number of electrons involved; analysing the heights of the steps therefore also helps identify which processes are due to minor species in solution. The LSV was measured at 10 mV s^{-1} with stirring of the solution, and revealed that **18** undergoes a two-electron, irreversible oxidation at E_p^a +0.66 V, as well as a one-electron, quasi-reversible oxidation at E_p^a +0.29 V. This latter oxidation process is assigned to the Fe(III)/Fe(II) redox couple, whilst the former oxidation process is tentatively assigned to a ligand-centred oxidation. Complex **18** also undergoes a series of irreversible, one-electron reduction processes, at E_p^c −0.76, −1.42 and −2.12 V, respectively. The reduction at −2.12 V is assigned to the Fe(II)/Fe(I) redox couple, as this reduction occurs at a similar potential to the Fe(II)/Fe(I) reduction observed for **15a**. By comparison with the CV of KL^2, which was measured in CH$_2$Cl$_2$ and undergoes irreversible reduction processes at E_p^c −1.29 and −1.57 V, the two reduction processes at −0.76 and −1.42 V for **18** are assigned to reduction of the dipyrrin ligand.

Whilst the complexity of the voltammetry was initially suspected to be a consequence of impure material, identical voltammograms were recorded for material that was three-times crystallised from hot toluene. Given the unusual dimeric structure that was identified in the solid state by X-ray crystallography, it may be that the complexity of the voltammetry is a consequence of complex speciation in solution.

In the presence of CO$_2$, there is quite a large current increase for the Fe(II)/Fe(I) reduction wave at −2.12 V; the peak of the wave is not observed, and the wave runs out of the edge of the electrochemical window. Addition of benzoic acid as a proton source for the electrochemical reaction allowed the peak for the catalytic wave to be observed, presumably because the reduction is more thermodynamically favoured when coupled with the addition of protons, and therefore occurs at more positive potential (Figure 4.20 (b)). There is an 18-fold increase in peak current for the Fe(II)/Fe(I) reduction process in the presence of both benzoic acid and CO$_2$, indicating that complex **18** has significant electro-catalytic activity after accessing the +1 oxidation state. Whether the complex is carrying out reduction of CO$_2$ or H$^+$ is not clear from the CV measurements. Unfortunately, due to a

lack of a GC instrument, the amount of H_2 produced from the electrochemical reaction has not been determined, and neither has the Faradaic efficiency.

From a foot-of-the-wave analysis of **18**, it was determined that the electrocatalysis begins at a high overpotential of +0.8 V. The catalytic rate constant was found to be 92.4 ± 8.8 s^{-1}, which results in a maximum TOF of 185 s^{-1} at an overpotential of 1.0 V. At zero overpotential, the intrinsic activity of the catalyst, $TOF_0 = 5 \times 10^{-14}$ M^{-1} s^{-1} (Figure 4.20 (c) and (d)). The performance of **18** is therefore comparable with Savéants iron TDMPP[ix] electrocatalyst ($\eta = 0.89$ – 1.04 V; $logTOF_0 = -13.9$ s^{-1}), but is inferior to the iron TDHPP[x] porphyrin catalyst that features an internal proton relay ($\eta = 0.41$ – 0.56 V; $logTOF_0 = -4.6$ s^{-1}).[46]

4.4.3 Screening of a nickel(II) complex

The bimetallic nickel(II) complex, **19**, undergoes a two-electron reduction to the $Ni^I Ni^I$ complex at E_p^c -1.84 V *versus* ferrocene, and also undergoes a two-electron oxidation to the $Ni^{III}Ni^{III}$ complex at the edge of the electrochemical window, at E_p^a $+0.34$ V (Figure 4.21 (a)).
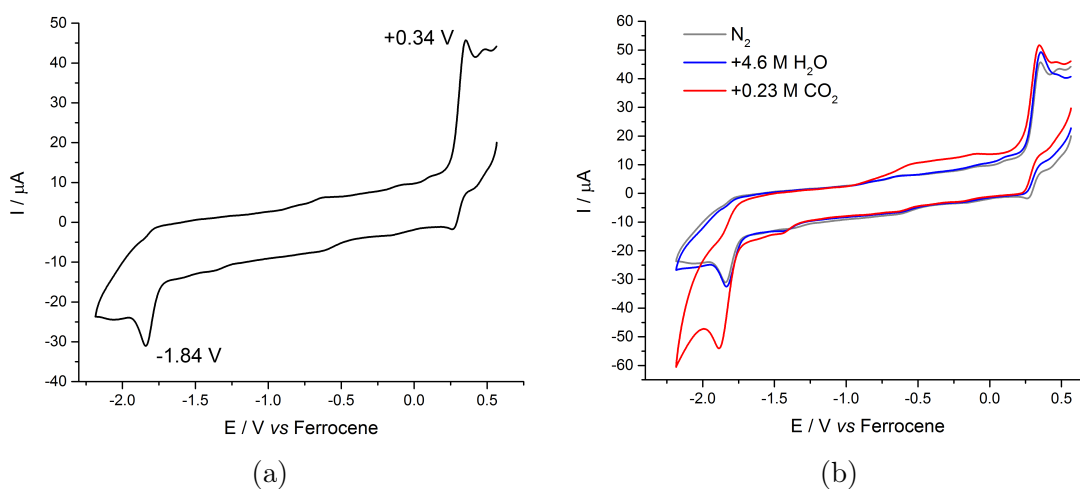
Figure 4.21: Cyclic voltammograms of **19**, measured at 100 mV s^{-1} on a glassy-carbon working electrode in a 0.1 M [$^nBu_4N$][PF_6] solution in DMF. (a) CV measured under N_2. (b) Overlaid CVs measured under N_2, then in the presence of 4.6 M water, and again after sparging with CO_2.

A CPE experiment was carried out to quantify the number of electrons involved in the reduction step. From an RVC electrode and at an applied potential of -2.0 V *versus* ferrocene, 27.73 C of charge was transferred to 0.14 mmol of **19** over

---

[ix]TDMPP = *tetrakis*(dimethoxy-phenyl)porphyrin.
[x]TDHPP = *tetrakis*(dihydroxy-phenyl)porphyrin.

5500 s. According to Equation 4.6[xi], this corresponds to a two-electron reduction process.

$$n_e = \frac{Q}{F.n_a} \tag{4.6}$$

Addition of water to the solution left the voltammogram entirely unchanged, and sparging with CO_2 resulted in a small increase in the peak current at the potential for Ni(II)/Ni(I) reduction (20 μA, Figure 4.21 (b)). In the absence of added water, and in anhydrous solvent, there is a current increase at the peak potential in the presence of CO_2 that increases further when water is added. This indicates that there is some intrinsic reactivity of **19** towards CO_2. However, it was deemed that this current response in the presence of CO_2 and water was not pronounced enough for the complex to be regarded as electro-catalytic, and was not studied further.

4.4.4 Screening of a palladium(II) complex

For the bimetallic palladium(II) complex, **20**, an irreversible reduction was observed at E_p^c −2.10 V *versus* ferrocene that, based on the quantitative CPE measurements carried out for **19** above, was similarly assigned to the concerted, two-electron reduction to the Pd^{I}Pd^I complex (Figure 4.22 (a)). An irreversible oxidation process was also measured at E_p^a +0.30 V, that is tentatively assigned to the Pd(III)/Pd(II) oxidation; however, its proximity with the edge of the electrochemical window precludes accurate integration of the anodic peak area to compare with the Pd(II)/Pd(I) reduction.

Whilst the addition of water or phenol to the solution left the voltammogram unchanged, so did sparging with CO_2, indicating that there is no reactivity between the electro-generated Pd(I) complex and CO_2. Addition of acetic acid to the solution of **20** resulted in a large increase in the peak current at the Pd(II)/Pd(I) reduction potential (50 μA), indicating significant proton reduction by Pd(I). This is unsurprising based on the pK_a of acetic acid (4.76) and propensity of palladium(II) complexes to catalyse proton-reduction.[49] Sparging this latter solution with CO_2 resulted in negligible increase in the peak current (Figure 4.22 (b)). Even in the presence of the strong proton-source to promote the proton-coupled reduction of CO_2, selective electro-catalytic reduction was not observed.

[xi]n_e is the number of electrons; Q is the charge / C, determined from integration of the amperogram; n_a is the concentration of the analyte / mol; and F is the Faraday constant, 96,485 C mol^{-1}.
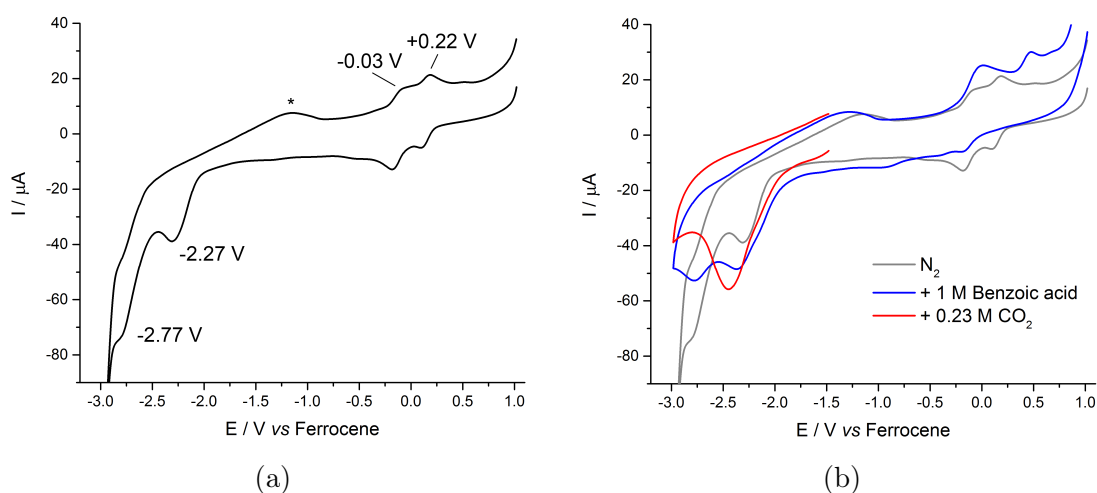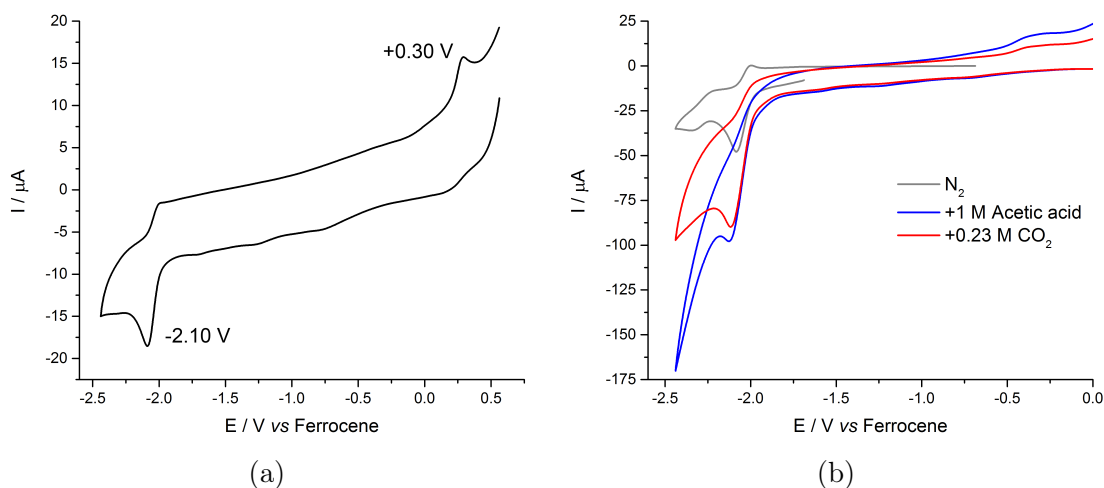
Figure 4.22: Cyclic voltammograms of **20**, measured at 100 mV s^{-1} on a glassy-carbon working electrode in a 0.1 M [^{n}Bu$_4$N][PF$_6$] solution in DMF. (a) CV measured under N$_2$. (b) Overlaid CVs measured under N$_2$, then in the presence of 1 M acetic acid, and again after sparging with CO$_2$.

References

[1] W. Reiter, A. Gerges, S. Lee, T. Deffo, T. Clifford, A. Danby and K. Bowman-James, *Coord. Chem. Rev.*, 1998, **174**, 343 .

[2] N. N. Gerasimchuk, A. Gerges, T. Clifford, A. Danby and K. Bowman-James, *Inorg. Chem.*, 1999, **38**, 5633.

[3] R. Angamuthu, P. Byers, M. Lutz, A. L. Spek and E. Bouwman, *Science*, 2010, **327**, 313.

[4] U. R. Pokharel, F. R. Fronczek and A. W. Maverick, *Nat. Commun.*, 2014, **5**, 5883.

[5] G. Givaja, A. J. Blake, C. Wilson, M. Schröder and J. B. Love, *Chem. Commun.*, 2003, 2508.

[6] J. B. Love, *Chem. Commun.*, 2009, 3154.

[7] E. Askarizadeh, A. M. J. Devoille, D. M. Boghaei, A. M. Z. Slawin and J. B. Love, *Inorg. Chem.*, 2009, **48**, 7491.

[8] G. Givaja, M. Volpe, J. Leeland, M. Edwards, T. Young, S. Darby, S. Reid, A. Blake, C. Wilson, J. Wolowska, E. McInnes, M. Schröder and J. Love, *Chem. Eur. J.*, 2007, **13**, 3707.

[9] E. A. Connolly, J. W. Leeland and J. B. Love, *Inorg. Chem.*, 2016, **55**, 840.

[10] P. L. Arnold, C. J. Stevens, J. H. Farnaby, M. G. Gardiner, G. S. Nichol and J. B. Love, *J. Am. Chem. Soc.*, 2014, **136**, 10218.

[11] R. D. Shannon, *Acta Crystallogr., Sect. A*, 1976, **32**, 751.

[12] G. Givaja, A. J. Blake, C. Wilson, M. Schroder and J. B. Love, *Chem. Commun.*, 2005, 4423.

[13] Q.-J. Pan, G. Schreckenbach, P. L. Arnold and J. B. Love, *Chem. Commun.*, 2011, **47**, 5720.

[14] A. M. J. Devoille and J. B. Love, *Dalton Trans.*, 2012, **41**, 65.

[15] P. L. Arnold, G. M. Jones, Q.-J. Pan, G. Schreckenbach and J. B. Love, *Dalton Trans.*, 2012, **41**, 6595.

[16] A. M. J. Devoille, P. Richardson, N. L. Bill, J. L. Sessler and J. B. Love, *Inorg. Chem.*, 2011, **50**, 3116.

[17] J. P. Fillers, K. G. Ravichandran, I. Abdalmuhdi, A. Tulinsky and C. K. Chang, *J. Am. Chem. Soc.*, 1986, **108**, 417.

[18] F. Bolze, M. Drouin, P. D. Harvey, C. P. Gros, E. Espinosa and R. Guilard, *J. Porphyr. Phthalocya.*, 2003, **07**, 474.

[19] F. Jerome, J.-M. Barbe, C. P. Gros, R. Guilard, J. Fischer and R. Weiss, *New J. Chem.*, 2001, **25**, 93.

[20] J. R. Pankhurst, T. Cadenbach, D. Betz, C. Finn and J. B. Love, *Dalton Trans.*, 2015, **44**, 2066.

[21] R. H. Dunhill, J. R. Pilbrow and T. D. Smith, *J. Chem. Phys.*, 1966, **45**, 1474.

[22] R. L. Belford, N. D. Chasteen, H. So and R. E. Tapscott, *J. Am. Chem. Soc.*, 1969, **91**, 4675.

[23] S. S. Eaton, K. M. More, B. M. Sawant and G. R. Eaton, *J. Am. Chem. Soc.*, 1983, **105**, 6560.

[24] S. S. Eaton, G. R. Eaton and C. K. Chang, *J. Am. Chem. Soc.*, 1985, **107**, 3177.

[25] N. G. Connelly and W. E. Geiger, *Chem. Rev.*, 1996, **96**, 877.

[26] E. A. Katayev, Y. A. Ustynyuk, V. M. Lynch and J. L. Sessler, *Chem. Commun.*, 2006, 4682.

[27] J. Cámpora, A. M. Naz, P. Palma, E. Álvarez and M. L. Reyes, *Organometallics*, 2005, **24**, 4878.

[28] M. D. Fryzuk and S. A. Johnson, *Coord. Chem. Rev.*, 2000, **200–202**, 379 .

[29] J. M. Smith, A. R. Sadique, T. R. Cundari, K. R. Rodgers, G. Lukat-Rodgers, R. J. Lachicotte, C. J. Flaschenriem, J. Vela and P. L. Holland, *J. Am. Chem. Soc.*, 2006, **128**, 756.

[30] N. Hazari, *Chem. Soc. Rev.*, 2010, **39**, 4044.

[31] J. L. Crossland and D. R. Tyler, *Coord. Chem. Rev.*, 2010, **254**, 1883 .

[32] J. S. Anderson, J. Rittle and J. C. Peters, *Nature*, 2013, **501**, 84.

[33] R. Custelcean, L. H. Delmau, B. A. Moyer, J. L. Sessler, W.-S. Cho, D. Gross, G. W. Bates, S. J. Brooks, M. E. Light and P. A. Gale, *Angew. Chem. Int. Ed.*, 2005, **44**, 2537.

[34] J. L. Sessler, D. E. Gross, W.-S. Cho, V. M. Lynch, F. P. Schmidtchen, G. W. Bates, M. E. Light and P. A. Gale, *J. Am. Chem. Soc.*, 2006, **128**, 12281.

[35] O. R. Allen, S. J. Dalgarno, L. D. Field, P. Jensen, A. J. Turnbull and A. C. Willis, *Organometallics*, 2008, **27**, 2092.

[36] J. M. Smith, R. J. Lachicotte and P. L. Holland, *Organometallics*, 2002, **21**, 4808.

[37] A. Buchard, M. R. Kember, K. G. Sandeman and C. K. Williams, *Chem. Commun.*, 2011, **47**, 212.

[38] A. R. Sadique, W. W. Brennessel and P. L. Holland, *Inorg. Chem.*, 2008, **47**, 784.

[39] B. Bichler, C. Holzhacker, B. Stöger, M. Puchberger, L. F. Veiros and K. Kirchner, *Organometallics*, 2013, **32**, 4114.

[40] H. Fong, M.-E. Moret, Y. Lee and J. C. Peters, *Organometallics*, 2013, **32**, 3053.

[41] X. Feng, I. Bischoff and M. O. Senge, *J. Org. Chem.*, 2001, **66**, 8693.

[42] J. Tessier, J.-P. Demoute and L. Taliani, "Novel pyrrole derivatives", US Patent 4,737,513, 1988.

[43] K. D. Barnes, V. M. Kamhi and R. E. Diehl, "Haloalkylthio, -sulfinyl and -sulfonyl arylpyrrole fungicidal agents", US Patent 5,284,863, 1994.

[44] C. Costentin, S. Drouet, M. Robert and J.-M. Savéant, *J. Am. Chem. Soc.*, 2012, **134**, 11235.

[45] A. Gennaro, A. A. Isse and E. Vianello, *J. Electroanal. Chem.*, 1990, **289**, 203.

[46] C. Costentin, S. Drouet, M. Robert and J.-M. Savéant, *Science*, 2012, **338**, 90.

[47] M. D. Liptak, K. C. Gross, P. G. Seybold, S. Feldgus and G. C. Shields, *J. Am. Chem. Soc.*, 2002, **124**, 6421.

[48] C. Costentin, G. Passard, M. Robert and J.-M. Savéant, *J. Am. Chem. Soc.*, 2014, **136**, 11821.

[49] D. Sirbu, C. Turta, E. A. Gibson and A. C. Benniston, *Dalton Trans.*, 2015, **44**, 14646.

Chapter 5

Mixed-metal catalysis for hydrocarbon oxygenation

In Chapter 4, the synthesis and characterisation of the proton *meso*-substituted, dinuclear copper(II) complexes **13a** and **13b** was discussed, and the related, previously reported, alkyl *meso*-disubstituted Pacman complex **13c** was also mentioned (Figure 5.1). In this Chapter, the use of these complexes as catalysts for the oxygenation of hydrocarbon substrates is presented. It was discovered that mixtures of the copper(II) complexes and $FeCl_3$ are catalytically superior in comparison with either component in isolation. As cooperative catalysis between copper(II) and iron(III) is novel in the area of oxygenation catalysis, attempts were made to characterise the catalyst, deduce the reaction mechanism, and explore the reaction scope.

13a **13b** **13c**
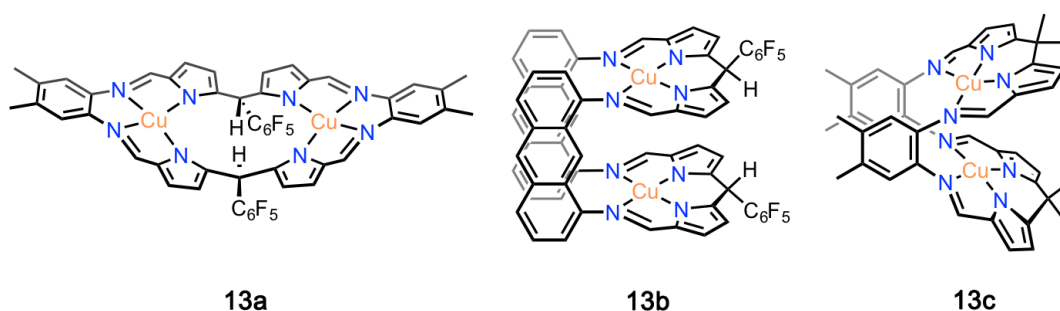
Figure 5.1: Dinuclear copper(II) hydrocarbon oxygenation catalysts: the bowl-shaped complex **13a** and the Pacman complexes **13b** and **13c**.

This research was inspired by previous, related chemistry of Pacman complexes in the literature. Dinuclear Pacman diporphyrin complexes of iron(II) activate O_2, leading to reactive iron(IV) μ_1-oxo complexes (through photolysis of iron(III) μ_2-oxo intermediates) that oxidise hydrocarbon substrates to alcohols.[1] As the structurally related Schiff-base Pacman complexes of cobalt(II) catalyse the microscopic-reverse O_2 reduction reaction,[2,3] it was anticipated that reactions between complexes **13a** – **13c** and hydroperoxides might form reactive species akin to butterfly MO_2M complexes.[4-6] Furthermore, electrochemical measurements for

both **13a** and **13c** indicated that the copper(III) oxidation state is also accessible for these complexes, leading to the possibility of the formation of reactive Cu^{III}-OH complexes which participate in hydrogen-atom abstraction (HAA) reactions.[7–10]

5.1 Catalysis with dinuclear copper(II) macrocycles

Preliminary catalytic reactions involving only the dinuclear copper(II) complexes **13a** – **13c** were carried out in d_3-MeCN. Xanthene was used as a substrate due to the low bond-dissociation energy of its benzylic C-H bond ($H_{Diss} = 75.5$ kcal mol^{-1})[11] and *tert*-butyl hydroperoxde (TBHP, 70 wt% in water) was used as an oxidant (Scheme 5.1). The use of complexes **13a** – **13c** as catalysts for this reaction was first tested at loadings of 0.2 mol% with respect to xanthene. All three complexes are catalytically inactive at room temperature, but with heating at 333 K, the substrate is consumed within 2 hours, as evinced by the loss of the benzylic proton resonance at 4.05 ppm in the ^{1}H NMR spectrum.
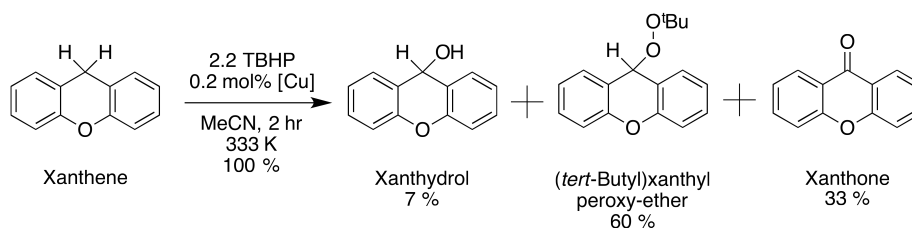
Scheme 5.1: Oxygenation of xanthene catalysed by the dinuclear copper(II) complexes **13a** – **13c** at 333 K. The yields of the alcohol, peroxy-ether and ketone products at 2 hours are shown and were determined by ^{1}H NMR spectroscopy.

Three oxidation products are formed and, after carrying out the reaction on a preparative scale (1 mmol), these products were isolated by column chromatography and identified as the benzylic alcohol (xanthydrol), the organo-peroxide ((*tert*-butyl)xanthyl peroxy-ether) and the benzylic ketone (xanthone). In d_3-MeCN, xanthydrol has a characteristic benzylic proton doublet resonance at 5.77 ppm, xanthone has a doublet resonance at 8.26 ppm due to a pair of equivalent aromatic protons, and (*tert*-butyl)xanthyl peroxy-ether has a singlet benzylic proton resonance at 5.98 ppm. The identity of (*tert*-butyl)xanthyl peroxy-ether is supported by elemental analysis and its mass spectrum that shows a molecular-ion peak and isotope distribution pattern consistent with its potassium adduct (309 m/z). One side-product of the reaction is *tert*-butanol, identified by the singlet resonance at 1.17 ppm due to the methyl protons. Importantly, 9,9'-bixanthene is not seen, a product which might be expected to form in a free-radical reaction mechanism through homo-coupling of organic radicals following HAA from

xanthene.[12] The characteristic resonances for xanthene and its three oxidation products are well resolved in the mixture and allowed the reaction to be monitored by ^{1}H NMR spectroscopy (Figure 5.2). At 333 K, in a quiescent reaction mixture, 93 % conversion of the substrate is seen within 30 minutes, giving a turnover frequency (TOF) of 1015 h^{-1}.
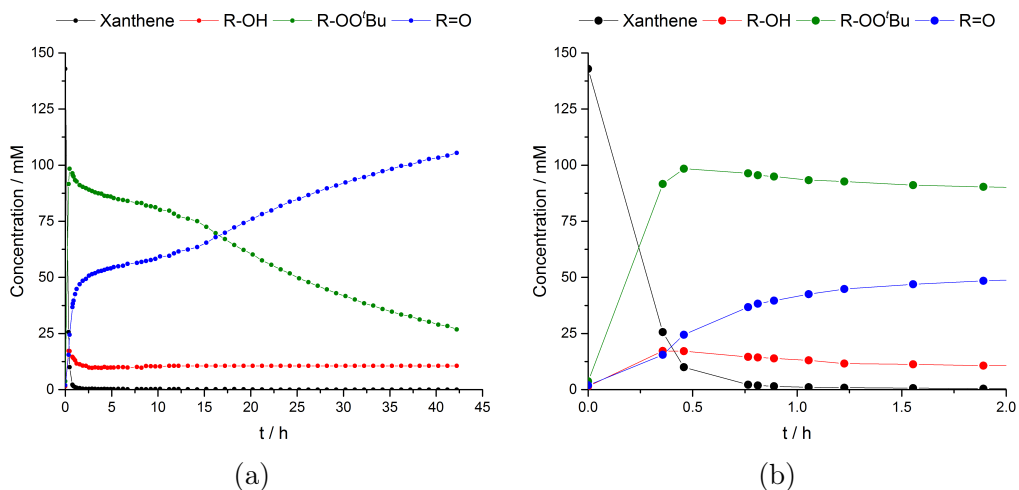
Figure 5.2: Monitoring the copper(II)-catalysed xanthene oxygenation reaction by *in situ* ^{1}H NMR spectroscopy, showing (a) the full reaction and (b) a detailed view of the start of the reaction. Reaction conditions: 0.2 mol% **13c**, [xanthene]$_0$ = 0.15 M, [TBHP]$_0$ = 0.30 M, 333 K, d_3-MeCN.

The peroxy-ether and ketone products form rapidly in yields of 60 % and 33 %, respectively at 2 hours, whilst xanthydrol is formed in 7 % yield. After this initial period, the concentrations of both the peroxy-ether and xanthone almost plateau for 10 hours before the peroxy-ether slowly oxidises to the ketone at a rate of 7.2×10^{-7} mol dm^{-3} s^{-1}, consistent with auto-oxidation. At room temperature, this non-catalysed peroxy-ether oxidation reaction is slow ($\nu_{300\text{ K}} = 1.1 \times 10^{-8}$ mol dm^{-3} s^{-1}) but is accelerated in the presence of 0.2 mol% of **13c** ($\nu_{300\text{ K}} = 1.8 \times 10^{-6}$ mol dm^{-3} s^{-1}), indicating that the copper catalyst undergoes deactivation in the high temperature xanthene reaction. Complete inhibition of the catalyst by xanthone or *tert*-butanol is ruled out by separate reactions in which these compounds are present in the initial reaction mixture but where the catalyst still displays high activity.

Chapter 4 showed that variation of the ligand scaffold in the macrocyclic complexes **13a** – **13c** causes dramatic changes in terms of their geometric and electronic properties. Despite these differences, varying the catalyst **13a** – **13c** did not change the activity or distribution of products, nor did it make the catalyst more or less susceptible to deactivation or inhibition. As the dipyrromethane groups containing *meso*-H substituents in complexes **13a** and **13b** could potentially

undergo oxidation chemistry to dipyrrins,[13,14] only complex **13c** was used to study these catalytic reactions in further detail, so that the geometry and electronic structure of the catalyst was better defined.

5.2   Cooperative catalysis with copper(II) and iron(III)

Whilst the copper(II) complexes are highly active towards catalysing xanthene oxidation, the activity quickly arrests. In order to address this issue, $FeCl_3$ was employed as a simple iron(III) co-catalyst, as it had been demonstrated previously to act as an effective catalyst for the oxidation of benzylic alcohol substrates.[15] It was hypothesised that this mixed-metal system would carry out *tandem* catalysis, with the copper(II) complex catalysing xanthene oxidation to form a mixture of xanthydrol and the peroxy-ether. After rapid deactivation of the copper(II) catalyst, $FeCl_3$ would then catalyse further oxidation of the intermediate products to form xanthone in improved yields at shorter reaction times.
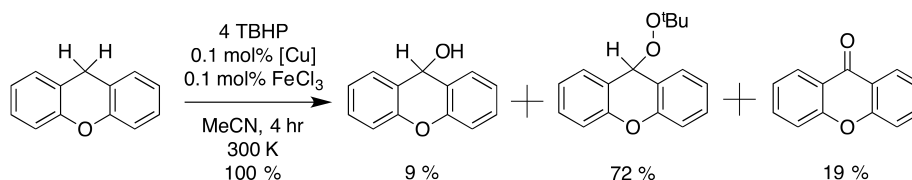
Scheme 5.2: Oxygenation of xanthene catalysed by the dinuclear copper(II) complex **13c** and $FeCl_3$ at 300 K. The yields of the alcohol, peroxy-ether and ketone products at 4 hours are shown and were determined by ^1H NMR spectroscopy.
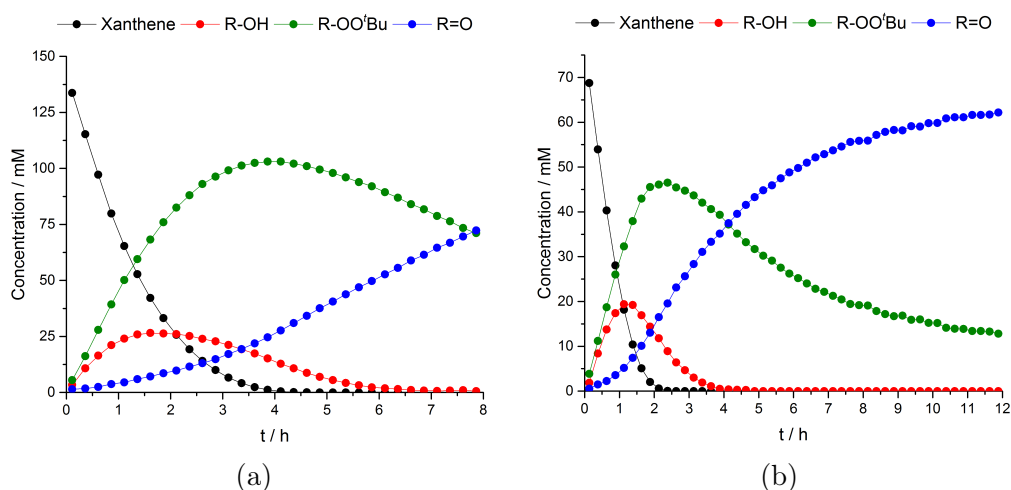
Figure 5.3: Representative plots showing progress of the copper(II)/iron(III)-catalysed xanthene oxygenation reaction, monitored by *in situ* ^1H NMR spectroscopy. Reaction conditions: (a) 0.1 mol% **13c**, 0.1 mol% $FeCl_3$, [xanthene]$_0$ = 0.15 M, [TBHP]$_0$ = 0.57 M, 300 K, d_3-MeCN; (b) 0.2 mol% **13c**, 0.2 mol% $FeCl_3$, [xanthene]$_0$ = 0.075 M, [TBHP]$_0$ = 0.30 M.

Surprisingly, at initial catalyst loadings of 0.2 mol% of **13c** and 10 mol% FeCl$_3$, the reaction proceeded at room temperature, achieving 30 % conversion of xanthene after just 30 minutes. By lowering the loadings of both catalysts to 0.1 mol%, the background activities of the individual catalysts are minimised; in isolation, **13c** shows negligible activity at room temperature, whilst FeCl$_3$ achieves only 13 % conversion after 2 hours. In contrast, the mixture of **13c** and FeCl$_3$ at 0.1 mol% loading achieves 80 % conversion within 2 hours. Reaction monitoring by ^{1}H NMR spectroscopy reveals that the substrate is completely consumed after 4 hours (Scheme 5.2, Figure 5.3), with product yields of 72 % for (*tert*-butyl)xanthyl peroxy-ether, 19 % for xanthone and 9 % for xanthydrol. Longer reaction times (12 hours) and higher relative concentrations of TBHP drive the selectivity towards the ketone product (in excess of 80 %).

In contrast to the high temperature reactions catalysed by **13a** – **13c** only, when FeCl$_3$ is present, oxidation of the intermediate products to yield xanthone continues at an enhanced rate compared to the non-catalysed reaction. Deactivation of the copper(II) catalyst is avoided by addition of FeCl$_3$, and the room-temperature activity seen indicates that tandem catalysis is not taking place as, in that case, the initial oxidation of xanthene catalysed by complex **13c** would still require heating to initiate the reaction. Instead, the addition of FeCl$_3$ appears to generate a new species that is able to catalyse the reaction at room temperature.

5.2.1 Cycling experiments

To test the stability of the mixed-metal catalyst further, recycling was attempted. Xanthone often precipitates from quiescent MeCN reaction mixtures when formed in high concentrations. Stirring a reaction mixture containing xanthene and four equivalents of TBHP at room temperature, in the presence of 0.1 mol% **13c** and FeCl$_3$, affords xanthone as a white precipitate after 16 hours. However, filtering the solution to remove xanthone and recharging the solution with more xanthene and TBHP led to no further conversion of the substrate. Therefore, under these conditions, the catalyst is stable for only one cycle of the xanthene oxidation reaction.

In contrast, the catalyst was much more stable at very low loading of 0.002 mol% **13c** and FeCl$_3$, and could be recycled multiple times. A stirred room temperature reaction between xanthene and four equivalents of TBHP was carried out in MeCN, and the reaction was monitored periodically by ^{1}H NMR spectroscopy. The catalyst is surprisingly active under these conditions, facilitating 90 % conversion of the substrate in just 30 hours; the TOF at 50 % conversion is high at 1595 h^{-1}. Under

these low-catalyst conditions, no xanthone precipitates because (*tert*-butyl)xanthyl peroxy-ether is instead formed as the major product (78 % selectivity at 30 hours). The solution was recharged with xanthene and TBHP and the reaction was carried out for a second cycle. The catalyst is slower in the second reaction, proceeding with an approximate 60 % reduction in the rate compared with the first reaction. However, 80 % conversion of xanthene is achieved after an additional 96 hours. After recharging the solution again, the catalyst activity depreciated significantly, carrying out only 13 % conversion in the next 48 hours; by this point the approximate rate had depreciated by 90 % compared with that of the first reaction. Nevertheless, the catalyst is able to carry out more than two sequential reactions at very low loading, giving a high final turnover number (TON) of 103,500. By monitoring the progress of the reaction, it was found that the TOF diminished by approximately 100 h^{-1} every 10 hours, indicating slow but steady catalyst deactivation (Figure 5.4). The solubility of xanthene in d_3-MeCN on successive recharging of the mixture is much lower than that in clean solvent, and it is plausible that saturation of the reaction mixture with the products also reduces the rate of reaction. These results indicate that the ketone product is partly responsible for catalyst decomposition or inhibition.
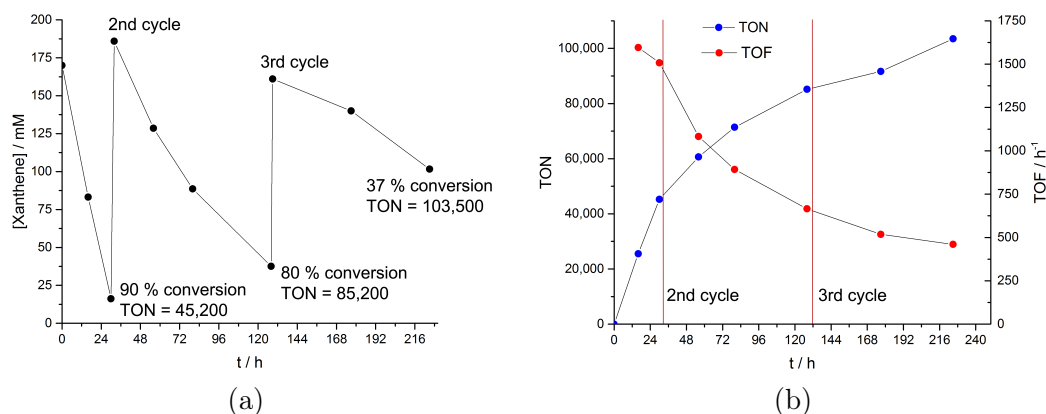
Figure 5.4: Assessing the stability of the **13c**/FeCl$_3$ catalyst in the xanthene oxygenation reaction through multiple reaction cycles. Reaction conditions: stirring d_3-MeCN, room temperature, [xanthene]$_0$ = 0.17 M, [TBHP]$_0$ = 0.68 M, 0.002 mol% **13c**, 0.002 mol% FeCl$_3$. (a) Monitoring of the xanthene concentration by ^{1}H NMR spectroscopy to determine the %conversion and TON. (b) Monitoring changes in TON and TOF during the course of the reaction.

5.2.2   Determining the role of FeCl$_3$

To investigate the role of FeCl$_3$, a catalytic reaction was carried out using **13c** (0.1 mol%) and InCl$_3$ (0.5 mol%) as a chloride-containing, redox-inactive Lewis acid (Table 5.1, entry 6). After 24 hours, the room temperature reaction between

xanthene and TBHP (2 equivalents) achieves only 3 % conversion. A similar reaction involving scandium(III) triflate (0.5 mol%) achieves higher conversion of 18 % after 24 hours, forming the peroxy-ether as the sole product (Table 5.1, entry 7). Under the same conditions, reactions involving **13c** and $FeCl_3$ achieve 90 % conversion at lower catalyst loading (0.1 mol%), yielding higher amounts of the alcohol and ketone products, in just 3 hours. These experiments indicate that $FeCl_3$ does not simply enhance the activity and stability of the catalyst due to its Lewis acidity, or by acting as a chloride source, but that its redox properties may also be important.

Table 5.1: Summary of initial activities for single- and mixed-metal catalytic systems, reported at reaction times of 1 hour. Reaction conditions: $[xanthene]_0$ = 0.15 M, $[TBHP]_0$ = 0.30 M, room temperature, quiescent d_3-MeCN. *Activities reported at 24 h.

Entry	Catalyst	Loading / mol%	Conversion / %	TOF / h^{-1}
1	**13c**	0.1	6	60
2	$CuCl_2$	0.1	13	130
3	$FeCl_3$	0.1	6	60
4	**13c** + $FeCl_3$	0.1, 0.1	55	550
5	$CuCl_2$ + $FeCl_3$	0.1, 0.1	15	150
6*	**13c** + $InCl_3$	0.1, 0.5	3	12
7*	**13c** + $Sc(OTf)_3$	0.1, 0.5	18	75

5.2.3 Broadening the applicability of the reaction

Whilst the work in this thesis is mainly concerned with the use of macrocyclic complexes in catalysis, the activity of a simplified mixed-metal system comprising $CuCl_2$ and $FeCl_3$ was explored. If this simplified system could also carry out cooperative oxygenation catalysis, in the absence of the macrocyclic ligand, the reaction would be more broadly applicable. The catalytic activity of $CuCl_2$ in hydrocarbon oxygenation has been reported previously,[16] and in this work it was also found that the use of $CuCl_2$ as a single catalyst (at 0.1 mol%) resulted in product distributions that were similar to those involving mixtures of **13c** and $FeCl_3$. However, in the room-temperature reaction between xanthene and 2 eq TBHP, the activity of 0.1 mol% $CuCl_2$ is quite slow (Table 5.1, entry 2), and with a TOF of 130 h^{-1} at 1 hour, it is significantly slower than the mixture of 0.1 mol% **13c** and 0.1 mol% $FeCl_3$ (TOF = 550 h^{-1}, Table 5.1, entry 4). In the reaction catalysed by 0.1 mol% $CuCl_2$, the addition of 0.1 mol% $FeCl_3$ made a negligible impact on the activity, improving the TOF by only 20 h^{-1} (Table 5.1, entry 5). In contrast, the mixture of **13c** and $FeCl_3$ exhibits much higher activity than

either component in isolation, indicating that cooperative catalysis between the copper(II) and iron(III) ions is encouraged by the macrocyclic ligand environment.

A series of N-donor pro-ligands were added to the xanthene oxygenation reaction, to investigate their effect on the activity of the $CuCl_2/FeCl_3$ catalyst (Scheme 5.3). The additives were used in a ten-fold excess relative to the catalyst (1.0 mol% additive, 0.1 mol% catalyst).
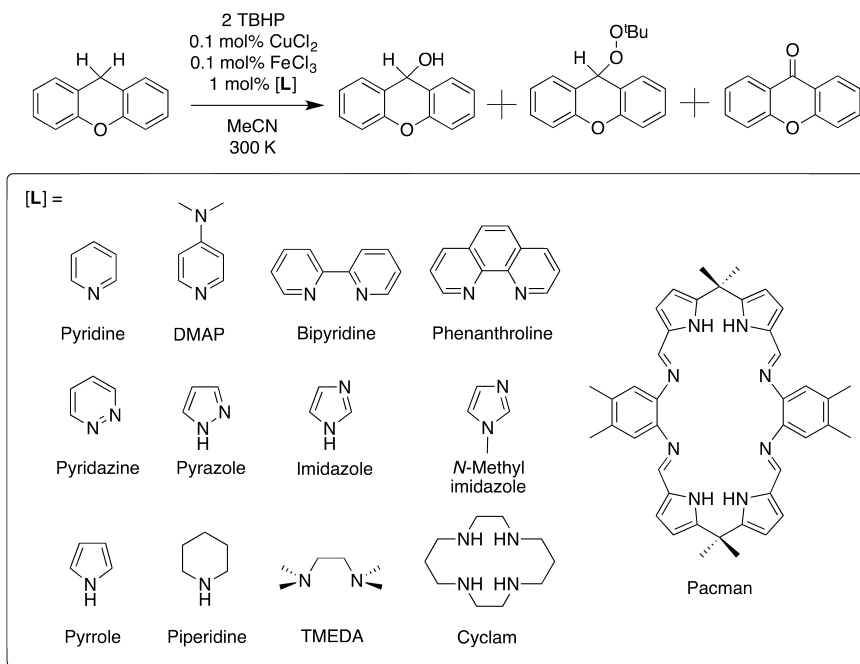
Scheme 5.3: Pro-ligands tested in the $CuCl_2/FeCl_3$ mixed-metal catalytic system. The macrocyclic Pacman ligand was implemented following *ex situ* synthesis of complex **13c**.

In the absence of any pro-ligands, the $CuCl_2/FeCl_3$ catalysed reaction results in 38 % conversion of xanthene after 3 hours, which is much lower than that achieved by the mixture of **13c**/$FeCl_3$ (90 % after 3 hours). Addition of pyridine, imidazole, N-methyl-imidazole, pyrrole or piperidine to the reaction mixture promoted a significant increase in the conversion of xanthene, all resulting in conversions in excess of 90 % at 3 hours (Figure 5.5). Selectivity for the peroxy-ether product was highest when either imidazole additives were used (87 – 92 %), and selectivity for the ketone was highest when pyridine was used (27 %). Xanthydrol was formed as a minor product in all cases, but selectivity for the alcohol product was highest when pyrrole was used as an additive (20 %). The use of N,N-dimethylaminopyridine (DMAP) or N,N,N',N'-tetramethylethylenediamine (TMEDA) as additives resulted in only moderate increases in the catalyst activity, resulting in 56 % and 61 % conversion at 3 hours, respectively.

Conversely, addition of 2,2'-bipyridine, 1,10-phenanthroline, pyridazine, or
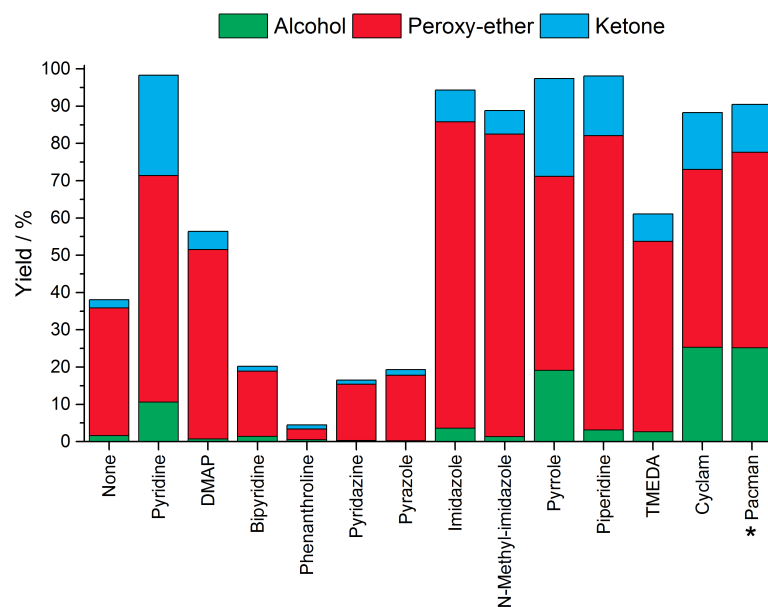
Figure 5.5: Influence of pro-ligands on conversion and selectivity in the xanthene oxygenation reaction. Reaction conditions: $[\text{xanthene}]_0 = 0.15$ M, $[\text{TBHP}]_0 = 0.30$ M, 0.1 mol% $CuCl_2$, 0.1 mol% $FeCl_3$, 1 mol% [L], quiescent d_3-MeCN, room temperature, 3 hours. *Outcome of reaction involving **13c** and $FeCl_3$ under the same conditions included for comparison. %Yields determined by ^{1}H NMR spectroscopy.

pyrazole inhibited the activity of the catalyst, with phenanthroline causing the most significant inhibition, limiting the conversion to just 5 %. Mixtures of $CuCl_2$ and $FeCl_3$ form heteronuclear clusters in solution (see below),[17] and one possibility is that these bidentate, chelating or bridging ligands disrupt cluster formation, thereby inhibiting catalysis. In that case TMEDA might be expected to also inhibit the activity, but that pro-ligand actually promoted activity.

Interestingly, the addition of the macrocyclic ligand, 1,4,8,11-tetraazacyclo-tetradecane (cyclam) resulted in a conversion and product distribution that was very similar to that achieved by the mixture of complex **13c** and $FeCl_3$. Table 5.2 summarises the influence of these pro-ligands on the TOF of the $CuCl_2$/$FeCl_3$ catalysed reaction.

Table 5.2: Influence of added pro-ligands on the turnover frequency for the xanthene oxygenation reaction with TBHP. Reaction conditions: $[\text{xanthene}]_0 = 0.15$ M, $[\text{TBHP}]_0 = 0.30$ M, 0.1 mol% $CuCl_2$, 0.1 mol% $FeCl_3$, 1 mol% [L]. *Outcome of reaction involving **13c** and $FeCl_3$ under the same conditions included for comparison.

Pro-ligand , [L]	TOF / h^{-1}	Pro-ligand, [L]	TOF / h^{-1}
None	150	Imidazole	830
Pyridine	900	N-Me-Imidazole	660
DMAP	370	Pyrrole	640
Bipyridine	80	Piperidine	680
Phenanthroline	25	TMEDA	380
Pyridazine	75	Cyclam	640
Pyrazole	65	Pacman*	550

5.3 Scope of the catalytic reaction

The xanthene oxygenation reaction, catalysed by 0.1 mol% **13c** and $FeCl_3$, was found to be tolerant of the choice of solvent, with identical conversion and product distributions seen after 2 hours in acetonitrile (polar, coordinating), dichloromethane (weakly polar, non-coordinating) and benzene (apolar). Of these, acetonitrile is the preferred solvent for laboratory scale reactions, as it is a good solvent for NMR spectroscopy, electrochemistry, GC-MS, and EPR spectroscopy, meaning that all catalytic reactions and characterisation of the catalyst can be carried out without changing the solvent.

5.3.1 Scope of the oxidant

A number of peroxide oxidants were tested in the xanthene oxygenation reaction, although TBHP was found to be the best by far (Figure 5.6). Where 90 % conversion of xanthene is seen after 3 hours when TBHP is used as the oxidant, with hydrogen peroxide, the conversion was lowered to 12 %. Use of the organo-peroxides di-*tert*-butyl peroxide (DTBP), *tert*-butyl peroxy-benzoate, or dicumyl peroxide give no reaction. Similarly, no reaction is seen when carried out in air in the absence of a hydroperoxide oxidant. Finally, adding cyclohexanecarbox-aldehyde as a co-oxidant to promote aerobic oxidation [18,19] does not yield any oxidation products. These latter two aerobic reactions were also attempted using an oxygen-rich atmosphere, which was generated by the decomposition of H_2O_2 on MnO_2 powder in a separate flask, but no improvement was observed. The oxidants were screened using a xanthene concentration of 0.15 M, two equivalents of oxidant, and catalyst loadings of 0.1 mol% for **13c** and $FeCl_3$.
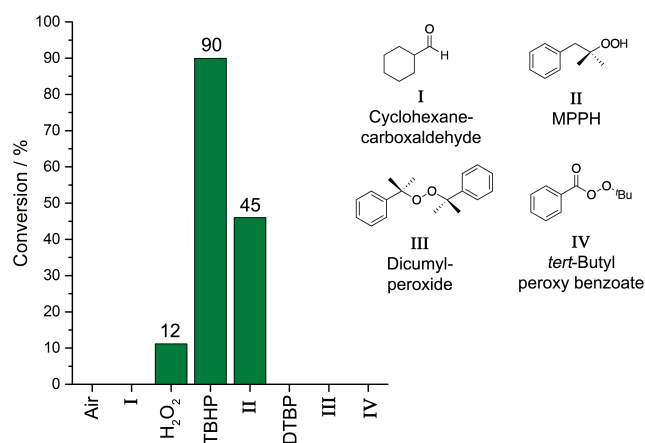
Figure 5.6: Oxidants tested in the xanthene oxygenation reaction, catalysed by **13c** and FeCl$_3$. Reaction conditions: 0.1 mol% **13c**, 0.1 mol% FeCl$_3$, [xanthene]$_0$ = 0.15 M, [oxidant]$_0$ = 0.30 M, room temperature, 3 hours, stirred MeCN. %Conversion of xanthene determined by ^{1}H NMR spectroscopy.

5.3.2 Scope of the oxygenation reaction type

The catalytic system consisting of **13c** only, at loadings between 0.2 and 1 mol%, using TBHP as the oxidant, was applied to a range of hydrocarbon substrates besides xanthene, with limited success. No reaction is seen with the aliphatic substrates *n*-decanol or cyclohexane. Similarly, attempted catalytic reactions between TBHP and cyclohexene results in only trace oxidation at the alkene, producing cyclohexene oxide, or at the allylic position, producing cyclohexenol and cyclohexenone. Greater success is met with the aromatic alkene, *trans*-stilbene, in which 97 % of the alkene substrate is consumed to yield the epoxide with 72 % selectivity; 17 % of the remaining products are accounted for as benzaldehyde and benzoic acid, which would result from oxidative cleavage at the alkene. Neither the Baeyer-Villiger reaction of cyclopentanone, nor the oxidation or oxidative-coupling of the *ortho*-directed phenol, 2,4-di-*tert*-butyl phenol, are catalysed using **13c**. Similarly, the *para*-directed phenol, 2,6-di-*tert*-butyl phenol does not react to give the expected *para*-quinone or diphenoquinoine products. Application of the mixed-metal system of **13c** and FeCl$_3$ does not improve the outcome of any of these reactions. Scheme 5.4 details the attempted oxidation reactions and their yields.
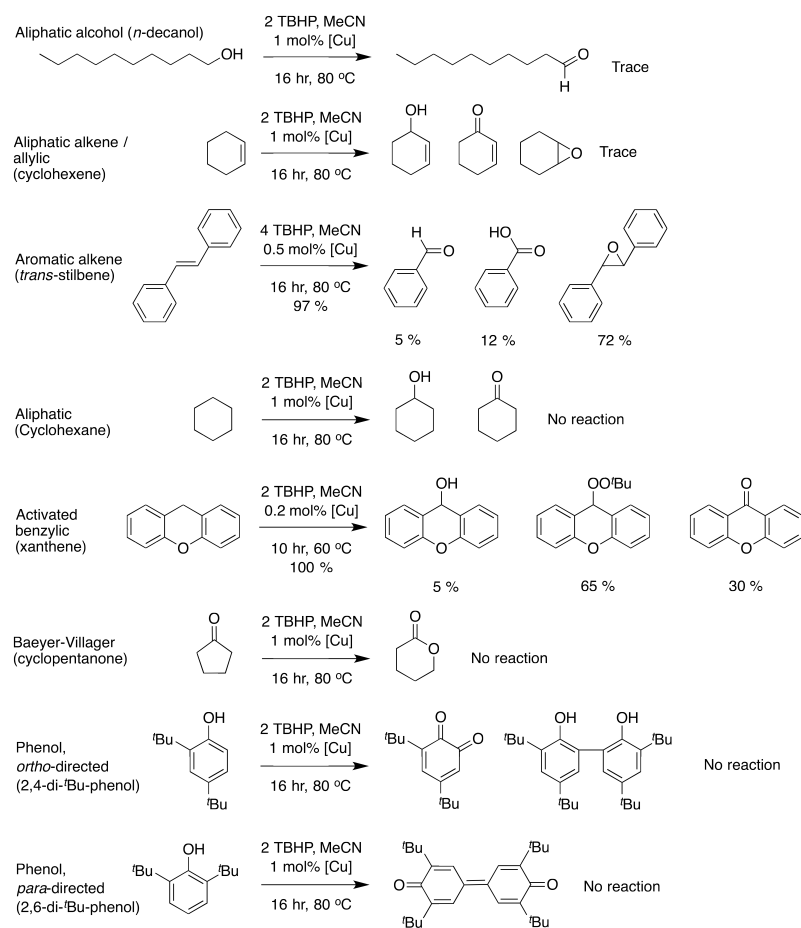
Scheme 5.4: Screening the oxidation reaction type facilitated by **13c**. All reactions were carried out using initial substrate concentrations of 0.15 – 0.20 M, using either **13a** or **13c** as the catalyst. Products and yields were determined by a mixture of ^{1}H NMR spectroscopy and GC-MS.

5.3.3   Benzylic substrate scope

The catalytic reaction involving **13c** and $FeCl_3$ appears to be restricted mainly to π-activated benzylic substrates, and so a wider screening of these substrates was undertaken. The reactions were analysed by a combination of ^{1}H NMR spectroscopy and GC-MS to determine the yields, identities and selectivities of the products, and in some cases the reactions were carried out on a preparative scale to fully determine what products were formed after isolation by column chromatography.[i] Scheme 5.5 details the general reaction conditions in these experiments, and Figure 5.7 summarises the yields.

Firstly, a series of simple substituted benzylic substrates was tested at catalyst loadings of 0.2 mol% **13c**/$FeCl_3$, with heating at 60 °C for 16 hours. Substrates

---

[i]1 mmol scale reactions, column chromatography and characterisation of the products from these reactions were carried out by Massimiliano Curcio, University of Edinburgh.
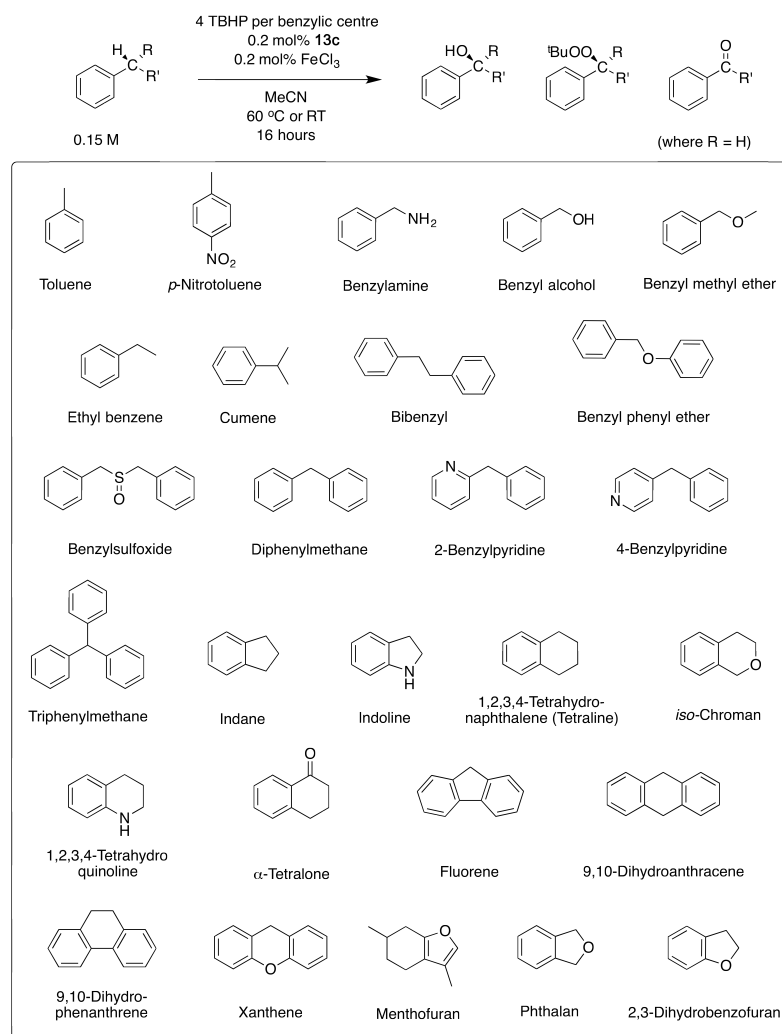
Scheme 5.5: Benzylic substrates tested in the copper(II)/iron(III) catalytic system. Substrates with 0, 1 and 2 substituents at the benzylic reaction centre were chosen, along with bicyclic, tricyclic and furan-containing benzylic compounds.

with high benzylic C-H bond dissociation energies *i.e.* toluene, *para*-nitro-toluene and benzyl sulfoxide, were not oxidised. Low to moderate conversion was seen for benzyl alcohol (51 %), ethyl benzene (26 %), cumene (20 %), bibenzyl (11 %), benzyl phenyl ether (24 %), diphenyl methane (35 %), 2-benzyl pyridine (21 %) and 4-benzyl pyridine (42 %). Of these, a few yield single carbonyl products with high selectivities: benzyl alcohol affords benzaldehyde (100 %); ethyl benzene affords acetophenone (90 %); benzyl-phenyl ether affords phenyl benzoate (69 %); diphenyl methane affords benzophenone (100 %); and both 2- and 4-benzyl pyridines afford the corresponding benzoyl pyridines (100 %). Three substrates in particular undergo high conversion. Benzyl amine is quantitatively consumed, but only affords 28 % of the carbonyl product (benzyl amide), with benzaldehyde (55 %) and benzonitrile (16 %, presumably from a radical reaction with the solvent)

seen as the other products. Benzyl methyl ether underwent 91 % conversion and is 94 % selective for the ester, methyl benzoate. Triphenyl methane also underwent 100 % conversion, and affords (*tert*-butyl)triphenyl methyl peroxy-ether as the sole product.
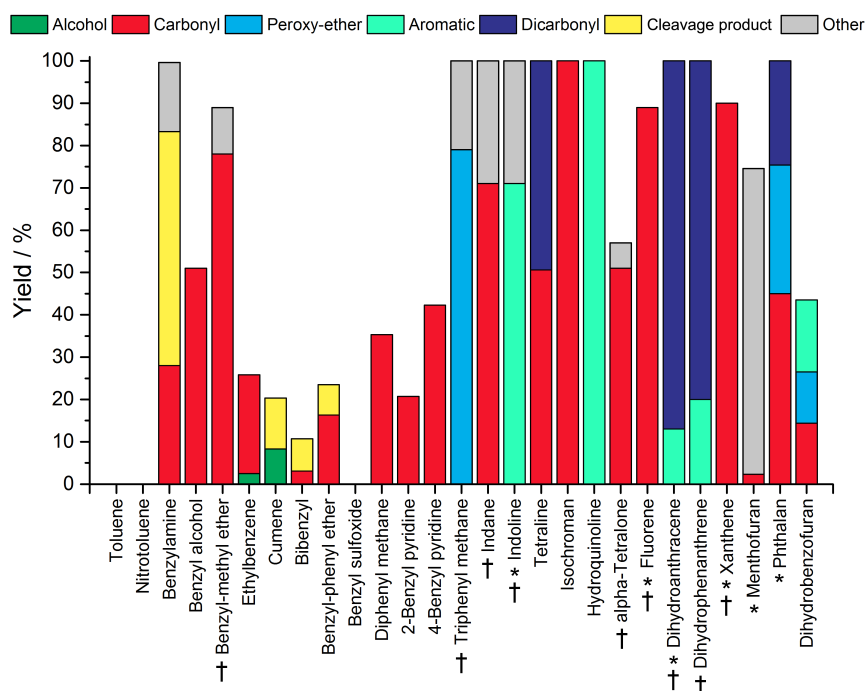
Figure 5.7: Products and yields from the oxygenation of benzylic substrates listed in Scheme 5.5, catalysed by **13c** and FeCl$_3$. Reaction conditions as outlined in Scheme 5.5, where * denotes reactions carried out at room temperature (others carried out at 60 °C). Yields determined by ^{1}H NMR spectroscopy and GC-MS, using mesitylene as an internal standard for both. † Denotes reactions carried out on 1 mmol scale; isolated yields are given from these reactions, following purification by column chromatography. Aromatic products are formed from organic-radical intermediates following HAA; dicarbonyl products form from substrates with two benzylic reaction centres; and cleavage products form following loss of some functional group from the substrate.

The oxidation reactions of benzyl methyl ether and triphenyl methane were also carried out on a 1 mmol scale. The crude product mixtures were purified by column chromatography, and the product distributions are in agreement with those determined from the small-scale reactions. The reaction of benzyl methyl ether results in 89 % conversion, affording methyl benzoate in 78 % isolated yield. Triphenyl methane reacts with 100 % conversion to give (*tert*-butyl)triphenyl methyl peroxy-ether in 79 % isolated yield.

Next, a series of bicyclic benzylic substrates were tested, all of which underwent high conversion, with the exception of α-tetralone (40 %). The *N*-heterocyclic compounds indoline and 1,2,3,4-tetrahydroquinoline both afford the aromatic compounds indole and quinolone quantitatively, with no oxygenation of the

substrate taking place following HAA. However, it is worth noting that this reaction took place at room temperature for indoline. In contrast, the *O*-heterocycle *iso*-chroman quantitatively affords the mono-ketone product 4-chromanone. Likewise, 94 % of indane reacts to afford the mono-ketone, indanone with 89 % selectivity. For 1,2,3,4-tetrahydronaphthalene, 100 % of the substrate is converted, forming a mixture of the mono-ketone, α-tetralone (51 %) and the *para*-quinone product 1,4-naphthoquinone (9.5 %).

Reactions involving indane, indoline and α-tetralone substrates were performed on a 1 mmol scale. Indane reacts quantitatively, and the mono-ketone product indanone is isolated in 71 % yield. Indole is isolated in 71 % yield from the reaction of indoline, which also reacted quantitatively. Finally, α-tetralone reacts with 57 % conversion, affording 2,3-dihydro-1,4-napthoquinone in 51 % isolated yield.

The tricyclic benzylic substrates xanthene, fluorene, 9,10-dihydroanthracene (DHA) and 9,10-dihydrophenanthrene were all screened on a preparative scale. All four substrates react with 100 % conversion, and the carbonyl products are isolated in high yields: xanthone, 90 %; fluorenone, 89 %; anthraquinone 87 %; and phenanthraquinone, 80 %. Only 9,10-dihydrophenanthrene required heating at 60 °C.

Finally, three furan derivatives of benzylic substrates were tested, as this would hold some relevance to natural product synthesis.[20,21] Phthalan reacts quantitatively at room temperature, with 45 % selectivity for the mono-ketone, phthalide. A second product is also formed in 30 % yield, but its identity could not be deduced by GC-MS; it is possibly a peroxy-ether compound that undergoes decomposition on the acidic GC column. Dihydrobenzofuran only undergoes 44 % conversion at 60 °C, to give a mixture of products; benzofuran is identified as the major product at 39 % selectivity. Finally, menthofuran has high conversion at 75 %, but the major product could not be identified by GC-MS and its selectivity is determined to be low at 34 %.

The benzylic substrates that were screened span bond dissociation energies (BDE) between 75 and 105 kcal mol^{-1}. Whilst that with the lowest BDE (xanthene) did undergo full conversion, and that with the highest BDE (toluene) did not react, there is no linear correlation between %conversion and BDE between these extremes. Comparing a set of substituted benzylic substrates with similar BDE values (85 − 87.5 kcal mol^{-1}) reveals that even in a narrow BDE range, there are vast differences in %conversion, which may be due to sensitivity of the catalyst towards different functional groups. The two alkyl-substituted substrates in this

sub-set, ethyl benzene and cumene, underwent similar conversion at 26 % and 22 %, respectively. In comparison, benzyl alcohol was higher (57 %) and benzylamine higher still (100 %). On the other hand, the two ether-containing compounds underwent very different conversions, at 33 % for benzyl-phenyl ether and 81 % for benzyl-methyl ether. Likewise, there is no obvious correlation between %conversion and pK_a.

5.4 Characterisation of the catalyst

In an attempt to identify the catalytically-active species in the copper(II)/iron(III) mixed-metal system, analyses on various mixtures were carried out using mass spectrometry, cyclic and square-wave voltammetry, electronic absorption spectroscopy, EPR spectroscopy and extended X-ray absorption fine structure (EXAFS) spectroscopy. Due to the strong paramagnetism exhibited by both complex **13c** and $FeCl_3$, structural characterisation of the catalytically-active species by NMR spectroscopy was not possible. Furthermore, single crystals of the catalyst could not be grown from a wide range of combinations and crystallisation conditions, and as such, the structure has not been determined by X-ray crystallography.

5.4.1 Mass spectrometry

The FT-ICR[ii] mass spectrum of a mixture of complex **13c** and excess TBHP in MeCN revealed a molecular ion peak at 873 m/z, consistent with coordination of TBHP to **13c** in 1:1 ratio. This adduct was evident when TBHP was present in a large excess, and no larger molecular ion peaks were seen. This might indicate that coordination of TBHP to **13c** occurs within the macrocyclic cleft, between the two copper(II) centres, in a similar manner to its dicobalt-dioxygen congeners, although exogenous coordination cannot be ruled out.[2,3,22]

A 1:1 mixture of $CuCl_2$ and $FeCl_3$ in MeCN was analysed by ESI-MS and was found to contain a mixture of pentanuclear and tetranuclear mixed-metal clusters, with formulae $[Cu_3Fe_2Cl_{12}(H_3O)]^+$ (746 m/z) and $[Cu_2Fe_2Cl_{10}(H_3O)]^+$ (612 m/z), respectively. Similar mass spectrometry experiments in the literature have also resulted in the observation of multinuclear, chloride-containing, heterometallic clusters.[17]

It was thought that addition of $FeCl_3$ to **13c** might cause trans-metalation of the copper(II) complex, forming a more reactive dinuclear iron(III) macrocycle

---

[ii]FT-ICR MS: Fourier-transform ion cyclotron resonance mass spectrometry. In these experiments, all FT-ICR MS were recorded using electro-spray ionisation (ESI).

or a hetero-dinuclear copper(II)/iron(III) complex. Another possibility might be formation of an "ate"-complex, or a loosely-associated adduct, with $FeCl_3$ incorporated within the copper(II) macrocycle through one or more bridging chloride ligands. Such a structure would be reminiscent of dinuclear zinc(II) macrocycles that act as anion-recognition complexes, which are capable of binding chloride in the cleft between the two metal centres.[23] However, in the FT-ICR mass spectrum recorded for a 1:1 mixture of **13c** and $FeCl_3$ in MeCN, no molecular ion peaks corresponding to trans-metalation products were seen. Significantly, a low-intensity peak at 980 m/z was seen, which matches that expected for an adduct of **13c** and $FeCl_3$ plus an additional chloride anion (Figure 5.8). This signal might arise from the **13c**/$FeCl_3$ adduct forming a further adduct with an exogenous chloride anion, as is common in mass spectrometry where ESI methods are used. On the other hand, $FeCl_3$ is known to form $[FeCl_2(MeCN)_4]^+[FeCl_4]^-$ in MeCN,[24] and so another possibility is that it is the formation of the $[FeCl_4]^-$ anion that encourages adduct formation with **13c**.

The major peak in the mass spectrum of the **13c**/$FeCl_3$ mixture is for the potassium-adduct of the free macrocycle, $[H_4L + K]^+$, at 697 m/z. Observation of the metal-free macrocycle might be due to instability of the **13c**/$FeCl_3$ adduct under ionising conditions (**13c** in isolation is stable under the same conditions). However, it was suspected that the role of $FeCl_3$ might be to act as a chloride source for copper(II), demetalating the macrocycle and forming $CuCl_2$, which yields similar reaction profiles in the catalytic reactions (see above). The observation of an additional peak at 853 m/z is consistent with **13c** plus two chloride ligands, and does offer some support to the copper(II) centres collecting chloride ligands in the presence of $FeCl_3$. However, MS signals arising from penta- or tetranuclear $Cu_xFe_yCl_z$ clusters, were not observed. Furthermore, reactions where $FeCl_3$ is replaced for $InCl_3$ rule this possibility out to some extent, as the outcomes of those reactions were poor in comparison. Nonetheless, further spectroscopic measurements were undertaken with this macrocycle demetalation process in mind.
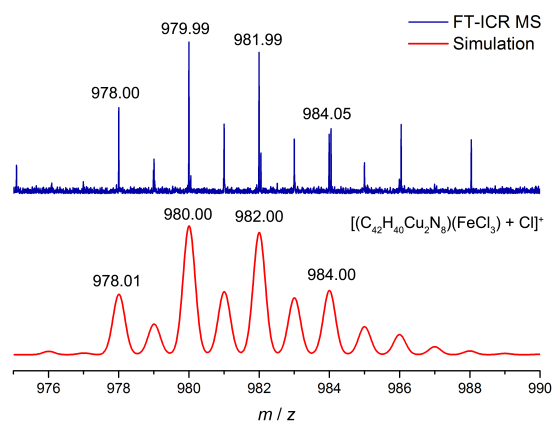
Figure 5.8: FT-ICR mass spectrum of a 1:1 mixture of **13c** and FeCl$_3$, focussing on the low-intensity molecular ion peak at 980 m/z. Measured as an MeCN solution using electro-spray ionisation.

5.4.2   Electronic absorption spectroscopy

The electronic absorption spectrum of **13c** in MeCN consists of three absorption bands at 240, 298 and 367 nm, as well as a shoulder at 400 nm (Figure 5.9). These are assigned to a mixture of charge-transfer and π-π* transitions and, with λ_{max} of 30,000 dm^3 mol^{-1} cm^{-1} (at 240 nm), these bands would obscure the low-intensity charge-transfer bands of CuCl$_2$ and FeCl$_3$ (ϵ = 2,700 at 310 nm for CuCl$_2$; 8,300 at 240 nm for FeCl$_3$). Nonetheless, the absorption spectrum of a 1:1 mixture of **13c** and FeCl$_3$ in MeCN is near-identical to that of **13c** and shows that the copper(II) macrocycle is not demetalated by FeCl$_3$.
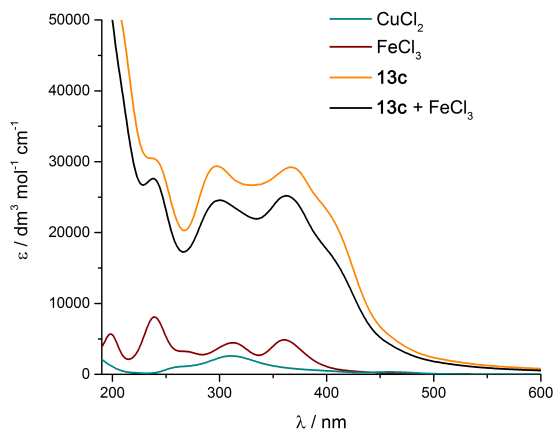
Figure 5.9: Characterisation of the catalytically-active species using UV/visible electronic absorption spectroscopy: spectra for **13c**, FeCl$_3$, CuCl$_2$ and a 1:1 mixture of FeCl$_3$ and **13c**.

5.4.3 Electrochemistry

In the cyclic voltammogram (CV) measured in MeCN at 100 mV s^{-1}, complex **13c** undergoes two irreversible Cu(II)/Cu(I) reduction processes at E_p^c -1.40 V and -1.71 V *versus* the ferrocenium/ferrocene couple (Fc$^+$/Fc = 0 V), and two irreversible Cu(III)/Cu(II) oxidation processes at E_p^a $+0.36$ V and $+0.60$ V (Figure 5.10 (a), orange trace). These step-wise redox processes indicate electronic communication between the two metal centres, which is consistent with the EPR spectrum measured for **13c** (discussed below). FeCl$_3$ undergoes irreversible Fe(III)/Fe(II) reduction at E_p^c -0.56 V, and CuCl$_2$ undergoes reversible Cu(III)/Cu(II) oxidation at $E_{1/2}$ $+0.11$ V, with the cathodic wave appearing at E_p^c $+0.05$ V.
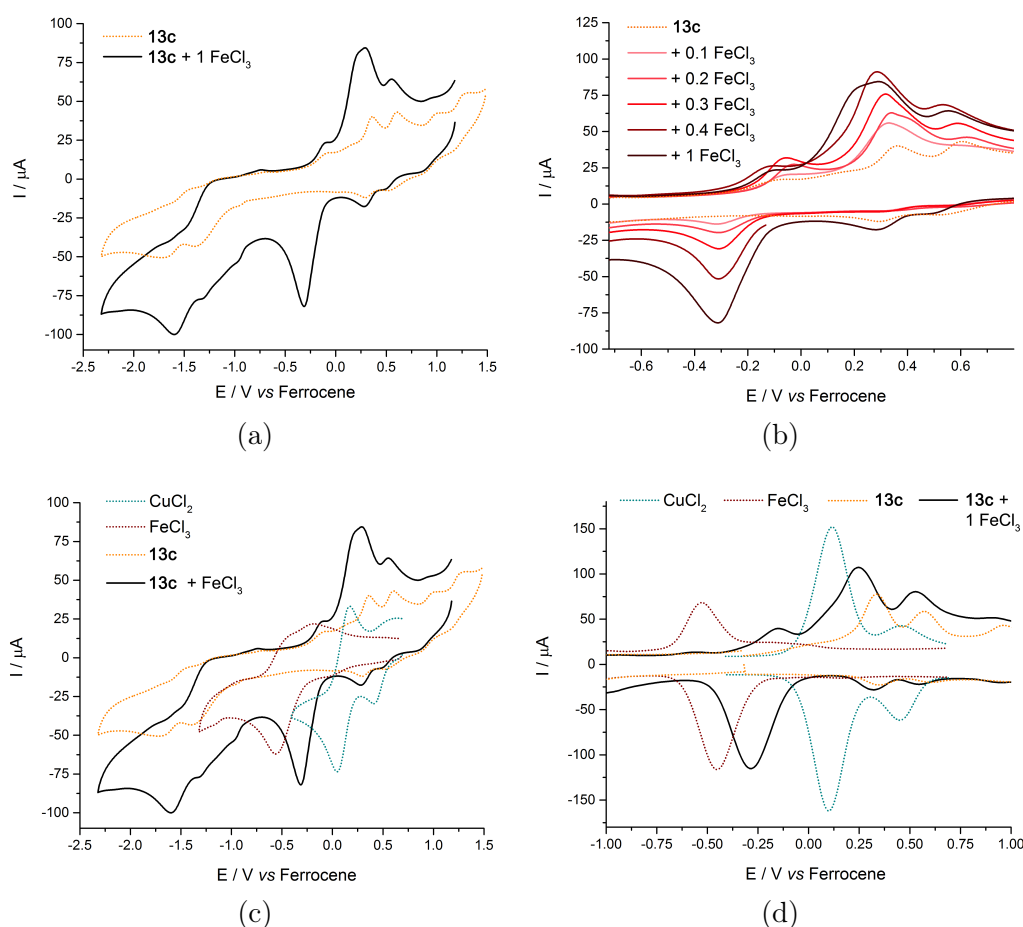
Figure 5.10: Characterisation of the catalytically-active species using voltammetry. (a) CVs of **13c** alone (orange dotted trace) and of a 1:1 mixture of **13c** and FeCl$_3$ (black trace). (b) CVs of **13c** following the addition of sequential amounts of FeCl$_3$. (c) Overlaid CVs of CuCl$_2$, FeCl$_3$, **13c** and a mixture of **13c** and FeCl$_3$. (d) Overlaid SWVs of CuCl$_2$, FeCl$_3$, **13c** and a mixture of **13c** and FeCl$_3$.

In the 1:1 mixture of **13c** and FeCl$_3$, a new, irreversible cathodic wave is seen in the CV, at E_p^c -0.31 V, approximately midway between the cathodic waves of

$CuCl_2$ and $FeCl_3$. The peak-height of this new wave is directly proportional to the concentration of $FeCl_3$, and increases steadily on addition of $FeCl_3$ in portions (Figure 5.10 (b)). In the square-wave voltammogram of the mixture (SWV, Figure 5.10 (d)), it is more apparent that this new reduction process (E_p^c −0.29 V), with its lower-intensity anodic wave on the return scan (E_p^a −0.15 V), resembles that of $FeCl_3$, albeit at 166 mV more positive potential than $FeCl_3$ measured in isolation. The presence of even trace $CuCl_2$ would be immediately obvious in the SWV, due to the nanomolar detection limit inherent with that technique.[25–27] The 166 mV anodic shift of the $FeCl_3$ reduction wave in the SWV is also accompanied by a 44 – 88 mV cathodic shift in the oxidation waves for **13c**, and therefore lends support to the formation of a copper(II)/iron(III) adduct. Furthermore, the persistence of the CV and SWV waves for complex **13c** in the presence of an equimolar amount of $FeCl_3$ provides proof that the macrocyclic complex is stable in solution, and that the decomposition that was implied by mass spectrometry results due to the instability of the complex under ionising conditions.

5.4.4 EPR spectroscopy

The EPR spectra of dinuclear copper(II) Pacman complexes that are structurally similar to **13c** have been reported previously.[28] Those spectra were consistent with an $S = 1$ triplet system, and both the $\Delta m_s = 1$ and $\Delta m_s = 2$ transitions were seen, with the latter "forbidden" transition seen at half-field. Nuclear hyperfine coupling to both ^{63,65}Cu(II) centres was also observed. The X-band EPR spectrum of **13c**, measured as a THF/MeCN glass at 130 K, is similar to those measured previously and is also consistent with an $S = 1$ spin system. Electronic communication between the two copper(II) centres is evident from the appearance of the half-field transition and is therefore in agreement with the electrochemical measurements discussed above.[iii]

The X-band EPR spectrum of $FeCl_3$ measured under the same conditions features a single signal with $g = 2$. Observation of hyperfine coupling to the iron centre is not expected as the major isotope, ^{56}Fe (91.75 % abundant) has no nuclear spin. Mixing equimolar amounts of **13c** and $FeCl_3$ produced EPR spectra that were most consistent with an overlay of each individual component (Figure 5.11). The half-field transition is still seen in the mixture, and there are no obvious spectral changes for the EPR signals arising from complex **13c**. Furthermore, there is no detectable indication of coupling between the copper(II) and iron(III) centres at 140 K, either through a dipolar or exchange interaction.

[iii]EPR spectroscopy was carried out by Dr Stephen Sproules, University of Glasgow.
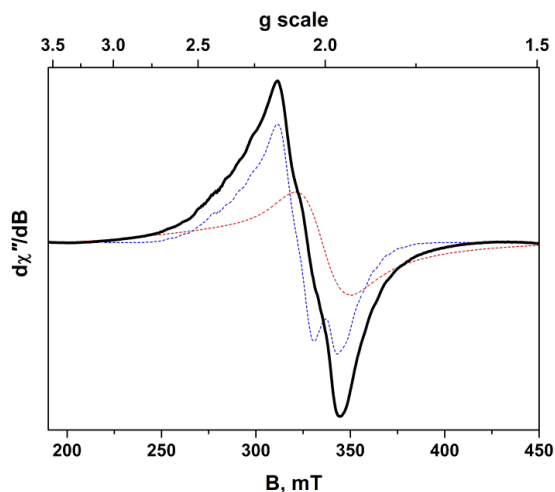
Figure 5.11: X-band EPR spectrum (solid line) of an equimolar mixture of complex **13c** and FeCl$_3$ recorded in MeCN/THF solution at 140 K. Spectra of complex **13c** (blue dashed line) and FeCl$_3$ (red dashed line) were recorded under identical conditions. Experimental conditions: frequency, 9.4247 GHz; power, 6.3 mW; modulation, 0.3 mT.

These observations further confirm that **13c** persists in solution when FeCl$_3$ is present, but do not support the formation of a formal "ate"-complex in the mixture; if an adduct is formed, it is likely weakly associated. It may be that the changes in electronic and magnetic properties are subtle, and therefore an interaction is not as pronounced in the EPR spectra as the changes in redox properties discussed above.

5.4.5 X-ray absorption spectroscopy

The solution-phase EXAFS spectrum was recorded for complex **13c** in MeCN at 95 K (Cu K-edge, Figure 5.12 (a) and (b), Table 5.3), and the fitted spectrum adequately represents the X-ray crystal structure.[iv] Crystallographic Cu-N distances in the first coordination sphere are 1.903(2) and 1.919(3) Å for pyrrolide donors, and 1.987(2) and 2.073(3) Å for imine donors. In comparison, the fitted EXAFS data predict Cu-N distances of 1.926, 2.016 and 2.066 Å. The Cu$\cdots$Cu distance of 3.95 $\pm$ 0.34 Å predicted by EXAFS is slightly longer than that determined crystallographically (3.6157(6) Å), but in quite close agreement with that distance previously predicted by EPR spectroscopy for a similar complex (3.8 Å).[28]

Copper K-edge EXAFS spectra were recorded under identical conditions following addition of FeCl$_3$ to **13c** (Figure 5.12 (c) and (d), Table 5.3). An additional scattering peak evident in the Fourier transform was modelled by including a chloride atom of a nearby FeCl$_3$ or [FeCl$_4$]$^-$ moiety. The best fit of

---

[iv]EXAFS data were recorded at the Diamond Light Source, UK, and data analysis was carried out by Dr Stephen Sproules, University of Glasgow.
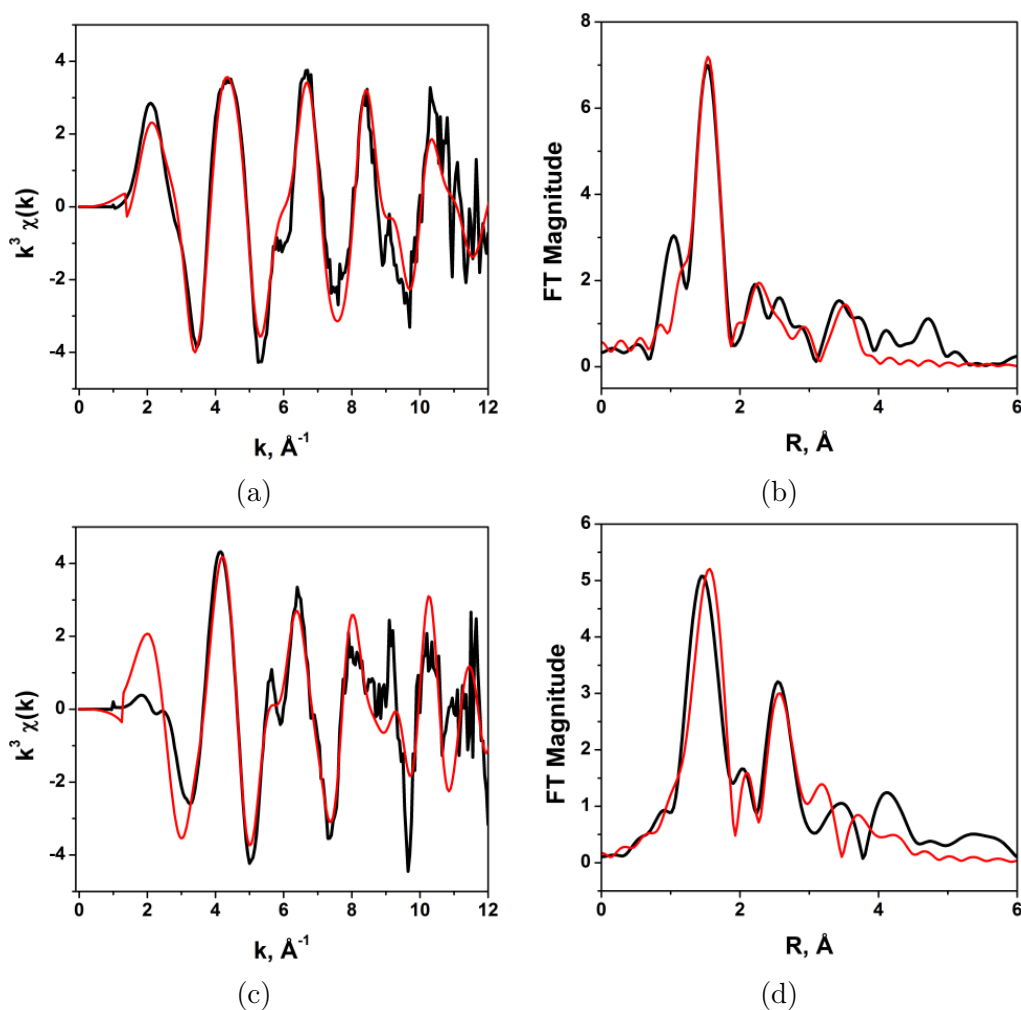
Figure 5.12: Cu K-edge EXAFS spectra measured as MeCN frozen solutions at 95 K. (a) EXAFS spectrum for **13c**. (b) Radial distribution function for **13c** following Fourier-transform of the EXAFS spectrum. (c) EXAFS spectrum for a 1:1 mixture of **13c** and FeCl$_3$. (d) Radial distribution function for the mixture of **13c** and FeCl$_3$ following Fourier-transform of the EXAFS spectrum. Experimental spectra are black and the red traces depict the simulated spectra.

the data places this chlorine atom 3.524 Å away from copper and is outside the distance anticipated for an "ate"-complex. The EXAFS data are in agreement with an intact dinuclear macrocycle and suggests a slight elongation of the Cu $\cdots$ Cu distance after the addition of FeCl$_3$ (4.39 ± 0.57 Å). Two chloride atoms from a nearby FeCl$_3$ or [FeCl$_4$]$^-$ species are modelled at 3.524 ± 0.32 Å and 4.054 ± 0.32 Å from the copper(II) ion, and these distances indicate that there is not a Cu-Cl bond, but a long-range interaction between **13c** and FeCl$_3$ or [FeCl$_4$]$^-$. These data are therefore also most consistent with a weakly-associated adduct rather than a formal "ate"-complex. Due to the scattering from the macrocyclic ligand, there is not enough resolution at sufficiently large wavenumbers to accurately determine a Cu $\cdots$ Fe separation. Although complementary data from iron K-edge

Table 5.3: EXAFS fitting parameters for **13c** and the 1:1 mixture of **13c** and $FeCl_3$. For **13c**, $E_0 = 8.86$ eV and the goodness of fit is 21.6 %. For the mixture, $E_0 = 6.23$ eV and the goodness of fit is 29.0 %. Goodness of fit, $F = [\Sigma k^6 (EXAFS_{expt} - EXAFS_{calc})^2 / \Sigma k^6 (EXAFS_{exp})^2]^{1/2}$

Sample	Path	CN$^{(a)}$	r / Å	Δr / Å	σ / Å$^{2(b)}$	Δσ / Å$^{2(b)}$	$r_{Cryst.}$ / Å$^{(c)}$
13c	Cu–N	2	1.926	0.025	4	15	1.922(3)
							1.891(3)
	Cu–N	1	2.016	0.026	7	29	1.991(3)
	Cu–N	1	2.066	0.027	7	29	2.043(3)
	Cu–N	1	3.178	0.148	3	45	3.081(2)
	Cu⋯Cu	1	3.951	0.335	127	193	3.556(6)
13c / $FeCl_3$	Cu–N	2	1.994	0.18	61	49	—
	Cu–N	2	2.106	0.19	133	92	—
	Cu⋯Cl	1	3.524	0.32	55	74	—
	Cu⋯Cl	2	4.054	0.32	3237	74	—
	Cu⋯Cu	1	4.393	0.57	76	140	—

$^{(a)}$Coordination numbers (CN) were held constant during fits. Errors in CN are estimated to be on the order of 25 %; $^{(b)}$Debye-Waller factors (σ) are multiplied by 10^4; $^{(c)}$Similar distances determined by single-crystal X-ray crystallography. The number of distances given is equal to the CN. All distances given are unique and involve a single metal centre.

measurements would provide a more complete dataset, especially pertaining to the number of chlorides coordinated to the iron(III) centre, these measurements have not been made due to restricted beam-time at the Diamond Light Source.

5.5 Reaction mechanism

5.5.1 The source of oxygen in the product

Atmospheric O_2 has been implicated in many free-radical reaction mechanisms involving hydrocarbon substrates, causing oxygenation of the intermediate organic radical following HAA.[29,30] In order to determine whether the catalytic reactions reported here also proceed through a similar auto-oxidation mechanism, several reactions were repeated after thoroughly freeze-pump-thaw degassing the solution and re-pressurising the NMR tube (fitted with a J Young's tap) with a N_2 atmosphere. In the catalytic reaction involving **13c** only (0.5 mol%, 2 eq TBHP, 60 °C), 98 % of xanthene is consumed after 3 hours, yielding (*tert*-butyl)xanthyl peroxy-ether and xanthone as major products, in 76 % and 22 % yield, respectively; xanthydrol is seen as a minor product in 2 % yield. Similarly, in the mixed-metal reaction (0.1 mol% **13c**, 0.1 mol% $FeCl_3$, 2 eq TBHP, room temperature), 98 % of xanthene is also consumed after 3 h, yielding a mixture of the alcohol, peroxy-ether and ketone products (19 %, 53 % and 26 %, respectively). No homo-coupled bixanthene product is seen, whether the reaction is carried out in air or under N_2. If the reaction mechanism involved auto-oxidation of a xanthyl

free-radical intermediate, then the reaction carried out under N_2 should lead to higher yields of the homo-coupled product and lower yields for the oxygenated products.[12] The product distributions seen for both the copper-only and mixed-metal catalytic reactions are similar regardless of the atmosphere and shows that it is the hydroperoxide that is responsible for both HAA and oxygenation of the substrate.

5.5.2 On the radical nature of the reaction mechanism

Whether a reaction mechanism proceeds through a free-radical pathway or through a reactive metal complex is a common point of contention in the literature. Iron-oxo complexes have been suggested to facilitate both HAA and oxygenation of hydrocarbon substrates (Gif chemistry);[31–33] in this case, however, HAA was later argued to take place due to hydroxyl radicals, forming organic radicals in turn (Fenton chemistry).[34–37] Oxygenation in postulated Gif reactions was also shown to proceed through an auto-oxidation mechanism involving O_2, which was proven by isotopic labelling[30] and argon purge experiments.[12] Interestingly, by taking into consideration both of these possible mechanisms, oxidation of benzylic alcohols to ketones has been achieved with enhanced selectivity by switching off the free-radical mechanism with a pH buffer, driving the reaction through an iron-oxo species instead.[38]

Assertions in the literature claim that the formation of alcohol, peroxy-ether and ketone, as have been observed in the catalytic reactions with xanthene described in this work, is a signature for a free-radical mechanism.[39] In this case, the formation of highly reactive, freely-diffusing hydroxyl, *tert*-butoxyl or *tert*-butylperoxyl radicals should lead to HAA from substrates with high bond-dissociation energies, such as toluene or cyclohexane. However, no reaction was seen between those substrates and TBHP in the presence of 0.1 mol% **13c** and $FeCl_3$. Furthermore, the β-scission decomposition reaction of the free *tert*-butoxyl radical is rapid ($k = 2.1 \times 10^4$ s^{-1}),[40] but this *tert*-butoxyl species is persistent in the catalytic system for long enough that HAA can be carried out, as seen by the formation of *tert*-butanol. This indicates that the *tert*-butoxyl species is associated with, and stabilised by, the catalyst. Concerning the radical nature of the substrate following HAA, in reactions where 9,10-dihydroanthracene (DHA) was used as a substrate, quantitative conversion was seen with high selectivity for anthraquinone (90 %); the remaining 10 % was accounted for as anthracene. Similarly, the reaction of 9,10-dihydrophenanthrene produced phenanthraquinone in 80 % yield. In a reaction mechanism that involved freely-diffusing benzylic

radicals, anthracene or phenanthrene would be expected as the sole products from these reactions. Based on the substrate scope of the catalytic reaction and the observed product distributions, the reaction mechanism appears consistent with elements of both free-radical and radical-free (metal-bound) mechanisms.

The mechanistic probe, 2-methyl-1-phenylpropan-2-yl hydroperoxide (MPPH) was employed to determine whether the reaction was proceeding through a free-radical or a metal-based mechanism.[41] The alkoxyl free-radical formed following homolytic O-O bond fission in MPPH is unstable and undergoes very rapid β-scission, forming acetone and benzyl radical ($k \approx 2.2 \times 10^8$ s^{-1}). In the case of a free-radical mechanism, the only products from a reaction involving xanthene and MPPH should be acetone and those derived from benzyl radicals, as the alkoxyl radicals are so short-lived that no HAA from xanthene should take place. The room temperature reaction between xanthene and one equivalent of MPPH, catalysed by 0.1 mol% **13c** and FeCl$_3$, resulted in 45 % conversion of xanthene after 3 hours and 90 % conversion after leaving the solution to evaporate to dryness (Scheme 5.6). The reaction between xanthene and two equivalents of MPPH resulted in quantitative consumption of xanthene after leaving the solution to evaporate to dryness.[v] In line with observations from the reactions of xanthene and TBHP, the stoichiometry of MPPH influenced the product distribution. When one equivalent of MPPH was used, xanthydrol, the peroxy-ether and xanthone were formed in yields of 30 %, 37 % and 33 %, respectively, similar to those when using TBHP as the oxidant. When two equivalents of MPPH were used in the reaction, xanthydrol, the peroxy-ether and xanthone were formed in yields of 6 %, 52 % and 42 %, respectively. Unreacted MPPH was observed in the final mixtures, indicating that a metal-hydroxide is also responsible for HAA in order to account for the amount of xanthene that is converted.

After evaporation of the solvent, a portion of the residues from the reaction of xanthene and one equivalent of MPPH was dissolved in d_3-MeCN. A resonance for the benzylic proton of 2-methyl-1-phenylpropan-2-ol (MPPOL) was seen at 2.72 ppm, and appeared in 4:5 ratio with that of unreacted MPPH. The presence of significant amounts of MPPOL further supports a metal-associated mechanism, as coordination of the alkoxide or alkoxyl radical to a metal centre stabilises the radical against β-scission. GC-MS analysis of the reaction mixtures involving MPPH did reveal that benzyl-radical derived products were present, including benzaldehyde, benzyl alcohol and bibenzyl, but these were formed in

---

[v]Acetonitrile was not evaporated on a rotary evaporator due to the explosion risk of heating solid hydroperoxide.
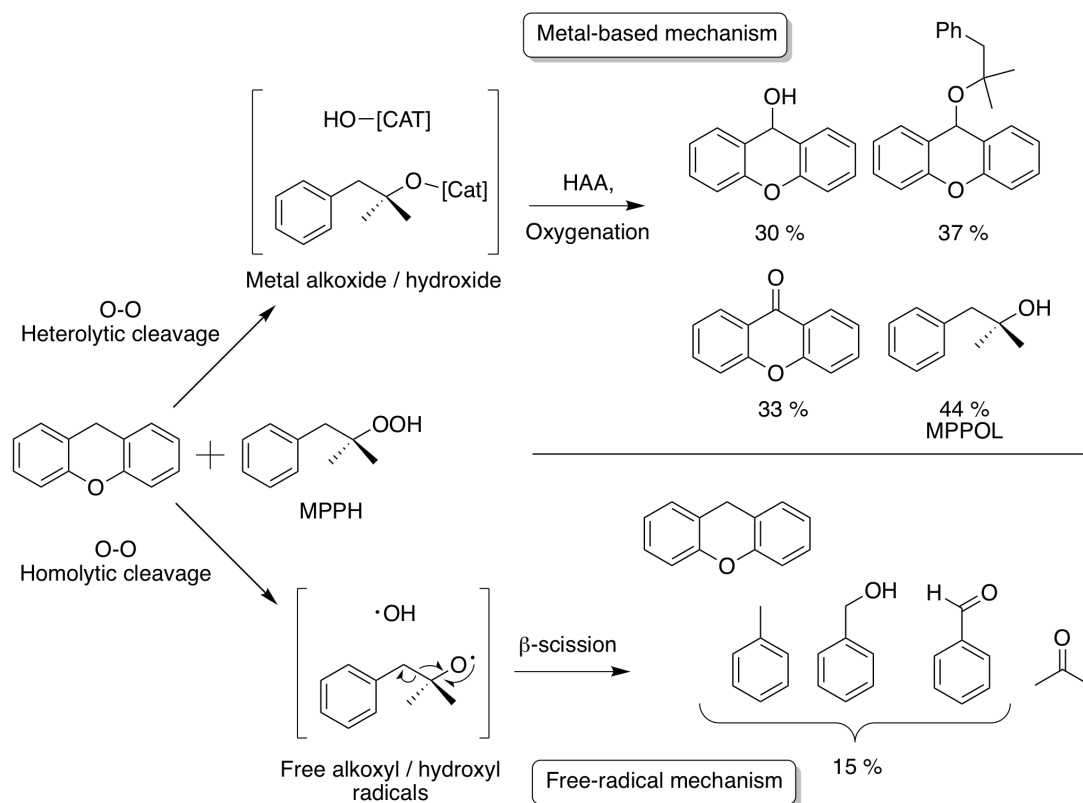
Scheme 5.6: Using MPPH as a mechanistic probe to discriminate between a free-radical or metal-based reaction mechanism, by observation of the product distribution. Selectivities / % for xanthene oxygenation products are given with respect to xanthene; selectivities / % for MPPOL and benzyl radical-derived products are given with respect to MPPH. Reaction conditions: $[\text{xanthene}]_0 = 0.15$ M, $[\text{MPPH}]_0 = 0.15$ M, 0.1 mol% **13c**, 0.1 mol% $FeCl_3$, MeCN stirred to dryness over 40 hours, room temperature.

low concentration (approximately 15 % compared with xanthene). The high conversion of xanthene indicates that a metal-associated mechanism is dominant, and fits well with the observations that anthraquinone and phenanthraquinone are formed from DHA and 9,10-dihydrophenanthrene, and that no reaction takes place with cyclohexane or toluene. In the case of a free-radical mechanism, HAA due to the *tert*-butoxyl radical is entropy-controlled.[42] In contrast, HAA occurring due to a metal-alkoxide or -hydroxide is governed by enthalpy and the nature of the metal-oxygen bond, and as such the rate and scope of the reaction is much more dependent on the BDE of the substrate in the latter case.[8]

The MPPH experiments suggest that the reaction mechanism is not truly free-radical in nature and does not therefore simply adhere to Kochi's equations.[43] Conversely, a truly radical-free mechanism, proceeding through a reactive metal-alkoxide or -hydroxide, should produce xanthydrol as the major product (*i.e.* the alcohol/ketone ratio should be large).[38,44] The observations presented concerning the mixed-metal catalytic system feature elements of both of these possible types

of mechanisms. Therefore, it was suspected that the reaction mechanism might involve "well-disguised", metal-associated radical species.[39] Alternatively, it might be that the reaction mechanism includes some elementary steps that occur at the metal and others that are radical; most oxygenation reactions feature some radical component in the mechanism.[45] A kinetics investigation was undertaken to elucidate a possible mechanism for the copper(II)/iron(III)-catalysed xanthene oxygenation reaction.

5.5.3 Kinetic analysis

Rate dependencies on initial concentrations

Under "standard" conditions (0.15 M xanthene, 0.30 M TBHP, 0.1 mol% **13c**, 0.1 mol% $FeCl_3$), the consumption of xanthene can be modelled adequately using a simple first-order integrated rate law, specifically $[\text{xanthene}]_t = [\text{xanthene}]_0 \, e^{-kt}$ ($k = 2.07 \times 10^{-4} \text{ s}^{-1}$; see Figure 5.13 (a) and (b)). The first three half-lives under these conditions are approximately consistent, and are in agreement with the mean value (3311 s) within 2σ. However, upon varying the xanthene concentration away from standard conditions, the reaction profile is not simulated well by the simple first-order rate law. When the xanthene concentration is raised (0.187 M), the measured reaction profile after 70 % conversion is slower than that predicted by the first-order rate law (Figure 5.13 (c)). Conversely, when the concentration is lowered (0.112 M to 0.004 M) the measured reaction profile after 70 % conversion is more rapid than that predicted by the rate-law (Figure 5.13 (d)).

Furthermore, when $[\text{xanthene}]_0$ is greater than 0.15 M, the reaction profile is most linear when plotted as $[\text{xanthene}]^{-0.5}$ against time ($R^2 = 0.9996$, up to 80 % conversion), implying that the reaction is ¾ order under these conditions. Under standard conditions, the reaction profile is most linear when plotted as $\ln[\text{xanthene}]$ against time ($R^2 = 0.9920$), indicating first-order kinetics. When $[\text{xanthene}]_0$ is less than 0.15 M, the reaction profiles are most linear when plotted as $[\text{xanthene}]^{0.5}$ against time ($R^2 = 0.9997$), indicating that the reaction is ½ order under these conditions. These observations show that there is a non-simple dependency of the reaction kinetics on xanthene concentration, and imply that the reaction proceeds according to a complex rate law.

A plot of the initial rate of xanthene consumption against $[\text{xanthene}]_0$ fitted well to a linear trend, although the projected intercept is non-zero (see Figure 5.14 (a)). The errors in the initial rates became significant at very dilute xanthene concentrations, as the reaction proceeded very quickly with the increasing excess of
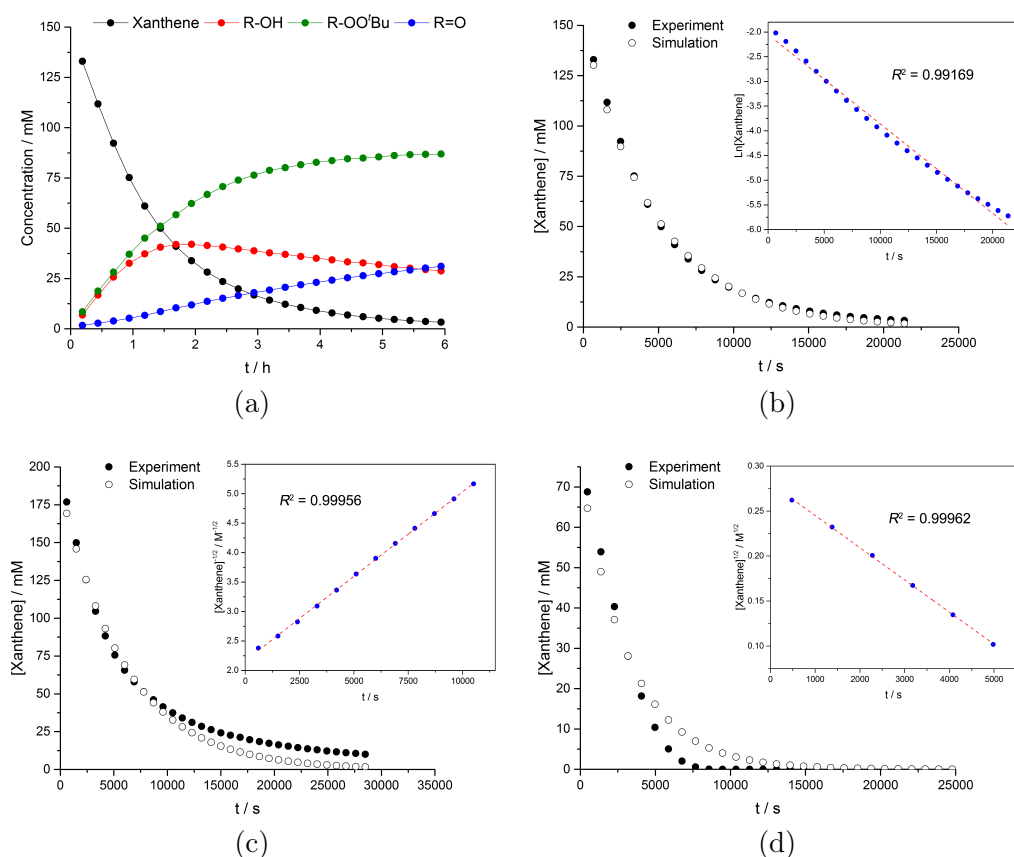
Figure 5.13: Simulating the first-order progression of the xanthene oxygenation reaction. The simulated plots were obtained by minimising the error in $[\text{xanthene}]_t = [\text{xanthene}]_0 \, e^{-kt}$ by varying k. (a) Progression of the xanthene oxygenation reaction under "standard" initial conditions (0.15 M xanthene, 0.30 M TBHP, 0.1 mol% **13c**, 0.1 mol% FeCl$_3$). (b) First-order simulation of the reaction under standard conditions; linear plot obtained as ln[xanthene] against t. (c) First-order simulation when [xanthene] is increased from standard conditions (0.187 M); linear plot obtained as [xanthene]$^{-0.5}$ against t. (d) First-order simulation when [xanthene] is decreased from standard conditions (0.075 M); linear plot obtained as [xanthene]$^{0.5}$ against t.

TBHP and catalyst loading. Therefore, it is not possible to accurately determine whether the initial rate changes dramatically to cross the origin at very dilute concentration, using this method.

When the TBHP concentration is increased from standard conditions, the reaction profiles appear similar to those cases discussed above when the concentration of xanthene is low. The measured profiles are more rapid than the first order rate-law predicts, and are most linear when plotted as [xanthene]$^{0.5}$ against time. The switching from first-order to ½ order kinetics is therefore not dependent on the absolute xanthene concentration, but rather the relative TBHP/xanthene concentrations. First-order behaviour is seen when [TBHP] is varied close to standard conditions (0.21 M), but deviates from first-order behaviour when [TBHP] is lowered further. At low TBHP concentration, the reaction profiles are fitted to
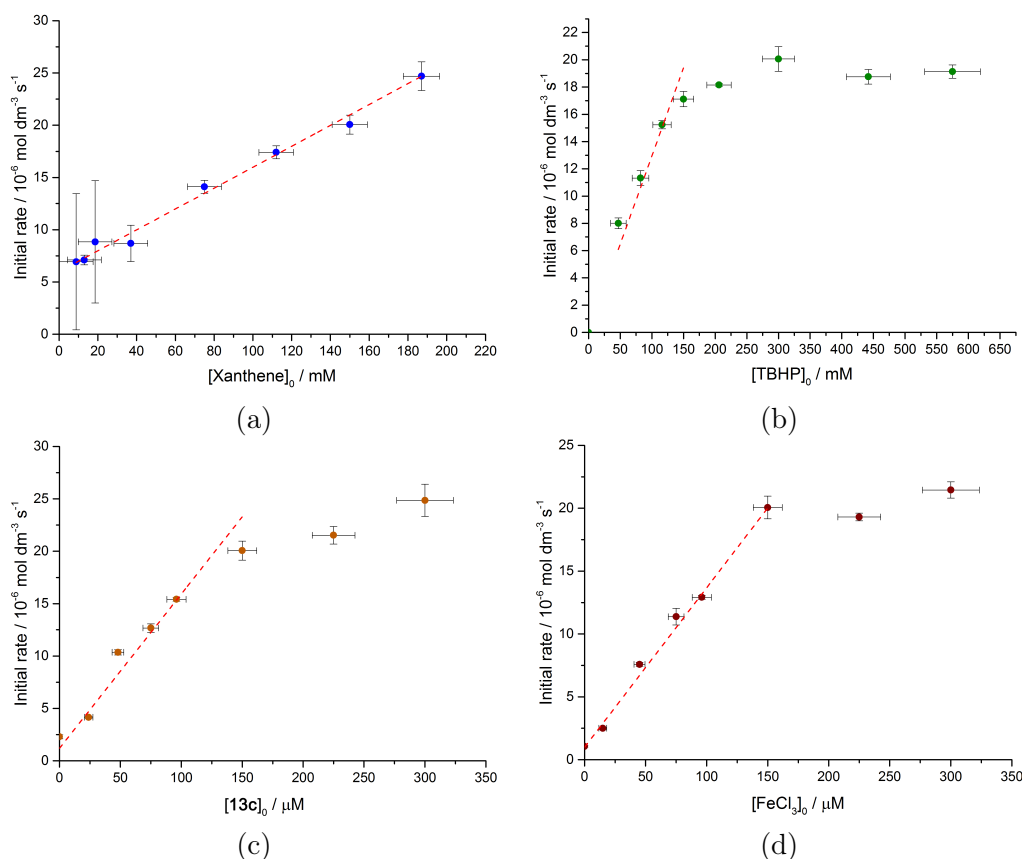
Figure 5.14: Dependencies of the initial rates of reaction on the initial concentrations of (a) xanthene, (b) TBHP, (c) **13c** and (d) FeCl$_3$. Rates determined by ^{1}H NMR reaction monitoring and errors determined by least-squares analysis of the slope; errors in concentrations calculated by error propagation. When not being varied, the initial concentration of xanthene was 0.15 M; that of TBHP was 0.30 M; and that of **13c** and FeCl$_3$ was 150 μM.

linear trends best when plotted as [xanthene]$^{-2}$.

A plot of initial rates against varying [TBHP]$_0$ also fitted well to a linear trend, in this case intercepting the origin (Figure 5.14 (b)). Saturation kinetics are seen at [TBHP]$_0$ concentrations higher than approximately 175 mM, where the initial rates approach a limiting value of approximately 1.9×10^{-5} mol dm^{-3} s^{-1}.

For both complex **13c** and FeCl$_3$, the initial rates also follow linear dependencies on their initial concentrations, suggesting first order kinetics with respect to each catalyst (Figure 5.14 (c) and (d)). The initial rates for both catalysts reach a plateau when their concentrations exceed 150 μM, *i.e.* when the concentration of one catalyst became super-stoichiometric over the other. This further reinforces the hypothesis that iron(III) and copper(II) carry out catalysis cooperatively, in a 1:1 ratio.

This initial rates study did not provide much insight into the reaction mechanism beyond highlighting that the reaction kinetics are complex and that the

rate law is similarly so. However, as the reactions from the initial rates study were monitored in full, the concentration *versus* time data were used to model the reaction kinetics under a variety of different starting conditions. How this modelling led to a possible reaction mechanism is discussed later in the Chapter.

Isotopic labelling experiments

Catalysed oxygenation reactions of xanthene and 9,9'-d_2-xanthene were carried out at 0.15 M xanthene, 0.57 M TBHP, 0.1 mol% **13c** and 0.1 mol% FeCl$_3$. Deuteration of xanthene at the benzylic 9-position slows the rate of xanthene consumption marginally, with a small primary kinetic isotope effect (KIE, ν_H/ν_D) of 1.5. Deuteration has a pronounced effect on the product formation, with much less alcohol being formed at a slower rate, giving a primary KIE of 6.2 for the formation of xanthydrol. Negligible amounts of ketone are formed in the reaction involving d_2-xanthene. In the case of protio-xanthene, at around 4 hours, the peroxy-ether concentration peaks and is then converted into ketone (Figure 5.3 (a)); conversely, under the same conditions for deutero-xanthene, there is no peak in the peroxy-ether concentration (Figure 5.16 (a)) and this latter product is formed with a negligible KIE of 1.1.
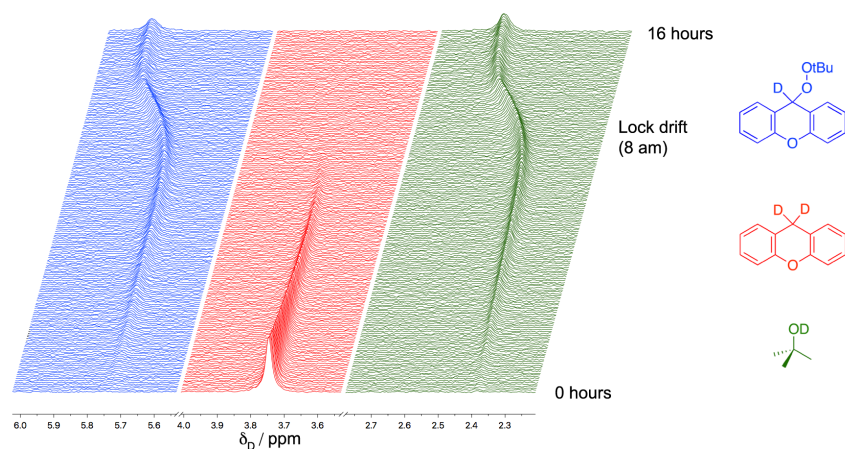
Figure 5.15: ^{2}H NMR reaction-monitoring of d_2-xanthene oxygenation, catalysed by **13c** and FeCl$_3$ (0.1 mol% each), using 4 equivalents of TBHP. The initial concentration of d_2-xanthene is 0.15 M. ^{2}H NMR spectra were pre-locked onto the C$_6$D$_6$ internal standard ^{2}H signal, and then measured on the lock channel.

Deuteration at the 9-position therefore has a more pronounced effect on the formation of xanthydrol as well as the second oxidation step, which suggests that HAA is turnover-limiting for the formation of xanthydrol and ketone only. The fact that there is practically no KIE for the peroxy-ether product and quite a significant KIE for the alcohol product is the first indication that these two
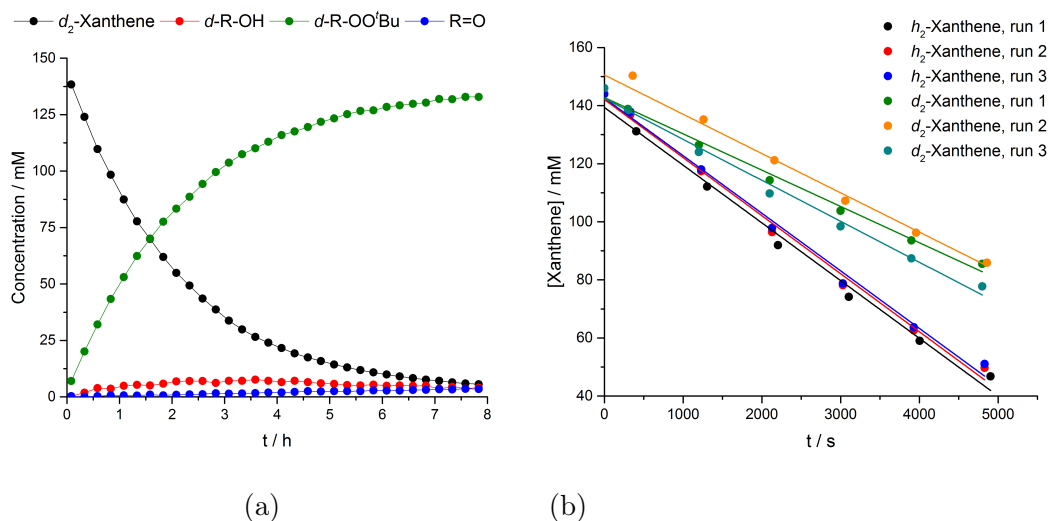
Figure 5.16: (a) Monitoring the progress of the d_2-xanthene oxygenation reaction, catalysed by **13c** and FeCl$_3$, using ^{1}H NMR spectroscopy. Reaction conditions: $[d_2$-xanthene$]_0 = 0.15$ M, $[$TBHP$]_0 = 0.57$ M, 0.1 mol% **13c**, 0.1 mol% FeCl$_3$, d_3-MeCN, 300 K. (b) Determination of the primary kinetic isotope effect for the rate of xanthene consumption, by comparison of the initial rates of h_2- and d_2-xanthene.

intermediate products are formed by different reaction pathways from the xanthene substrate.

The oxygenation reaction of d_2-xanthene was also monitored by ^{2}H NMR spectroscopy (Figure 5.15). This experiment confirmed that tBuOD is formed as a side-product, with the OD resonance observed at 2.40 ppm. Neither D$_2$O or HDO are seen, but are still considered possible side-products of the reaction as they are likely to undergo rapid H/D exchange with H$_2$O (from aqueous TBHP) and evade observation.

Hammett analysis

The influence of the electronic properties of the substrate on the rate of the reaction was investigated using a series of xanthene substrates substituted at the 2-position, under standard conditions where pseudo-first order kinetics are seen. The plot of $\log(k_{\text{obs, X}} / k_{\text{obs, 0}})$, where $k_{\text{obs, X}}$ is the pseudo-first order rate constant for the substituted substrate and $k_{\text{obs, 0}}$ is that for the unsubstituted substrate, against the Hammett σ parameters shows a linear correlation (Figure 5.17). Due to poor solubility of 2-chloro-xanthene in d_3-MeCN, the rate of reaction for that substrate was instead measured in CDCl$_3$, and the obtained data point for this substrate does not therefore fit well in the Hammett plot. The reaction constant, ρ, is given by the slope of the linear fit and is found to be positive and small in

magnitude (1.17 ± 0.18). This shows that there is a small rate enhancement when electron-withdrawing groups are present on the xanthene substrate and implies that there is some build-up of electron density at the benzylic reaction centre. For some radical reactions, the reaction constant is reported as less than 1.[46,47] The slightly larger value of 1.17 for the xanthene oxidation reaction therefore fits with the other observations that elements of both free-radical and radical-free processes are present in the mechanism. Therefore, this Hammett analysis does not support a truly radical-free reaction mechanism (proceeding *via* a metal-alkoxide complex). Combined with the other results discussed above, that indicate that the reaction is not truly free-radical, it seems that the mechanism is best described as proceeding *via* a metal-associated alkoxy-radical.
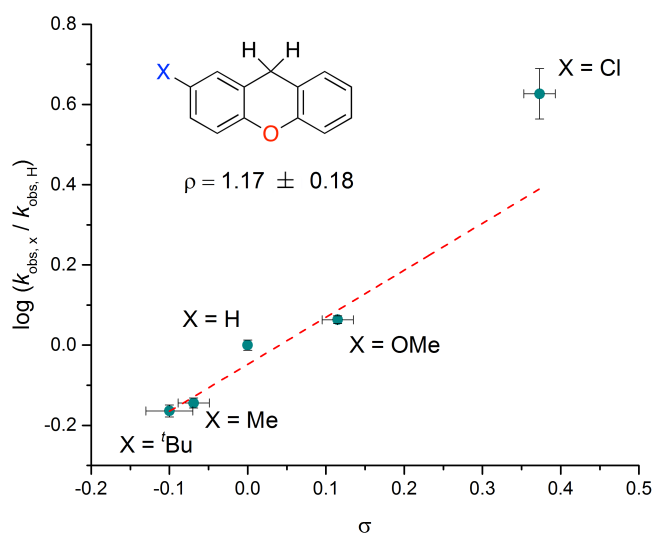
Figure 5.17: Hammett analysis for the xanthene oxygenation reaction. The pseudo-first order rate constants were determined by ^{1}H NMR reaction monitoring. The point for 2-chloroxanthene was determined from a reaction in a different solvent and is therefore not included in the linear fit. Reaction conditions: [xanthene]$_0$ = 0.15 M, [TBHP]$_0$ = 0.30 M, 0.1 mol% **13c**, 0.1 mol% FeCl$_3$, d_3-MeCN, 300 K.

General observations from NMR reaction monitoring

In addition to the kinetic observations discussed above, some important qualitative trends were also identified. Firstly, and in all cases, the concentration of the peroxy-ether intermediate only reaches a peak value when the xanthene substrate is entirely consumed, and it is only after this point that it is converted to the final ketone product, indicating that there is some competition between xanthene and the peroxy-ether. Secondly, the alcohol and peroxy-ether products form at identical rates when the initial concentrations of xanthene and TBHP are equimolar. However, increasing the TBHP concentration above that of xanthene

causes the peroxy-ether to be formed at a faster rate than the alcohol (Figure 5.18 (a)), indicating that these two products are being formed *via* different reaction pathways in the mechanism, with different dependencies on [TBHP]. Thirdly, in cases where there is enough oxidant for the intermediate products to convert to ketone, the alcohol concentration peaks just after the xanthene and peroxy-ether concentration values cross. This final point was explored in a more quantitative way, by plotting the correlated concentration profiles of [xanthene] against [xanthydrol], and also the [peroxy-ether] against [xanthydrol] (see Figure 5.18 (b) as an example, and Table 5.4). As a general trend, the value of $[\text{xanthydrol}]_{max}$ is always reached after the xanthene and peroxy-ether values have crossed. Furthermore, for the range of experiments where the $[\text{TBHP}]_0$: $[\text{xanthene}]_0$ ratio lies between the quite broad range of 1.6 and 4.0, the $[\text{peroxy-ether}]_t$: $[\text{xanthene}]_t$ ratio is between 1.6 and 2.2 at $[\text{xanthydrol}]_{max}$. Whilst this third point is quite abstract, it does highlight some of the interdependencies of the various species in the complex reaction mechanism. It might be that the rate of xanthydrol consumption outpaces that of its formation after xanthene concentration reaches a critical point, in which case it seems reasonable that xanthene and xanthydrol are converted to products from a common intermediate.

(a)

(b)
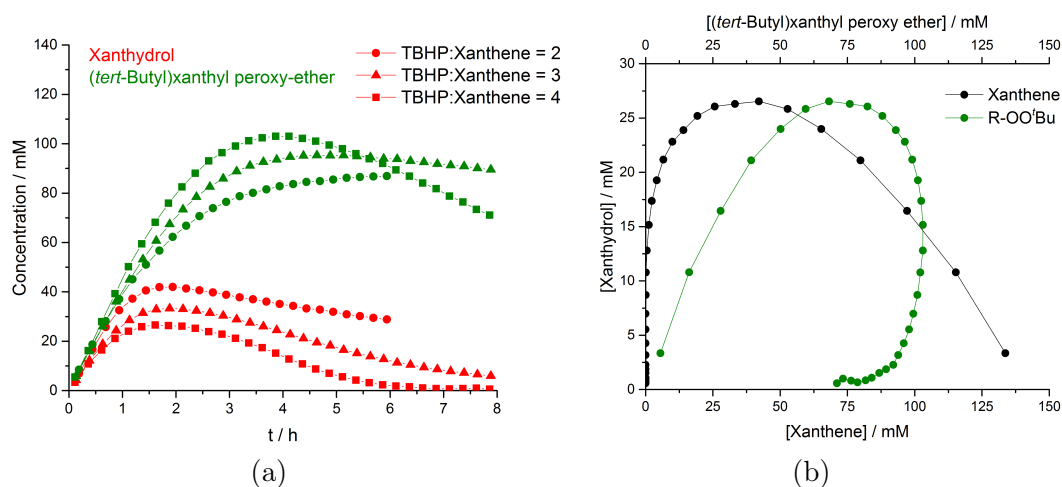
Figure 5.18: General observations from monitoring the xanthene oxygenation reaction catalysed by **13c**/FeCl$_3$. (a) Effect of increasing the oxidant:xanthene ratio on the peroxy-ether/alcohol partition. (b) Representative concentration / time plot showing correlation between [xanthene] and [xanthydrol], and also the correlation between the [peroxy ether] and [xanthydrol].

The initial rates of reaction of xanthydrol and the (*tert*-butyl)peroxy-ether were explored with different catalyst combinations and compared with those for the xanthene oxygenation reaction. By carrying out catalysed reactions with the isolated intermediate products it was confirmed that both the alcohol and peroxy-ether compounds contribute to the formation of xanthone. As summarised in Table

5.5, in all cases, the mixtures of **13c** and FeCl$_3$ promote an order-of-magnitude increase in the rate of reaction compared with either catalyst in isolation. This shows that the proposed adduct of **13c** and FeCl$_3$ improves all aspects of the xanthene oxygenation reaction to form xanthone, and does not only act on one substrate.

Table 5.4: Summary of information from correlated concentration plots, showing that for a certain [xanthene] range, the value of [xanthydrol]$_{max}$ is dependent on the ratio of [xanthene] : [(*tert*-butyl)xanthyl peroxy-ether].

[TBHP]$_0$: [xanthene]$_0$	[xanthene]$_0$ / mM	[peroxy-ether] : [xanthene] at [xanthydrol]$_{max}$
2.0	150	1.6
1.6	187	1.7
2.7	112	2.2
4.0	75	1.8
2.9	150	1.9
3.8	150	1.7

Table 5.5: Comparison of the impact of the different catalysts on the rate of oxygenation of xanthene, as well as the rate of oxidation of the intermediate products, which were isolated and studied in separate reactions. Reaction conditions: d_3-MeCN, 300 K, [xanthene]$_0$ = 0.15 M, [TBHP]$_0$ = 0.30 M; [xanthydrol]$_0$ = 0.15 M, [TBHP]$_0$ = 0.30 M; and [peroxy-ether]$_0$ = 0.10 M, [TBHP]$_0$ = 0.30 M.

Substrate	[**13c**] / mol%	[FeCl$_3$] / mol%	ν / mol dm^{-3} s^{-1}	Rate increase
Xanthene	0	0	1.10 E^{-8}	–
	0.1	0	1.18 E^{-6}	118
	0	0.1	2.38 E^{-6}	238
	0.1	0.1	2.14 E^{-5}	2144
Xanthydrol	0	0	1.11 E^{-8}	–
	0.1	0	1.06 E^{-6}	95
	0	0.1	3.13 E^{-8}	3
	0.1	0.1	4.65 E^{-6}	417
(*tert*-Butyl)	0	0	1.06 E^{-8}	–
xanthyl	0.1	0	1.82 E^{-6}	172
peroxy-ether	0	0.1	1.72 E^{-7}	16
	0.1	0.1	2.04 E^{-5}	1936

Kinetic modelling of the reaction mechanism

Taking into account all of the kinetic details discussed above, kinetic models – sets of elementary reactions, with individual rate constants – were built and fitted to some of the typical concentration-over-time data (such as Figure 5.3).[vi] The proposed kinetic model was assessed on how well it could simulate data sets it

[vi]All kinetic modelling was carried out by Prof. Guy C. Lloyd-Jones, University of Edinburgh.

had not been fitted to, and then altered in an iterative way until the simulations resembled the experimental data. Simple models could not adequately simulate the curvature of the experimental data, and also failed to accurately simulate experimental data from a range of starting conditions. The most satisfactory model that was obtained is complex and is highly sensitive to small changes in the individual rate constants. However, it adequately simulates some of the typical experimental data (see Figure 5.19) that feature high curvature in the concentration profiles. Importantly, the peroxy-ether concentration peaks as xanthene is depleted, and also the alcohol concentration peaks after the xanthene and peroxy-ether concentrations cross, which is discussed in more detail below.
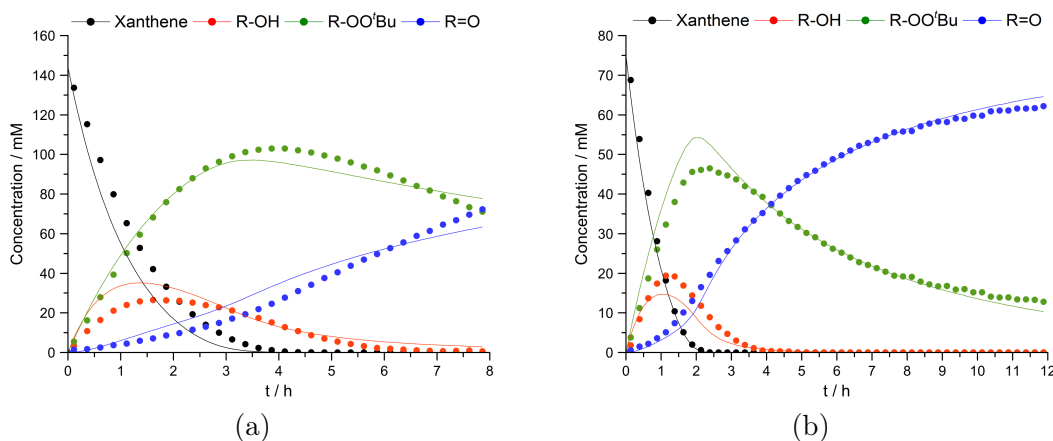
Figure 5.19: Representative plots showing simulation of the copper(II)/iron(III)-catalysed xanthene oxygenation reaction, monitored experimentally by *in situ* ^{1}H NMR spectroscopy. Reaction conditions: (a) 0.1 mol% **13c**, 0.1 mol% FeCl$_3$, [xanthene]$_0$ = 0.15 M, [TBHP]$_0$ = 0.57 M, 300 K, d_3-MeCN; (b) 0.2 mol% **13c**, 0.2 mol% FeCl$_3$, [xanthene]$_0$ = 0.075 M, [TBHP]$_0$ = 0.30 M. Experimental data plotted as points; simulated data plotted as curves.

In the proposed reaction mechanism (Scheme 5.7), the **13c**/FeCl$_3$ catalyst is first formed through an induction step (k_{ind}), before reacting with the TBHP oxidant to form "CAT·Ox" (k_1), which is assumed to feature TBHP coordinated to any combination of copper and/or iron centres. In the following reaction with xanthene (k_2), the activated TBHP carries out HAA from the substrate, yielding tBuOH; in the same elementary step, the remaining hydroxyl moiety from TBHP forms xanthydrol with the substrate, which remains bound to the catalyst. The resulting "CAT·Alc" intermediate reacts with a second equivalent of TBHP to form "CAT·Ox·Alc" (k_3), which is an important intermediate. From this intermediate, xanthene is converted to xanthydrol, and xanthydrol is also converted to the peroxy-ether and the ketone (k_{alc}, k_{eth} and k_{ket}, respectively); the "CAT·Alc" intermediate is regenerated in each case. The "CAT·Ox·Alc" intermediate also generates the peroxy-ether from the reaction with a further

equivalent of external oxidant to reform "CAT·Ox" (k_4), and also using the oxidant that is already bound, which reforms the catalyst on liberation of the peroxy-ether (k_5).

In a separate subcycle, "CAT·Ox" reacts with xanthydrol to form peroxy-ether that remains bound to the catalyst ("CAT·Eth", k_6). The catalyst is regenerated after the peroxy-ether is liberated (k_7). Ketone is formed from the peroxy-ether reacting with intermediate "CAT·Ox" (k_8), where the bound TBHP on the catalyst carries out HAA, yielding the ketone and tBuOH; "CAT·Ox" is reformed from the hydroxyl moiety remaining on "CAT·Ox" and the *tert*-butoxyl moiety that is cleaved from the peroxy-ether substrate.

Finally, the overall rates have been attenuated by including a slow catalyst decomposition step, that also consumes oxidant to give "Z" (k_{dec}). Slight inhibition of the catalyst was observed experimentally after addition of water or ketone to the initial reaction mixture, and this has been included in the kinetic model by adding a fast equilibrium step from "CAT·Ox", which generates a resting state on reaction with ketone (k_{inh}, K_{eq}). A full list of elementary reactions in the kinetic model is given in Scheme 5.7, along with the associated rate and equilibrium constants.

Despite its complexity, the proposed mechanism captures the main qualitative trends observed from reaction monitoring. Competition between xanthene and peroxy-ether exists at the "CAT·Ox" intermediate, in that the reaction with xanthene (k_2) is *ca.* 25 times faster than the reaction with the peroxy-ether. Conversion of the peroxy-ether to ketone will therefore only take place at an appreciable rate once xanthene has been depleted. Furthermore, the partitioning between the formation of the alcohol product and the peroxy-ether is captured as they are both formed from different reaction pathways in the model; xanthydrol is formed from k_{alc}, whereas the peroxy-ether is formed from reactions k_4, k_5 and k_7. Only k_4 is directly dependent on [TBHP], giving different sensitivities to the rates of formation for these intermediate products. Finally, the point that xanthydrol consumption outpaces that of its formation after xanthene concentration reaches a critical value is addressed; both xanthene and two equivalents of xanthydrol react with the "CAT·Ox·Alc" intermediate, with xanthene forming more xanthydrol, and xanthydrol in turn forming peroxy-ether and ketone (k_{alc}, k_{eth} and k_{ket}). As k_{alc} is larger than k_{eth} and k_{ket}, xanthydrol concentration should only be expected to peak when xanthene concentration is diminished, as is observed.

However, it is important to note that the proposed reaction mechanism has not been thoroughly interrogated experimentally. Many of the elementary steps

Complex **13c** =

Cu^{II}
Cu^{II}

Induction — $Fe^{III}Cl_3$ k_{ind}

Decomposition

Ox — "Z" k_{dec}

Cu^{II} Cl
Eth — $Cl-Fe^{III}$ = [CAT]
Cu^{II} Cl

Eth k_7

CAT–Eth

k_x	Reactant	Product
k_{alc}	Xanth	Alc
k_{eth}	Alc	Eth
k_{ket}	Alc	Ket

Reactant

Product

k_5 Eth   Ox k_1 Ox

Ox k_4

CAT   Ox   Alc

k_6 Alc

CAT–Ox

k_3 Ox   Xanth k_8 k_{inh}, K_{eq} Ox

CAT–Alc   Ket   CAT   Ket

Ket   Eth

Inhibition

OOH   H OH   H OOtBu   O

"Ox"   "Xanth"   "Alc"   "Eth"   "Ket"

$$Cu_2(L) + FeCl_3 \longrightarrow CAT \qquad k_{ind} = 0.392 \text{ M}^{-1}\text{ s}^{-1}$$
$$CAT + Ox \longrightarrow Z \qquad k_{dec} = 0.0026 \text{ M}^{-1}\text{ s}^{-1}$$
$$CAT + Ox \longrightarrow (CAT \cdot Ox) \qquad k_1 = 1.83 \text{ M}^{-1}\text{ s}^{-1}$$
$$(CAT \cdot Ox) + Ket \longrightarrow (CAT \cdot Ox \cdot Ket) \qquad k_{inh} = 1000 \text{ M}^{-1}\text{ s}^{-1}$$
$$K_{eq} = 6.18 \times 10^{-2} \text{ M}^{-1}\text{ s}^{-1}$$
$$(CAT \cdot Ox) + Xanth \longrightarrow (CAT \cdot Alc) \qquad k_2 = 62.53 \text{ M}^{-1}\text{ s}^{-1}$$
$$(CAT \cdot Alc) + Ox \longrightarrow (CAT \cdot Alc \cdot Ox) \qquad k_3 = 62950 \text{ M}^{-1}\text{ s}^{-1}$$
$$(CAT \cdot Ox \cdot Alc) + Xanth \longrightarrow (CAT \cdot Alc) + Alc \qquad k_{alc} = 1 \text{ M}^{-1}\text{ s}^{-1}$$
$$(CAT \cdot Ox \cdot Alc) + Alc \longrightarrow (CAT \cdot Alc) + Eth \qquad k_{eth} = 1 \times 10^{-8} \text{ M}^{-1}\text{ s}^{-1}$$
$$(CAT \cdot Ox \cdot Alc) + Alc \longrightarrow (CAT \cdot Alc) + Ket \qquad k_{ket} = 0.59 \text{ M}^{-1}\text{ s}^{-1}$$
$$(CAT \cdot Ox \cdot Alc) + Ox \longrightarrow (CAT \cdot Ox) + Eth \qquad k_4 = 0.15 \text{ M}^{-1}\text{ s}^{-1}$$
$$(CAT \cdot Ox \cdot Alc) \longrightarrow CAT + Eth \qquad k_5 = 0.047 \text{ s}^{-1}$$
$$(CAT \cdot Ox) + Alc \longrightarrow (CAT \cdot Eth) \qquad k_6 = 11.4 \text{ M}^{-1}\text{ s}^{-1}$$
$$(CAT \cdot Eth) \longrightarrow CAT + Eth \qquad k_7 = 0.306 \text{ s}^{-1}$$
$$(CAT \cdot Ox) + Eth \longrightarrow (CAT \cdot Ox) + Ket \qquad k_8 = 2.47 \text{ M}^{-1}\text{ s}^{-1}$$

Scheme 5.7: Top: proposed mechanism for the xanthene oxygenation reaction, catalysed by a mixture of the dinuclear copper(II) complex **13c** and FeCl$_3$. Bottom: rate and equilibrium constants for the kinetic model. All constants have been determined by fitting the kinetic model to experimental concentration / time data.

and intermediates have been built in to the model in order to attenuate the rates of reaction and improve the overall fit, and therefore some assumptions have

been made regarding the nature of the intermediates and the stoichiometries in the reaction. The main purpose of the model is to highlight that the reaction mechanism is complex and includes a number of interdependencies. Whilst most of the simulated data sets fit the experimental data quite well, a number of fits are quite poor, which highlights that further work is required to determine some of the details of the mechanism.

References

[1] J. Rosenthal, T. D. Luckett, J. M. Hodgkiss and D. G. Nocera, *J. Am. Chem. Soc.*, 2006, **128**, 6546.

[2] A. M. J. Devoille and J. B. Love, *Dalton Trans.*, 2012, **41**, 65.

[3] G. Givaja, M. Volpe, M. Edwards, A. Blake, C. Wilson, M. Schröder and J. Love, *Angew. Chem. Int. Ed.*, 2007, **46**, 584.

[4] I. Garcia-Bosch, R. E. Cowley, D. E. Diaz, M. A. Siegler, W. Nam, E. I. Solomon and K. D. Karlin, *Chem. -Eur. J.*, 2016, **22**, 5133.

[5] E. A. Lewis and W. B. Tolman, *Chem. Rev.*, 2004, **104**, 1047.

[6] P. L. Holland and W. B. Tolman, *Coord. Chem. Rev.*, 1999, **190–192**, 855.

[7] D. Dhar, G. M. Yee, A. D. Spaeth, D. W. Boyce, H. Zhang, B. Dereli, C. J. Cramer and W. B. Tolman, *J. Am. Chem. Soc.*, 2016, **138**, 356.

[8] D. Dhar and W. B. Tolman, *J. Am. Chem. Soc.*, 2015, **137**, 1322.

[9] N. Gagnon and W. B. Tolman, *Acc. Chem. Res.*, 2015, **48**, 2126.

[10] M. R. Halvagar, P. V. Solntsev, H. Lim, B. Hedman, K. O. Hodgson, E. I. Solomon, C. J. Cramer and W. B. Tolman, *J. Am. Chem. Soc.*, 2014, **136**, 7269.

[11] F. G. Bordwell, J. Cheng, G. Z. Ji, A. V. Satish and X. Zhang, *J. Am. Chem. Soc.*, 1991, **113**, 9790.

[12] D. W. Snelgrove, P. A. MacFaul, I. Keith U and D. D. M. Wayner, *Tetrahedron Lett.*, 1996, **37**, 823.

[13] E. A. Katayev, Y. A. Ustynyuk, V. M. Lynch and J. L. Sessler, *Chem. Commun.*, 2006, 4682.

[14] W. Reiter, A. Gerges, S. Lee, T. Deffo, T. Clifford, A. Danby and K. Bowman-James, *Coord. Chem. Rev.*, 1998, **174**, 343 .

[15] B. Join, K. Möller, C. Ziebart, K. Schröder, D. Gördes, K. Thurow, A. Spannenberg, K. Junge and M. Beller, *Adv. Synth. Catal.*, 2011, **353**, 3023.

[16] G. Rothenberg, L. Feldberg, H. Wiener and Y. Sasson, *J. Chem. Soc. Perk. T. 2*, 1998, 2429.

[17] P. J. A. Ruttink, J. K. Terlouw, T. M. Luider and P. C. Burgers, *J. Mass Spectrom.*, 2011, **46**, 223.

[18] S. E. Allen, R. R. Walvoord, R. Padilla-Salinas and M. C. Kozlowski, *Chem. Rev.*, 2013, **113**, 6234.

[19] N. Komiya, T. Naota, Y. Oda and S.-I. Murahashi, *J. Mol. Catal. A-Chem.*, 1997, **117**, 21.

[20] J. Yamaguchi, A. D. Yamaguchi and K. Itami, *Angew. Chem. Int. Ed.*, 2012, **51**, 8960.

[21] D. J. Faulkner, *Tetrahedron*, 1977, **33**, 1421.

[22] E. Askarizadeh, S. B. Yaghoob, D. M. Boghaei, A. M. Z. Slawin and J. B. Love, *Chem. Commun.*, 2010, **46**, 710.

[23] A. M. J. Devoille, P. Richardson, N. L. Bill, J. L. Sessler and J. B. Love, *Inorg. Chem.*, 2011, **50**, 3116.

[24] Y. Gao, J. Guery and C. Jacoboni, *Acta Crystallogr., Sect. C*, 1993, **49**, 147.

[25] R. İnam and C. Bilgin, *J. Appl. Electrochem.*, 2013, **43**, 425.

[26] Y. Tang, R. Huang, C. Liu, S. Yang, Z. Lu and S. Luo, *Anal. Methods*, 2013, **5**, 5508.

[27] A.-C. Lee, G. Liu, C.-K. Heng, S.-N. Tan, T.-M. Lim and Y. Lin, *Electroanalysis*, 2008, **20**, 2040.

[28] G. Givaja, M. Volpe, J. Leeland, M. Edwards, T. Young, S. Darby, S. Reid, A. Blake, C. Wilson, J. Wolowska, E. McInnes, M. Schröder and J. Love, *Chem. Eur. J.*, 2007, **13**, 3707.

[29] H. Muchalski, A. J. Levonyak, L. Xu, K. U. Ingold and N. A. Porter, *J. Am. Chem. Soc.*, 2015, **137**, 94.

[30] C. Knight and M. J. Perkins, *J. Chem. Soc. Chem. Comm.*, 1991, 925.

[31] D. H. R. Barton, *Tetrahedron*, 1998, **54**, 5805.

[32] D. H. R. Barton, B. Hu, D. K. Taylor and R. U. R. Wahl, *J. Chem. Soc. Perk. T. 2*, 1996, 1031.

[33] D. H. R. Barton, M. Costas Salgueiro and J. MacKinnon, *Tetrahedron*, 1997, **53**, 7417.

[34] F. Gozzo, *J. Mol. Catal. A-Chem.*, 2001, **171**, 1.

[35] M. J. Perkins, *Chem. Soc. Rev.*, 1996, **25**, 229.

[36] F. Minisci, F. Fontana, S. Araneo and F. Recupero, *J. Chem. Soc. Chem. Comm.*, 1994, 1823.

[37] F. Minisci, F. Fontana, S. Araneo and F. Recupero, *Tetrahedron Lett.*, 1994, **35**, 3759.

[38] F. Shi, M. K. Tse, Z. Li and M. Beller, *Chem. -Eur. J.*, 2008, **14**, 8793.

[39] P. A. MacFaul, K. U. Ingold, D. D. M. Wayner and L. Que, *J. Am. Chem. Soc.*, 1997, **119**, 10594.

[40] M. Weber and H. Fischer, *J. Am. Chem. Soc.*, 1999, **121**, 7381.

[41] I. W. C. E. Arends, K. U. Ingold and D. D. M. Wayner, *J. Am. Chem. Soc.*, 1995, **117**, 4710.

[42] M. Finn, R. Friedline, N. K. Suleman, C. J. Wohl and J. M. Tanko, *J. Am. Chem. Soc.*, 2004, **126**, 7578.

[43] J. K. Kochi, *Tetrahedron*, 1962, **18**, 483.

[44] J. England, R. Gondhia, L. Bigorra-Lopez, A. R. Petersen, A. J. P. White and G. J. P. Britovsek, *Dalton Trans.*, 2009, 5319.

[45] C. Limberg, *Angew. Chem. Int. Ed.*, 2003, **42**, 5932.

[46] R. Itô, T. Migita, N. Morikawa and O. Simamura, *Tetrahedron*, 1965, **21**, 955.

[47] D. V. Avila, K. U. Ingold, J. Lusztyk, W. R. Dolbier, H. Q. Pan and M. Muir, *J. Am. Chem. Soc.*, 1994, **116**, 99.

Chapter 6

Uranyl dipyrrin complexes

In this Chapter, the reduction chemistry of the uranyl complexes of the donor-expanded dipyrrin ligand L^2 is presented. As discussed in the introduction, achieving two-electron reduction of uranyl is important due to its relevance to uranium remediation by immobilisation. The involvement of a redox-active ligand in the uranyl reduction process represents a novel reduction mechanism.

The synthetic work presented in this chapter is the result of a collaborative effort, carried out mainly by Dr Markus Zegke, Dr Nicola Bell and Lucy Platts.

6.1 Synthesis

6.1.1 Synthesis of a uranyl(VI) dipyrrin complex

Metalation of the donor-expanded dipyrrin, HL^2, was first attempted through the trans-amination reaction with the uranyl silyl-amide complex $UO_2\{N(SiMe_3)_2\}_2(py)_2$, at -60 °C in pyridine. The amido-uranyl dipyrrin complex could not be isolated as a clean product, yielding only viscous oils that produced uninformative NMR spectra. This amido complex was therefore only formed *in situ*. Room temperature protonolysis with pyridinium chloride exchanged the silyl-amido ligand for a chlorido ligand, slightly reducing the solubility of the product in hexanes. Washing the crude material with hexanes afforded the chlorido uranyl dipyrrin complex, $UO_2(Cl)(L^2)$ (**21**), as a blue solid in much higher purity, in 76 % yield (Scheme 6.1).

An alternative synthesis of **21** involved the addition of HL^2 to a 1:1 mixture of $UO_2\{N(SiMe_3)_2\}_2(thf)_2$ and $UO_2Cl_2(thf)_2$ in toluene. The mixture of uranyl starting materials equilibrate to $UO_2\{N(SiMe_3)_2\}(Cl)(thf)_2$ *in situ*, and react with HL^2 to yield **21** in a single step through a trans-amination reaction, in a slightly lower yield of 63 %.

In C_6D_6, there are four resonances in the ^1H NMR spectrum of **21**. The imine
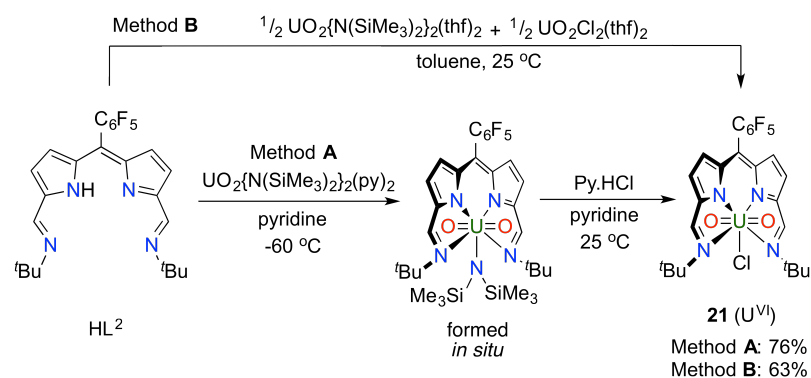
Scheme 6.1: Synthetic pathways to the uranyl dipyrrin complex, **21**.

protons appear at 9.52 ppm, equivalent pyrrole protons appear as doublets at 7.30 and 7.18 ppm, and *tert*-butyl protons give rise to a single resonance at 2.01 ppm. In the ^{19}F NMR spectrum, a single set of sharp resonances are observed for the C_6F_5-substituent, at -140.68, -155.19 and -163.34 ppm.

Noteworthy absorption bands in the IR spectrum of **21** are those ascribed to the imine functional group at 1556 cm^{-1}, which is lower in energy compared to the free ligand HL^2, and also the asymmetric stretching mode of the uranyl group (ν_3) at 878 cm^{-1}, which is typical for uranyl(VI) complexes.[1,2]
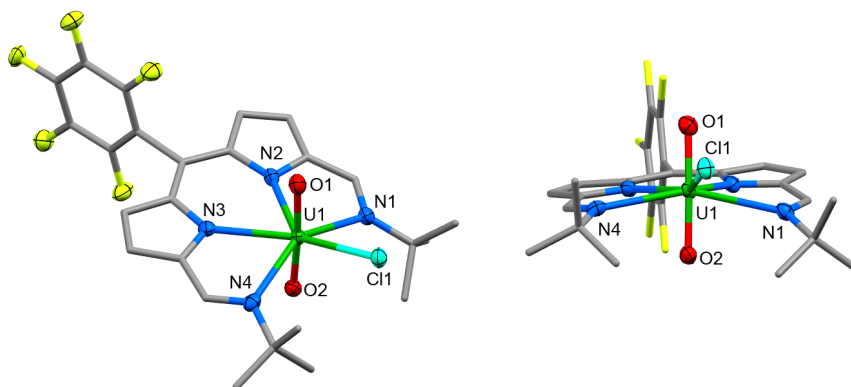
Figure 6.1: Alternative views of the solid-state structure of **21**. Displacement ellipsoids are drawn at 50 % probability and for clarity, two benzene solvent molecules and all protons have been omitted.

Purple/blue pleochroic single crystals of **21** were grown from a concentrated benzene solution, and the solid-state structure was determined by X-ray crystallography (Figure 6.1). For complex **21**, the seven-coordinate uranium(VI) centre resides in a distorted pentagonal-bipyramidal coordination geometry, where the nitrogen atoms of the donor-expanded dipyrrin and the chloride ligand occupy the equatorial positions, with the equatorial bond angles summing to 368.26°. The chloride ligand is situated 1.647 Å above the mean N$_4$-plane, and its displacement

from its position in the idealised geometry means that steric interactions with the nearby *tert*-butyl groups are minimised. These *tert*-butyl groups bend away from the same face of the dipyrrin N_4-donor-plane, meaning that the C_{2v} symmetry that is observed in solution is not retained in the solid state. The two equivalent U-O bond lengths of 1.766(4) Å are typical for a uranyl(VI) complex,[1,2] and the O-U-O angle is essentially linear at 175.5(2)°.

6.1.2 Synthesis of a U(IV) dipyrrin complex

Reaction of **21** with one equivalent of the inner-sphere titanium(III) reductant $[TiCp_2Cl]_2$ forms the titanium oxo-functionalised uranium(IV) complex $[(TiCp_2Cl)–OUO–(TiCp_2Cl)(Cl)(L^2)]$ (**22**, Scheme 6.2). The dark blue compound is paramagnetic but displays ^1H NMR resonances between -40 ppm and $+50$ ppm. A single resonance is observed for the imine protons at -37.33 pm, and the *tert*-butyl protons appear at -31.68 ppm. Magnetisation transfer was observed for the two resonances at -17.90 and -22.80 ppm by correlation spectroscopy, and these resonances are therefore assigned to the pyrrole protons. A single resonance at 43.63 ppm integrates as 20H per dipyrrin and is therefore assigned to four equivalent cyclopentadienyl ligands of the two titanocene chloride units. In the ^{19}F NMR spectrum, a single set of resonances was observed for the C_6F_5 group, at -153.48, -161.97 and -170.44 ppm.
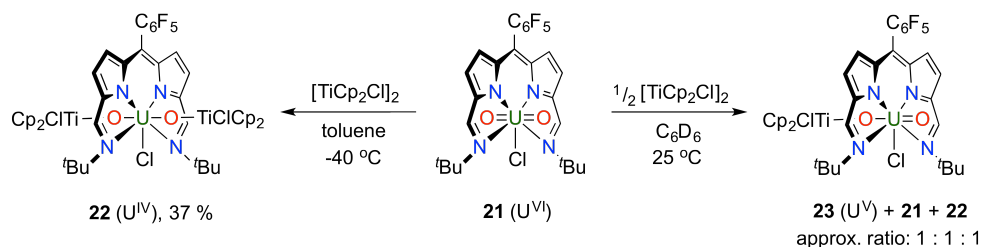
Scheme 6.2: Synthesis of **22** and **23** by reduction of the uranyl complex **21** with an inner-sphere titanium(III) reductant.

Dark blue crystals of **22** were grown from a concentrated benzene solution and the solid-state structure was determined by X-ray crystallography (Figure 6.2). No counter-ions are present in the asymmetric unit, meaning **22** is charge-neutral; both the uranium and titanium centres are therefore assigned formal oxidation states of $+4$. The pentagonal-bipyramidal coordination geometry around uranium is more regular in **22** compared to **21**, with the equatorial bond angles summing to 360.6°. This may be due to the *tert*-butyl groups bending away from opposite faces of the dipyrrin N_4-donor plane. The steric constraints around the uranium centre are more relaxed in **22** due to an elongation of the U-N bond distances,
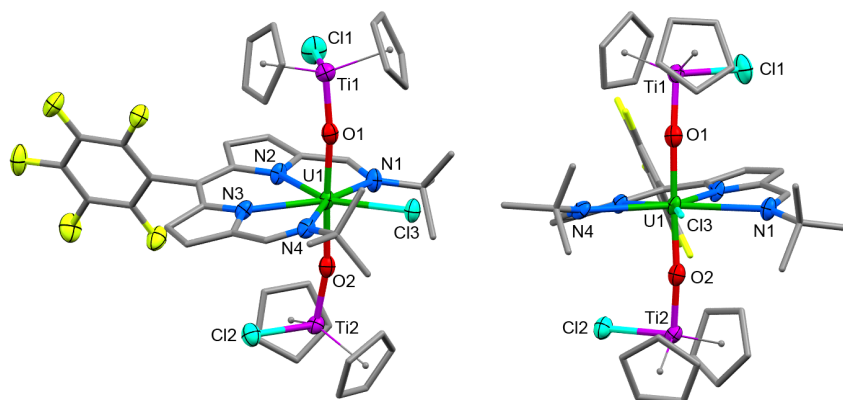
Figure 6.2: Alternative views of the solid-state structure of **22**. Displacement ellipsoids are drawn at 50 % probability and for clarity, one benzene solvent molecule and all protons have been omitted.

by 0.06 to 0.12 Å, which is also consistent with reduction of U(VI) to a lower oxidation state.

Importantly, at 2.062(7) to 2.066(7) Å, the U-O bonds are elongated significantly in comparison with **21** and are similar to U(IV) siloxide complexes (2.065 Å),[3] but are longer than U(V) siloxide complexes (1.993 Å).[4] These U-O bond lengths therefore support the +4 oxidation state for uranium. Based on a CCD search that generated 3028 related complexes, single U-O bond lengths are on average 2.361 Å, which suggests that the U-O bonds in **22** retain some multiple-bond character. The Ti-O bond lengths in **22**, of 1.841(7) Å, are similar to that found in the Ti(IV) oxo-bridged dimer $[TiCp_2Cl]_2(\mu-O)$ (1.837(2) Å).[5]

An intense IR absorption band at 630 cm^{-1} was observed for **22** and is assigned to the asymmetric O-U-O stretching mode.[3,6] This stretching frequency is 250 cm^{-1} lower in energy compared to **21** but approximately 200 cm^{-1} higher in energy than the equatorial U-O single bonds found in U(VI)-alkoxide[7] and -thiocarbamato complexes,[8] again suggesting some retention of multiple-bond character. In comparison, oxo-functionalised uranyl(V) Pacman complexes display uranyl stretching frequencies at higher energies, between 709 and 765 cm^{-1}.[9]

Looking at the X-ray crystal structure alone, there is some ambiguity in the formal oxidation state on uranium, as the reduction by titanium(III) could conceivably also produce a uranium(V) complex ligated by a dipyrrin radical. In support of the +4 oxidation state on uranium, a comparison of the solid-state structures of **21** and **22** reveals that the bond lengths in the dipyrrin ligand are identical, which is shown pictorially in Figure 6.3. If **22** was a uranium(V) complex supported by a radical dipyrrin ligand, an elongation of the C-C bond lengths in the ligand framework would be expected.
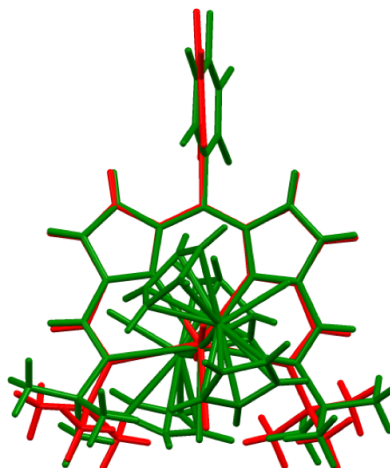
Figure 6.3: Overlaid solid-state structures of **21** (red) and **22** (green), highlighting similarities in the dipyrrin ligand bond distances in each structure.

Furthermore, on an X-band spectrometer, no EPR signal was observed for a CH_2Cl_2 / toluene solution of **22**, at either 300 K or 223 K, further supporting the assigned uranium(IV)/titanium(IV) oxidation states. Generally, it is difficult to observe uranium-centred EPR signals without cooling to very low temperatures.[10,11] In particular, EPR signals arising from the two unpaired electrons in the $^3H_4$ uranium(IV) ion are rarely observable even at low temperatures, due to the large number of thermally-accessible J-states that facilitate spin-pairing. In contrast, organic-based radicals often produce strong EPR signals even at room temperature.[12]

6.1.3 Attempted synthesis of a uranium(V) dipyrrin complex

Isolation of an intermediate, mono-titanated uranium(V) complex (**23**) was attempted from the reaction of **21** and 0.5 equivalents of $[TiCp_2Cl]_2$ (Scheme 6.2). Reactions in both C_6D_6 and d_8-THF did not lead to clean formation of the uranium(V) complex, but ^1H NMR spectra of the reaction mixture indicated that a 1:1:1 mixture of the uranium(VI) starting material (**21**), the uranium(V) complex (**23**), and the uranium(IV) complex (**22**) was formed. The uranium(V) complex could not be isolated and is only identified by its ^1H NMR spectrum, with resonances appearing between $+20$ and -10 ppm; the *tert*-butyl protons appear as a single resonance at -8.58 ppm, and a resonance at 19.35 ppm, integrating as 10H per dipyrrin, is assigned to one titanocene chloride unit.

Although the uranium(V) complex could not be isolated, its observation by NMR spectroscopy provides useful information on its disproportionation kinetics. Over a 24 hour period, **23** disproportionates very slowly (by approximately 11 %)

to produce more of **21** and **22**, with the latter precipitating out of C_6D_6. This 11 % increase in disproportionation products over 24 hours does not account for the immediate formation of the uranium(IV) complex on reaction with 1 equivalent of $[TiCp_2Cl]_2$, and suggests that **22** is formed by a more direct reduction pathway.

6.2 Electronic spectroscopy

In the visible region, the electronic absorption spectrum of HL^2 features a single, broad absorption band centred with λ_{max} at 485 nm.[13] Upon coordination to uranyl, the lowest-energy absorption is bathochromically shifted, with two absorption bands observed for **21** at 598 nm and 557 nm, and a shoulder at 511 nm (Figure 6.4 (a)). Changing the polarity of the solvent, from toluene to THF, gives rise to a small hypsochromic shift for the band at 557 nm, and that band is therefore assigned to a charge-transfer transition. In contrast, solvatochromism was not observed for the band at 598 nm, and this band is therefore assigned to a π-π^* transition, which is a common feature for dipyrrin complexes of the transition metals.[14–16] The molecular orbitals of **21** were determined by DFT calculations, as discussed below (see Figure 6.9), and a group-theoretical analysis in the C_{2v} point group reveals that many of the transitions in the frontier orbital set are orbitally-allowed; this includes the HOMO-LUMO transition and gives rise to a large extinction coefficient of 43,000 dm^3 mol^{-1} cm^{-1} for the lowest energy absorption band.

The doubly titanated complex **22** has a near-identical absorption spectrum to **21**, albeit with a significantly reduced molar absorptivity of 11,000 dm^3 mol^{-1} cm^{-1} at 598 nm. Complex **22** also exhibits several weak absorption bands in the near-infra-red (NIR) region, with extinction coefficients less than 50 dm^3 mol^{-1} cm^{-1} (Figure 6.4 (b)). These are assigned to formally forbidden, intra-configurational f-f transitions. Absorption bands of similar shape and energy were previously reported for uranium(IV) pentahalide anions, and these similarities support the +4 oxidation state for uranium.[17,18] Higher energy f-f transitions for the ground-state $^3H_4$ ion could not be observed due to the strong absorption of the dipyrrin chromophore in the visible region.

Room temperature excitation of HL^2 in THF at 280, 405, 425 and 550 nm produces broad fluorescence spectra with emission bands centred at 490 and 600 nm in all cases (Figure 6.4 (c)).[i] The fluorescence lifetimes of the emission features for HL^2 were recorded following 405 nm excitation with a picosecond pulsed diode

---

[i]Emission spectroscopy was carried out by Dr Louise Natrajan, University of Manchester.
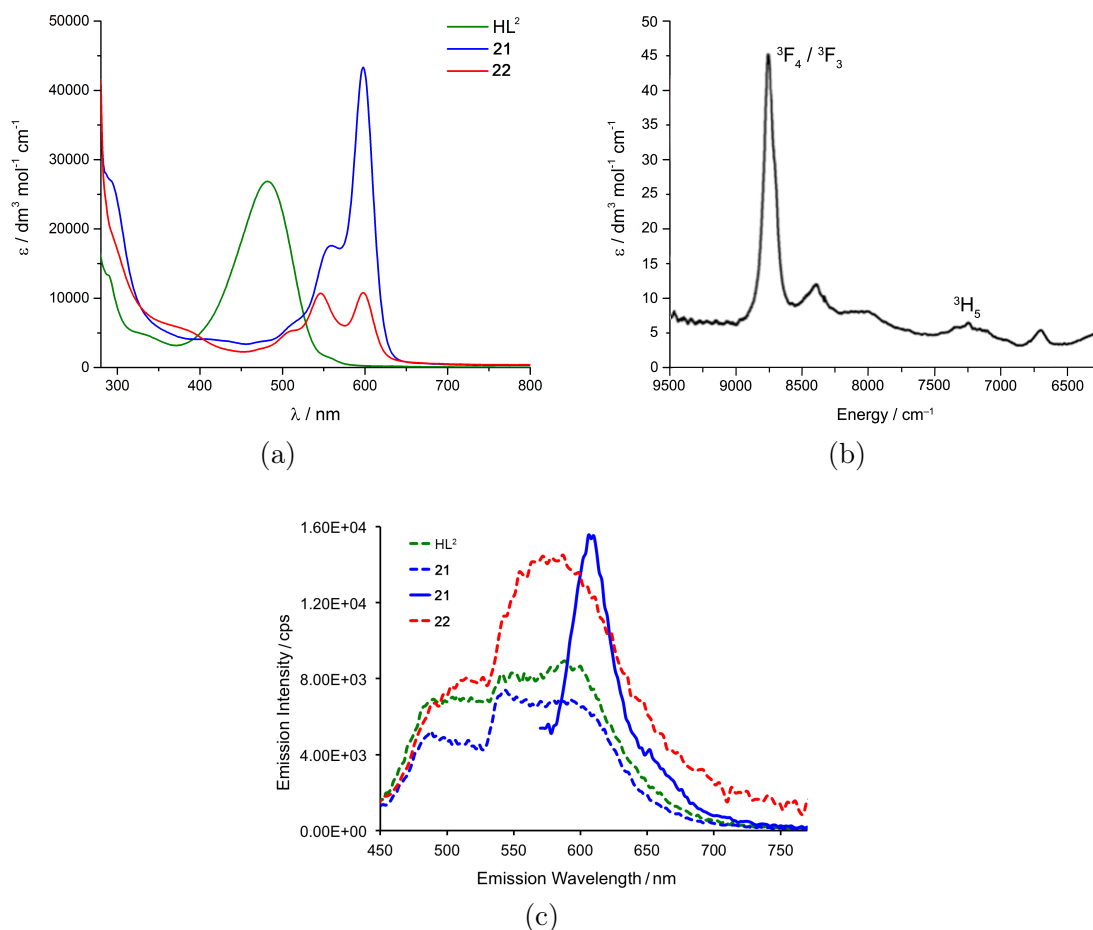
Figure 6.4: (a) UV/visible absorption spectra of HL^2, **21** and **22**, measured at room temperature in toluene. (b) NIR absorption spectrum of **22** measured at room temperature in toluene. (c) Emission spectra of HL^2, **21** and **22** following excitation at 425 nm (dashed traces), and emission spectrum of **21** following excitation at 550 nm (solid trace).

LASER and were measured in the nanosecond regime.[19] All lifetimes fit well to biexponential decay kinetics, with components of approximately 1 and 5 ns. In a frozen glass at 77 K, following excitation at 240, 405 and 550 nm, the resulting emission spectra are essentially identical to those recorded in fluid solution at room temperature. The fluorescence lifetimes at 77 K are only slightly longer from those recorded in fluid solution and again are biexponential at approximately 1 and 4 ns for both the emission at 490 and 600 nm.

In the uranium complexes **21** and **22**, excitation into the dipyrrin ligand absorption bands at 240, 405 and 425 nm affords spectra that are similar to those of HL^2. However, for complex **21**, the larger molar absorption coefficient in the band at 593 nm enabled spectral isolation of the emission arising from this transition. The recorded emission spectrum is essentially a mirror image of the absorption band with only a marginal Stokes shift of 8 nm (Figure 6.4 (c), solid trace). Room temperature time-resolved measurements enabled the luminescence

lifetimes of all the emission bands in **21** and **22** to be measured following excitation at 405 nm, and these were found to be biexponential and comparable to those measured for HL^2 in fluid solution. Unfortunately, accurate lifetime data were not obtained for complexes **21** and **22** at 77 K due to the comparatively weaker emission intensities compared to HL^2 in frozen THF in optically dilute samples.

The short lifetimes of the excited states of **21** and **22** indicate that those complexes possess high ligand-character in the frontier set of molecular orbitals. Therefore, redox processes for **21** are expected to occur at the ligand before they occur at the metal centre. In contrast, the excited state of the uranyl ion is much longer lived, giving rise to μs-scale phosphorescence.[20] Insight into the emission profile of the uranyl ion in the dipyrrin setting is precluded by the dominance of the ligand in the absorption and emission spectra.

6.3 Electrochemical characterisation

Due to the redox non-innocence of the dipyrrin ligand, thorough electrochemical characterisation was carried out. To aid assignment of the redox processes observed by voltammetry, chemical reductants were chosen to target individual reduction processes, allowing further characterisation of the reduced species using EPR spectroscopy[ii] and electronic absorption spectroscopy.
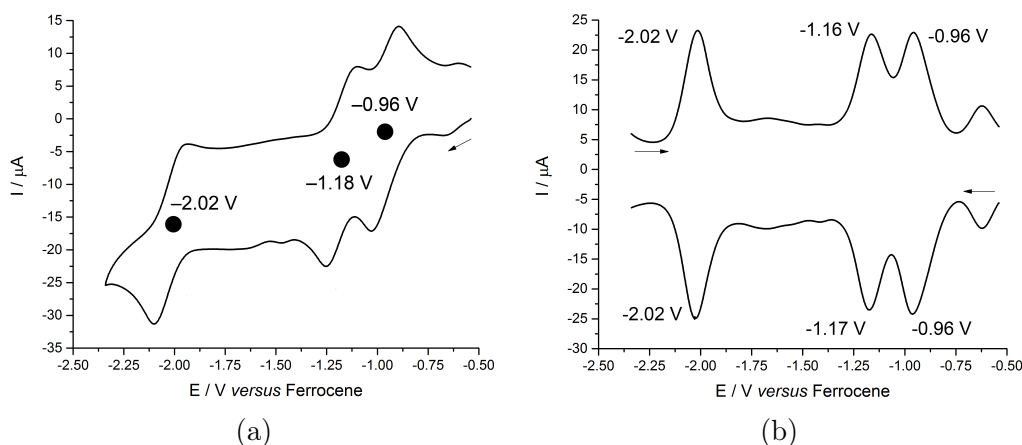
Figure 6.5: Electrochemical characterisation of **21** by (a) cyclic voltammetry and (b) square-wave voltammetry. Both measured at 100 mV s^{-1} in 0.1 M [^{n}Bu$_4$N][BPh$_4$] solution in CH$_2$Cl$_2$, using a glassy-carbon working electrode.

The CV of the uranyl dipyrrin complex **21** in CH_2Cl_2 features three reversible reduction processes at $E_{1/2}$ -0.96 V, -1.18 V and -2.02 V *versus* ferrocene (Figure 6.5 (a)). The waves of the first two reduction processes were overlapping,

---

[ii]EPR spectroscopy was carried out by Dr Stephen Sproules, University of Glasgow.

and the third process occurred near the edge of the CH_2Cl_2 / [$^nBu_4N$][BPh_4] electrochemical window, meaning that a reliable assessment of their peak heights or areas was not possible. However, the higher resolution inherent in the square-wave voltammogram (Figure 6.5 (b)) makes an assessment of their peak areas more reliable; in that case, 92 – 98 % of the charge passed in the forward scan was passed back in the return scan, indicating high stability of all three reduced species on the timescale of the experiment. Furthermore, the peak potentials in the forward and return scans in the SWV were identical, and also matched the $E_{1/2}$ potentials determined by CV exactly, further supporting that these reduction processes are reversible.

6.3.1 Chemical outer-sphere reduction

Both of the first two reduction processes for **21** are in the region previously reported for U(VI)/U(V) redox couples.[3,4,21–23] It was suspected that one of these reduction processes is due to ligand-reduction, and EPR spectroscopy was used to characterise the electronic structure of the products following targeted chemical reduction. Whilst the first two reduction processes appear to be overlapping in the CV, they are resolved by 220 mV, giving a relatively small comproportionation constant ($K_c = 10^{\Delta E/59} = 5356$). This indicates that the two electronic states observed by CV are stable against comproportionation and are likely to be isolable.

First reduction

The formal redox potential for chromium(0) bis(benzene), $Cr(\eta\text{-}C_6H_6)_2$, in CH_2Cl_2 is -1.15 V *versus* ferrocene,[24] and is well-suited to carry out the first outer-sphere reduction of **21** only. Addition of one equivalent of $Cr(\eta\text{-}C_6H_6)_2$ to **21** in CH_2Cl_2 / toluene turned the blue solution magenta immediately. The product of the reduction was strongly paramagnetic due to the presence of the chromium(I) species, and as such, NMR spectroscopy could not be used to characterise the product.

An *in situ* reduction of **21** with $Cr(\eta\text{-}C_6H_6)_2$ was carried out again, and the reaction mixture was analysed by EPR spectroscopy. The resulting spectrum was dominated by the chromium(I) paramagnet, which included super-hyperfine coupling to the twelve arene protons. Whilst the reduction of the uranyl dipyrrin complex was clearly successful, the resulting chromium(I) counter-ion precludes an assessment of its electronic structure by EPR spectroscopy.

$CoCp_2$ is more strongly reducing than $Cr(\eta\text{-}C_6H_6)_2$, with a formal Co(III)/
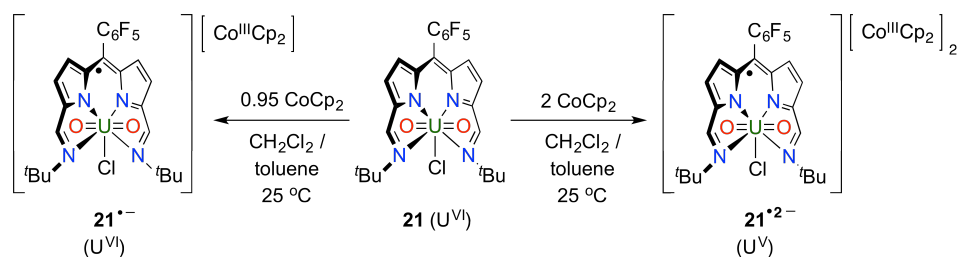
Scheme 6.3: Chemical outer-sphere reduction of **21** with CoCp$_2$, affording **21**$^{\cdot-}$ and **21**$^{\cdot 2-}$.

Co(II) redox potential of -1.33 V in CH$_2$Cl$_2$,[24] and should therefore be able to carry out both the first and second outer-sphere reductions of the uranyl dipyrrin complex. However, the first reduction can be carried out selectively using sub-stoichiometric amounts of the reductant (Scheme 6.3). This is due to the fact that the first and second reduction processes are well separated by 220 mV, giving a small K_c value as mentioned above. The reaction between **21** and 0.95 equivalents of CoCp$_2$ in CH$_2$Cl$_2$ forms a strongly paramagnetic, magenta solution of [UO$_2$(Cl)(L^2)][CoCp$_2$] (**21**$^{\cdot-}$). In this case the cobaltocenium counter-ion is 18-electron on cobalt and therefore closed-shell, meaning that the paramagnetism arises from the uranyl dipyrrin complex only.
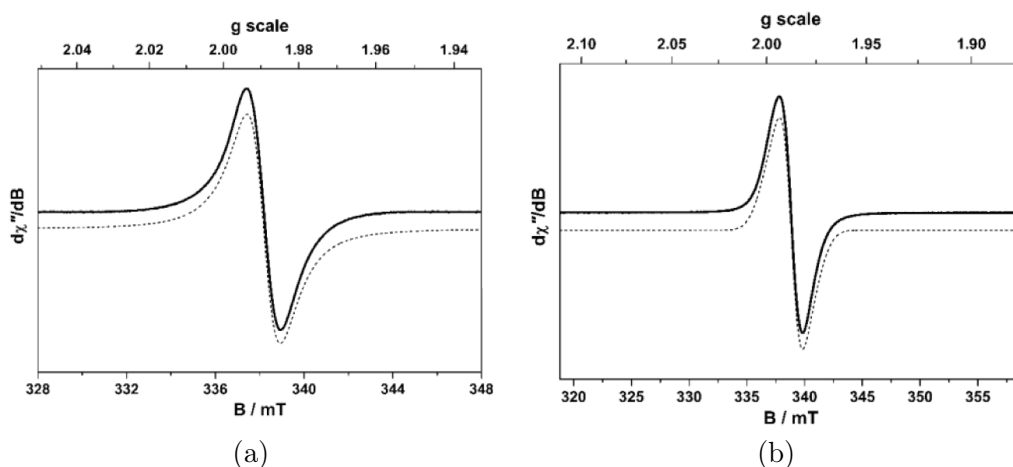
Figure 6.6: X-band EPR spectra of **21**$^{\cdot-}$, formed from the one-electron reduction of **21** by 0.95 equivalents CoCp$_2$ in CH$_2$Cl$_2$ / toluene. (a) Fluid-solution spectrum measured at 223 K (g_{iso} = 1.9893). (b) Frozen-solution measured at 130 K (g_{anis} = 1.9974, 1.9872, 1.9786). The measured spectra are shown as solid lines, and the simulated spectra are shown as dashed lines.

The EPR spectrum of **21**$^{\cdot-}$ consists of a relatively sharp signal that is consistent with an $S = 1/2$ spin-system. No hyperfine structure was resolved at room temperature or at 223 K (Figure 6.6 (a)), and simulation of the signal yielded g_{iso} 1.9893, which is significantly shifted from that of the free electron (2.0023). The EPR spectrum is most consistent with the formation of a ligand-centred radical species, where the coordinated uranium(VI) centre causes both the g-shift

and line-broadening in the signal, obscuring the hyperfine coupling that would be expected with the various spin-active nuclei present in the dipyrrin ligand. Other uranium(VI)-L$^{\cdot}$ species in the literature have displayed similar g-shifts and line-broadening in their fluid solution EPR spectra.[25–27] The observation of an EPR signal at room temperature also attests to the formation of a ligand-centred radical, as the formation of a $5f^1$ uranium(V) complex would display drastically different magnetic behaviour and is unlikely to be observed until cooling to much lower temperatures (5 – 100 K).[11,28]

The spectrum measured for a frozen solution, at 130 K, is highly isotropic, and similar g-values of 1.9974, 1.9872 and 1.9786 were obtained from the simulation (Figure 6.6 (b)). The lack of g-anisotropy and the small g-shift is strong evidence that there is negligible uranium-character in the SOMO that contains the unpaired electron, *i.e.* that which arises from the LUMO of **21**.

From one reaction of **21** with an excess of CoCp$_2$ in THF, single crystals were grown that were suitable for X-ray crystallography, and the crystal structure of the reduction product was determined (Figure 6.7). Despite the excess CoCp$_2$ in the reaction, only one equivalent of the [CoCp$_2$]$^+$ ion is present per molecule of **21**$^{\cdot-}$, with two near-equivalent molecules of [**21**$^{\cdot-}$][CoCp$_2$] found in the asymmetric unit. The single cobaltocenium ion per uranyl dipyrrin complex indicates that a single-electron reduction has taken place. At 1.772(3) Å and 1.779(3) Å, the uranyl-oxo bond distances are equivalent to those in the parent compound, **21**, and indicate that the reduction has not occurred at the metal centre. Instead, there are some changes in the bond lengths within the dipyrrin structure, although these could be seen as statistically insignificant to 3σ. Generally, the changes in the dipyrrin match those expected based on the LUMO of **21** (see below), in that bond contraction is observed where there is a bonding MO interaction in the LUMO, and bond elongation is observed where there is an anti-bonding MO interaction in the LUMO. The X-ray crystal structure therefore supports that the first reduction of **21** forms a radical-dipyrrin uranium(VI) complex.
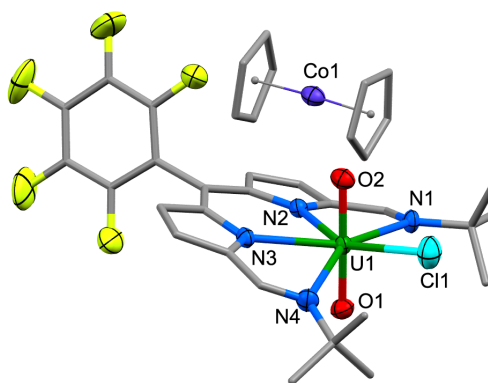
Figure 6.7: Solid-state structure of [**21**·⁻][CoCp₂]. Displacement ellipsoids are drawn at 50 % probability and for clarity, protons, one THF solvent molecule and another equivalent of **21**·⁻ present in the asymmetric unit have been omitted.

Second reduction

Both the first and second outer-sphere reductions of **21** were carried out by the reaction with two equivalents of CoCp₂. The blue solution of **21** immediately turned magenta to yield a strongly paramagnetic, NMR-silent product. If this second reduction was also ligand-based, the product would be a closed-shell, dianionic dipyrrin ligand coordinated to a uranium(VI) centre, which would be diamagnetic. The formation of a paramagnetic product is a strong indication that the second reduction is metal-based, forming a uranium(V) complex of a dipyrrin-radical, **21**·²⁻.
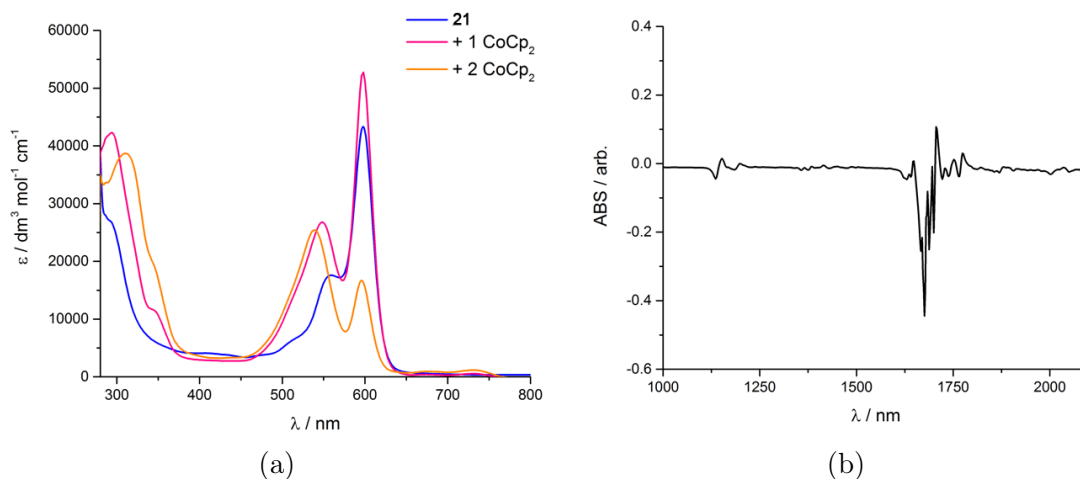
Figure 6.8: Electronic absorption spectra of **21** following *in situ* reduction with CoCp₂. (a) UV-visible absorption spectra and (b) NIR absorption spectrum, both measured at room temperature as toluene solutions.

Single crystals of the suspected radical dianionic complex could not be isolated. In this case, EPR spectroscopy would not provide any further information, as

the spectrum would be dominated by the dipyrrin radical signal. Instead, the *in situ* reduction of **21** by one and two equivalents of $CoCp_2$ in toluene was carried out and the reaction mixtures were analysed by UV-vis-NIR spectrophotometry (Figure 6.8). Reaction of **21** with one equivalent of $CoCp_2$ caused a significant hypsochromic shift in the charge-transfer band, observed at 557 nm ($\epsilon = 43,000$ dm^3 mol^{-1} cm^{-1}) in **21**, to 548 nm (27,000) in **21**$^{\cdot-}$. Addition of a second equivalent of $CoCp_2$, forming **21**$^{\cdot 2-}$, caused a further hypsochromic shift to 539 nm (26,000). It should be noted that the electronic absorption spectrum obtained from the *in situ* reduction with one equivalent of $CoCp_2$ matched the spectrum obtained by dissolving the single crystals of [**21**$^{\cdot-}$][$CoCp_2$].

These absorption spectra confirm that the products from reduction of **21** with one and two equivalents of $CoCp_2$ yield different compounds, that are spectrally distinct. This is evident from the different relative heights of the charge-transfer and π-π^* bands in **21**$^{\cdot-}$ and **21**$^{\cdot 2-}$. No *f-f* transitions were observed in the NIR spectrum of **21**$^{\cdot-}$, providing further evidence that the product of that reaction is a uranium(VI) complex of a dipyrrin-radical (Figure 6.8 (b)). On the other hand, no *f-f* transitions were observed for the two-electron reduction product, which therefore opposes the assigned metal-based reduction in that case.

Third reduction

The third reduction of **21** is in a similar region for previously reported U(V)/U(IV) redox couples, albeit at more positive potential than previously reported uranium(V) Pacman complexes,[4,22,23] and is tentatively assigned as such. However, the potassium complex of the dipyrrin, KL^2, also undergoes a second ligand-based reduction at strongly negative potential, and so this third reduction of **21** could also be assigned as a second ligand-based reduction.

Attempts were made to carry out a chemical reduction of **21** with potassium metal, which has a formal redox potential of approximately -3 V *versus* ferrocene.[24] However, the reaction did not proceed cleanly, and no single product could be isolated from the reaction mixture, so this was not pursued further.

6.4   Inner-sphere reduction vs. outer-sphere reduction

The uranyl(VI) compound **21** undergoes a one-electron outer-sphere reduction to afford a uranium(VI) radical-dipyrrin complex in the first instance, with the second outer-sphere reduction affording a uranium(V) radical-dipyrrin complex. Therefore, through chemical outer-sphere reduction using $CoCp_2$, with its formal

Co(III)/Co(II) redox potential of -1.33 V, the lowest uranium oxidation state that is attainable is uranium(V). In comparison, the Ti(IV)/Ti(III) redox potential for the inner-sphere reductant, $[TiCp_2Cl]_2$, has been measured between -0.81 and -1.27 V,[29,30] and is therefore similarly, if not slightly less, reducing. Nevertheless, chemical reduction using the titanium(III) reductant yields the uranium(IV) complex only, even though the U(V)/U(IV) redox couple for **21** was measured at much more negative potential by voltammetry, at -2.02 V. It was suspected that both the dipyrrin redox non-innocence and coordination of the Lewis acidic Ti(IV) centre to the uranyl oxo-atoms were responsible for an overall metal-based reduction, and a DFT investigation was undertaken to study this in more detail.

6.4.1 DFT investigation of the reduction mechanisms

Density functional theory was used to provide insight into the molecular orbital structures, oxidation states and energetics of the reduction pathway. The B3PW91 hybrid functional was employed, and small atoms were treated using the 6-31G(d,p) basis-set. For the larger uranium, titanium and chlorine atoms, effective core-potentials and accompanying basis sets from the Stuttgart-Köln ECP library were used.[iii]

The first inner-sphere, one-electron reduction of **21** could occur in two ways. The first is a direct reduction of the uranium(VI) centre to yield the [U(V)-Ti(IV)-(L)] complex (**23**). The second is an indirect reduction, forming a dipyrrin-radical in the first instance, [U(VI)-Ti(IV)-(L$^{\cdot-}$)], then forming **23** by ligand-to-metal electron transfer. A second inner-sphere reduction of **23** would yield the observed [U(IV)-Ti(IV)$_2$-(L)] product, **22**. Based on the spectroscopic evidence discussed above, principally the EPR data that indicates that the first outer-sphere reduction with CoCp$_2$ affords a dipyrrin-centred radical uranium(VI) complex, and also the electronic absorption and emission spectroscopies, which indicate that the frontier set of molecular orbitals contain high ligand-character, an initial ligand-based reduction was thought most likely. Inspection of the molecular orbitals for **21** reveals that the LUMO, that will accept the first electron, is purely ligand-based, whereas the metal-based LUMO+1 is 19.7 kcal mol^{-1} higher in energy (Figure 6.9).

The geometry of the first reduction product, [U(VI)-Ti(IV)-(L$^{\cdot-}$)], was optimised using an "f-in-core" relativistic effective core potential (RECP) to fix the oxidation state of uranium at +6. It was found that this first reduction step

---

[iii]DFT calculations were carried out by Prof. Laurent Maron and Carlos Alvarez Lamfsus, Université de Toulouse.

LUMO, **21** (ligand-based)   LUMO+1, **21** (metal-based)

SOMO, **22** (metal-based)   LUMO, **22** (mixed-character)
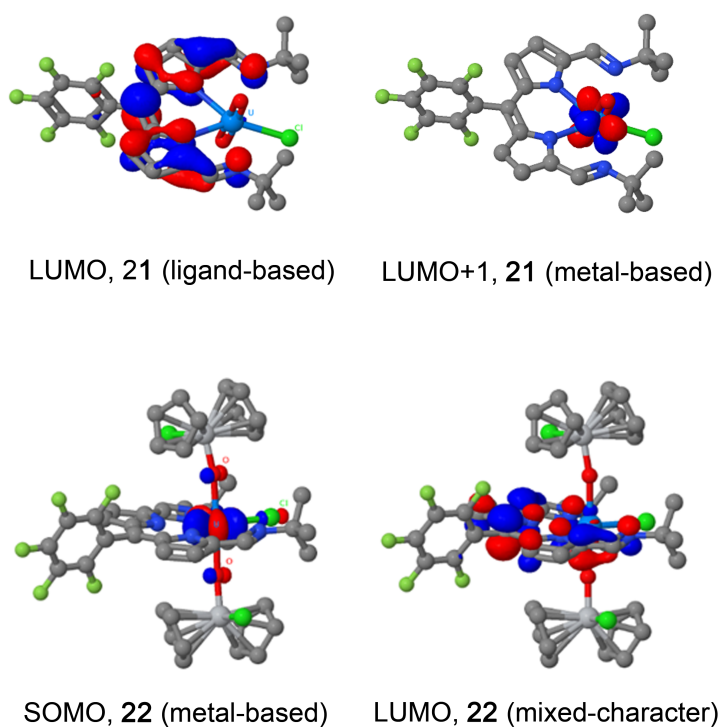
Figure 6.9: Molecular orbitals of **21** and **22**, obtained from DFT optimised geometries.

is exergonic by 5.7 kcal mol^{-1} with respect to the separated reactants (**21** + [TiCp$_2$Cl]$_2$). Removing the constraint on the uranium oxidation state, by performing a small-core calculation, forms the more stable [U(V)-Ti(IV)-(L)] intermediate, **23**; this ligand-to-metal electron-transfer process is exergonic by a further 4.0 kcal mol^{-1}. The first reduction of **21** by [TiCp$_2$Cl]$_2$ is therefore occurring in two steps, with a ligand-based reduction occurring in the first instance. Importantly, it is the dipyrrin radical that ultimately facilitates reduction of the uranium(VI) centre, and this appears to be thermodynamically driven by coordination of the Lewis acidic titanium(IV) centre. Modulation of the thermodynamics of uranyl redox processes by coordination of Lewis acids is well documented in the literature.[3,21,31] Such an electron-transfer process was clearly not operative when the non-coordinating CoCp$_2$ reductant was used, as the dipyrrin radical was observable by EPR spectroscopy.

Due to the mixed uranium/ligand character in the LUMO of the intermediate uranium(V) complex, it is not straightforward to determine the extent of involvement of the dipyrrin ligand in the second reduction step. Nevertheless, the second reduction of the uranium(V) complex to give the [U(IV)-Ti(IV)$_2$-(L)] complex, **22**, was determined to be exergonic by 12.5 kcal mol^{-1}. The energetics of this ligand-mediated, inner-sphere reduction mechanism are represented in Figure
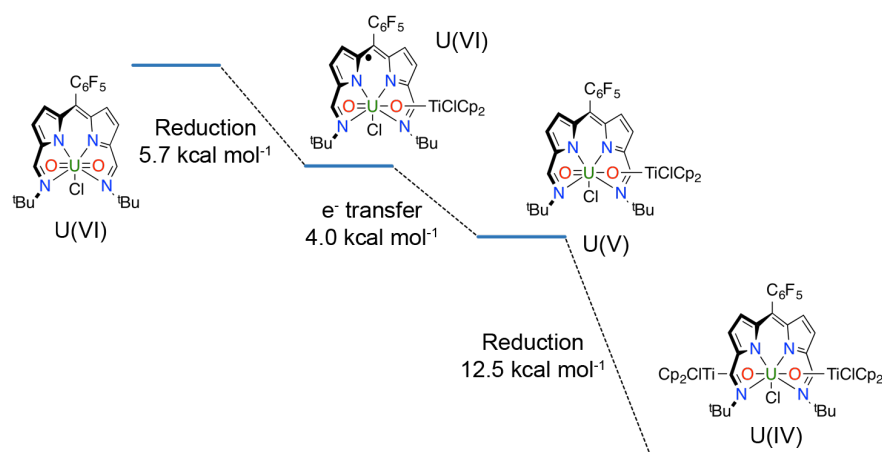
Figure 6.10: Energetics of the inner-sphere reduction of **21** by $[TiCp_2Cl]_2$, facilitated by initial reduction of the dipyrrin ligand and consequent ligand-to-metal electron-transfer.
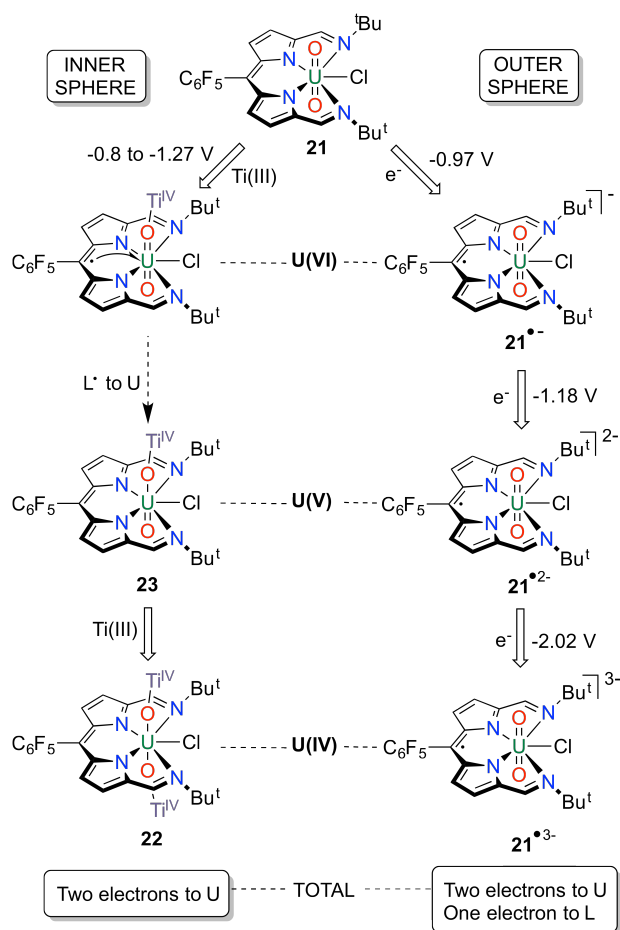
Scheme 6.4: Summary of the contrasting outer-sphere and inner-sphere reduction pathways for **21**.

6.10. It should be noted that the optimised DFT geometry for **22** is in close agreement with the solid-state structure for **22**. The oxidation state in the DFT

structure is unambiguously +4 as the main contributor to the SOMO is clearly the uranium $5f_{x^3-3xy^2}$ orbital (Figure 6.9). An alternative pathway, to afford **22** by disproportionation of the uranium(V) intermediate, was also investigated, and this was found to be 11.2 kcal mol^{-1} higher in energy compared to the reduction by sequential reaction with titanium(III). This is in line with the experimental observations, that the reaction of **21** with $[Cp_2TiCl]_2$ to afford **22** is rapid, whereas disproportion accounts for only 11 % conversion of **23** after 24 hours.

From the combined spectroscopic/voltammetric/computational study, it is clear that the reduction of the uranyl dipyrrin complex **21** by outer-sphere and inner-sphere reductants proceeds by different pathways, as summarised in Scheme 6.4. The involvement of the dipyrrin in the inner-sphere reduction mechanism means that the uranium(IV) oxidation state is much more readily obtainable, and may be accessed using "weaker" reductants. Without the Lewis-acid promoted transfer of the electron from the dipyrrin to the uranium centre, the outer-sphere reduction pathway requires three electrons to reach the +4 oxidation state on uranium, whereas the inner-sphere pathway requires only two.

References

[1] P. L. Arnold, A. J. Blake, C. Wilson and J. B. Love, *Inorg. Chem.*, 2004, **43**, 8206.

[2] T. W. Hayton and G. Wu, *J. Am. Chem. Soc.*, 2008, **130**, 2005.

[3] J. L. Brown, C. C. Mokhtarzadeh, J. M. Lever, G. Wu and T. W. Hayton, *Inorg. Chem.*, 2011, **50**, 5105.

[4] P. L. Arnold, D. Patel, C. Wilson and J. B. Love, *Nature*, 2008, **451**, 315.

[5] Y. L. Page, J. McCowan, B. Hunter and R. Heyding, *J. Organomet. Chem.*, 1980, **193**, 201 .

[6] S. Fortier and T. W. Hayton, *Coord. Chem. Rev.*, 2010, **254**, 197.

[7] D. L. Perry, *Inorg. Chim. Acta*, 1981, **48**, 117 .

[8] D. L. Perry, A. Zalkin, H. Ruben and D. H. Templeton, *Inorg. Chem.*, 1982, **21**, 237.

[9] P. L. Arnold, A.-F. Pécharman and J. B. Love, *Angew. Chem. Int. Ed.*, 2011, **50**, 9456.

[10] H. Nakai, X. Hu, L. N. Zakharov, A. L. Rheingold and K. Meyer, *Inorg. Chem.*, 2004, **43**, 855.

[11] D. M. King, F. Tuna, E. J. L. McInnes, J. McMaster, W. Lewis, A. J. Blake and S. T. Liddle, *Science*, 2012, **337**, 717.

[12] A. A. Kuzhelev, D. V. Trukhin, O. A. Krumkacheva, R. K. Strizhakov, O. Y. Rogozhnikova, T. I. Troitskaya, M. V. Fedin, V. M. Tormyshev and E. G. Bagryanskaya, *J. Phys. Chem. B*, 2015, **119**, 13630.

[13] J. R. Pankhurst, T. Cadenbach, D. Betz, C. Finn and J. B. Love, *Dalton Trans.*, 2015, **44**, 2066.

[14] E. R. King and T. A. Betley, *Inorg. Chem.*, 2009, **48**, 2361.

[15] C. Bronner, S. A. Baudron, M. W. Hosseini, C. A. Strassert, A. Guenet and L. De Cola, *Dalton Trans.*, 2010, **39**, 180.

[16] T. E. Hewat, L. J. Yellowlees and N. Robertson, *Dalton Trans.*, 2014, **43**, 4127.

[17] M. Karbowiak, A. Mech and J. Drożdżyński, *Chem. Phys.*, 2005, **308**, 135.

[18] E. Hashem, A. N. Swinburne, C. Schulzke, R. C. Evans, J. A. Platts, A. Kerridge, L. S. Natrajan and R. J. Baker, *RSC Advances*, 2013, **3**, 4350.

[19] H. L. Kee, C. Kirmaier, L. Yu, P. Thamyongkit, W. J. Youngblood, M. E. Calder, L. Ramos, B. C. Noll, D. F. Bocian, W. R. Scheidt, R. R. Birge, J. S. Lindsey and D. Holten, *J. Phys. Chem. B*, 2005, **109**, 20433.

[20] L. S. Natrajan, *Coord. Chem. Rev.*, 2012, **256**, 1583.

[21] P. L. Arnold, A.-F. Pécharman, E. Hollis, A. Yahia, L. Maron, S. Parsons and J. B. Love, *Nat. Chem.*, 2010, **2**, 1056.

[22] P. L. Arnold, G. M. Jones, S. O. Odoh, G. Schreckenbach, N. Magnani and J. B. Love, *Nat. Chem.*, 2012, **4**, 221.

[23] P. L. Arnold, G. M. Jones, Q.-J. Pan, G. Schreckenbach and J. B. Love, *Dalton Trans.*, 2012, **41**, 6595.

[24] N. G. Connelly and W. E. Geiger, *Chem. Rev.*, 1996, **96**, 877.

[25] P. J. Melfi, S. K. Kim, J. T. Lee, F. Bolze, D. Seidel, V. M. Lynch, J. M. Veauthier, A. J. Gaunt, M. P. Neu, Z. Ou, K. M. Kadish, S. Fukuzumi, K. Ohkubo and J. L. Sessler, *Inorg. Chem.*, 2007, **46**, 5143.

[26] N. H. Anderson, S. O. Odoh, U. J. Williams, A. J. Lewis, G. L. Wagner, J. Lezama Pacheco, S. A. Kozimor, L. Gagliardi, E. J. Schelter and S. C. Bart, *J. Am. Chem. Soc.*, 2015, **137**, 4690.

[27] J. J. Kiernicki, D. P. Cladis, P. E. Fanwick, M. Zeller and S. C. Bart, *J. Am. Chem. Soc.*, 2015, **137**, 11115.

[28] K. Meyer, D. Mindiola, T. Baker, W. Davis and C. Cummins, *Angew. Chem. Int. Ed.*, 2000, **39**, 3063.

[29] R. J. Enemærke, J. Larsen, T. Skrydstrup and K. Daasbjerg, *J. Am. Chem. Soc.*, 2004, **126**, 7853.

[30] R. J. Enemærke, J. Larsen, T. Skrydstrup and K. Daasbjerg, *Organometallics*, 2004, **23**, 1866.

[31] D. D. Schnaars, G. Wu and T. W. Hayton, *J. Am. Chem. Soc.*, 2009, **131**, 17532.

Chapter 7

Conclusions

Two new macrocyclic Schiff-base ligands bearing proton *meso*-substituents have been prepared as part of this work; L^3 features an *ortho*-phenylene spacer group between the two donor-expanded dipyrromethane coordination pockets, whereas L^4 features a 1,8-anthracenyl spacer group. These macrocycles could not be oxidised to their macrocyclic dipyrrins using a range of oxidants and synthetic strategies, either in their metal-free, protonated forms or in their metal complexes. The macrocyclic dipyrrin complex **14**, which is best described as a copper(II) complex of a radical dipyrrin ligand based on DFT calculations, was only isolated as a small batch of poorly-diffracting single crystals after slow aerobic oxidation of the dipyrromethane copper(II) complex **13a**. The difficulty in oxidising these macrocyclic dipyrromethanes is ascribed to their rigidity, as the resulting N_4-donor pocket in the dipyrrin is fully π-conjugated and bonded directly to planar aromatic spacer groups; decomposition is likely to occur when the oxidation of the macrocycle is not concerted with folding to the Pacman geometry. This highlights a major barrier in the synthesis of binucleating, non-porphyrin, Pacman dipyrrin ligands. As discussed in the introduction, alkyl-bridged, macrocyclic "accordian" dipyrrins and an asymmetric Pacman dipyrrin (**XXIII** and **XXIV** in the introduction) are able to incorporate a dipyrrin group into a macrocyclic setting due to greater flexibility in the macrocycle, but neither of these types of complexes offer the reactive cleft between two metal centres found in symmetric Pacman complexes.

Whilst attempting to prepare macrocyclic dipyrrin complexes, it was discovered that the small proton *meso*-substituent in $L^{3,4}$ induces significant differences in the macrocyclic dipyrromethane complexes, in comparison with complexes of dialkyl *meso*-disubstituted macrocycles. With L^3, bowl conformations are adopted with small +2 metal ions of the first-row transition metals and zinc(II), instead of classic Pacman geometries. Consequently, the degree of electronic communication between

paramagnetic metal ions is greatly reduced in complexes of L^3 in comparison with Pacman complexes. This is evident from cyclic voltammetry experiments that feature more reversible redox features and, where geometric changes are not associated with the change in oxidation state, concerted multi-electron redox. In agreement, EPR spectroscopy also shows that the two copper(II) ions in **13a** are isolated, with the spectrum resembling that of an $S = \frac{1}{2}$ system.

The zinc(II) chemistry of macrocycles $L^{3,4}$ contrasts with that of dialkyl *meso*-disubstituted macrocycles. The speciation of the dinuclear zinc(II) complexes is much better defined where the proton and C_6F_5 substituents are present, leading to more informative NMR spectra and the crystallographic characterisation of complex **7b** without the need for coordinated anions between the two metal centres. These subtle changes in the macrocycle also influence new reactivity, such that metallation of $L^{3,4}$ with $ZnEt_2$ results in unusual tetranuclear zinc(II) complexes; the tetranuclear complex of L^4 (**8b**) is the first bowl-shaped complex of an anthracenyl-pillared Schiff-base macrocycle. The ancillary ethyl ligands in the tetranuclear zinc(II) complexes of $L^{3,4}$ also open routes to the synthesis of macrocycle-supported molecular clusters of zinc(II) and oxo, hydroxide, phenoxide and alkoxide ligands, and whilst the $\{Zn(\mu_2-OH)\}_4$ cluster reacts with CO_2 to precipitate $ZnCO_3$ in a stoichiometric reaction, the alkoxide complexes have been used successfully in ROCOP catalysis. The catalytic formation of polycarbonate materials from CO_2 and cyclohexene oxide is a new form of reactivity for this class of Schiff-base macrocycle, and whilst there remains a number of open questions regarding the ROCOP catalysis studies, mainly involving the speciation of the active catalyst and characterisation of some of the polymers, this study highlights how sensitive catalysts are to quite subtle changes in molecular structure. Given the similar coordination environments around the zinc centres, it is surprising that the *ortho*-phenylene macrocyclic complex achieves high conversion of the epoxide substrate, with good selectivity for carbonate linkages, whereas the related anthracenyl-containing complex is essentially inactive. This highlights how the design of the supporting ligands in molecular clusters effect the reactivity, perhaps by imparting differences in the relative stabilities of the zinc-alkoxide clusters in this case.

The dinuclear copper(II) complexes **13a**, **13b** and **13c** (the latter being a classic Pacman complex) have also been used as hydrocarbon oxygenation catalysts, a previously unexplored application for these Schiff-base macrocycles, and it was discovered that the catalyst stability and reaction temperature were improved after addition of $FeCl_3$. An array of analytical techniques points towards a loosely-

associated adduct between the copper(II) macrocycle and $FeCl_3$ acting as the catalytically-active species, an interaction that is directed by the macrocycle scaffold. Such cooperative action between two different metal catalysts has not previously been explored in oxidation catalysis. Whilst the product distribution in this work is similar to that obtained from $CuCl_2$, the turnover frequency of **13c**/$FeCl_3$ is four times as fast due to the macrocyclic ligand. This work also acts as a proof of principle in that ligands can be designed to encourage cooperativity between different metal ions in solution to improve catalysis. Perhaps a similar strategy might be applied to other catalytic reactions in the future, offering improvement to promising catalysts that undergo decomposition, or affording novel catalytic reactivity that cannot be achieved using single-metal catalysts. The mechanistic investigation that forms part of this work highlights the complexity of the reaction mechanism in the xanthene oxygenation reaction and is an ongoing effort. This work conflicts with some of the entrenched views in the literature concerning when a reaction mechanism is radical or non-radical, with the reaction catalysed by mixtures of **13c** and $FeCl_3$ seeming to incorporate elements of both types of mechanism, suggesting that the intermediates might be metal-associated radicals rather than freely-diffusing radicals or formal metal-bound alkoxide or organometallic species. Detailed reaction monitoring has been used to determine a plausible reaction mechanism through the observation of qualitative trends and kinetic modelling; this model does not perfectly simulate the reaction under all starting conditions, but does satisfactorily reproduce the important qualitative trends. Further work must be done to fine-tune and chemically authenticate the mechanism, but it is a good starting point.

A third area of catalysis that has been explored in this thesis is the electro-catalytic reduction of CO_2. Unfortunately, the dinuclear macrocycles of copper(II), iron(II), nickel(II) and palladium(II) are not active in this type of catalysis. However, an iron(II) complex of the acyclic, donor-expanded dipyrrin ligand L^2 (complex **18**) is very active at an overpotential of 1 V and has a similar intrinsic activity at zero overpotential as some state-of-the-art iron porphyrin complexes. Further work is required to determine which products are formed from this reaction by gas chromatography, and to determine the Faradaic yields of the products. The solution-state structure of **18** is evidently complex based on its convoluted cyclic voltammogram; its X-ray crystal structure also shows that the complex is prone to halide ligand-scrambling and that the dipyrrin ligand is surprisingly flexible at the *meso*-position, allowing the N_4-donor pocket to split into two imino-pyrrolide coordinating units. Macrocyclic dipyrrin ligands would enforce more defined

solution-state structures, and combined with the dipyrrin electronic structure that seems to promote high activity in the reduction of CO_2, complexes of these ligands remain desirable synthetic targets.

The uranyl complex of the dipyrrin ligand L^2 (complex **21**) is the first example of a uranyl-dipyrrin complex, and despite offering a similar coordination geometry to uranyl Pacman complexes, changes in electronic structure in the N_4-donor pocket influence drastically different reduction chemistry. Where Pacman ligands influence direct, one-electron reduction of uranyl, the first reduction of **21** occurs at the ligand, and it is only after coordination of a Lewis acid to the uranyl oxo-groups that this electron is transferred to the metal, ultimately resulting in metal-based reduction. The two-electron reduction of uranyl is preferred over the one-electron reduction in the dipyrrin setting, and the ligand-mediated reduction means that the overall two-electron reduction of uranyl occurs at more positive potential than the outer-sphere reduction. Whilst the imine groups in L^2 make the ligand and its complexes moisture-sensitive, this research highlights that the mixture of redox-active ligands and coordinating Lewis acids is a potent combination for affecting the two-electron reduction of uranyl. Perhaps future work could involve more simple and robust combinations to carry out similar reduction of uranyl under conditions more relevant to nuclear waste mixtures.

Chapter 8

Experimental

8.1 General considerations

Syntheses of all organic compounds were carried out under a flow of dry N_2, having previously degassed the reaction solvent by sparging with N_2. All light-sensitive compounds were synthesised and handled in amber glassware or in standard glassware wrapped in aluminium foil. All air- and moisture-sensitive compounds were synthesised and handled using standard Schlenk-line techniques. Vacuum Atmospheres and MBraun glove boxes were used to manipulate and store air- and moisture-sensitive compounds under an atmosphere of dried and deoxygenated N_2. All gases were supplied by BOC gases UK. All glassware for use with moisture-sensitive compounds was dried in an oven at 160 °C, cooled under 10^{-3} mbar vacuum and then purged with N_2. Prior to use, all Fisherbrand$^®$ 1.2 µm retention glass microfiber filters and cannulae were dried in an oven at 160 °C overnight. All coordination complexes were synthesised under dry N_2 unless stated otherwise. Photolysis reactions were carried out inside a quartz UV cuvette or in a Young's tap fitted NMR tube, using a Sankyo Denki PCQ-9G1-2.5 Pen-Ray Light Source at 254 nm.

All solvents for use with air- and moisture-sensitive compounds were stored in Young's tap fitted flasks containing pre-dried 4 Å molecular sieves. Solvents were collected from a Vacuum Atmospheres solvent purification system, where they had been passed over a column of molecular sieves for 24 hours prior to collection. They were then degassed prior to use and subsequent storage. The solvents d_6-benzene, d_8-THF, d_8-toluene and d_5-pyridine were dried by refluxing over fresh, molten potassium metal overnight; they were then freeze-pump-thaw degassed three times before distillation into a Young's tap fitted flask for storage in the glove box. Pyridine was dried by refluxing in a N_2 atmosphere, over molten potassium metal on a still for four consecutive days; it was then collected and

stored over 4 Å molecular sieves in a Young's tap fitted flask.

Pyrrole was freshly distilled prior to each use, using a rotary evaporator at 80 °C. 4,5-dimethyl-1,2-phenylenediamine was purified by vacuum sublimation at 120 °C using a turbo vacuum pump. Phenolic compounds were purified by vacuum sublimation in a Schlenk tube, collecting the sublimate on the walls of the tube; the residues were washed from the flask by pipetting THF. Alcohols n-hexanol, methanol and *iso*-propanol were dried over several batches of freshly dried and activated 4 Å molecular sieves. Transition metal halide salts were dried thoroughly by heating at 135 °C under vacuum before storing under N_2. Cyclohexene oxide was dried over 4 Å molecular sieves and distilled prior to polymerisation reactions. Dipyrromethanes **1**[1] and **1b**,[2] dipyrrins **4**[3] and **4b**,[4] BODIPYs **5**[5] and **5b**,[6] diformyl dipyrromethanes **2**[7] and **2b**,[8] 1,8-diaminoanthracene,[9] $KN(SiMe_3)_2$,[10] $Zn\{N(SiMe_3)_2\}_2$,[11] $FeCl_2(Py)_4$,[12] $Fe\{CH_2(SiMe_3)\}_2(Py)_2$,[13] MPPH,[14] $UO_2\{N(SiMe_3)_2\}_2(Py)_2$,[15] $UO_2\{N(SiMe_3)_2\}_2(THF)_2$,[15] $UO_2Cl_2(THF)_2$[16] and $[TiCp_2Cl]_2$[17] were prepared according to literature procedures. All other reagents were used as supplied, either by Sigma Aldrich, Fisher Scientific UK, VWR or Acros Organics.

^{1}H NMR spectra were recorded on a Bruker AVA400 spectrometer operating at 399.90 MHz, a Bruker AVA500 or Bruker PRO500 spectrometer operating at 500.12 MHz, or a Bruker AVA600 spectrometer operating at 599.81 MHz. ^{13}C$\{^1$H$\}$ NMR spectra were recorded on a Bruker AVA500 or Bruker PRO500 operating at 125.76 MHz. ^{19}F and ^{19}F$\{^1$H$\}$ NMR spectra were recorded on a Bruker AVA500 spectrometer operating at 470.59 MHz, or on a Bruker AVA400 spectrometer operating at 376.50 MHz. Chemical shifts are reported in parts per million (δ / ppm). ^{1}H and ^{13}C$\{^1$H$\}$ NMR spectra are referenced to residual solvent resonances calibrated against an external standard, $SiMe_4$ ($\delta = 0$ ppm). ^{19}F$\{^1$H$\}$ NMR spectra are referenced to an external standard, CCl_3F ($\delta = 0$ ppm). All spectra were recorded at 300 K unless otherwise stated. All data were processed using MestReNova 10.

Electrochemical measurements were made using an Autolab ECO Chemie PGSTAT bipotentiostat and the data processed using GPES Manager version 4.9. Experiments were typically undertaken under a flow of N_2 in a 30 cm^3 electrochemical cell; air-sensitive complexes were measured in the same cell, either by attachment to a Schlenk line, or in an open cell in a glove box. The solution employed was typically 1 – 5 mM of the analyte and 0.1 M of the supporting electrolyte, [^{n}Bu$_4$N][BF$_4$], [^{n}Bu$_4$N][PF$_6$] or [^{n}Bu$_4$N][BPh$_4$], in 12 cm^3 THF, DMF, MeCN or CH_2Cl_2. For small-scale experiments, the working electrode was either a

glassy-carbon disc (d = 3 mm) or a platinum disc (d = 1.6 mm), using a Pt-gauze as the counter electrode and a silver wire as the quasi-reference electrode. For bulk electrolysis and chrono-amperometry/coulometry experiments, either a reticulated vitreous carbon (RVC) electrode (surface area = 10.5 cm^2 cm^{-2}) or a Pt basket electrode (height = 50 mm, d = 39 mm) was used; for these experiments, where a fixed potential is required for the duration of the measurement, an aqueous Ag/AgCl reference electrode was used. Where a quasi-reference electrode was used, the potentials were calibrated at the end of the experiment by addition of ferrocene and determination of the ferrocinium/ferrocene couple (E, Fc$^+$/Fc = 0 V).

Elemental analyses were conducted by Mr Stephen Boyer at the London Metropolitan University, measured in duplicate. All FT-IR spectra were recorded using JASCO 410 or JASCO 460+ spectrometers, typically in the solid state, deposited on a KBr plate as a thin film after evaporation of a volatile solvent. For air-stable compounds, the solid was deposited directly onto an ATR plate. EI and FT-ICR-ESI mass spectra were recorded by Dr Alan Taylor and Dr Logan McKay, respectively, at the University of Edinburgh. All UV/visible/NIR electronic absorption spectra were recorded on a JASCO V-670 spectrophotometer in a 10 mm quartz cuvette fitted with a Young's tap; extinction coefficients were determined from five independent μM solutions, taken from the slope of least-squares fitted plots of absorption against varying concentration. All spectra are presented using Origin 2015 software.

X-ray crystallographic data were recorded at 170 K on an Oxford Diffraction Excalibur diffractometer equipped with an Eos CCD detector, using graphite monochromated Mo-Kα radiation (λ = 0.71073 Å), or at 120 K on a Supernova, Dual, Cu at Zero Atlas diffractometer using Cu-Kα radiation (λ = 1.5418 Å). Structures were solved using SIR-92[18] or SHELX-2014[19] direct methods and refined using a full-matrix least square refinement on $|F|^2$ using SHELX-2014. All programs were used within Olex2.[20] All non-hydrogen atoms were refined with anisotropic displacement parameters and H-parameters were constrained to parent atoms and refined using a variety of models (stated in Tables 8.1 to 8.5). The PLATON "SQUEEZE" algorithm[21] was used in some cases to remove solvent-accessible voids or solvent molecules that could not be adequately modelled. All X-ray crystal structures were analysed and presented using Mercury 3.8.

Density functional theory calculations were conducted using the Gaussian09 package[22] on the Eddie3 server system at the University of Edinburgh. Initial guess geometries were either generated from X-ray crystal structures or from a

drawn molecule using the Avogadro program (version 1.1.0). All structures were optimised and converged according to the criteria for maximum displacement and maximum force. Frequency calculations were conducted to confirm that the optimised geometries possessed no imaginary frequencies and represented true minimum-energy structures. The "opt=noraman" and "freq=noraman" keywords were employed to improve computational efficiency. For open-shell calculations, the amount of spin-contamination in the optimised geometries was less than 10 %. Pople basis sets were typically used with added polarisation functions; 6-31G(d,p) for large and/or open-shell molecules, or 6-311G(d,p) for purely organic molecules.[23–31] The hybrid functionals B3LYP[32–35] or CAM-B3LYP[36] were used for organic molecules, zinc(II) complexes and transition metal complexes. For the uranyl dipyrrin DFT studies, the B3PW91 functional was used.[34,37] Two different effective core potentials from Stuttgart-Dresden were used for describing the uranium atoms. The relativistic energy-consistent small-core pseudopotential of the Stuttgart-Köln ECP library was used in combination with its adapted segmented basis.[38–40] For comparison, the corresponding $5f$-in-core ECP augmented by a f-polarisation function was used.[41,42] Ti and Cl centres were also treated with an energy-consistent pseudopotential of the Stuttgart-Köln ECP library in combination with its adapted segmented basis.[43] TD-DFT calculations were performed on the first 40 excited states using the default PCM solvent model.[44] Where a comparison of energies between different geometries or spin-states was required, Grimme's empirical dispersion correction was added along with Becke and Johnson's damping factors, denoted GD3BJ in Gaussian 09.[45–47] Data for plotting simulated absorption spectra were prepared using GaussSum software (version 3.0).[48] All molecular orbital and spin-density surfaces were analysed using Jmol software, and presented using UCSF Chimera software.

8.2 Specific procedures

8.2.1 Gas reactions

Gas reactions were carried out in Young's tap fitted flasks or NMR tubes. A solution containing the compound was three times freeze-pump-thaw degassed and the vessel was thoroughly evacuated. The sealed vessel was then attached to a drying column containing an 80:20 mixture of P_2O_5 (with moisture indicator) and $MgSO_4$. The drying column had previously been dried overnight in the oven at 200 °C, and was also heated thoroughly under vacuum on the Schlenk line. The drying column was cooled under vacuum and purged with N_2 before it was

thoroughly evacuated. The drying column was attached to the gas cylinder and filled to the desired pressure (typically a maximum pressure of 2 bar); the reaction vessel was then opened to the drying column, starting the gas reaction. Reactions were depressurised prior to work-up, using a mercury bubbler on the Schlenk line.

8.2.2   Copolymerisation reactions

For low-pressure copolymerisation reactions, distilled and dried cyclohexene oxide, catalyst and n-hexanol were added to a Schlenk flask. The reaction mixture was degassed and then heated to 80 °C at 1 bar CO_2 pressure. After 24 h, the mixture was quenched by exposure to air and a ^{1}H NMR spectrum of the crude mixture was recorded. Cyclohexene oxide was removed under vacuum to yield the polycarbonate, which was purified by precipitation from a THF solution using methanol.

For high-pressure copolymerisation reactions, a Parr reactor was pre-dried for 20 h at 140 °C. The reactor was purged with CO_2 three times and allowed to cool to room temperature. Then, the catalyst and n-hexanol were dissolved in cyclohexene oxide and added to the Parr reactor. After sealing the reactor, $30 - 50$ bar of CO_2 was added whilst the reaction mixture was stirring at a low-frequency in order to facilitate CO_2 dissolution. This step was repeated several times until the CO_2 dissolution reached equilibrium and the headspace pressure remained constant. The vessel was heated to the appropriate temperature and stirred for 24 hours before the reaction was quenched and a ^{1}H NMR spectrum of the crude reaction mixture was recorded. The mixture was then taken up in CH_2Cl_2 and evaporated to dryness. The polymer was purified by precipitation from a THF solution using methanol.

Characterisation of the polymers by ^{1}H and ^{13}C$\{^1$H$\}$ NMR spectroscopy were carried out on a Bruker AVA-400 instrument. A Shimadzu LC-20AD instrument was used to characterise the molecular weights and dispersities, using a Wyatt MALLS detector, with two Mixed Bed PSS SDV linear S columns and THF as the eluent, at a flow rate of $1.0 \, \mathrm{mL \, min^{-1}}$ at 30 °C. Near mono-disperse polystyrene standards were used to calibrate the instrument. The polyesters were dissolved in SEC grade THF and filtered prior to analysis.

8.2.3   Electro-catalytic reactions with CO_2

For initial screening of electro-catalytic activity towards CO_2 reduction, the CV of the complex was first recorded under N_2, in dry and deoxygenated solvent. A

proton source was then added, and the CV was recorded again to determine if the complex was active towards the electo-catalytic proton-reduction reaction. Proton sources were typically 1 M water, phenol or benzoic acid. The solution was then sparged with CO_2 for 10 minutes with slow stirring of the solution. The CV was then recorded to qualitatively assess the activity of the complex; catalysis is observed as a very large increase in current at, or near, one of the metal-based redox processes. Complexes that showed high activity in these preliminary screenings were analysed in more detail by foot-of-the-wave analysis (FOWA). High solubility of CO_2, low solubility of CO and low intrinsic resistance make DMF the ideal solvent for all of these CV experiments.

The methodology for foot-of-the-wave analysis is discussed in Chapter 4.

For CPE experiments, the concentrations from CV experiments were scaled to a solution volume of 80 cm^3 DMF (1 mM complex, 0.1 M electrolyte, 1 M proton source, 0.23 M CO_2). The electrochemical cell was a H-cell fitted with a frit separating the Pt-mesh counter-electrode from the RVC working-electrode and Ag/AgCl reference electrode. The solution was stirred for the duration of the experiment and the reaction was monitored by amperometry (the charge passed can be obtained by integration of the amperogram).

8.2.4 Oxygenation reactions

The catalysed oxidation reaction of xanthene was monitored by ^{1}H NMR spectroscopy. Catalysts were prepared in stock solutions of d_3-MeCN and added to a vial containing a solution of the substrate and internal standard (mesitylene) using a Gilson 100 μL pipette. The solution was mixed and then transferred to a Young's tap fitted NMR tube, so that evaporation of the solvent is avoided. The NMR spectrometer was locked to the deuterium signal of the solvent and then tuned. The sample was removed from the spectrometer and the oxidant was added using a 100 μL glass syringe; a timer was started. The solution was shaken in the NMR tube before being quickly returned to the spectrometer, where the magnetic field was shimmed for the sample and the receiver gain was set. A pseudo-2D ^{1}H NMR experiment was recorded (a series of 1D spectra are recorded against time), collecting spectra every 15 minutes for long reaction times (6+ hours) or every 5 minutes for short reaction times ($\leq$ 2 hours). The spectra were phased using uniform phasing parameters and then integrated using MestReNova. To ensure accurate integration and to account for the disruption of the baseline after phasing of the spectra, all resonances for a unique proton environment in the set were integrated between the same two points on the x-axis. An automatic linear

baseline correction was applied to each integral, to take into account the local baseline and to ensure that all integrals were positive, even at small values. The integrals for xanthene, xanthydrol, (*tert*-butyl)xanthyl peroxy-ether and xanthone were normalised through division of the integral by the number of associated protons for that resonance. The normalised integrals were then divided by that of the internal standard. These normalised and standardised integrals were then converted into mole fractions, in order to make the integrals internally consistent, before being converted to concentration values. This method gave smooth concentration *versus* time plots that were reproducible in triplicate measurements.

Determination of the substrate scope was undertaken in three stages. In the first stage, small-scale reactions were carried out in NMR tubes, in order to establish whether heating was required to achieve high conversion of the substrate. Due to the complexity of the resulting NMR spectra, in particular those for substrates containing cyclo-aliphatic groups that contained many overlapping resonances, these NMR-scale reactions were used to deduce the %conversion of the substrate only. The catalyst loading in this stage was 0.2 mol% for both **13c** and $FeCl_3$, the substrate concentration was set at 0.15 M, and four equivalents of TBHP were used per reactive benzylic site. The reaction mixtures were prepared as for the kinetics experiments, using Gilson 10 – 100 μL pipettes to measure mesitylene, d_3-MeCN and the **13c** and $FeCl_3$ stock solutions. Where heating of the reaction mixture was required, an oil bath was used at 60 °C.

In the second stage, the reactions were repeated on a 100 to 200 mg scale in 7 cm^3 vials, using the same concentrations as in the previous stage, and were stirred using a magnetic stirrer. The reactions were run for 16 hours, and if heating was required it was done so at 60 °C in an oil bath. At the end of the reaction, six drops of the reaction mixture were added to 1 cm^3 of acetonitrile and filtered into a vial for analysis by GC-MS. The retention factors for each compound were not determined, nor were they considered. Instead, the %conversion of the substrate and %yield of the products were approximated from the relative integrals of the GC peaks observed. The %conversion values determined from this method tarried well with the NMR-yields from the previous stage, and from the GC-MS data the identity of the products from the reactions were determined, along with their approximate yields. These results provided insight into how further scale-up reactions could be tailored to obtain individual products with high selectivity.

In the final stage of the substrate screen, the reactions were repeated on a 1 mmol scale, and were again stirred. In this stage, two procedures were used:

1. A 70 wt% aqueous solution of TBHP (4 mmol, 554 μL per reactive benzylic

position) was added to a solution of substrate (1 mmol), complex **13c** (5 μmol) and FeCl$_3$ (5 μmol) in acetonitrile (4.1 mL or 3.5 mL depending on the volume of TBHP used) and the resulting mixture was stirred at room temperature for 16 h. The crude mixture was passed through a silica pad and eluted with ethyl acetate. Solvent was removed under reduced pressure to yield a crude product which was purified by column chromatography (95:5 hexanes:ethyl acetate, silica).

2. As for procedure 1, but the reaction was carried out at 60 °C in an oil bath.

The isolated yields of the products were recorded after drying, as were their NMR spectra for identification.

8.3 Synthetic procedures

8.3.1 Synthesis of organic compounds

1,9-diformyl-5-pentafluorophenyl-dipyrromethane, 2

Synthesised as a brown solid, according to published procedures.[7] Attempts to purify the compound by vacuum sublimation or column chromatography led to decomposition. Very large, colourless, diffraction-quality block crystals were grown from a hot aqueous ethanol solution (80 % ethanol v/v) on cooling to room temperature. ^{1}H NMR (CDCl$_3$): δ_H / ppm: 10.39 (broad s, 2H, pyrrole N-H), 9.29 (s, 2H, aldehyde), 6.90 (m, 2H, pyrrole β-H), 6.15 (m, 2H, pyrrole β-H), 6.02 (s, 1H, *meso*-H).

Diimino-dipyrromethane 3

To a brown solution of **2** (8.54 g, 23 mmol) in methanol (350 cm^3) was added *para-tert*-butylaniline (6.22 g, 42 mmol, 1.8 eq). The solution was heated to 50 °C and stirred for 30 minutes. Trifluoroacetic acid (3.5 cm^3, 46 mmol, 2 eq) was drop-wise added to the solution, turning the solution dark green. The solution was stirred for 2 hours before NEt$_3$ (6.4 cm^3, 46 mmol, 2 eq) was slowly added, turning the solution dark blue and then dark pink. The mixture was stirred for 30 minutes before methanol was evaporated from the mixture under vacuum. The dark pink residues were dissolved in toluene (200 cm^3) and washed with deionised water (3 × 50 cm^3); the yellow aqueous fractions were discarded. The organic fraction was dried with MgSO$_4$ and toluene was evaporated to yield a dark purple solid. The product was dried under vacuum at 70 °C, overnight. Yield: 10.81 g,

74 %. ^{1}H NMR (CDCl$_3$): δ_H / ppm: 8.18 (s, 2H, imine), 7.36 (d, 4H, $^3J_\text{HH} =$ 10 Hz, Ph), 7.12 (d, 4H, $^3J_\text{HH} =$ 10 Hz, Ph), 6.56 (d, 2H, $^3J_\text{HH} =$ 5 Hz, pyrrole β-H), 6.02 (broad s, 2H, pyrrole β-H), 5.69 (s, 1H, *meso*-H), 1.32 (s, 18H, *t*Bu). ^{13}C{^{1}H} NMR (CDCl$_3$): δ_C / ppm: 149.0, 148.8, 148.1, 145.8, 144.1, 143.8, 141.6, 138.5, 136.9, 133.8, 131.5, 126.2, 117.0, 115.1, 110.0, 34.6, 31.5. EI-MS: *m/z*: 630.3 (M$^+$). FT-IR (ATR, solid state): ν / cm^{-1}: 1623 (imine). UV/vis (CH$_2$Cl$_2$): λ_max 372 nm, $\epsilon = 41{,}000$ dm^3 mol^{-1} cm^{-1}. No satisfactory elemental analyses obtained.

Diimino-dipyrrin HL^1

To a dark purple solution of **3** (6.03 g, 10 mmol) in CH$_2$Cl$_2$ (100 cm^3) was added 2,3-dichloro-5,6-dicyanobenzoquinone (DDQ, 2.17 g, 10 mmol, 1 eq). The mixture was stirred for 1 hour, turning the solution red/purple. Tan solids were removed from the mixture by suction filtration and CH$_2$Cl$_2$ was removed from the filtrate to yield a dark purple solid. The product was dried under vacuum at 70 °C, overnight. Yield: 6.29 g, 100 %. ^{1}H NMR (CDCl$_3$): δ_H / ppm: 8.57 (s, 2H, imine), 7.45 (d, 4H, $^3J_\text{HH} =$ 10 Hz, Ph), 7.30 (d, 4H, $^3J_\text{HH} =$ 10 Hz, Ph), 7.02 (broad s, 2H, pyrrole β-H), 6.58 (broad s, 2H, pyrrole β-H), 1.37 (s, 18H, *t*Bu). ^{13}C{^{1}H} NMR (C$_6$D$_6$): δ_C / ppm: 155.7, 153.7, 151.3, 150.3, 149.5, 145.1 (d, $^1J_\text{CF} =$ 250 Hz, Ar$^\text{F}$), 143.9, 141.9 (d, $^1J_\text{CF} =$ 251 Hz, Ar$^\text{F}$), 137.7 (d, $^1J_\text{CF} =$ 250 Hz, Ar$^\text{F}$), 134.1, 126.6, 126.5, 122.04, 121.53, 34.62, 31.46. ^{19}F{^{1}H} NMR (CDCl$_3$): δ_F / ppm: -137.9 (m, 2F, Ar$^\text{F}$ *ortho*-F), -151.6 (t, 1F, $^3J_\text{FF} =$ 20 Hz, Ar$^\text{F}$ *para*-F), -160.5 (m, 2F, Ar$^\text{F}$ *meta*-F). ESI-MS: *m/z*: 628.2 (M$^+$). FT-IR (ATR, solid state): ν / cm^{-1}: 1662 (imine). UV/vis (CH$_2$Cl$_2$): λ_max 290 nm, $\epsilon = 19{,}000$ dm^3 mol^{-1} cm^{-1}. No satisfactory elemental analyses obtained.

Alternative synthesis for dipyrrin HL^1

Prepared as described for HL^2, below. A mixture of **2** (523 mg, 1.4 mmol), *para-tert*-butylaniline (380 mg, 2.6 mmol, 1.8 eq) and Na$_2$SO$_4$ (1 g) in toluene (100 cm^3) was refluxed at 70 °C for 48 hours. Yield: 225 mg, 26 %.

Diimino-dipyrrin HL^2

To a brown solution of **2** (1.562 g, 4 mmol) in toluene (250 cm^3) was added Na$_2$SO$_4$ (3 g) and then *tert*-butylamine (3 cm^3, 28 mmol, 7 eq). The solution was heated to the boiling temperature of the amine (45 °C), quickly turning the solution dark orange. The mixture was stirred for 48 hours and then cooled to room temperature. Na$_2$SO$_4$ was removed from the mixture by filtration, washing

with toluene. Removal of the solvent under vacuum afforded a dark orange oil. Addition of hexanes gave an orange solution and suspension of brown solids, that were removed by filtration. Removal of the solvent from the filtrate afforded the product as a red solid. Diffraction-quality crystals were grown from a hexanes solution cooled to $-30\,°C$. Yield: 0.98 g, 48 %. ^{1}H NMR (CDCl$_3$): δ_H / ppm: 7.71 (s, 2H, imine), 6.34 (broad s, 2H, pyrrole β-H), 5.76 (broad s, 2H, pyrrole β-H), 0.76 (s, 18H, tBu). ^{13}C{^{1}H} NMR (CDCl$_3$): δ_C / ppm: 155.3 (pyrrole α-C), 148.8 (imine), 144.0 (d, $^{1}J_\mathrm{CF} = 251$ Hz, Ar$^\mathrm{F}$), 142.3 (pyrrole α-C), 140.8 (d, $^{1}J_\mathrm{CF} = 252$ Hz, Ar$^\mathrm{F}$), 136.6 (d, $^{1}J_\mathrm{CF} = 252$ Hz, Ar$^\mathrm{F}$), 127.3 (pyrrole β-C), 123.0 (*meso*-C), 119.8 (pyrrole β-C), 58.2 (CMe$_3$), 29.7 (CMe$_3$). ^{19}F{^{1}H} NMR (CDCl$_3$): δ_F / ppm: -138.2 (dd, 2F, $^{3}J_\mathrm{FF} = 4, 24$ Hz, Ar$^\mathrm{F}$ *ortho*-F), -152.2 (t, 1F, $^{3}J_\mathrm{FF} = 24$ Hz, Ar$^\mathrm{F}$ *para*-F), -160.9 (m, 2F, $^{3}J_\mathrm{FF} = 4$ Hz, Ar$^\mathrm{F}$ *meta*-F). EI-MS: m/z: 478 (M$^+$). FT-IR (ATR, solid state): ν / cm^{-1}: 1582 (imine). UV/vis (CH$_2$Cl$_2$): λ_max 486 nm, $\epsilon = 24,329 \pm 1262$ dm^3 mol^{-1} cm^{-1}. Anal. Calcd for C$_{25}$H$_{25}$F$_5$N$_4$ (M$_r$ = 476.48 g mol^{-1}): C, 63.02 %; H, 5.29 %; N, 11.76 %. Found: C, 62.88 %; H, 5.37 %; N, 11.63 %.

Macrocycle H$_4$L^3

To a brown solution of **2** (2.17 g, 6 mmol) in methanol (180 cm^3) was added 4,5-dimethyl-1,2-phenylenediamine (0.80 g, 6 mmol, 1 eq). Trifluoroacetic acid (0.9 cm^3, 12 mmol, 2 eq) diluted in methanol (20 cm^3) was added, forming a yellow/brown solution that was stirred for 3 hours at room temperature. NEt$_3$ (1.8 cm^3, 13 mmol, 2.1 eq) in methanol (20 cm^3) was added to the mixture and was stirred for 1 hour, over which time a yellow solid precipitated. The product was isolated by vacuum filtration on a cintered funnel, washed with methanol until the washings were colourless (5 $\times$ 30 cm^3) and then dried overnight at 70 °C under vacuum. Diffraction-quality crystals were grown from a THF solution cooled to $-30\,°C$. Yield: 2.134 g, 38 %. ^{1}H NMR (CDCl$_3$): δ_H / ppm: 8.09 (s, 4H, imine), 6.84 (s, 4H, Ar C-H), 6.53 (d, 4H, $^{3}J_\mathrm{HH} = 5$ Hz, pyrrole β-H), 6.12 (d, 4H, $^{3}J_\mathrm{HH} = 5$ Hz, pyrrole β-H), 5.89 (s, 2H, *meso*-H), 2.26 (s, 12H, Ar-CH$_3$). ^{13}C{^{1}H} NMR (CDCl$_3$): δ_C / ppm: 149.4 (imine), 145.2 (d, $^{1}J_\mathrm{CF} = 247$ Hz, Ar$^\mathrm{F}$), 142.5 (Ar$^\mathrm{F}$, *ipso*-C), 140.9 (d, $^{1}J_\mathrm{CF} = 253$ Hz, Ar$^\mathrm{F}$), 138.1 (d, $^{1}J_\mathrm{CF} = 246$ Hz, Ar$^\mathrm{F}$), 137.1 (Ar, *ipso*-C next to imine), 134.8 (Ar *ipso*-C-CH$_3$), 133.4 (pyrrole α-C), 131.6 (pyrrole α-C), 120.6 (Ar C-H), 116.8 (pyrrole β-C), 114.3, 110.0 (pyrrole β-C), 33.9 (*meso*-C), 19.6 (Ar-CH$_3$). ^{19}F{^{1}H} NMR (CDCl$_3$): δ_F / ppm: -139.8 (m, 4F, Ar$^\mathrm{F}$ *ortho*-F), -154.8 (t, 2F, $^{3}J_\mathrm{FF} = 24$ Hz, Ar$^\mathrm{F}$ *para*-F), -160.9 (m, 4F, Ar$^\mathrm{F}$ *meta*-F). ESI-MS: m/z: 937 (M$^+$), 959 [M + Na]$^+$, 977 [M + Ca]$^+$.

FT-IR (ATR, solid state): ν / cm^{-1}: 1620 (imine). UV/vis (CH$_2$Cl$_2$): λ_{max} 320 nm, $\epsilon = 67,416 \pm 1588$ dm^3 mol^{-1} cm^{-1}. Anal. Calcd for C$_{50}$H$_{34}$F$_{10}$N$_8$ (M$_r$ = 937 g mol^{-1}): C, 64.10 %; H, 3.66 %; N, 11.96 %. Found: C, 63.70 %; H, 3.56 %; N, 11.82 %.

Macrocycle H$_8$L^3

To a brown solution of H$_4$L^3 (830 mg, 0.89 mmol) in THF (100 cm^3) was slowly added a solution of NaBH$_4$ (268 mg, 7.1 mmol, 8 eq) in THF (100 cm^3). The solution turned pale orange on stirring for 16 hours, after which time dilute hydrochloric acid was added (50 cm^3, 0.1 M). The mixture was stirred for a further 30 minutes before it was evaporated to dryness, yielding light brown residues. These residues were dissolved in CH$_2$Cl$_2$ and the solution was washed with deionised water (3 × 30 cm^3). The organic layer was dried over MgSO$_4$, filtered and evaporated to dryness to yield the product as a light brown solid. Yield: 670 mg, 80 %. ^{1}H NMR (CDCl$_3$): δ_{H} / ppm: 8.35 (s, 4H, pyrrole N-H), 6.98 (s, 4H, amine N-H), 6.56 (s, 4H, Ar C-H), 6.01 (t, 4H, $^3J_{\mathrm{HH}}$ = 3 Hz, pyrrole β-H), 5.84 (t, 4H, $^3J_{\mathrm{HH}}$ = 3 Hz, pyrrole β-H nearest *meso*-C), 5.78 (s, 2H, *meso*-H), 4.14 (s, 8H, CH$_2$, next to amine), 2.16 (s, 12H, Ar-CH$_3$). ^{13}C{^{1}H} NMR (CDCl$_3$): δ_{C} / ppm: 135.9, 135.0, 130.3, 128.4, 128.0, 127.9, 125.7, 115.1, 107.6, 107.1, 19.4. ^{19}F{^{1}H} NMR (CDCl$_3$): δ_{F} / ppm: −141.63 (broad s, 4F, Ar$^{\mathrm{F}}$ *ortho*-F), −156.08 (t, 2F, $^3J_{\mathrm{FF}}$ = 22 Hz, Ar$^{\mathrm{F}}$ *para*-F), −161.47 (td, 4F, $^3J_{\mathrm{FF}}$ = 23, 8 Hz, Ar$^{\mathrm{F}}$ *meta*-F). No elemental analyses obtained.

Macrocycle H$_4$L^4

Prepared as described for H$_4$L^3, above. A solution of **2** (1.432 g, 4 mmol), 1,8-diaminoanthracene (0.809 g, 4 mmol, 1 eq) and *para*-toluenesulfonic acid (1.38 g, 8 mmol, 2 eq) in methanol (150 cm^3) was stirred for 3 hours. NEt$_3$ (1.1 cm^3, 8.4 mmol, 2.1 eq) in methanol (20 cm^3) was added and the mixture was stirred for a further 1 hour. The product was first isolated as a dull yellow solid on a cintered funnel. Precipitation of the compound on addition of methanol to a brown chloroform solution afforded bright yellow solids that were of higher purity and crystallised more readily. Diffraction-quality crystals were obtained from a concentrated chloroform solution layered with methanol. Yield: 0.766 g, 42 %. ^{1}H NMR (CDCl$_3$): δ_{H} / ppm: 9.35 (broad s, 4H, pyrrole N-H), 9.20 (s, 2H, 9-anth), 8.43 (s, 2H, 10-anth), 8.40 (s, 4H, imine), 7.86 (d, 4H, $^3J_{\mathrm{HH}}$ = 10 Hz, 2,7-anth), 7.44 (t, 4H, $^3J_{\mathrm{HH}}$ = 10 Hz, 3,6-anth), 7.00 (d,

4H, $^3J_{HH} = 10$ Hz, 4,5-anth), 6.65 (d, 4H, $^3J_{HH} = 5$ Hz, pyrrole β-H), 6.20 (d, 4H, $^3J_{HH} = 5$ Hz, pyrrole β-H), 5.97 (s, 2H, *meso*-H). ^{13}C{^{1}H} NMR (CDCl$_3$): δ_C / ppm: 150.2 (1,8-anth), 150.0 (imine), 145.4 (d, $^1J_{CF} = 253$ Hz, Ar^F), 141.4 (d, $^1J_{CF} = 263$ Hz, Ar^F), 138.2 (d, $^1J_{CF} = 253$ Hz, Ar^F), 133.1 (pyrrole α-C), 132.7 (pyrrole α-C), 132.0 (anth), 131.5 (Ar^F, *ipso*-C), 127.4 (anth), 126.5 (10-anth), 126.0 (3,6-anth), 125.8 (4,5-anth), 118.8 (9-anth), 117.0 (pyrrole β-C), 112.61 (2,7-anth), 110.4 (pyrrole β-C), 33.8 (*meso*-C). ^{19}F{^{1}H} NMR (CDCl$_3$): δ_F / ppm: -140.88 (d, 4F, $^3J_{FF} = 14$ Hz, Ar^F *ortho*-F), -153.98 (t, 2F, $^3J_{FF} = 23$ Hz, Ar^F *para*-F), -160.66 (t of d, 4F, $^3J_{FF} = 9, 23$ Hz, Ar^F *meta*-F). ESI-MS: *m/z*: 1080 (M$^+$). FT-IR (ATR, solid state): ν / cm^{-1}: 1614 (imine). UV/vis (CH$_2$Cl$_2$): λ_{max} 262 nm, $\epsilon = 56,262 \pm 3886$ dm^3 mol^{-1} cm^{-1}. No satisfactory elemental analyses obtained. Anal. Calcd for C$_{62}$H$_{34}$F$_{10}$N$_8$ (M$_r$ = 1080 g mol^{-1}): C, 68.89 %; H, 3.17 %; N, 10.37 %. Found: C, 64.48 %; H, 2.68 %; N, 9.90 %.

1,9-diacetal-dipyrromethane 6

To a brown solution of **2** (128 mg, 0.35 mmol) in methanol (50 cm^3) was added *para*-toluene sulfonic acid (3 mg, 17 μmol, 0.05 eq), turning the solution dark within minutes. Triethylorthoformate (89 mg, 0.6 mmol, 1.7 eq) was added as a water scavenger. The mixture was stirred for 10 minutes and then evaporated to dryness under vacuum, affording a dark brown solid. Yield: 152 mg, 95 %. ^{1}H NMR (CDCl$_3$): δ_H / ppm: 10.02 (broad s, 2H, pyrrole N-H), 9.34 (s, 2H, acetal C-H), 6.94 (m, 2H, pyrrole β-H), 6.19 (m, 2H, pyrrole β-H), 5.98 (s, 1H, *meso*-H), 3.49 (s, 12H, acetal O-CH$_3$). ^{19}F{^{1}H} NMR (CDCl$_3$): δ_F / ppm: -140.56 (m, 2F, Ar^F *ortho*-F), -152.99 (t, 1F, $^3J_{FF} = 28$ Hz, Ar^F *para*-F), -159.02 (m, 2F, Ar^F *meta*-F).

(*tert*-Butyl)xanthyl peroxy-ether

Xanthene (182 mg, 1 mmol) and TBHP (70 wt%, 0.56 mL, 4 mmol, 4 eq) were mixed in MeCN (6.3 cm^3). Cu$_2$(L^{8Me}) (**13c**, 0.2 mol%) and FeCl$_3$ (0.2 mol%) were added and the light yellow solution was stirred for 4 hours. The solvent was removed under vacuum and the residues were purified by column chromatography, using silica and hexanes:ethyl acetate as the eluent (95:5). The peroxy-ether was isolated as a gummy white solid. Yield: 213 mg, 79 %. ^{1}H NMR (d_3-MeCN): δ_H / ppm: 7.62 (dd, 2H, $^3J_{FF} = 7.6, 1.7$ Hz, 1,8-xanth), 7.45 (ddd, 2H, $^3J_{FF} = 8.3, 7.6, 1.7$ Hz, 3,6-xanth), 7.22 (m, 4H, overlapping 2,7-xanth and 4,5-xanth), 5.99 (s, 1H, benzylic-H), 1.06 (s, 9H, OOtBu). ^{13}C{^{1}H} NMR (d_3-MeCN): δ_C / ppm: 153.6

(quaternary-C, next to benzylic position), 132.5 (1,8-xanth), 131.2 (5,6-xanth), 124.1 (2,7-xanth), 120.3 (quaternary-C, next to ether), 117.3 (4,5-xanth), 80.9 (OOC$\underline{\text{C}}$CH$_3$), 76.2 (benzylic-C), 26.6 (OOCC$\underline{\text{H}}_3$). Anal. Calcd for C$_{17}$H$_{18}$O$_3$ (M$_r$ = 270.13 g mol^{-1}): C, 75.52 %; H, 6.72 %. Found: C, 75.14 %; H, 8.02 %.

8.3.2   Synthesis of metal complexes

Zn$_2$(L^3), 7a

To a brown solution of H$_4$L^3 (410 mg, 0.45 mmol) in THF (20 cm^3) was added a solution of Zn{N(SiMe$_3$)$_2$}$_2$ (0.36 cm^3, 0.9 mmol, 2 eq) in THF (*ca.* 2 cm^3) at room temperature. The mixture was stirred for 24 hours, after which the solvent was removed under vacuum, yielding a brown solid that was dried under vacuum at 70 °C. Yield: 430 mg (91 %). ^{1}H NMR (C$_6$D$_6$): δ_H / ppm: 7.79 (s, 4H, imine), 6.99 (s, 2H, *meso*-H), 6.80 (d, 4H, $^3J_{HH}$ = 5 Hz, pyrrole β-H), 6.73 (s, 4H, Ar C-H), 6.42 (d, 4H, $^3J_{HH}$ = 5 Hz, pyrrole β-H), 2.00 (s, 12H, Ar-C$\underline{\text{H}}_3$). ^{13}C{^{1}H} NMR (C$_6$D$_6$): δ_C / ppm: 150.5 (pyrrole α-C, next to *meso*-C), 146.8 (imine), 146.4 (d, $^1J_{CF}$ = 246 Hz, Ar^F *ortho*-C), 140.0 (pyrrole α-C, next to imine), 137.9 (d, $^1J_{CF}$ = 242 Hz, overlapping Ar^F *meta*- and *para*-C), 136.8 (Ar, next to imine-N), 134.2 (Ar^F, *ipso*-C), 133.8 (Ar, $\underline{\text{C}}$-CH$_3$), 119.7 (pyrrole β-C), 116.3 (Ar C-H), 114.9 (pyrrole β-C), 42.2 (*meso*-C), 19.7 (Ar-C$\underline{\text{H}}_3$). ^{19}F{^{1}H} NMR (C$_6$D$_6$): δ_F / ppm: −139.90 (d, 4H, $^3J_{FF}$ = 20 Hz, Ar^F *ortho*-F), −158.16 (t, 2F, $^3J_{FF}$ = 20 Hz, Ar^F *para*-F), −163.75 (t, 4F, $^3J_{FF}$ = 20 Hz, Ar^F *meta*-F). MALDI-TOF-TOF-MS (DCTB matrix): m/z: 1063 [M + H]$^+$. Anal. Calcd for C$_{50}$H$_{30}$F$_{10}$N$_8$Zn$_2$ (M$_r$ = 1063.6 g mol^{-1}): C, 56.46 %; H, 2.84 %; N, 10.54 %. Found: C, 56.28 %; H, 2.95 %; N, 10.42 %.

Zn$_2$(L^4), 7b

Prepared as described for Zn$_2$(L^3), above. To a solution of H$_4$L^4 (500 mg, 0.46 mmol) in THF (50 cm^3) was added Zn{N(SiMe$_3$)$_2$}$_2$ (391 mg, 1.0 mmol, 2.2 eq). The resulting brown solid was washed with pentane (3 × 2 cm^3) and dried at 60 °C. Diffraction-quality crystals were grown from slow diffusion of hexanes into a saturated THF solution in a semi-open vessel. Yield: 398 mg, 71.2 %. ^{1}H NMR, major isomer (d_8-THF): δ_H / ppm: 8.66 (s, 2H, 9-anth), 8.21 (s, 4H, imine), 7.84 (s, 2H, 10-anth), 7.29 (d, 4H, $^3J_{HH}$ = 8.4 Hz, 2,7-anth), 6.84 (t, 4H, $^3J_{HH}$ = 10 Hz, 3,6-anth, overlap with minor isomer), 6.78 (d, 4H, $^3J_{HH}$ = 6.3 Hz, 4,5-anth), 6.43 (d, 4H, $^3J_{HH}$ = 3.4 Hz, pyrrole β-H), 5.72 (d, 4H, $^3J_{HH}$ = 3.4 Hz, pyrrole β-H), 5.69 (s, 2H, *meso*-H). ^{1}H NMR, minor isomer (d_8-THF):

δ_H / ppm: 8.56 (s, 2H, 9-anth), 8.00 (s, 4H, imine), 7.77 (s, 2H, 10-anth), 7.24 (d, 4H, $^3J_{HH}$ = 8.6 Hz, 2,7-anth), 6.84 (t, 4H, $^3J_{HH}$ = 10 Hz, 3,6-anth, overlap with major isomer), 6.70 (d, 4H, $^3J_{HH}$ = 6.7 Hz, 4,5-anth), 6.32 (d, 4H, $^3J_{HH}$ = 3.4 Hz, pyrrole β-H), 6.06 (d, 4H, $^3J_{HH}$ = 3.4 Hz, pyrrole β-H), 5.99 (s, 2H, *meso*-H). $^{13}C\{^1H\}$ NMR (d_8-THF): δ_C / ppm: 158.6, 148.5, 146.2 (d, $^1J_{CF}$ = 249 Hz, Ar^F), 141.2 (d, $^1J_{CF}$ = 244 Hz, Ar^F), 138.6 (d, $^1J_{CF}$ = 260 Hz, Ar^F), 135.4, 134.1, 133.1, 129.1, 127.3, 127.2, 126.7, 124.8, 119.2, 117.7, 115.6, 112.6, 36.2. $^{19}F\{^1H\}$ NMR, major isomer (d_8-THF): δ_F / ppm: −144.68 (d, 4F, $^3J_{FF}$ = 22.4 Hz, Ar^F *ortho*-F, overlap with minor isomer), −160.25 (t, 2F, $^3J_{FF}$ = 21.8 Hz, Ar^F *para*-F), −165.31 (m, 4F, Ar^F *meta*-F). $^{19}F\{^1H\}$ NMR, minor isomer (d_8-THF): δ_F / ppm: −144.68 (d, 4F, $^3J_{FF}$ = 22 Hz, Ar^F *ortho*-F, overlap with major isomer), −161.27 (t, 2F, $^3J_{FF}$ = 22 Hz, Ar^F *para*-F), −165.76 (m, 4F, Ar^F *meta*-F). Anal. Calcd for $C_{62}H_{30}F_{10}N_8Zn_2$ (M_r = 1207.76 g mol^{-1}): C, 61.66 %; H, 2.50 %; N, 9.28 %. Found: C, 61.45 %; H, 2.35 %; N, 9.16 %.

$Zn_4Et_4(L^3)$, 8a

A brown solution of H_4L^3 (100 mg, 0.1 mmol) in THF (10 cm^3) was treated with a solution of ZnEt$_2$ in hexanes (0.5 cm^3, 1 mol dm^{-3}, 0.5 mmol, 5 eq) at −80 °C; the solution quickly turned dark yellow. The solution was warmed to room temperature and stirred for 18 hours, after which the solvent was removed under vacuum and the resulting dark yellow/brown solid was dried at 70 °C. Yield: 120 mg, 94 %. ^1H NMR (C_6D_6): δ_H / ppm: 7.68 (s, 4H, imine), 6.75 (d, 4H, $^3J_{HH}$ = 5 Hz, pyrrole β-H), 6.55 (s, 4H, Ar C-H), 6.26 (d, 4H, $^3J_{HH}$ = 5 Hz, pyrrole β-H), 6.03 (s, 2H, *meso*-H), 1.99 (s, 12H, Ar-C$\underline{H}_3$), 1.32 (t, 12H, $^3J_{HH}$ = 8 Hz, ethyl-CH_3), 0.42 (q, 8H, $^3J_{HH}$ = 8 Hz, ethyl-C$\underline{H}_2$). $^{13}C\{^1H\}$ NMR (C_6D_6): δ_C / ppm: 156.7 (imine), 149.6 (pyrrole α-C), 149.0 (Ar^F *ipso*-C), 145.9 (d, $^1J_{CF}$ = 248 Hz, Ar^F *ortho*-C), 140.6 (d, $^1J_{CF}$ = 251 Hz, Ar^F *para*-C), 139.4 (Ar, next to imine-N), 138.2 (d, $^1J_{CF}$ = 250 Hz, Ar^F *meta*-C), 137.8 (pyrrole α-C), 134.8 (Ar, $\underline{C}$-CH$_3$), 124.4 (Ar C-H), 122.0 (pyrrole β-C, nearest to imine), 114.3 (pyrrole β-C, nearest to *meso*-C), 40.1 (*meso*-C), 19.2 (Ar-$\underline{C}H_3$), 12.6 (ethyl-CH$_3$), 0.07 (ethyl-CH$_2$). $^{19}F\{^1H\}$ NMR (C_6D_6, 333 K): δ_F / ppm: −140.24 (broad s, 3F, Ar^F *ortho*-F), −156.94 (t, 2F, $^3J_{FF}$ = 22 Hz, Ar^F *para*-F), −162.26 (t of d, $^3J_{FF}$ = 22, 8 Hz, Ar^F *meta*-F). Anal. Calcd for $C_{58}H_{50}F_{10}N_8Zn_4$ (M_r = 1310.7 g mol^{-1}): C, 53.15 %; H, 3.85 %; N, 8.55 %. Found: C, 52.87 %; H, 3.71 %; N, 8.46 %.

$\mathbf{Zn_4Et_4(THF)_4(L^4)}$, 8b

Prepared as described for **8a**, above. To a solution of H_4L^4 (200 mg, 0.18 mmol) in THF (30 cm^3) was added a solution of ZnEt$_2$ in hexanes (0.75 cm^3, 1 mol dm^{-3}, 0.75 mmol, 4.2 eq). Diffraction-quality crystals were grown from slow diffusion of hexanes into a saturated THF solution in a semi-open vessel. Yield: 128 mg, 49 %. ^{1}H NMR (d_8-THF): δ_H / ppm: 8.89 (s, 2H, 9-anth), 8.55 (s, 2H, 10-anth), 8.40 (s, 4H, imine), 7.84 (d, 4H, $^3J_{HH} = 7$ Hz, 2,7-anth), 7.44 (dd, 4H, $^3J_{HH} = 5$ Hz, 3,6-anth), 7.14 (d, 4H, $^3J_{HH} = 5$ Hz, 4,5-anth), 6.75 (broad s, 4H, pyrrole β-H), 6.54 (broad s, 4H, pyrrole β-H), 5.81 (s, 2H, *meso*-H), 0.99 (t, 12H, $^3J_{HH} = 8$ Hz, ethyl-CH$_3$), 0.10 (q, 8H, $^3J_{HH} = 8$ Hz, ethyl-CH$_2$). ^{13}C{^{1}H} NMR (d_8-THF): δ_C / ppm: 158.4 (imine), 148.4 (1,8-anth), 146.9 (anth, quarternary-C), 145.3 (d, $^1J_{CF} = 246$ Hz, Ar^F *ortho*-C), 139.7 (d, $^1J_{CF} = 256$ Hz, Ar^F *para*-C), 137.6 ($^1J_{CF} = 255$ Hz, Ar^F *meta*-C), 136.8 (pyrrole α-C), 133.1 (pyrrole α-C), 128.0 (10-anth), 127.2 (Ar^F *ipso*-C), 126.3 (3,6-anth), 125.4 (2,7-anth), 124.6 (anth, quarternary-C), 120.8 (pyrrole β-C), 118.2 (9-anth), 117.2 (4,5-anth), 114.0 (pyrrole β-C), 41.0 (*meso*-C), 12.1 (ethyl-CH$_3$), -3.2 (ethyl-CH$_2$). ^{19}F{^{1}H} NMR (d_8-THF, 333 K): δ_F / ppm: -140.27 (broad s, 2F, Ar^F *ortho*-F), -161.21 (t, 2F, $^3J_{FF} = 20$ Hz, Ar^F *para*-F), -164.93 (broad t, 4F, $^3J_{FF} = 18$ Hz, Ar^F *meta*-F). Anal. Calcd for C$_{70}$H$_{50}$F$_{10}$N$_8$Zn$_4$ (M$_r$ = 1454.82 g mol^{-1}): C, 57.79 %; H, 3.46 %; N, 7.70 %. Found: C, 57.68 %; H, 3.52 %; N, 7.62 %.

$\mathbf{Zn_4(\mu-O)Et_2(THF)_2(L^3)}$, 9

Diffraction-quality crystals of **9** were repeatedly grown after slow diffusion of hexanes into a saturated THF solution of **8a** in an open vial in the glove box. Complex **9** was prepared rationally: **8a** (10 mg, 8 μmol) was dissolved in a solution of H$_2$O in C$_6$D$_6$ (0.9 cm^3, [H$_2$O] = 8.6 mM by ^{1}H NMR integration, 8 μmol H$_2$O, 1 eq). Yield: 5 mg, 50 % by ^{1}H NMR integration. ^{1}H NMR (C$_6$D$_6$): δ_H / ppm: 7.95 (s, 4H, imine), 6.90 (d, 4H, $^3J_{HH} = 5$ Hz, pyrrole β-H), 6.58 (s, 4H, Ar C-H), 6.43 (s, 2H, *meso*-H), 6.22 (broad s, 4H, pyrrole β-H), 2.05 (s, 12H, Ar-C$\underline{H}_3$), 1.51 (t, 6H, $^3J_{HH} = 10$ Hz, ethyl-CH$_3$), 0.30 (q, 4H, $^3J_{HH} = 10$ Hz, ethyl-C$\underline{H}_2$). ^{13}C{^{1}H} NMR (d_8-THF): δ_C / ppm: 153.6 (imine), 148.9 (Ar^F *ipso*-C), 147.1 (d, $^1J_{CF} = 246$ Hz, Ar^F *ortho*-C), 142.6 (Ar, next to imine), 139.1 (d, $^1J_{CF} = 251$ Hz, Ar^F *para*-C), 138.7 (Ar, $\underline{C}$-CH$_3$), 135.4 (pyrrole α-C, next to *meso*-C), 124.1 (pyrrole α-C, next to imine), 121.6 (Ar C-H), 119.7 (pyrrole β-C), 118.2 (d, $^1J_{CF} = 246$ Hz, Ar^F *meta*-C), 112.0 (pyrrole β-C), 32.7 (*meso*-C), 19.6 (Ar-C$\underline{H}_3$), 7.1 (ethyl-CH$_3$), 2.5 (ethyl-CH$_2$). ^{19}F{^{1}H} NMR (d_8-THF):

δ_F / ppm: -137.74 (d, 4F, $^3J_{FF} = 20$ Hz, Ar^F *ortho*-F), -158.72 (t, 2F, $^3J_{FF} = 20$ Hz, Ar^F *para*-F), -164.52 (t of d, 4F, $^3J_{FF} = 25, 5$ Hz, Ar^F *meta*-F). No satisfactory elemental analyses obtained.

$Zn_4(\mu_2-OH)_4(L^4)$, 10

To a dark yellow solution of **8b** (180 mg, 0.17 mmol) in THF (10 cm^3), was added H_2O previously degassed by sparging with N_2 (12 μL, 0.67 mmol, 4 eq). The solution was stirred for 1 hour, after which the solvent was removed under vacuum, yielding a red solid that was dried under vacuum at 70 °C. Yield: 209 mg, 82 %. ^{1}H NMR (d_8-THF): δ_H / ppm: 9.78 (s, 2H, 9-anth), 8.45 (s, 4H, imine), 8.43 (s, 2H, 10-anth), 7.76 (d, 4H, $^3J_{HH} = 10$ Hz, 2,7-anth), 7.35 (t, 4H, $^3J_{HH} = 10$ Hz, 3,6-anth), 7.12 (d, 4H, $^3J_{HH} = 10$ Hz, 4,5-anth), 6.86 (d, 4H, $^3J_{HH} = 5$ Hz, pyrrole β-H), 6.54 (d, 4H, $^3J_{HH} = 5$ Hz, pyrrole β-H), 6.44 (s, 2H, *meso*-H), 4.14 (s, 2H, μ_2-OH), 3.36 (s, 2H, μ_2-OH). ^{13}C\{^{1}H\} NMR (d_8-THF): δ_C / ppm: 156.7, 149.8, 148.3, 138.3, 133.7, 129.0, 128.9, 126.7, 126.4, 122.9, 117.6, 117.1, 113.2, 42.6. No satisfactory elemental analyses obtained. Anal. Calcd for $C_{62}H_{34}F_{10}N_8O_4Zn_4$ ($M_r = 1406.61$ g mol^{-1}): C, 52.95 %; H, 2.44 %; N, 7.97 %. Found: C, 50.04 %; H, 1.83 %; N, 6.77 %.

$Zn_4(\mu_2-OHex)_4(L^3)$, 11

To a brown/yellow solution of **8a** (500 mg, 0.38 mmol) in THF (5 cm^3) was added *n*-hexanol (182 μL, 1.4 mmol, 3.8 eq) at room temperature. The solution warmed instantly and gentle effervescence was observed. The solution was stirred for 3 hours before the solvent was removed under vacuum; the resulting dark yellow solid was washed twice with hexane and then dried at 70 °C under vacuum. Yield: 360 mg (84 %). ^{1}H NMR (C_6D_6): δ_H / ppm: 8.07 (s, 4H, imine), 7.02 (d, 4H, $^3J_{HH} = 5$ Hz, pyrrole β-H), 6.94 (s, 4H, Ar C-H), 6.38 (s, 2H, *meso*-H), 6.17 (broad s, 4H, pyrrole β-H), 3.83 (t, 4H, $^3J_{HH} = 7.5$ Hz, Zn-OC$\underline{H}_2$C$_5$H$_{11}$), 3.70 (t, 4H, $^3J_{HH} = 7.5$ Hz, Zn-OC$\underline{H}_2$C$_5$H$_{11}$), 2.01 (s, 12H, Ar-C$\underline{H_3}$), 1.83 – 0.62 (multiple resonances, Zn-OCH$_2$C$_5$$\underline{H}_{11}$). ^{19}F\{^{1}H\} ($C_6D_6$): δ_F / ppm: -154.7 (t, Ar^F *para*-F), -161.6 (broad s, Ar^F *meta*-F). Anal. Calcd for $C_{74}H_{82}F_{10}N_8O_4Zn_4$ ($M_r = 1599.0$ g mol^{-1}): C, 55.58 %; H, 5.17 %; N, 7.01 %. Found: C, 55.33 %; H, 5.32 %; N, 6.93 %.

$Zn_3(\mu_2-O^iPr)_2(\mu_3-O^iPr)(HL^3)$, 12

Prepared as for **11**. To a solution of **8a** (360 mg, 0.28 mmol) in THF (4 cm^3) was added *iso*-propanol (80 μL, 1.04 mmol, 3.8 eq) at room temperature. Very large, diffraction-quality block crystals were grown from slow diffusion of hexanes into a saturated benzene solution, which were isolated by decanting the supernatant and were washed with hexane. Crystal yield: 160 mg, 45 %. ^{1}H NMR (d_8-THF, 330 K): δ_H / ppm: 8.36 (broad s, 4H, imine), 7.07 (broad s, 4H, Ar C-H), 6.74 (d, 4H, $^3J_{HH}$ = 4 Hz, pyrrole β-H), 6.25 (broad s, 4H, pyrrole β-H), 6.12 (broad s, 2H, *meso*-H), 4.11 (broad s, 3H, ^{i}Pr C-H), 2.24 (s, 12H, Ar-CH$_3$), 1.02 (broad s, 18H, ^{i}Pr CH$_3$). ^{1}H NMR (d_8-THF, 213 K): δ_H / ppm: 11.98 (s, 1H, pyrrole N-H), 8.86 (s, 1H, imine), 8.68 (s, 1H, imine), 8.48 (s, 1H, imine), 8.40 (s, 1H, imine), 7.56 (s, 1H, Ar C-H), 7.35 (s, 1H, Ar C-H), 7.29 (s, 1H, Ar C-H), 7.04 (s, 2H, Ar C-H and pyrrole β-H), 6.97 (s, 1H, pyrrole β-H), 6.90 (s, 1H, pyrrole β-H), 6.80 (s, 1H, pyrrole β-H), 6.54 – 6.37 (multiple resonances, 4H, pyrrole β-H), 6.22 (s, 1H, *meso*-H), 5.97 (s, 1H, *meso*-H), 4.29 (broad s, 3H, ^{i}Pr C-H), 2.22 (s, 12H, Ar C-CH$_3$), 1.45 (s, 3H, ^{i}Pr CH$_3$), 1.23 (s, 3H, ^{i}Pr CH$_3$), 1.03 (s, 3H, ^{i}Pr CH$_3$), 0.90 (s, 3H, ^{i}Pr CH$_3$), 0.88 (s, 3H, ^{i}Pr CH$_3$), 0.66 (s, 3H, ^{i}Pr CH$_3$). ^{19}F{^{1}H} NMR (d_8-THF, 330 K): δ_F / ppm: -135.49 (broad s, Ar^F *ortho*-F), -158.82 (broad s, Ar^F *para*-F), -164.07 (broad s, Ar^F *meta*-F). Anal. Calcd for C$_{59}$H$_{52}$F$_{10}$N$_8$O$_3$Zn$_3$ (M$_r$ = 1371.5 g mol^{-1}): C, 54.21 %; H, 4.01 %; N, 8.57 %. Found: C, 54.12 %; H, 3.97 %; N, 8.46 %.

$Cu_2(L^3)$, 13a

To a dark yellow solution of H$_4$L^3 (200 mg, 0.21 mmol) in THF (25 cm^3) was added Cu(OAc)$_2 \cdot$H$_2$O (85 mg, 0.43 mmol, 2 eq), turning dark after stirring for 10 minutes in air. The mixture was stirred for 20 hours before THF was evaporated, affording dark green residues that were washed with hexanes (3 $\times$ 10 cm^3). The crude product was purified by flash column chromatography, eluting an orange fraction through aluminium oxide with CH$_2$Cl$_2$. Evaporation of the solvent afforded the product as an orange solid. Diffraction-quality crystals were obtained from a pyridine solution on slow evaporation of the solvent. Yield: 1.25 g, 59 %. ESI-MS: m/z: 1058 [M $-$ 2H]$^+$, 529 [M $-$ 2H]$^{2+}$. FT-IR (ATR, solid state): ν / cm^{-1}: 1552 (imine). UV/vis (THF): λ_{max} 220 nm, $\epsilon = 26,148\pm$ 2326 dm^3 mol^{-1} cm^{-1}. Anal. Calcd for C$_{70}$H$_{30}$F$_{10}$N$_{12}$Cu$_2$ (M$_r$ = 1374 g mol^{-1}): C, 61.12 %; H, 3.64 %; N, 12.22 %. Found: C, 60.86 %; H, 3.48 %; N, 11.88 %.

Alternative synthesis for Cu$_2$(L^3), 13a

To a dark yellow solution of H$_4$L^3 (500 mg, 0.5 mmol) in THF (75 cm^3) was added a solution of KN(SiMe$_3$) (400 mg, 2 mmol, 4 eq) in THF (20 cm^3). The solution was stirred for 4 hours, over which time the solution slowly turned dark green. The mixture was added to a slurry of brown, anhydrous CuCl$_2$ (134 mg, 1 mmol, 2 eq) in THF (10 cm^3) previously cooled to -50 °C. On warming to room temperature, the mixture turned dark brown. After stirring for 16 hours the solvent was removed under vacuum. The crude product was purified by flash column chromatography in air, eluting an orange fraction with CH$_2$Cl$_2$ through aluminium oxide. Evaporation of the solvent afforded a dark orange solid. Yield: 440 mg, 75 %.

[CoCp$_2^*$]$_2$[Cu$_2$(L^3)], 13a^{2-}

To an orange solution of Cu$_2$(L^3) (20 mg, 20 μmol) in C$_6$D$_6$ (0.7 cm^3) was added a solution of CoCp$_2^*$ (13 mg, 40 μmol, 2 eq) in d_3-MeCN (0.3 cm^3). The solution rapidly turned dark indigo. ^{1}H NMR (C$_6$D$_6$): δ_H / ppm: 9.06 (s, 4H, imine), 7.73 (broad s, 65 H, CoCp$_2^*$), 7.08 (s, 4H, Ar C-H), 6.72 (s, 2H, *meso*-H), 6.70 (d, 4H, $^3J_{HH}$ = 3.4 Hz, pyrrole β-H), 6.57 (d, 4H, $^3J_{HH}$ = 3.4 Hz, pyrrole β-H), 2.09 (s, 12H, Ar-CH$_3$). ^{13}C{^{1}H} NMR (C$_6$D$_6$): δ_C / ppm: 156.6 (imine), 146.3, 143.0, 138.4, 136.0, 131.5, 124.5 (*meso*-C), 122.7 (Ar C-H), 113.9 (pyrrole β-C), 110.3 (pyrrole β-C), 19.2 (Ar-CH$_3$). ^{19}F{^{1}H} NMR (C$_6$D$_6$): δ_F / ppm: -139.97 (d, $^3J_{FF}$ = 19.1 Hz, Ar^F *ortho*-F), -162.46 (t, $^3J_{FF}$ = 22.0 Hz, Ar^F *para*-F) , -166.16 (broad t, $^3J_{FF}$ = 23.2 Hz, Ar^F *meta*-F).

Cu$_2$(L^4), 13b

To a dark yellow solution of H$_4$L^4 (190 mg, 0.17 mmol) in THF (60 cm^3) was added a solution of KN(SiMe$_3$) (141 mg, 0.7 mmol, 4 eq) in THF (15 cm^3), forming a mixture of a dark green solution with some suspended green solids. After 4 hours of stirring the entire mixture was added to a cooled slurry of brown, anhydrous CuCl$_2$ (47 mg, 0.35 mmol, 2 eq) in THF (5 cm^3). The mixture was stirred for 16 hours, during which time the green mixture darkened further. THF was removed under vacuum and the green solids were dissolved in CH$_2$Cl$_2$, in air. An orange fraction was eluted through a column of aluminium oxide using CH$_2$Cl$_2$ to yield the pure product as an orange solid after evaporation of the solvent. Diffraction-quality crystals were grown by slow vapour diffusion of hexanes into a saturated THF solution, in a semi-open vial. Yield: 150 mg, 74 %. ESI-MS: m/z: 1203

(M^+). FT-IR (ATR, solid state): ν / cm^{-1}: 1574 (imine). UV/vis (THF): λ_{max} 240 nm, $\epsilon = 102,218 \pm 1653$ dm^3 mol^{-1} cm^{-1}. Anal. Calcd for $C_{62}H_{30}F_{10}N_8Cu_2$ ($M_r = 1203$ g mol^{-1}): C, 61.85 %; H, 2.51 %; N, 9.31 %. Found: C, 61.71 %; H, 2.60 %; N, 9.19 %.

$Cu_2(L^5)$ dipyrrin macrocycle, 14

A benzene solution of **13a** (20 mg, 2 μmol) was left to stand in benzene for 10 days, in an attempt to grow single crystals of that compound without coordinated solvent molecules. The solution turned dark indigo over this time, and the small amount of crystals that were obtained were of the dipyrrin Pacman macrocycle. Similar colour changes also occur in THF, CH$_2$Cl$_2$ and MeCN.

Attempted rational syntheses included: stirring a benzene solution (100 cm^3) of **13a** (200 mg, 0.19 mmol) for 5 days at room temperature, in air; sparging air through a second solution for 5 days at room temperature, whilst stirring; and refluxing a third solution in air for 3 days at 80 °C. Finally, a 5 cm^3 benzene solution of **3a** (80 mg, 0.08 mmol) was irradiated for 24 hours under an atmosphere of air, using a quartz UV cuvette ($\lambda = 254$ nm). In all cases, solutions darkened significantly, but TLC and UV/vis analysis indicated that the %conversion was low. **14** may be separated from **13a** by column chromatography, as **13a** elutes through aluminium oxide with high retention in CH$_2$Cl$_2$, whereas **14** does not; the latter can be eluted from the column using methanol after **13a** has been removed. However, the yields from these reactions were miniscule, and the dark blue solids could only be isolated in milligram quantities. As **13a** and **14** have similar masses and are both paramagnetic, the formation of **14** cannot reliably be differentiated from **13a** by mass spectrometry, NMR spectroscopy or elemental analysis.

$Fe_2(L^3)$, 15a

A slurry of FeCl$_2$Py$_4$ (354 mg, 0.8 mmol, 2 eq) in hexanes (10 cm^3) was cooled to -35 °C. To the slurry was added a pentane solution of LiCH$_2$SiMe$_3$ (1.8 cm^3, 1 mol dm^{-3}, 1.8 mmol, 2.25 eq), rapidly forming a dark orange solution. As the solution warmed to room temperature, a purple precipitate formed in a colourless solution, which redissolved within minutes to form a red/purple solution. This solution of Fe(CH$_2$SiMe$_3$)$_2$Py$_2$ was stirred for 3 hours at room temperature before it was added by filter cannula to a dark orange solution of H$_4$L^3 (356 mg, 0.4 mmol, 1 eq) in THF (50 cm^3), which immediately turned dark red. The mixture was stirred for a further 6 hours before the solvent was removed under vacuum,

affording a red solid that was dried at 60 °C under vacuum. Diffraction-quality crystals were grown from a standing THF solution layered with hexane. Yield: 290 mg, 78 %. Red solids of **15a** turn black within days inside the glove box, and within tens of seconds in air under fomblin oil. X-ray crystallography was achieved by covering crystals with fomblin oil in a sealed vial and rapidly mounting the first crystal onto the goniometer head and freezing in the cryo-stream; all other crystals turned black during the cell-check part of the crystallography experiment. This sensitivity precluded further characterisation by mass spectrometry and elemental analysis. Anal. Calcd for $C_{50}H_{30}F_{10}Fe_2N_8 \cdot 3\,(C_4H_8O_1)$ ($M_r = 1260.11$ g mol^{-1}): C, 59.04 %; H, 4.32 %; N, 8.89 %. Found: C, 50.32 %; H, 4.41 %; N, 7.47 %.

$Fe_2(L^4)$, 15b

Prepared as described for **15a**, above. $Fe(CH_2SiMe_3)_2Py_2$ was first prepared *in situ* from the reaction of $FeCl_2Py_4$ (420 mg, 0.9 mmol, 2 eq) and a pentane solution of $LiCH_2SiMe_3$ (2.1 cm^3, 1 mol dm^{-3}, 2.1 mmol, 2.3 eq) at -35 °C. It was then added to a THF solution of H_4L^4 (512 mg, 0.45 mmol, 1 eq, 50 cm^3), which quickly turned red. The solvent was removed under vacuum and the red solids were dried at 70 °C. Diffraction-quality crystals were grown by slow diffusion of hexanes into a THF solution in a semi-open vessel. Yield: 394 mg, 70 %. **15b** was as sensitive as **15a**; this compound has not been characterised by mass spectrometry or elemental analysis.

$Fe(Py)(L^2\text{-}CH_2SiMe_3)$, 17

Prepared as described for **15a**, above. $Fe(CH_2SiMe_3)_2Py_2$ was first prepared *in situ* from the reaction of $FeCl_2Py_4$ (446 mg, 1 mmol, 1 eq) and a pentane solution of $LiCH_2SiMe_3$ (1.34 cm^3, 1 mol dm^{-3}, 1.34 mmol, 1.34 eq) at -35 °C. It was then added to a hexane solution of HL^2 (480 mg, 1 mmol, 1 eq, 50 cm^3), which immediately turned dark red. The solvent was removed under vacuum and the red solids were dried at 70 °C. Diffraction-quality crystals were grown from a hot hexanes solution on slow cooling to room temperature. Yield after crystallisation: 290 mg, 42 %. Repeated syntheses did not give single crystals of the desired iron-alkyl complex from cold crystallisation attempts. No satisfactory elemental analyses obtained. Anal. Calcd for $C_{29}H_{35}F_5Fe_1N_4Si_1$ ($M_r = 618.10$ g mol^{-1}): C, 56.30 %; H, 5.71 %; N, 9.06 %. Found: C, 51.74 %; H, 6.67 %; N, 7.46 %.

FeBr(L^2), 18

To a dark orange solution of HL^2 (200 mg, 0.4 mmol) in THF (20 cm^3) was added a solution of KN(SiMe$_3$) (84 mg, 0.4 mmol, 1 eq) in THF (5 cm^3), instantly forming a dark magenta solution. The solution was stirred for 1 hour before it was added to a slurry of FeBr$_2$(THF)$_2$ (151 mg, 0.4 mmol, 1 eq) in THF (5 cm^3), cooled to -30 °C. The mixture rapidly turned dark blue and white solids precipitated from the solution. After 16 hours of stirring, the solvent was removed under vacuum and the solids were dried. The crude product was dissolved in toluene and filtered by cannula. The blue toluene solution was concentrated and then stored at -30 °C, yielding yellow microcrystalline material that was isolated by filtration and dried under vacuum at 60 °C. The blue supernatant was concentrated and again cooled to yield a second crop that was similarly isolated. Diffraction-quality, yellow crystals were grown by slow vapour diffusion of hexanes into a saturated THF solution, in a semi-open vessel. Yield: 200 mg, 82 %. MALDI-TOF-TOF-MS (anthracene matrix): m/z: 1221.9 M$^+$, dimer; 1062.1 [M $-$ Br]$^+$, dimer; 610.0 M$^+$, monomer. No satisfactory elemental analyses obtained. Anal. Calcd for C$_{25}$H$_{24}$Br$_1$F$_5$Fe$_1$N$_4$ (M$_r$ = 610.9 g mol^{-1}): C, 49.10 %; H, 3.96 %; N, 9.17 %. Found: C, 43.45 %; H, 3.95 %; N, 7.62 %.

Ni$_2$(L^3), 19

A dark yellow solution of H$_4$L^3 (350 mg, 0.37 mmol) in THF (100 cm^3) was stirred in air and Ni(OAc)$\cdot$4 H$_2$O (194 mg, 0.78 mmol, 2.1 eq) was added as a solid. The solution turned dark red/brown over 20 hours, after which time the solvent was removed under vacuum. The dark residues were dissolved in CH$_2$Cl$_2$ and eluted through an aluminium oxide column. The pure product was isolated from the first, red fraction after removal of the solvent. Yield: 78 mg, 20 %. ESI-MS: m/z: 1048 [M $-$ 2H]$^+$. No satisfactory elemental analyses obtained. Anal. Calcd for C$_{50}$H$_{30}$F$_{10}$N$_8$Ni$_2$ (M$_r$ = 1050 g mol^{-1}): C, 57.18 %; H, 2.88 %; N, 10.67 %. Found: C, 58.41 %; H, 2.66 %; N, 9.79 %.

Alternative synthesis of Ni$_2$(L^3), 19

To a dark yellow solution of H$_4$L^3 (500 mg, 0.53 mmol) in THF (100 cm^3) was added a solution of KN(SiMe$_3$) (427 mg, 2.1 mmol, 4 eq) in THF (50 cm^3), slowly turning the solution dark green. After 16 hours, the green solution was added to a slurry of NiBr$_2$(DME) (339 mg, 1.1 mmol, 2 eq) in THF (5 cm^3) at -80 °C and the mixture was stirred for a further 24 hours. The solution slowly turned dark

red/brown over this time. Removal of the solvent under vacuum afforded dark red residues that were purified in air as described above. Yield: 278 mg, 50 %.

Pd$_2$(L^3), 20

To a dark yellow solution of H$_4$L^3 (500 mg, 0.5 mmol) in THF (100 cm^3) was added Pd(OAc)$_2$ (252 mg, 1.1 mmol, 2.1 eq), in portions, in air. The mixture was stirred for 16 hours, over which time the solution turned dark red. The solvent was removed under vacuum and the dark red residues were washed with MeCN (3 × 5 cm^3), and then Et$_2$O (3 × 5 cm^3). The dark red solids were dried under vacuum. Diffraction-quality crystals were grown by slow vapour diffusion of hexanes into a saturated THF solution, in a semi-open vessel. Yield: 343 mg, 56 %. ^{1}H NMR (CDCl$_3$): δ_H / ppm: 7.30 (s, 4H, imine), 6.81 (s, 4H, Ar C-H), 6.74 (d, 4H, $^3J_{HH}$ = 4 Hz, pyrrole β-H), 6.43 (s, 2H, *meso*-H), 5.90 (d, 4H, $^3J_{HH}$ = 4 Hz, pyrrole β-H), 2.08 (s, 12H, Ar-CH$_3$). ^{19}F{^{1}H} NMR (CDCl$_3$): δ_F / ppm: −137.8 (broad s, 4F, Ar^F *ortho*-F), −156.7 (t, 2F, $^3J_{FF}$ = 23 Hz, Ar^F *para*-F), −162.3 (broad s, 4F, Ar^F *meta*-F). Anal. Calcd for C$_{50}$H$_{30}$F$_{10}$N$_8$Pd$_2$ (M$_r$ = 1144.8 g mol^{-1}): C, 52.42 %; H, 2.64 %; N, 9.78 %. Found: C, 52.33 %; H, 2.76 %; N, 9.72 %.

UO$_2$Cl(L^2), 21

Pyridine (15 cm^3) was added to a stirred mixture of HL^2 (400 mg, 0.84 mmol) and UO$_2${N(SiMe$_3$)$_2$}$_2$(Py)$_2$ (630 mg, 0.84 mmol, 1 eq) at −60 °C, forming a purple solution. The solution was stirred at this temperature for 2 hours and at room temperature for a further 12 hours, after which it had become dark blue in colour. A solution of pyridinium chloride (97.0 mg, 0.84 mmol, 1 eq) in pyridine (4 cm^3) was added to the blue solution and the mixture stirred for 12 hours. The solvent was removed under vacuum, affording dark blue solids that were washed with hexanes (2 × 20 cm^3) and dried under vacuum for 12 hours. Purple/blue single crystals suitable for X-ray crystallography were obtained from a concentrated benzene solution. Yield: 500 mg, 76 %. ^{1}H NMR (d$_8$-THF): δ_H / ppm: 9.52 (s, 2H, imine), 8.53 (m, 2H, 2,6-pyridine), 7.65 (m, 1H, 4-pyridine), 7.30 (d, 2H, $^3J_{HH}$ = 4.3 Hz, pyrrole β-H), 7.25 (m, 2H, 3,5-pyridine), 7.18 (d, 2H, $^3J_{HH}$ = 4.3 Hz, pyrrole β-H), 2.01 (s, 18H, *t*Bu). ^{13}C{^{1}H} NMR (d$_8$-THF): δ_C / ppm: 160.9, 159.8, 151.0, 147.6, 136.4, 135.9, 135.2, 129.2, 124.9, 124.5, 66.2, 32.7, 31.1, 23.7, 14.6. ^{19}F{^{1}H} NMR (d$_8$-THF): δ_F / ppm: −140.68 (m, 2F, Ar^F *ortho*-F), −155.19 (t, 1F, $^3J_{FF}$ = 23.5 Hz, Ar^F

para-F), -163.34 (m, 2F, Ar^F *meta*-F). FT-IR (Nujol): ν / cm^{-1}: 1556 (imine), 847 (asym. UO$_2$ stretch). UV/vis (toluene): λ_{max} 598 nm, $\epsilon = 43,400$ dm^3 mol^{-1} cm^{-1}. Anal. Calcd for C$_{25}$H$_{24}$ClF$_5$N$_4$O$_2$U (M$_r$ = 780.96 g mol^{-1}): C, 38.45 %; H, 3.10 %; N, 7.17 %. Found: C, 38.40 %; H, 3.25 %; N, 7.04 %.

Alternative synthesis of UO$_2$Cl(L^2), 21

A mixture of UO$_2${N(SiMe$_3$)$_2$}$_2$(THF)$_2$ (1.536 g, 2.1 mmol) and UO$_2$Cl$_2$(THF)$_2$ (1.014 g, 2.1 mmol, 1 eq) was suspended in toluene (10 cm^3) and stirred for 10 minutes, resulting in a dark orange suspension which was added to a red solution of HL^2 (2.0 g, 4.2 mmol, 2 eq) in toluene (10 cm^3). The solution immediately turned purple. After stirring for 2 hours the solution was filtered and the filtrate cooled overnight at -30 °C, yielding **21** as a crop of dark purple crystals which were isolated by filtration and dried under vacuum for 16 hours. Yield: 1.76 g, 63 %. ^{1}H NMR (C$_6$D$_6$): δ_H / ppm: 8.75 (s, 2H, imine), 6.67 (d, 2H, $^3J_{HH}$ = 4.4 Hz, pyrrole β-H), 6.52 (d, 2H, $^3J_{HH}$ = 4.4 Hz, pyrrole β-H), 1.92 (s, 18H, tBu). ^{13}C{^{1}H} NMR (C$_6$D$_6$): δ_C / ppm: 159.8, 157.8, 146.7, 146.0, 144.1, 138.8, 136.7, 134.1, 124.0, 65.7, 30.7. ^{19}F{^{1}H} NMR (C$_6$D$_6$): δ_F / ppm: -138.76 (m, 2F, Ar^F *ortho*-F), -151.43 (t, 1F, $^3J_{FF}$ = 23.5 Hz, Ar^F *para*-F), -160.45 (m, 2F, Ar^F *meta*-F).

(TiCp$_2$Cl)OUO(TiCp$_2$Cl)(Cl)(L^2), 22

To a purple/blue solution of **21** (200 mg, 0.26 mmol) in toluene (15 cm^3) was added a solution of [Cp$_2$TiCl]$_2$ (120 mg, 0.28 mmol, 1.1 eq) in toluene (10 cm^3), at -40 °C. The solution was stirred for 12 hours at this temperature, forming a dark blue solution which was allowed to warm to room temperature, and then stirred for a further 48 hours, affording a blue precipitate. The blue solids of **22** were isolated by filtration and dried under vacuum. Single crystals suitable for X-ray diffraction were grown from a concentrated benzene solution at room temperature. Yield: 115 mg, 37 %. ^{1}H NMR (d_8-THF): δ_H / ppm: 43.63 (s, 20H, Cp), -17.38 (s, 2H, pyrrole β-H), -22.45 (s, 2H, pyrrole β-H), -31.68 (s, 18H, tBu), -37.33 (s, 2H, imine). ^{19}F{^{1}H} NMR (d_8-THF): δ_F / ppm: -153.48 (d, 2F, $^3J_{FF}$ = 20.0 Hz, Ar^F *ortho*-F,), -161.97 (t, 1F, $^3J_{FF}$ = 22.6 Hz, Ar^F *para*-F), -170.44 (t, 2F, $^3J_{FF}$ = 20.1 Hz, Ar^F *meta*-F). FT-IR (Nujol): ν / cm^{-1}: 1560 (imine), 630 (asym. UO$_2$ stretch). UV/vis/NIR (toluene): λ_{max} 598 nm, $\epsilon = 11,000$ dm^3 mol^{-1} cm^{-1}. Anal. Calcd for C$_{45}$H$_{44}$Cl$_3$F$_5$N$_4$O$_2$Ti$_2$U (M$_r$ = 1207.98 g mol^{-1}): C, 44.74 %; H, 3.67 %; N, 4.64 %. Found: C, 44.59 %; H, 3.69 %; N, 4.51 %.

Attempted synthesis of $(TiCp_2Cl)OUO(Cl)(L^2)$, 23

To a purple/blue solution of **21** (50 mg, 0.06 mmol) in d_8-THF (0.5 cm^3) was added $[TiCp_2Cl]_2$ (13 mg, 0.03 mmol, 0.5 eq), giving a purple solution. The ^{1}H NMR spectrum taken after 5 minutes contained resonances corresponding to complex **21**, smaller resonances corresponding to complex **22** and a set of resonances which were assigned to the U^V species $[(Cp_2ClTi)OUO(L^2)]$ (**23**). After approximately 1 hour, microcrystalline precipitate was evident in the NMR tube. After 48 hours at room temperature, all three species were still present in solution. ^{1}H NMR (d_8-THF): δ_H / ppm: 19.35 (s, 10H, Cp), -1.12 (d, 2H, $^3J_{HH}$ = 3.6 Hz, pyrrole β-H), -3.11 (d, 2H, $^3J_{HH}$ = 3.6 Hz, pyrrole β-H), -7.84 (s, 2H, imine C-H), -8.58 (s, 18H, tBu). ^{19}F$\{^1$H$\}$ NMR (d_8-THF): δ_F / ppm: -141.35 (d, 2F, $^3J_{FF}$ = 32.7 Hz, Ar^F $ortho$-F,), -145.82 (d, 2F, $^3J_{FF}$ = 32.7 Hz, Ar^F $ortho$-F,), -158.00 (t, 1F, $^3J_{FF}$ = 22.1 Hz, Ar^F $para$-F), -165.96 (t, 2F, $^3J_{FF}$ = 23.2 Hz, Ar^F $meta$-F), -166.24 (t, 2F, $^3J_{FF}$ = 23.2 Hz, Ar^F $meta$-F).

Attempted synthesis of $[Cr^I(C_6H_6)_2][UO_2Cl(L^2)]$

To a purple/blue solution of **21** (50 mg, 0.06 mmol) in CH_2Cl_2 was added $Cr^0(C_6H_6)_2$ (12.5 mg, 0.06 mmol, 1 eq), instantly forming a magenta solution. The X-band EPR spectrum was dominated by the resulting Cr^I signal, complete with hyperfine coupling to both the ^{53}Cr nucleus and all 12 benzene protons.

Attempted synthesis of $[CoCp_2][UO_2Cl(L^2)]$, 21 $^{\cdot-}$

$CoCp_2$ (23 mg, 0.12 mmol) was added to a purple/blue solution of **21** (100 mg, 0.13 mmol, 1.1 eq) in C_6D_6 (2 cm^3), immediately forming a magenta solution. The product was strongly paramagnetic and NMR-silent. Single crystals of **21** $^{\cdot-}$ were grown from THF from a reaction between **21** and two equivalents of $CoCp_2$. UV/vis/NIR (toluene): λ / nm 294 (ϵ = 42,000 dm^3 mol^{-1} cm^{-1}), 346sh (12,000), 548 (27,000), 598 (50,000). No absorption observed in the NIR region. Dilute solution of **21** $^{\cdot-}$ in toluene has a more purple hue than that of **21**, which appears distinctly blue.

Attempted synthesis of $[CoCp_2]_2[UO_2Cl(L^2)]$, 21 $^{\cdot 2-}$

$CoCp_2$ (47 mg, 0.25 mmol, 1.92 eq) was added to a purple/blue solution of **21** (100 mg, 0.13 mmol) in C_6D_6 (2 cm^3), immediately forming a magenta solution. The product was strongly paramagnetic and NMR-silent. Attempts were made to grow single crystals of the product, without success. UV/vis/NIR (toluene):

λ / nm 311 (ϵ = 39,000 dm^3 mol^{-1} cm^{-1}), 345sh (19,000), 539 (26,000), 595 (17,000). No absorption observed in the NIR region. Dilute solution of **21**$^{\cdot 2-}$ in toluene is red/purple, in contrast to that of **21**$^{\cdot -}$, which is purple.

Attempted synthesis of [UO$_2$(L^2)]K$_2$

Pyridine (5 cm^3) was added to a mixture of **21** (36 mg, 46 μmol) and potassium metal (5 mg, 0.13 mmol, 2.8 eq), forming a dark purple solution. A multitude of paramagnetically-shifted ^{1}H NMR resonances were observed shortly after the reaction was started, providing no definitive structural information and indicating that a large number of products are formed from the reaction. Attempts were made, without success, to isolate single crystals from the reaction mixture.

8.4 X-ray crystallographic data

Table 8.1: Summary of X-ray crystallographic data for compounds **2**, HL^2, H_4L^3 and H_4L^4.

	2	HL^2	H_4L^3	H_4L^4
CCDC Registry	1032820	1032821	1032823	1032824
Formula	$C_{17}H_9F_5N_2O_2$	$C_{25}H_{25}F_5N_4$	$C_{50}H_{34}F_{10}N_8$, $4(C_4H_8O)$	$C_{62}H_{34}F_{10}N_8$, $4(CH_3OH)$, H_2O
M_r / g mol^{-1}	368.26	476.49	1225.26	1227.15
Colour, habit	Colourless block	Red plate	Yellow plate	Pale brown needle
Crystal size / mm^3	$0.51 \times 0.26 \times 0.07$	$0.43 \times 0.20 \times 0.07$	$0.60 \times 0.34 \times 0.18$	$0.3512 \times 0.0378 \times 0.0262$
Crystal system	Triclinic	Triclinic	Orthorhombic	Triclinic
Space group	$P\bar{1}$ (no. 2)	$P\bar{1}$ (no. 2)	$Pnn2$ (no. 34)	$P\bar{1}$ (no. 2)
a / Å	10.0877(8)	12.0938(6)	29.85511(18)	13.5433(7)
b / Å	11.7180(8)	14.2191(11)	27.674(2)	14.8529(9)
c / Å	13.6686(9)	14.6822(11)	7.7730(8)	17.1922(7)
α / deg	95.540(6)	104.393(7)	90	107.163(5)
β / deg	93.267(6)	90.013(5)	90	98.360(4)
γ / deg	95.334(6)	95.477(5)	90	108.596(5)
V / Å^3	1597.7(2)	2433.6(3)	6421.3(9)	3020.3(3)
Z	4	4	4	2
T / K	170(2)	170(2)	170(2)	120(2)
$F(000)$	744	992	2560	1268
Radiation type	Mo Kα	Mo Kα	Mo Kα	Cu Kα
μ / mm^{-1}	0.141	0.110	0.100	0.917
Absorption correction	Multi-scan	Multi-scan	Multi-scan	Gaussian
Transmission factors	$0.51189 - 1.0$	$0.909 - 1.0$	$0.61005 - 1.0$	$0.929 - 0.991$
$2\theta_{max}$ / deg	54.968	53.764	52.1	102.5
Total no. of reflns	15,419	14,436	31,363	31,215
No. of unique reflns	7326	14,436	9433	6323
No. of reflns with $I \geq 2\sigma(I)$	3678	9136	5814	3782
R_{int}	0.052	–	0.047	0.089
$(\sin\theta)/\lambda$ / Å^{-1}	0.649	0.662	0.618	0.230
No. of parameters	469	634	797	837
H-atom treatment	Constrained	Mixed	Constrained	Mixed
R (F^2, all data)	0.1438	0.1404	0.1145	0.1361
R$_w$ (F^2, all data)	0.1939	0.1692	0.2004	0.2337
R (F, I> 2θ(I))	0.0626	0.0831	0.0651	0.0781
R$_w$ (F, I> 2θ(I))	0.1379	0.1487	0.1737	0.1949
G.O.F.	1.018	1.125	0.961	1.024

Table 8.2: Summary of X-ray crystallographic data for compounds **7b**, **8b**, **9** and **10**.

	7b	8b	9	10
CCDC Registry	1037480	1037478	1037477	1037479
Formula	$2(C_{70}H_{46}F_{10}N_8O_2Zn_2)$	$C_{86}H_{82}F_{10}N_8O_4Zn_4$	$C_{62}H_{56}F_{10}N_8O_3Zn_4$	$C_{66}H_{36}F_{10}N_8O_5Zn_4$
M_r / g mol^{-1}	2702.76	1743.07	1396.50	1472.13
Colour, habit	Yellow plate	Dark yellow block	Yellow block	Yellow block
Crystal size / mm^3	$0.6411 \times 0.1615 \times 0.0893$	$0.9868 \times 0.7507 \times 0.6993$	$0.8173 \times 0.4652 \times 0.0622$	$0.3120 \times 0.2660 \times 0.1000$
Crystal system	Monoclinic	Trigonal	Monoclinic	Triclinic
Space group	$P2_1/c$ (no. 14)	$R3c$ (no. 161)	$P2_1/c$ (no. 14)	$P\bar{1}$ (no. 2)
a / Å	16.2526(7)	24.4911(4)	16.5879(5)	12.5794(3)
b / Å	32.0839(14)	24.4911(4)	19.5250(6)	14.5209(8)
c / Å	31.1888(15)	89.0912(17)	20.8445(7)	21.8649(10)
α / deg	90	90	90	104.772(4)
β / deg	114.868(4)	90	94.577(3)	99.895(3)
γ / deg	90	120	90	102.885(4)
V / Å^3	14,755.3(12)	46,278.9(17)	6729.6(4)	3652.2(3)
Z	4	18	4	2
T / K	173(2)	170(2)	170(2)	173(2)
F(000)	5500	16,128	2808	1476
Radiation type	Mo Kα	Mo Kα	Mo Kα	Mo Kα
μ / mm^{-1}	0.72	0.98	1.48	1.37
Absorption correction	Multi-scan	Multi-scan	Analytical	Multi-scan
Transmission factors	$0.870 - 0.938$	$0.299 - 0.410$	$0.573 - 0.951$	$0.418 - 1.000$
$2\theta_{max}$ / deg	54.768	46.498	52.744	58.448
Total no. of reflns	101,227	92,030	55,629	83,941
No. of unique reflns	28,568	14,042	13,739	18,282
No. of reflns with I$\geq 2\sigma$(I)	11,790	12,365	9459	11,480
R_{int}	0.128	0.044	0.048	0.095
$(\sin\theta)/\lambda$ / Å^{-1}	0.648	0.555	0.625	0.687
No. of parameters	1633	1324	812	938
H-atom treatment	Constrained	Constrained	Constrained	Constrained
R (F^2, all data)	0.1083	0.0516	0.0830	0.1379
R_w (F^2, all data)	0.3154	0.1267	0.1403	0.3069
R (F, I> 2σ(I))	0.1055	0.0435	0.0480	0.0992
R_w (F, I> 2σ(I))	0.2624	0.1202	0.1230	0.2673
G.O.F.	0.963	1.047	1.029	1.054

Table 8.3: Summary of X-ray crystallographic data for compounds **12**, **13a**, **13b** and **14**.

	12	**13a**	**13b**	**14**
CCDC Registry	1509316	1032825	1032826	—
Formula	$C_{59}H_{52}F_{10}N_8O_3Zn_3$, $3.5\,(C_6H_6)$	$C_{70}H_{50}Cu_2F_{10}N_{12}$, $3\,(C_5H_5N)$	$C_{62}H_{30}Cu_2F_{10}N_8$	$2\,(C_{50}H_{28}Cu_2F_{10}N_8)$, C_6H_6, $2\,(C_6H_{14})$
M_r / g mol^{-1}	1580.57	1613.60	1204.02	2366.21
Colour, habit	Yellow block	Red block	Dark brown block	Black blade
Crystal size / mm^3	$0.44 \times 0.42 \times 0.13$	$0.59 \times 0.23 \times 0.17$	$0.5629 \times 0.2172 \times 0.0353$	$? \times ? \times ?$
Crystal system	Triclinic	Triclinic	Triclinic	Monoclinic
Space group	$P\bar{1}$ (no. 2)	$P\bar{1}$ (no. 2)	$P\bar{1}$ (no. 2)	$P2_1/c$ (no. 2)
a / Å	13.6817(3)	12.1160(3)	8.0044(2)	14.10948(14)
b / Å	17.1958(4)	14.6689(4)	16.3501(4)	20.67334(16)
c / Å	17.9104(4)	21.0498(5)	20.0568(4)	37.7371(4)
α / deg	105.877(2)	89.765(2)	97.223(2)	90
β / deg	105.185(2)	86.422(2)	98.673(2)	98.0578(10)
γ / deg	104.788(2)	85.304(2)	92.044(2)	90
V / Å^3	3660.90(17)	3721.32(16)	2570.28(10)	10,898.87(18)
Z	2	2	2	4
T / K	170(2)	170(2)	170(2)	—
$F(000)$	1626	1656	1212	4824
Radiation type	Mo Kα	Mo Kα	Mo Kα	Cu Kα
μ / mm^{-1}	1.06	0.655	0.915	1.66
Absorption correction	Analytical	Multi-scan	Multi-scan	—
Transmission factors	0.472 – 0.780	0.94412 – 1.0	0.82365 – 1.0	—
$2\theta_{max}$ / deg	55.464	58.4	58.772	153.166
Total no. of refns	88,885	42,650	13,667	175,565
No. of unique refns	13,872	17,034	13,667	22,705
No. of refns with $I \geq 2\sigma(I)$	10,986	12,537	10,767	18,500
R_{int}	0.063	0.033	0.040	0.108
$(\sin\theta)/\lambda$ / Å^{-1}	0.610	0.649	0.707	0.631
No. of parameters	946	990	740	1435
H-atom treatment	Constrained	Mixed	Mixed	Constrained
R (F^2, all data)	0.0579	0.0872	0.0556	0.0751
R_w (F^2, all data)	0.0880	0.1779	0.1182	0.1691
R (F, I> 2θ(I))	0.0401	0.0607	0.0405	0.0616
R_w (F, I> 2θ(I))	0.0816	0.1605	0.1109	0.1586
G.O.F.	1.044	1.024	1.026	1.037

Table 8.4: Summary of X-ray crystallographic data for compounds **15a**, **15b**, **16**, **17** and **18**.

	15a	15b	16	17	18
CCDC Registry	—	—	—	—	—
Formula	$C_{62}H_{24}F_{10}Fe_2N_8O_3$	2 $(C_{72}H_{40}F_{10}Fe_2N_{10})$, 5 (C_4H_8O)	$C_{78}H_{60}F_{10}Fe_2LiN_8O_5$	$C_{34}H_{40}F_5FeN_5Si$ 0.5 (C_6H_{14})	$C_{50}H_{48}Br_2F_{10}Fe_2N_8$, C_4H_8O
M_r / g mol^{-1}	1260.83	3054.19	1497.98	740.73	1294.58
Colour, habit	Red needle	Red plate	Red needle	Violet block	Yellow block
Crystal size / mm^3	—	0.13 × 0.04 × 0.03	—	0.39 × 0.17 × 0.11	0.42 × 0.26 × 0.09
Crystal system	Triclinic	Triclinic	Monoclinic	Triclinic	Triclinic
Space group	P1̄ (no. 2)	P1̄ (no. 2)	P2$_1$ (no. 4)	P1̄ (no. 2)	P1̄ (no. 2)
a / Å	12.005(5)	17.0574(6)	12.5556(16)	10.4749(2)	11.0997(2)
b / Å	12.670(5)	19.9848(9)	24.7455(19)	13.0465(3)	17.2840(3)
c / Å	19.082(5)	22.4454(8)	13.1600(11)	14.7265(3)	17.9945(3)
α / deg	96.270(5)	90.315(3)	90	80.456(2)	109.0758(15)
β / deg	100.077(5)	109.320(3)	110.532(3)	86.2584(18)	94.1059(14)
γ / deg	95.402(5)	96.790(3)	90	81.093(2)	100.7736(16)
V / Å^3	2821.5(18)	7161.7(5)	3829.0(7)	1959.12(8)	3172.21(10)
Z	2	2	2	2	2
T / K	173(2)	120(2)	120(2)	173(2)	170(2)
F(000)	1296	3136	1538	778	1296.0
Radiation type	Mo Kα	Cu Kα	Mo Kα	Mo Kα	Mo Kα
μ / mm^{-1}	0.60	3.96	0.457	0.47	1.786
Absorption correction	—	Gaussian	—	Analytical	Multi-scan
Transmission factors	0.769 − 0.813	0.780 − 0.939	—	0.926 − 0.979	—
2θ$_{max}$ / deg	59.724	53.4	57.056	52.744	50.054
Total no. of reflns	53,715	121,166	19,891	67,058	60,964
No. of unique reflns	14,481	15,720	13,954	8013	11,194
No. of reflns with I≥2σ(I)	12,380	6821	6129	5589	8316
R$_{int}$	0.018	0.209	0.060	0.085	0.059
(sin θ)/λ / Å^{-1}	0.701	0.509	0.672	0.625	0.595
No. of parameters	816	1861	805	452	737
H-atom treatment	Constrained	Constrained	Constrained	Constrained	Constrained
R (F^2, all data)	0.0413	0.2327	0.2172	0.0938	0.0832
R$_w$ (F^2, all data)	0.0875	0.3959	0.3698	0.1204	0.2017
R (F, I> 2θ(I))	0.0330	0.1253	0.1212	0.0571	0.0584
R$_w$ (F, I> 2θ(I))	0.0820	0.3228	0.3145	0.1074	0.1869
G.O.F.	1.024	1.086	1.016	1.021	1.076

Table 8.5: Summary of X-ray crystallographic data for compounds **20**, **21**, **21a** and **22**.

	20	**21**	**21a**	**22**
CCDC Registry	–	1446511	1507634	1446512
Formula	$C_{50}F_{10}N_8Pd_2$	$C_{37}H_{36}ClF_5N_4O_2U$	$2(C_{25}H_{24}ClF_5N_4O_2U)$, $2(C_{10}H_{10}Co)$, C_4H_8O	$C_{51}H_{50}Cl_3F_5N_4O_2Ti_2U$
M_r / g mol^{-1}	1115.38	937.18	2012.24	1286.13
Colour, habit	Red plate	Red plate	Red plate	Blue plate
Crystal size / mm^3	$0.38 \times 0.24 \times 0.08$	$0.11 \times 0.05 \times 0.04$	$0.51 \times 0.16 \times 0.06$	$0.12 \times 0.04 \times 0.02$
Crystal system	Orthorhombic	Monoclinic	Monoclinic	Monoclinic
Space group	$P2_12_12_1$ (no. 19)	Cc (no. 9)	$P2_1/c$ (no. 14)	$P2_1/c$ (no. 14)
a / Å	16.6901(3)	24.5647(2)	16.0945(2)	14.486(5)
b / Å	24.7460(5)	8.4279(1)	28.2241(4)	30.377(5)
c / Å	42.1350(7)	16.8859(1)	19.2594(3)	12.092(5)
α / deg	90	90	90	90
β / deg	90	91.172(1)	105.247(2)	107.081(5)
γ / deg	90	90	90	90
V / Å^3	17,402.3(6)	3495.14(5)	8440.7(2)	5086(3)
Z	12	4	4	4
T / K	170(2)	120(2)	170(2)	120(2)
F(000)	6456	1824	3912	2528
Radiation type	Mo Kα	Cu Kα	Mo Kα	Cu Kα
μ / mm^{-1}	0.69	14.35	4.35	13.44
Absorption correction	Analytical	Gaussian	Analytical	Gaussian
Transmission factors	0.933 – 0.984	0.743 – 0.871	0.757 – 0.950	0.982 – 0.996
$2\theta_{max}$ / deg	41.6	152.28	58.868	151.006
Total no. of reflns	180,151	34,748	117,037	75,069
No. of unique reflns	18,162	7244	19,317	9330
No. of reflns with I$\geq 2\sigma$(I)	14,068	7139	16,343	7021
R_{int}	0.161	0.033	0.036	0.158
$(\sin\theta)/\lambda$ / Å^{-1}	0.500	0.630	0.649	0.602
No. of parameters	1021	439	940	601
H-atom treatment	n/a	Mixed	Riding	Mixed
R (F^2, all data)	0.2429	0.0273	0.0451	0.0843
R_w (F^2, all data)	0.3344	0.0680	0.0757	0.1115
R (F, I> 2θ(I))	0.2117	0.0270	0.0334	0.0561
R_w (F, I> 2θ(I))	0.3294	0.0677	0.0711	0.1010
G.O.F.	7.267	1.038	1.069	1.063

References

[1] J. K. Laha, S. Dhanalekshmi, M. Taniguchi, A. Ambroise and J. S. Lindsey, *Org. Process Res. Dev.*, 2003, **7**, 799.

[2] C. M. Lemon, E. Karnas, M. G. Bawendi and D. G. Nocera, *Inorg. Chem.*, 2013, **52**, 10394.

[3] Z. Abada, S. Cojean, S. Pomel, L. Ferrié, B. Akagah, A. T. Lormier, P. M. Loiseau and B. Figadère, *Eur. J. Med. Chem.*, 2013, **67**, 158.

[4] C. Brückner, V. Karunaratne, S. J. Rettig and D. Dolphin, *Can. J. Chem.*, 1996, **74**, 2182.

[5] H. R. A. Golf, H.-U. Reissig and A. Wiehe, *Org. Lett.*, 2015, **17**, 982.

[6] V. Leen, M. V. der Auweraer, N. Boens and W. Dehaen, *Org. Lett.*, 2011, **13**, 1470.

[7] J. Lindsey, M. Taniguchi and D. Fan, "Methods and Intermediates for the Synthesis of Porphyrins", US Patent 7,951,939, 2011.

[8] J. S. Lindsey, G. R. G. III and L. Yu, US Patent 2003/0096978 A1, 2003.

[9] A. Dahan, T. Ashkenazi, V. Kuznetsov, S. Makievski, E. Drug, L. Fadeev, M. Bramson, S. Schokoroy, E. Rozenshine-Kemelmakher and M. Gozin, *J. Org. Chem.*, 2007, **72**, 2289.

[10] J. Eppinger, E. Herdtweck and R. Anwander, *Polyhedron*, 1998, **17**, 1195 .

[11] D. J. Darensbourg, M. W. Holtcamp, G. E. Struck, M. S. Zimmer, S. A. Niezgoda, P. Rainey, J. B. Robertson, J. D. Draper and J. H. Reibenspies, *J. Am. Chem. Soc.*, 1999, **121**, 107.

[12] C. Sheu, S. A. Richert, P. Cofre, B. Ross, A. Sobkowiak, D. T. Sawyer and J. R. Kanofsky, *J. Am. Chem. Soc.*, 1990, **112**, 1936.

[13] J. Cámpora, A. M. Naz, P. Palma, E. Álvarez and M. L. Reyes, *Organometallics*, 2005, **24**, 4878.

[14] G. Rowe, E. Rybak-Akimova and J. Caradonna, *Chem. -Eur. J.*, 2008, **14**, 8303.

[15] D. M. Barnhart, C. J. Burns, N. N. Sauer and J. G. Watkin, *Inorg. Chem.*, 1995, **34**, 4079.

[16] M. P. Wilkerson, C. J. Burns, R. T. Paine and B. L. Scott, *Inorg. Chem.*, 1999, **38**, 4156.

[17] H. Arp, M. Zirngast, C. Marschner, J. Baumgartner, K. Rasmussen, P. Zark and T. Müller, *Organometallics*, 2012, **31**, 4309.

[18] A. Altomare, G. Cascarano, C. Giacovazzo, A. Guagliardi, M. C. Burla, G. Polidori and M. Camalli, *J. Appl. Cryst.*, 1994, **27**, 435.

[19] G. M. Sheldrick, *Acta Cryst.*, 2008, **A64**, 112.

[20] O. V. Dolomanov, L. J. Bourhis, R. J. Gildea, J. A. K. Howard and H. Puschmann, *J. Appl. Cryst.*, 2009, **42**, 339.

[21] A. L. Spek, *Acta Cryst.*, 1990, **A46**, C34.

[22] M. J. Frisch, G. W. Trucks, H. B. Schlegel, G. E. Scuseria, M. A. Robb, J. R. Cheeseman, G. Scalmani, V. Barone, B. Mennucci, G. A. Petersson, H. Nakatsuji, M. Caricato, X. Li, H. P. Hratchian, A. F. Izmaylov, J. Bloino, G. Zheng, J. L. Sonnenberg, M. Hada, M. Ehara, K. Toyota, R. Fukuda, J. Hasegawa, M. Ishida, T. Nakajima, Y. Honda, O. Kitao, H. Nakai, T. Vreven, J. A. Montgomery, Jr., J. E. Peralta, F. Ogliaro, M. Bearpark, J. J. Heyd, E. Brothers, K. N. Kudin, V. N. Staroverov, R. Kobayashi, J. Normand, K. Raghavachari, A. Rendell, J. C. Burant, S. S. Iyengar, J. Tomasi, M. Cossi, N. Rega, J. M. Millam, M. Klene, J. E. Knox, J. B. Cross, V. Bakken, C. Adamo, J. Jaramillo, R. Gomperts, R. E. Stratmann, O. Yazyev, A. J. Austin, R. Cammi, C. Pomelli, J. W. Ochterski, R. L. Martin, K. Morokuma, V. G. Zakrzewski, G. A. Voth, P. Salvador, J. J. Dannenberg, S. Dapprich, A. D. Daniels, Ö. Farkas, J. B. Foresman, J. V. Ortiz, J. Cioslowski and D. J. Fox, Guassian09 Revision E.01, Gaussian Inc. Wallingford CT 2009.

[23] A. J. H. Wachters, *J. Chem. Phys.*, 1970, **52**, 1033.

[24] P. J. Hay, *J. Chem. Phys.*, 1977, **66**, 4377.

[25] A. D. McLean and G. S. Chandler, *J. Chem. Phys.*, 1980, **72**, 5639.

[26] K. Raghavachari, J. S. Binkley, R. Seeger and J. A. Pople, *J. Chem. Phys.*, 1980, **72**, 650.

[27] K. Raghavachari and G. W. Trucks, *J. Chem. Phys.*, 1989, **91**, 1062.

[28] R. C. B. Jr and L. A. Curtiss, *J. Comp. Chem.*, 1990, **11**, 1206.

[29] M. P. McGrath and L. Radom, *J. Chem. Phys.*, 1991, **94**, 511.

[30] L. A. Curtiss, M. P. McGrath, J. P. Blaudeau, N. E. Davis, R. C. Binning and L. Radom, *J. Chem. Phys.*, 1995, **103**, 6104.

[31] J. P. Blaudeau, M. P. McGrath, L. A. Curtiss and L. Radom, *J. Chem. Phys.*, 1997, **107**, 5016.

[32] S. H. Vosko, L. Wilk and M. Nusair, *Can. J. Phys.*, 1980, **58**, 1200.

[33] C. Lee, W. Yang and R. G. Parr, *Phys. Rev. B*, 1988, **37**, 785.

[34] A. D. Becke, *J. Chem. Phys.*, 1993, **98**, 5648.

[35] P. J. Stephens, F. J. Devlin, C. F. Chabalowski and M. J. Frisch, *J. Phys. Chem.*, 1994, **98**, 11623.

[36] T. Yanai, D. P. Tew and N. C. Handy, *Chem. Phys. Lett.*, 2004, **393**, 51.

[37] J. P. Perdew and Y. Wang, *Phys. Rev. B*, 1992, **45**, 13244.

[38] W. Küchle, M. Dolg, H. Stoll and H. Preuss, *J. Chem. Phys.*, 1994, **100**, 7535.

[39] X. Cao, M. Dolg and H. Stoll, *J. Chem. Phys.*, 2003, **118**, 487.

[40] X. Cao and M. Dolg, *J. Mol. Struct. (Theochem.)*, 2004, **673**, 203.

[41] A. Moritz, X. Cao and M. Dolg, *Theor. Chem. Acc.*, 2007, **118**, 845.

[42] A. Moritz and M. Dolg, *Theor. Chem. Acc.*, 2008, **121**, 297.

[43] M. Dolg, U. Wedig, H. Stoll and H. Preuss, *J. Chem. Phys.*, 1987, **86**, 866.

[44] G. Scalmani and M. J. Frisch, *J. Chem. Phys.*, 2010, **132**, 114110.

[45] S. Grimme, J. Antony, S. Ehrlich and H. Krieg, *J. Chem. Phys.*, 2010, **132**, 154104.

[46] L. Goerigk and S. Grimme, *Phys. Chem. Chem. Phys.*, 2011, **13**, 6670.

[47] S. Grimme, S. Ehrlich and L. Goerigk, *J. Comp. Chem.*, 2011, **32**, 1456.

[48] N. M. O'Boyle, A. L. Tenderholt and K. M. Langner, *J. Comp. Chem.*, 2008, **29**, 839.